NONLINEAR AEROELASTIC MODELLING OF LARGE WIND TURBINE COMPOSITE BLADES

by

Lin Wang

A thesis submitted in partial fulfilment for the requirements for the degree of Doctor of Philosophy at the University of Central Lancashire

May 2015

DECLARATION

I declare that while registered as a candidate for the research degree, I have not been a registered candidate or enrolled student for another award of the University or other academic or professional institution. I declare that no material contained in the thesis has been used in any other submission for an academic award and is solely my own work.

Signature of Candidate Lin Wang

ABSTRACT

The increasing size and flexibility of large wind turbine blades introduces significant aeroelastic effects, which are caused by fluid-structure interaction. These effects might result in aeroelastic instability problems, such as edgewise instability and flutter, which can be devastating to the blades and the wind turbine. Therefore, developing a reliable and efficient aeroelastic model to investigate the aeroelasticity characterisation of large wind turbine blades is crucial in the development of large wind turbines.

There are several aeroelastic models available today for wind turbine blades. Almost all of them are linear models based on assumption of small blade deflections, and do not take account of large deflection effects on modelling responses and loads. However, with the increasing size and flexibility of large wind turbine blades, this assumption is not valid anymore because the blades often experience large deflections, which introduce significant geometric nonlinearities. Additionally, existing cross-sectional analysis models, which are used to extract cross-sectional properties of wind turbine composite blades for aeroelastic modelling, are either time-consuming or inaccurate.

This thesis aims to provide a reliable and efficient aeroelastic modelling of large wind turbine blades through developing 1) a cross-sectional model, which can extract cross-sectional properties of wind turbine composite blades in a reliable and efficient way; and 2) a nonlinear aeroelastic model, which is capable of handling large blade deflections.

In this thesis, a cross-sectional analysis model for calculating the cross-sectional properties of composite blades has been developed by incorporating classical lamination theory (CLT) with extended Bredt-Batho shear flow theory (EBSFT). The model considers the shear web effects and warping effects of composite blades and thus greatly improves the accuracy of torsional stiffness calculation. It also avoids complicated post-processing of force-displacement data from computationally expensive 3D finite-element analysis (FEA) and thus considerably improves the computational efficiency. A MATLAB program was developed to verify the accuracy and efficiency of the cross-sectional analysis model, and a series of benchmark calculation tests were undertaken. The results show that good agreement is achieved comparing with the data from experiment and FEA, and improved accuracy of torsional

stiffness calculation due to consideration of the shear web effects is observed comparing with an existing cross-sectional analysis code PreComp.

Additionally, a nonlinear aeroelastic model for large wind turbine blades has been developed by combining 1) a blade structural model, which is based on a mixed-form formulation of geometrically exact beam theory (GEBT), taking account of geometric nonlinearities; and 2) a blade load model, which takes account of gravity loads, centrifugal loads and aerodynamic loads. The aerodynamic loads are calculated based on combining the blade element momentum (BEM) model and the Beddoes-Leishman (BL) dynamic stall model. The nonlinear aeroelastic model takes account of large blade deflections and thus greatly improves the accuracy of aeroelastic analysis of wind turbine blades. The nonlinear aeroelastic model was implemented in COMSOL Multiphysics, and a series of benchmark calculation tests were undertaken. The results show that good agreement is achieved when compared with experimental data, and its capability of handling large deflections is demonstrated. After the validation, the nonlinear aeroelastic model was applied to the aeroelastic simulation of the parked WindPACT 1.5MW wind turbine blade and to the stability analysis of the blade. Reduced flapwise deflection from the nonlinear aeroelastic model is observed compared to the linear aeroelastic code FAST. The calculated damping ratio of the edgewise mode is much lower than the calculated damping ratio of the flapwise mode, indicating that edgewise instability is more likely to occur than flapwise instability. It is also demonstrated that improper rotor rotational speeds can result in edgewise instability.

Keywords: Wind Turbine Blade; Cross-sectional Analysis; Classical Lamination Theory (CLT); Extended Bredt-Batho Shear Flow Theory (EBSFT); Nonlinear Aeroelastic Model; Blade Element Momentum (BEM); Geometrically Exact Beam Theory (GEBT)

Dedicated to

My daughter SiMin and my wife Qiong

CONTENTS

LIST OF TABLES

LIST OF FIGURES

ACKNOWLEDGEMENTS

First of all, I would like to express my appreciation to all my supervisors Professor Xiongwei Liu, Dr Nathalie Renevier, Dr Matthew Stables, and the research tutor Professor Bogdan J. Matuszewski who provided me with support throughout the study. I am especially thankful to Professor Xiongwei Liu who provided me with valuable guidance in conducting research, delivering lectures and solving problems.

Thanks to Dr George Michael Hall, Dr Christopher Lawrence Hill, Dr Alex Mayers and other members within the wind energy engineering research group for providing me with a friendly research and working atmosphere. I enjoyed working with all of you as a par-time research assistant in the research group.

Thanks to Dr Xinzi Tang, Dr Ruitao Peng and Dr Lianggang Guo who gave me useful advice in academic writing.

Last but not least, thanks to my wife Qiong Li who always trusts me and supports me.

ACRONYMS/ABBREVIATIONS

APDL	ANSYS Parametric Design Language
BEM	Blade Element Momentum
BL	Beddoes-Leishman
BSFT	Bredt-Batho Shear Flow Theory
CAD	Computer Aided Design
CBCSA	Composite Blade Cross-Section Analysis
CER	Combined Experiment Rotor
CFD	Computational Fluid Dynamics
CLT	Classical Lamination Theory
DES	Detached Eddy Simulations
DOF	Degree of Freedom
DOFs	Degrees of Freedom
DNS	Direct Numerical Simulation
EBSFT	Extended Bredt-Batho Shear Flow Theory
FDM	Finite-Difference Method
FEA	Finite-Element Analysis
FEM	Finite-Element Method
FVM	Finite-Volume Method
GEBT	Geometrically Exact Beam Theory
GUI	Graphical User Interface
LES	Large Eddy Simulations
MA	Modal Approach
MBD	Multi-Body Dynamics
NAM_WTB	Nonlinear Aeroelastic Model for Wind Turbine Blades
NS	Navier-Stokes
PDE	Partial Differential Equation
RANS	Reynolds Averaged Navier-Stokes
1D	One-Dimensional
2D	Two-Dimensional
3D	Three-Dimensional

LIST OF SYMBOLS

a	axial induction factor
a'	angular induction factor
a_s	speed of sound; unit: m/s; SI unit is used throughout the thesis
$\boldsymbol{A_{sys}}$	state space matrix
$\boldsymbol{A}_{sys}^{avg}$	averaged state space matrix
A^*	area enclosed by the middle line of the wall
A_i^{ply}	area of the i th ply
A_{equ}^{seg}	equivalent area of each area segment
$A_{equ}^{seg,I}$	equivalent area of I th area segment
A_1, A_2, A_3, A_4	empirical constants used in dynamic stall model
B_N	number of blades
$\boldsymbol{B_{sys}}$	input matrix of the system
b_1, b_2, b_3	orthonormal triad of un-deformed blade frame b
B_1, B_2, B_3	orthonormal triad of deformed blade frame B
c	chord
$\boldsymbol{C}$	damping matrix
C_l	lift coefficient
C_d	drag coefficient
C_N	static normal force coefficient
C_T	thrust coefficient
C_{N_0}	normal force coefficient at zero angle of attack
C_{Na}	static C_N curve slope near zero lift
$C_{C,n}$	unsteady tangential force coefficient at the n th time step
$C_{d,n}$	unsteady drag coefficient at the n th time step
$C_{l,n}$	unsteady lift coefficient at the n th time step

$C_{m,n}$	unsteady moment coefficient at the nth time step
$C_{N,I}$	critical value of normal coefficient
$C_{N,n}$	unsteady normal force coefficient at the nth time step
$C_{V,n}$	vortex lift at the nth time step
$C_{N,n}^{C}$	circulatory normal force coefficient at the nth time step
$C_{N,n}^{f}$	unsteady normal force coefficient calculated in separated flow model at the nth time step,
$C_{N,n}^{I}$	impulsive normal force coefficient at the nth time step
$C_{N,n}^{P}$	unsteady attached-flow normal force coefficient at the nth time step
$C_{N,n}^{V}$	vortex contribution at the nth time step
$\boldsymbol{C}^{bG}, \boldsymbol{C}^{Gb}, \boldsymbol{C}^{bB}, \boldsymbol{C}^{Bb}\ \boldsymbol{C}^{GB}, \boldsymbol{C}^{BG}, \boldsymbol{C}$	transformation matrices between frames
$D_n,\ D_{p,n}, D_{f,n}$	deficiency functions used in dynamic stall model
dF_N	blade-element normal force per unit length
dF_T	blade-element tangential forces per unit length
$\boldsymbol{e}$	unit vector describing the rotation axis
$\boldsymbol{e}_1$	$\begin{bmatrix}1 & 0 & 0\end{bmatrix}^T$
E_x^{ply}	effective Young's modulus of an angled ply
$E_{x,i}^{ply}$	effective Young's modulus of the i th ply
E_1	Young's modulus along the direction parallel to the fiber direction
E_2	Young's modulus along the direction perpendicular to the fiber direction
E_{equ}^{seg}	equivalent Young's modulus of each area segment
$E_{equ}^{seg,I}$	equivalent Young's modulus of the I th area segment
f	dimensionless suction side separation point position used in dynamic stall model

f_n'	effective separation point considering pressure lag
f_n''	effective separation point considering both pressure lag and viscous lag
$\boldsymbol{f_B}$	column matrix that contains applied forces per unit length measured in frame B
f_{Hz}	un-damped frequency in Hz
$f_{D,Hz}$	damped frequency in Hz
$\boldsymbol{F}$	applied load matrix
$\boldsymbol{F_B}, F_G$	column matrices that contain the force resultants measured in frames B and G, respectively
$\boldsymbol{F_c^G}$	centrifugal-load vector with respect to frame G
$\boldsymbol{F_c^B}$	centrifugal-load vector with respect to frame B
$\boldsymbol{F_g^G}$	gravity-load vector with respect to frame G
$\boldsymbol{F_g^B}$	gravity-load vector with respect to frame B
$\boldsymbol{F_{aero}^B}$	aerodynamic-force vector with respect to frame B
$\boldsymbol{F_{AL}^B}$	applied-load vector with respect to frame B
$F_{tip-loss}$	Prandtl tip loss factor
g	gravity constant
G_{xy}^{ply}	effective shear modulus of an angled ply
$\boldsymbol{G_{12}}$	shear modulus of a unidirectional ply
G_{equ}^{seg}	equivalent shear modulus of each segment
$G_{xy,i}^{ply}$	effective shear modulus of the i th ply
G_1, G_2, G_3	orthonormal triad of global frame G
H	a parameter used for the situation when large axial induction factor occurs
$\boldsymbol{H_G}, \boldsymbol{H_B}$	column matrices that contain the angular momentum measured in frames G and B, respectively
$\boldsymbol{I_M}$	mass matrix

$I_{\overline{xx}}^{seg}, I_{\overline{yy}}^{seg}$	area moments of inertia about local axes of each area segment
$I_{\overline{xy}}^{seg}$	product of inertia about local axes of each area segment
$I_{X_E X_E}^{seg}$, $I_{Y_E Y_E}^{seg}$	area moments of inertia of area segment around elastic axes (X_E, Y_E)
$I_{X_M X_M}^{seg}$, $I_{Y_M Y_M}^{seg}$	area moments of inertia of area segment around mass axes (X_M, Y_M)
$I_{X_E, X_E}^{\sec}, I_{Y_E, Y_E}^{\sec}$	area moments of inertia of area segment around elastic centre (X_{EC}, Y_{EC})
$I_{X_M, X_M}^{\sec}, I_{Y_M, Y_M}^{\sec}$	area moments of inertia of area segment around mass centre (X_{MC}, Y_{MC})
$\boldsymbol{k_b}$	curvature vector for the un-deformed beam
$\boldsymbol{K}$	stiffness matrix
$\boldsymbol{K_B}$	curvature vector for the deformed beam
$\boldsymbol{K_E}$	kinetic energy
K_a	a constant used in dynamic stall model
L	length of the blade
$\boldsymbol{m_B}$	column matrix that contains applied moments per unit length measured in frame B
m_{ply}	number of plies in an area segment
$\boldsymbol{M}$	mass matrix
M_T	torsional moment
$\boldsymbol{M}_{\boldsymbol{AL}}^{\boldsymbol{B}}$	applied-moment vector with respect to frame B
$\boldsymbol{M}_{\boldsymbol{aero}}^{B}$	aerodynamic-moment vector with respect to frame B
$\boldsymbol{M_B}, \boldsymbol{M_G}$	column matrices that contain the moment resultants measured in frames B and G, respectively
N	total number of degrees of freedom of the system
N_A	total number of azimuth position
N_R	real part number of eigenvalue

N_I	imaginary part number of eigenvalue
N_{seg}	number of area segments
$\boldsymbol{P_B}, \boldsymbol{P_G}$	column matrices that contain the linear momentum measured in frames B and G, respectively
q_s	shear flow
Q	reduced stiffness matrix used in cross-sectional analysis
r	distance from blade element to the rotor centre
R	blade radius
R_m	Reuter matrix used in cross-sectional analysis
s_c	perimeter coordinate of a cross-section
$\boldsymbol{S}$	constitutive matrix
$\boldsymbol{S_E}$	strain energy
ΔS	dimensionless time used in dynamic stall model
t_c	thickness of cross-section
t_1, t_2	arbitrary fixed times
Δt	time interval
t_i^{ply}	thickness of the i th ply
$\boldsymbol{t}_{equ}^{seg}$	equivalent thickness of each area segment
$\boldsymbol{T}$	transpose symbol
T_f	viscous-lag time constant used in dynamic stall model
T_I	non-circulatory time constant used in dynamic stall model
T_m	transformation matrix used in cross-sectional analysis
T_P	pressure-lag time constant used in dynamic stall model
T_v	vortex delay constant used in dynamic stall model
T_{vl}	an empirical time constant used in dynamic stall model
$\boldsymbol{u}$	input vector expressed in rotating frame
$\boldsymbol{u_b}$	column matrix that contains displacement of beam reference line measured in frame b

$\boldsymbol{u}_G$	column matrix that contains displacement of beam reference line measured in frame G
U_{rel}	relative wind speed
$\boldsymbol{v}_b$	column matrix that contains linear velocity of the un-deformed beam reference line measured in frame b
ν_{12}	Poisson's ratio
V_0	upcoming wind velocity on each blade element
$\boldsymbol{v}_B, V_G$	column matrices that contain linear velocities of deformed beam reference line measured in frames B and G, respectively
w_{seg}	width of an area segment
$\boldsymbol{x}$	rotating degrees of freedom vector
X_{EC}, Y_{EC}	elastic centre of blade cross-section
X_{MC}, Y_{MC}	mass centre of blade cross-section
X_R, Y_R	reference axes of blade cross-section
X_E, Y_E	elastic axes of blade cross-section
X_M, Y_M	mass axes of blade cross-section
X_n, Y_n	deficiency functions used in dynamic stall model
$\bar{x}_c^{seg,I}, \bar{y}_c^{seg,I}$	centroid coordinates of the I th area segment
$\boldsymbol{z}$	state space vector expressed in rotating frame
EA	axial stiffness
EI_X	flapwise bending stiffness
EI_Y	edgewise bending stiffness
GJ	torsional stiffness
GK_X	flapwise shear stiffness
GK_Y	edgewise shear stiffness
$rhoI_X$	flapwise mass moment of inertia
$rhoI_Y$	edgewise mass moment of inertia
α	angle of attack
α_0	angle of attack for zero lift

α_n	angle of attack at the nth time step
α_{ply}	ply angle
$\alpha_{E,n}$	equivalent angle of attack at the nth time step
$\alpha_{f,n}$	another effective angle of attack at the nth time step
$\Delta\alpha_n$	change in angle of attack at the nth time step
$\Delta\alpha_{n-1}$	change in angle of attack at the $n-1$th time step
β_1	rotor cone angle
β_2	tilt angle
β_3	azimuth angle
β_r	magnitude of rotation
δ	Lagrangean variation
δ_w	warping flexibility
$\delta\boldsymbol{A}$	virtual action at the ends of time interval and at the ends of the blade
$\overline{\delta\boldsymbol{q}_{\boldsymbol{B}}}$, $\delta\boldsymbol{u}_{\boldsymbol{G}}$	virtual displacement measured in frames B and G, respectively
$\delta\boldsymbol{W}$	virtual work of applied loads
$\overline{\delta\boldsymbol{\psi}_{\boldsymbol{B}}}$, $\overline{\delta\boldsymbol{\psi}_{\boldsymbol{G}}}$	virtual rotation measured in frames B and G, respectively
φ	angle of relative wind
φ_{seg}	angle between the local axes of each area segment and the elastic axes
$\boldsymbol{\gamma}$, $\boldsymbol{\kappa}$	column matrices that contain force and momentum strains, respectively
η	recovery factor used in dynamic stall model
λ	eigenvalue
μ	mass per unit length of each blade element
$\theta, \boldsymbol{\theta}_{\boldsymbol{G}}$	Rodrigues parameters
θ_p	twist angle of each blade element
ρ	air density

ρ_{equ}^{seg}	equivalent density of each segment of blade cross-section
ρ_i^{ply}	density of the i th ply
σ'	local solidity
τ	torsional stress
$\tau_{v.n}$	vortex time parameter used in dynamic stall model
ω	un-damped frequency in rad/s
ω_D	damped frequency in rad/s
ω_b, ω_G	column matrices that contain angular velocity of the un-deformed beam reference line measured in frames b and G, respectively
ξ	damping ratio
$\mathbf{\Delta}$	3-by-3 identity matrix
Ω	rotor rotational speed
$\boldsymbol{\Omega}_B, \boldsymbol{\Omega}_G$	column matrices that contain angular velocities of deformed beam reference line measured in frames B and G, respectively
$(\tilde{\cdot})$	defines a second-order, skew-symmetric tensor corresponding to the given vector

CHAPTER 1 INTRODUCTION

1.1. Background

With the depletion of fossil fuel resources and the growing demand of energy consumption, renewable energy resources such as wind and solar have received great attention in recent years. Compared to fossil fuel resources, most renewable energy resources (such as wind and solar) are inexhaustible and environmentally friendly. Therefore, many countries are making considerable efforts to exploit renewable energy resources. In 2010, renewable power generation contributed around a third of the world's newly constructed power generation capacities [1]. Projections show that it is possible to power 100 percent of the world's energy demand with renewable energy resources by the year of 2030 [2].

Wind power is the most promising renewable energy resource, and is capable of providing a competitive solution to battle the global climate change and energy crisis. As an inexhaustible and free energy resource, it is available and deployable in most regions of the world. Currently, wind power is the fastest growing renewable power industry. Fig. 1.1 depicts the global wind power cumulative capacity between years 1996 and 2013. From Fig. 1.1 we can see that the global wind power cumulative capacity has increased dramatically in the past decade. At the end of 2013, worldwide cumulative capacity of wind power reached 318.1GW, growing by 34.9GW over the previous year [3].

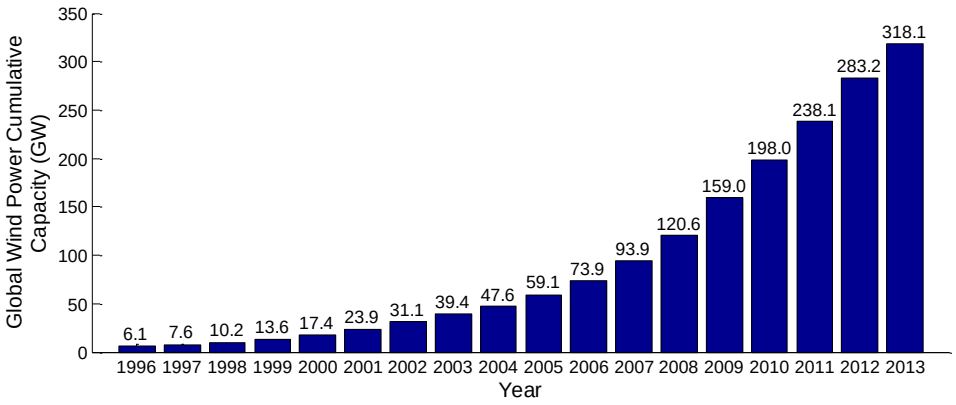

Figure 1.1. Global wind power cumulative capacity

With the growth in wind power capacity, wind power technology itself has also moved rapidly towards new dimensions. As wind velocity increases with increasing altitude

and therefore it is possible to harvest more wind power at higher altitudes, the size of wind turbines is getting larger and larger. Another important reason for the growth in the size of wind turbines is to place wind turbines at sea. Compared to the land, there is more available space to install wind turbines at sea and the wind is steadier and stronger in offshore locations. However, the installation and maintenance of offshore wind turbines are very expensive. Therefore, for offshore wind farms, placing fewer wind turbines that are larger is more beneficial than placing many smaller turbines. The incentive to reduce the price for the electricity per kWh has led to increasingly large commercial wind turbines. Fig. 1.2 presents the growth in size of commercial wind turbines between years 1980 and 2011. As it can be seen from Fig. 1.2, the dimension of commercial wind turbines has increased significantly over the past three decades, from a rated power of 75kW and a rotor diameter of 17m for earlier designs up to a rated power of 7.5MW and a rotor diameter of over 125m for modern machines. The trend of increasing size of large wind turbines is expected to continue in the next decade. The power rating of wind turbines has gone up to 8MW recently [4], and the potential of 10-20MW wind turbine is being investigated [5].

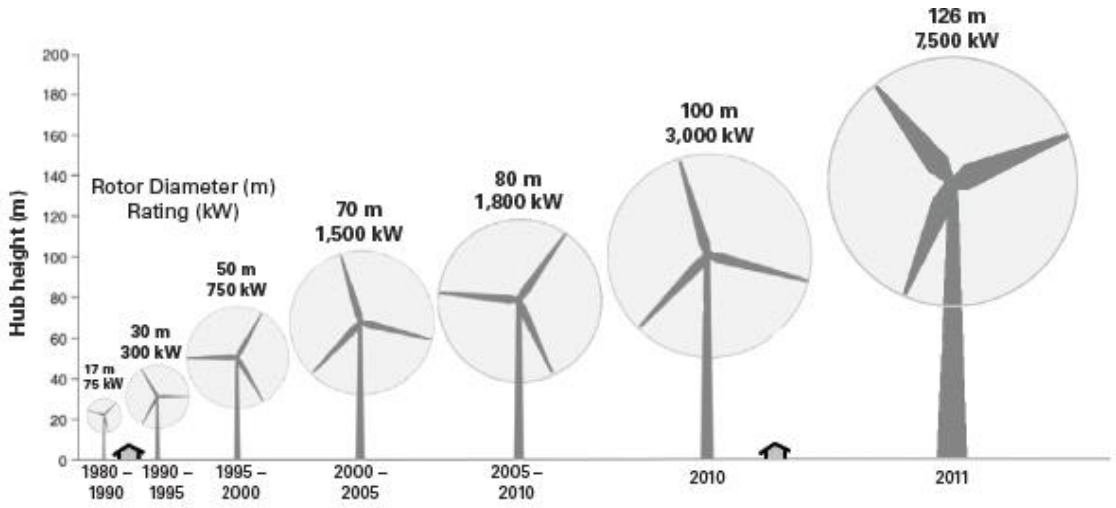

Figure 1.2. Growth in size of commercial wind turbines [6]

The increasing size of large wind turbines lowers the cost of wind power per kWh; however it introduces significant aeroelastic effects, which are caused by fluid-structure interaction. These effects might result in instability problems, such as edgewise instability and flutter, which can be devastating to the blades and wind turbine. For instance, as reported in Ref. [7], 0.5% of the LM (Lunderskov Mobelfabrik) 19m wind turbine blades were damaged within one year. These blades were mounted on 600kW wind turbines around the world and were damaged due to blade edgewise instability.

The changes in wind turbine blade design due to the growth in size might lead to other not yet recognised aeroelastic instabilities. Therefore, investigating the aeroelasticity characterisation of large wind turbine blades is playing an important role in the development of large wind turbines.

1.2. Aeroelasticity of Wind Turbine Blades

Aeroelasticity concerns the interaction of the aerodynamic loads, elastic deflections and inertial dynamics for a flexible structure [8]. For wind turbine blades, the interaction is strong. During the operation of a wind turbine, the blades experience elastic deflections due to aerodynamic loads exerted by the airflow passing the blades. The deformed blade affects, in turn, the flow field around the blade, which in return influences the aerodynamic loads on the blade. The inertia dynamics play a significant role in the correlation between the aerodynamic loads and elastic deflections, and the resulting accelerations. The blade can experience oscillation due to the changing loads, and it becomes unstable under harmonic conditions and/or when the damping is negative.

Aeroelasticity phenomena can be classified into either static or dynamic problems. Static aeroelasticity studies the deflections of flexible structures caused by the interaction of aerodynamic loads and elastic deflections, where the oscillatory effects are ignored. Dynamic aeroelasticity investigates the oscillatory effects of the aeroelastic interactions, and its major area of interest is the stability of the structure. The study of aeroelasticity can be clearly illustrated by the Collar aeroelastic triangle [9], as shown in Fig. 1.3.

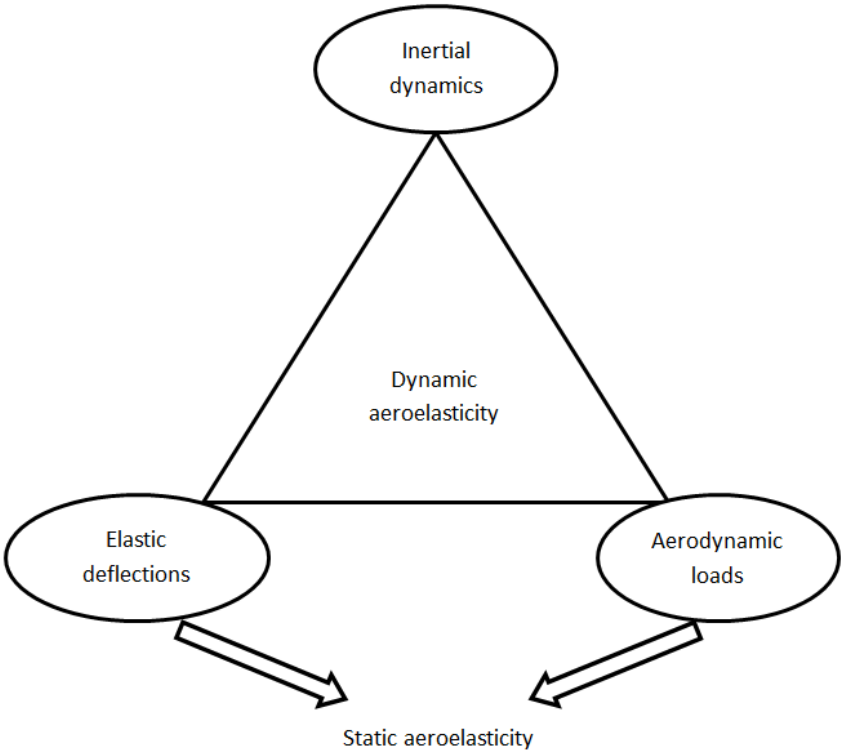

Figure 1.3. Collar aeroelastic triangle

1.2.1. Steady Aeroelasticity

In the aircraft industry, the study of steady aeroelasticity mainly focuses on the divergence, which occurs when the torsional moment introduced by aerodynamic loads is higher than the restoring moments due to structural stiffness [10]. The principle of divergence can be illustrated using a simple differential equation governing the wing deflection. For instance, modelling the aircraft wing depicted in Fig. 1.4 as an Euler-Bernoulli beam, the uncoupled torsional equation of deflection can be expressed as [11]:

$$GJ\frac{d^2\theta_{ET}}{dy^2} = -M'_A, \quad y \in [0, L_B] \tag{1.1}$$

where y is the spanwise dimension of the beam, θ_{ET} is the elastic twist angle of the beam, GJ is the torsional stiffness of the beam, L_B is the length of the beam, M_A is the aerodynamic moment per unit length.

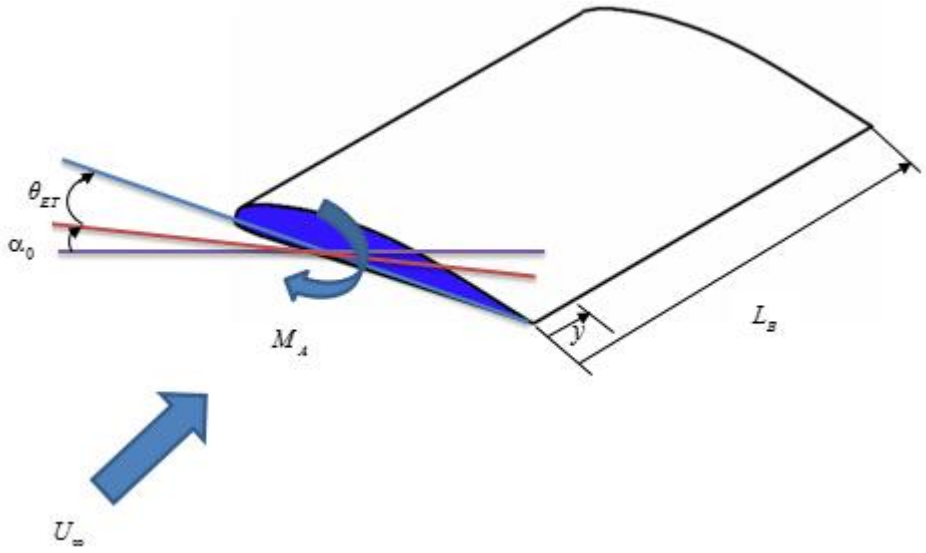

Figure 1.4. An example of simple aircraft wing

According to a simple lift forcing theory, the aerodynamic moment M_A in Eq. (1.1) can be expressed in the following form [11]:

$$M'_A = A_C U_\infty{}^2 \left(\theta_{ET} + \alpha_0\right) \tag{1.2}$$

where A_C is a coefficient, U_∞ is the free-stream wind velocity, and α_0 is the initial angle of attack.

Substituting Eq. (1.2) into Eq. (1.1) yields:

$$\frac{d^2\theta_{ET}}{dy^2} + B_S^2\theta_{ET} = -B_S^2\alpha_0 \tag{1.3}$$

Eq. (1.3) is valid for both small and large deflections. B_S^2 in Eq. (1.3) is defined by:

$$B_S^2 = A_C U_\infty^2 / (GJ) \tag{1.4}$$

The boundary conditions for a cantilever beam are:

$$\theta_{ET}\big|_{y=0} = 0 \tag{1.5a}$$

$$\left.\frac{d\theta_{ET}}{dy}\right|_{y=L_B} = 0 \tag{1.5b}$$

Solving Eq. (1.3) yields the solution:

$$\theta_{ET} = \alpha_0\left[\tan\left(B_S L_B\right)\sin\left(B_S y\right) + \cos\left(B_S y\right) - 1\right] \tag{1.6}$$

As can be seen from Eq. (1.6), for $B_S L_B = \pi/2 + n\pi$, with any integer number n, $\tan(B_S L_B)$ is infinite. $n = 0$ corresponds to the divergence point. For given structural parameters, such as length L_B and torsional rigidity GJ, this will correspond to the torsional divergence speed, a certain value of free-stream wind velocity U_∞.

In the development of aircrafts, aircraft wings have encountered divergence. For instance, Langley's aircraft failed due to the onset of divergence [12]. However, in terms of wind turbines, the divergence phenomenon has not been observed in commercial wind turbines and is not likely to happen in the future. This is mainly due to the fact that the torsional moments on wind turbine blades are generally small. Even when the blade is pitching, the torsional moments are not high enough for the onset of divergence.

For the static aeroelasticity analysis of wind turbine blades, aeroelastic models are mainly used to calculate the steady-state blade tip deflection and perform load calculations considering blade deflections.

The blade tip deflection is an important parameter for wind turbine designers to determine the blade tip clearance (see Fig. 1.5), the distance between blade tip and the tower. The Blade tip clearance of a wind turbine is a critical operating parameter to avoid disastrous failure caused by the blade striking the tower. Accurately predicting blade tip deflection requires a reliable aeroelastic model to capture the interaction of the aerodynamic loads and blade structural deflections.

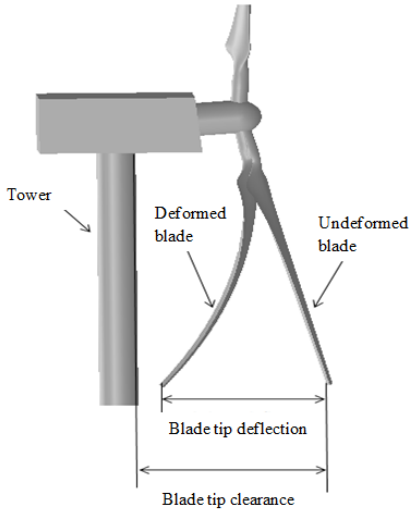

Figure 1.5. Blade tip deflection and blade tip clearance

Large wind turbines are generally required to be designed to meet the international safety standard IEC 61400-1 [13]. According to the requirements of IEC 61400-1, the load calculations of wind turbines should be based on aeroelastic modelling. Therefore, one of the main roles of wind turbine aeroelastic models is to perform load calculations for certification. A comparison of existing wind turbine aeroelastic models used for certification can be found in Ref. [14]. The results from these models show good agreement for the selected case studies.

1.2.2. Dynamic Aeroelasticity

Dynamic aeroelasticity studies the oscillatory effects of the aeroelastic interactions and concerns the aeroelastic instabilities of wind turbine blades, such as flutter and edgewise instability.

1.2.2.1. Flutter

Flutter is a two-dimensional vibration problem involving the coupling of two degrees of freedom (DOFs) of the blade. Fig. 1.6 depicts the typical three DOFs of a blade, including torsional (pitch), flapwise (flap) and edgewise (lag) DOFs. The details of the three DOFs can be found in Appendix A2. Based on the different combinations of any two DOFs of the blade, flutter can be roughly classified into the following three types: 1) flap-pitch flutter, which involves the coupling of flapwise and torsional blade motions; 2) lag-pitch flutter, which involves the coupling of edgewise and torsional blade motions; 3) flap-lag flutter, which involves the coupling of flapwise and edgewise blade motions. Among these types of flutter, the flap-pitch flutter, also known as classic flutter, is the most common one.

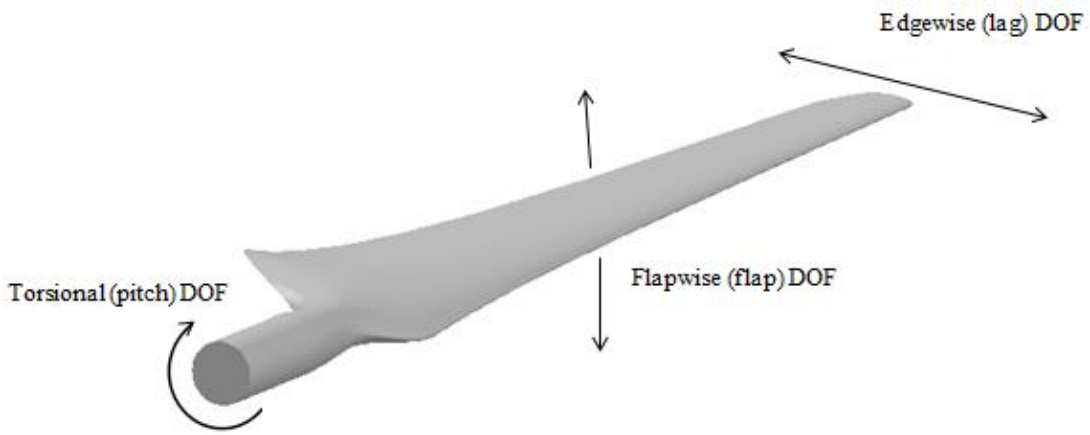

Figure 1.6. Degrees of freedom of a blade

Fig. 1.7 depicts the frequency and damping trends of a typical flap-pitch flutter. As can be seen from Fig. 1.7a, as air speed increases, the frequency of pitch mode gets closer to that of flap mode, possibly resulting in one combined mode. At the flutter speed, a certain critical wind speed, the structure sustains oscillations (see Fig. 1.7d) and one of the modes (the pitch mode in this example) has zero net damping (see Fig. 1.7b). The net damping is the sum of structural damping and aerodynamic damping. Below the flutter speed, the oscillations are damped and the structure is stable (see Fig. 1.7c). When wind speed exceeds the flutter speed, the net damping becomes negative and the unstable oscillations occur (see Fig. 1.7e), resulting in eventual failure of the structure.

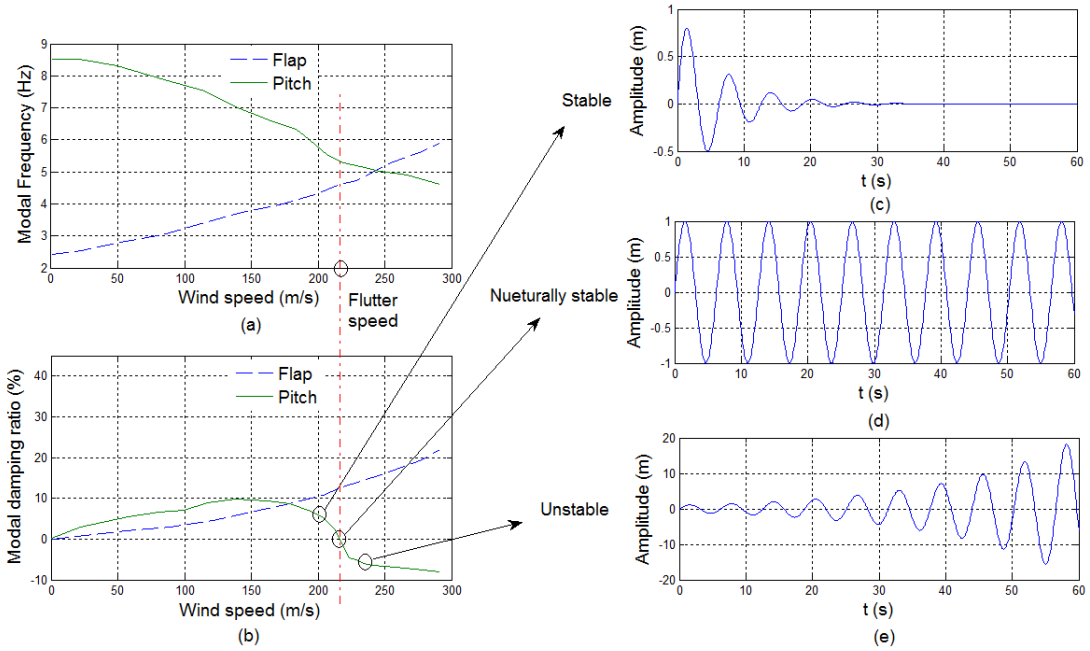

Figure 1.7. An example of flap-pitch flutter

Flutter is a well-known dynamic aeroelasticity phenomenon in the aerospace field. The investigations of flutter are generally based on the theory of aeroelasticity [15] and the theory of composite thin-walled structures [16]. In order to avoid flutter, a number of studies [17-19] have been carried out on aeroelastic optimisation of composite wing and helicopter blade structures.

In terms of wind turbines, flutter has not yet been observed on commercial wind turbines [20]. However, the increasing size and flexibility of large wind turbine blades decreases torsional frequency, and therefore decreases flutter speed. Therefore, predicting flutter speed of the large wind turbine blades is a good practice in the design process of large wind turbines.

1.2.2.2. Edgewise Instability

Modern wind turbine blades generally have an inherent positive aerodynamic damping for their flapwise motions but a relatively smaller, even negative aerodynamic damping for edgewise modes. Therefore, the edgewise instability is considered the most important instability problem for wind turbines [20].

In the development of large wind turbines, some commercial wind turbine blades have suffered from the blade edgewise instability. In 1994, Stiesdal [21] firstly reported the edgewise instability problem on stall-regulated wind turbines with a 37m diameter rotor. This instability problem had not been observed on earlier wind turbines, but it quickly became a significant issue for large wind turbines with the increase in rotor size. Another example of the blades suffering from this instability problem is the APX40T blade [22], which was installed on a 600kW wind turbine with a 37m-diameter rotor. Fig. 1.8 depicts the edgewise oscillation measured at 85% span location of the APX40T blade at high wind speeds. As it can be seen from Fig. 1.8, violent edgewise oscillations are observed between 35s and 55s. The instability of the APX40T blade was caused by negative aerodynamic damping of the first edgewise mode.

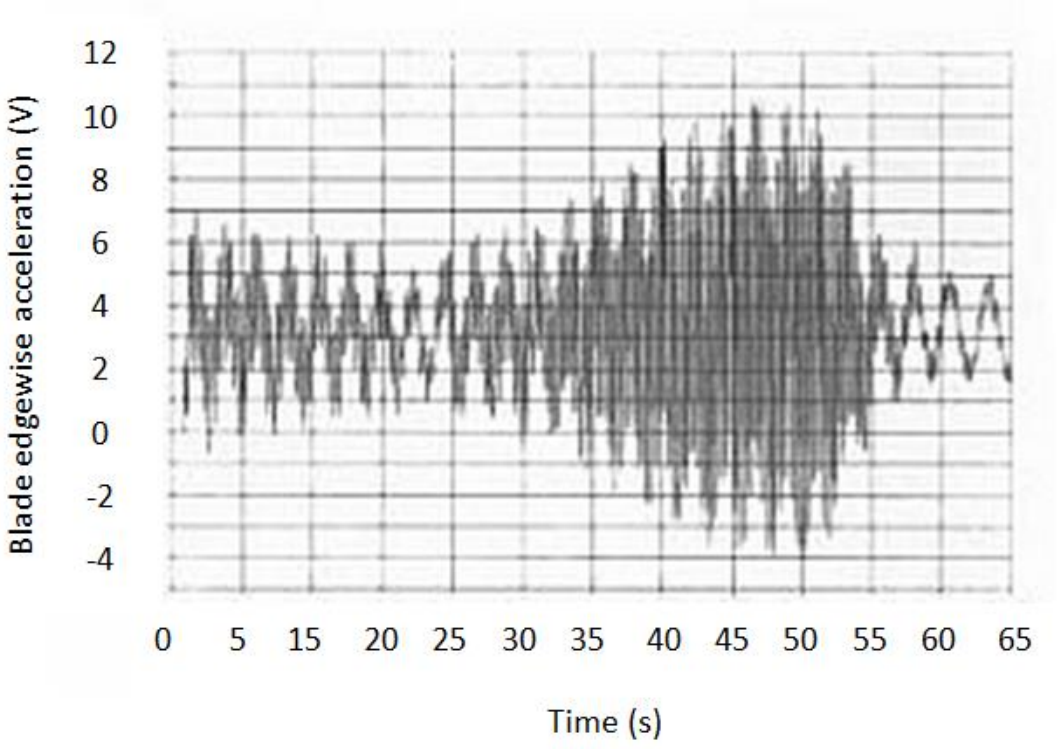

Figure 1.8. Edgewise oscillations of the APX40T blade at high winds (edgewise acceleration at 85% blade span) [22]

Edgewise instability is single DOF instability, and it occurs when edgewise aerodynamic damping coefficient becomes negative. As depicted in Fig 1.9 from Ref. [23], if an airfoil cross-section is harmonically translated along an axis x_B (see Fig. 1.9a) and the direction of this axis θ_{RB} relative to the orientation x_R of the wind turbine rotor plane is changed, the aerodynamic damping coefficient for the cross-section changes significantly. As it can be seen form Fig. 1.9b, For small θ_{RB} , which corresponds to in-plane or edgewise vibration direction, the negative aerodynamic damping coefficient is observed even at low wind speeds. In order to avoid blade edgewise instability, predicting edgewise aerodynamic damping coefficient and exploring effective ways to damp edgewise oscillations becomes necessary.

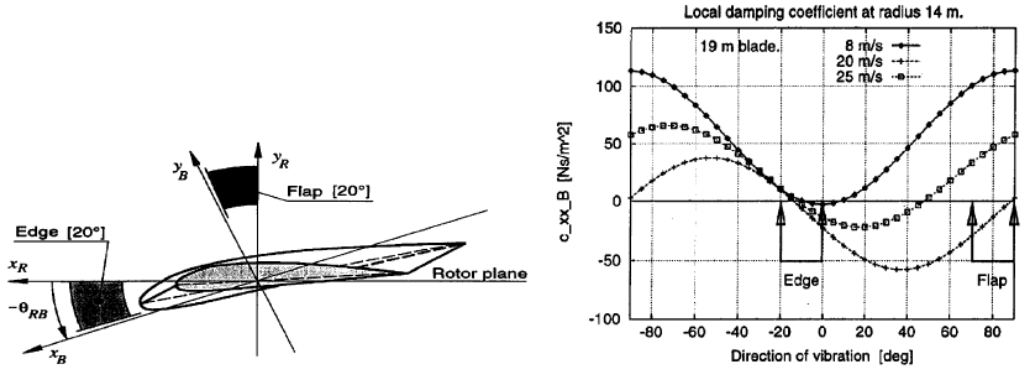

(a) (b)

Figure 1.9. Distribution of aerodynamic damping coefficient c_xx_B for an airfoil cross-section against vibration direction θ_{RB} and three different wind speed [23]

1.3. Present Wind Turbine Aeroelastic Models

Investigating the aeroelasticity of wind turbine blades needs a wind-turbine-specific aeroelastic model. One of the earliest wind turbine aeroelastic models, STALLVIB [24], was developed within the European Non-Nuclear Energy project JOULE III. This model was developed for predicting dynamic loads and investigating the edgewise instability problems.

After the first attempts, a considerable number of aeroelastic models have been developed. The models being widely used in wind turbine research organisations and industrial practices are listed below with short descriptions.

- ADAMS/WT (Automatic Dynamic Analysis of Mechanical Systems – Wind Turbine)
    - ADAMS/WT is a wind-turbine-specific add-on for ADAMS, which is a widely used commercial multi-body dynamics software package. ADAMS/WT is developed by Mechanical Dynamics Inc. (MDI) with the help of National Renewable Energy Laboratory (NREL) [25].
- FAST (Fatigue, Aerodynamics, Structures, and Turbulence)
    - FAST has been developed by National Renewable Energy Laboratory (NREL) to model both two- and three-bladed horizontal-axis wind turbines. In 2005, Germanisher Lloyd (GL), one of the leading certification organisations in wind energy area, issued FAST a certification on its load calculation of onshore wind turbines [26].

- FLEX5
    - FLEX5 has been developed by the Fluid Mechanics Department at the Technical University of Denmark (DTU). This code is capable of simulating wind turbines with different configurations, e.g. turbines with one to three blades [27].

- GAST (General Aerodynamic and Structural Prediction Tool for Wind Turbines)
    - GAST has been developed by the National Technical University of Athens. The code contains an additional module to generate turbulent wind fields and a post-processing module to perform fatigue analysis [28].

- GH-Bladed
    - GH-Bladed is an integrated commercial software package developed by Garrad Hassan (GH) Ltd. GH-Bladed has a friendly windows-based graphical user interface (GUI), and it has been validated against experimental data for a number of wind turbines with different size and configurations [29].

- HAWC2 (Horizontal Axis Wind Turbine Code 2nd generation)
    - HAWC2 has been developed by Technical University of Denmark (DTU). The code analyse the aeroelastic behaviour of horizontal axis wind turbine in time domain [30].

- PHATAS (Program for Horizontal Axis Wind Turbine Analysis Simulation)
    - PHATAS has been developed by ECN (Energy research Centre of the Netherlands) for predicting the dynamic behaviour and the corresponding loads on horizontal axis wind turbines. PHATAS includes additional programs used to generate load-case files following IEC or GL [31].

The features of the above seven aeroelastic models are summarised in Table 1.1. From Table 1.1 we can see that most of the aeroelastic models use blade element momentum (BEM) theory as the aerodynamic part. For the structural part, all of these models represent wind turbine blades as a series of one-dimensional (1D) beam elements, and requires blade cross-sectional properties as input. The discretisation method used in these models can be categorised into three types of approach: modal approach (MA), multi-body dynamics (MBD) and 1D finite-element method (FEM).

Table 1.1. Overview of wind turbine aeroelastic models

Name	Structural part		Aerodynamic part	Require blade cross-sectional properties as input?
	Blade representation	Discretisation method		
ADAMS/WT	1D beam	MBD	BEM	Yes
FAST	1D beam	MA	BEM	Yes
FLEX5	1D beam	MA	BEM	Yes
GAST	1D beam	1D FEM	Free wake panel	Yes
GH-Bladed	1D beam	MA	BEM	Yes
HAWC2	1D beam	MBD	BEM	Yes
PHATAS	1D beam	1D FEM	BEM	Yes

1.4. Problem Statement

As shown in Table 1.1, almost all aeroelastic models for wind turbines represent the blades as a series of 1D beam elements. In order to construct the beam elements for aeroelastic modelling, the blade cross-sectional properties (such as mass per unit length and cross-sectional stiffness) are essential information. Obtaining these properties requires a specialised cross-sectional analysis model. However, existing cross-sectional analysis models are either time-consuming or inaccurate [32]. Therefore, it is necessary to develop a cross-sectional analysis model, which is capable of rapidly and accurately extracting cross-sectional properties of wind turbine composite blades for aeroelastic modelling.

Additionally, most existing aeroelastic models are linear models based on assumption of small blade deflections, and do not take account of large deflection effects on modelling responses and loads [20]. However, with the increasing size and flexibility of large wind turbine blades, this assumption is not valid anymore because the blades often experience large deflections, which introduce significant geometric nonlinearities. Therefore, developing a nonlinear aeroelastic model to take account of geometric nonlinearities is essential for reliable aeroelastic modelling of large wind turbine blades.

So far, only a few nonlinear aeroelastic models have been developed. One example is HAWC2 (Horizontal Axis Wind turbine simulation Code 2nd generation) [30], which is an in-house nonlinear aeroelastic model developed by Technical University of Denmark (DTU). The aerodynamic model of HAWC2 is based on BEM and its structural model is based on a MBD formulation where each body is a linear Timoshenko beam element, which is an extension of Bernoulli-Euler beam element [33] to cover shear deformation. The geometric nonlinearities are captured by the MBD formulation, in which the flexible blades are modelled, for example, by 40 bodies each. However, if only one body per blade is used, HAWC2 will become a linear model because the Timoshenko beam model in each body is linear. In other words, the results of HAWC2 are sensitive to the number of bodies, which one chooses to model the flexible blade. Additionally, HAWC2 contains assumption that relative displacement between two adjacent bodies is small and it assumes some simplifications for the kinematic equations, which introduces uncertainties in its results.

An alternative way to handle the geometric nonlinearities is the geometrically exact beam theory (GEBT) [34], in which the deformed beam geometry, i.e. the displacements and rotations of the beam reference line, is represented exactly. Various nonlinear formulations have been proposed for GEBT, which can be classified on the basis of solution methodology, namely displacement-based formulation, strain-based formulation and mixed-form formulation [35]. The main differences between these formulations are the definition of the dependent variables and the treatment of the rotation of the beam reference line in the solution. The displacement-based formulation defines the displacements and rotations of the beam reference line as the irreducible set of dependent variables, which include high order nonlinearities. The main advantage of this formulation is that the displacement constraints can be easily applied. However, the solution of this formulation demands high computational cost due to its high order nonlinearities. In order to solve the geometrically nonlinear beam problems more efficiently, an alternative way is the strain-based formulation, which uses the strains and curvatures of the beam reference line as the primary variables to represent the beam deformation. A more efficient way to solve the geometrically nonlinear beams is to use the mixed-form formulation proposed by Hodges [36], which introduces Lagrange multipliers to satisfy the equations of motion with constitutive and kinematic relationships. The mixed-form formulation allows the lowest order of shape functions for all dependent variables, which makes it a viable solution for modelling geometric nonlinearities and has been widely used for flexible aircraft wings [37].

The similarities between the aircraft wings and wind turbine blades, i.e. both of them are long, slender and flexible structures, provide us with the possibility to borrow the aeroelastic modelling techniques from aircraft applications for wind turbine blades. To the best of the author's knowledge, the combination of BEM and the mixed-form formulation of GEBT for aeroelastic modelling of wind turbine blades has not been found in the literature.

1.5. Aims and Objectives

This project aims to provide a reliable and efficient aeroelastic modelling of large wind turbine blades through developing 1) a cross-sectional analysis model, which can rapidly and accurately extract cross-sectional properties of wind turbine composite

blades for aeroelastic modelling of the blades; and 2) a nonlinear aeroelastic model, which is capable of handling large blade deflections.

The objectives of the project are as follows:

- To review the aerodynamic model, structural model and cross-sectional analysis model used in aeroelastic modelling of wind turbine blades.
- To develop a cross-sectional analysis model for efficiently and accurately extracting the cross-sectional properties of wind turbine blades using MATLAB.
- To develop an aerodynamic model of wind turbine blades based on combining the blade element momentum (BEM) model with the Beddoes-Leishman (BL) dynamic stall model using MATLAB.
- To develop a nonlinear structural model of wind turbine blades based on mixed-form formulation of geometrically exact beam theory (GEBT).
- To couple the developed aerodynamic model and nonlinear structural model to develop a nonlinear aeroelastic model.
- To apply the developed nonlinear aeroelastic model to the aeroelastic simulation and stability analysis of large wind turbine blades.

1.6. Outline of Thesis

This thesis is organised as follows.

Chapter 2 reviews the key components in aeroelastic modelling, including aerodynamic models, structural models and cross-sectional analysis models.

Chapter 3 summarises the development of a cross-sectional analysis model for calculating cross-sectional properties of wind turbine composite blades.

Chapter 4 details the blade structural modelling based on mixed-form formulation of GEBT.

Chapter 5 presents the methods used for blade load modelling. Aerodynamic loads, gravity loads, centrifugal loads and applied loads are discussed.

Chapter 6 presents the implementation of the nonlinear aeroelastic model for wind turbine blades by coupling the blade structural modelling module and blade load modelling module. The computational scheme and flowchart of the aeroelastic model are presented. The strategies for applying the nonlinear aeroelastic model to four types of studies, i.e. static analysis, modal analysis, time-dependent analysis and stability analysis, are illustrated.

Chapter 7 presents the validation of the nonlinear aeroelastic model. The main components of the nonlinear aeroelastic model, i.e. the aerodynamic part (based on combining the BEM model with the BL dynamic stall model) and the structural part (based on mixed-form formulation of GEBT), are validated separately. Then a case study is performed to validate the time-dependent aeroelastic simulation results.

Chapter 8 presents the application of the nonlinear aeroelastic model, including the aeroelastic simulation of a parked wind turbine blade and the stability analysis of the blade.

Chapter 9 concludes the research work and presents some suggestions for future research.

1.7. Contributions

A summary of the research work conducted during the three-year PhD study is presented below. This comprises topics which will not be discussed in detail in this thesis.

- A cross-sectional analysis model, which is capable of extracting cross-sectional properties of wind turbine blades in a fast and reliable way, has been developed. A journal paper on the cross-sectional analysis model has been published in Renewable Energy [32] (Appendix G1).

- A nonlinear aeroelastic model based on combining BEM theory with geometrically exact beam theory (GEBT) has been developed. A journal paper on the nonlinear aeroelastic model has been published in Energy [38] (Appendix G2).

- An efficient and reliable aerodynamic model for wind turbine blades has been developed using MATLAB based on BEM theory. The high efficiency of the aerodynamic model makes it suitable for optimisation design, which commonly involves a large number of case studies. Based on the aerodynamic model and different optimisation strategies, two academic papers have been completed. One paper [39] (Appendix G3), which proposes an optimal blade design strategy for a fixed-pitch fixed-speed wind turbine through optimised linearisation of the blade chord and twist angle distributions, has been published in Renewable Energy. The other paper [40] (Appendix G4), which optimises aerodynamic shape of wind turbine blades considering Reynolds number effects, has been delivered in the form of an oral presentation at international conference on Wind Energy: Materials, Engineering and Policies (WEMEP 2012).

- Contributions have been made to a journal paper [41] (Appendix G5) on the optimisation of primary aerodynamic design parameters for fixed-pitch fixed-speed wind turbines.

CHAPTER 2 LITERATURE REVIEW

2.1. Introduction

Due to the fact that aeroelastic effects are introduced by the interaction of the aerodynamic loads and structural dynamics, an aeroelastic model should contain an aerodynamic part to calculate the aerodynamic loads and a structural part to determine the structural dynamic responses. In aeroelastic modelling, wind turbine blade structure is often represented as a series of 1D beam elements, which are characterised by cross-sectional properties of the blade, such as mass per unit length and cross-sectional stiffness. It should be noted that wind turbine blades are generally made of composite materials and have complicated structural layout. Obtaining the cross-sectional properties of the composite blades is quite challenging and requires a specialised cross-sectional analysis model. Fig. 2.1 presents the components of aeroelastic modelling of wind turbine blades, and each component is reviewed in this chapter.

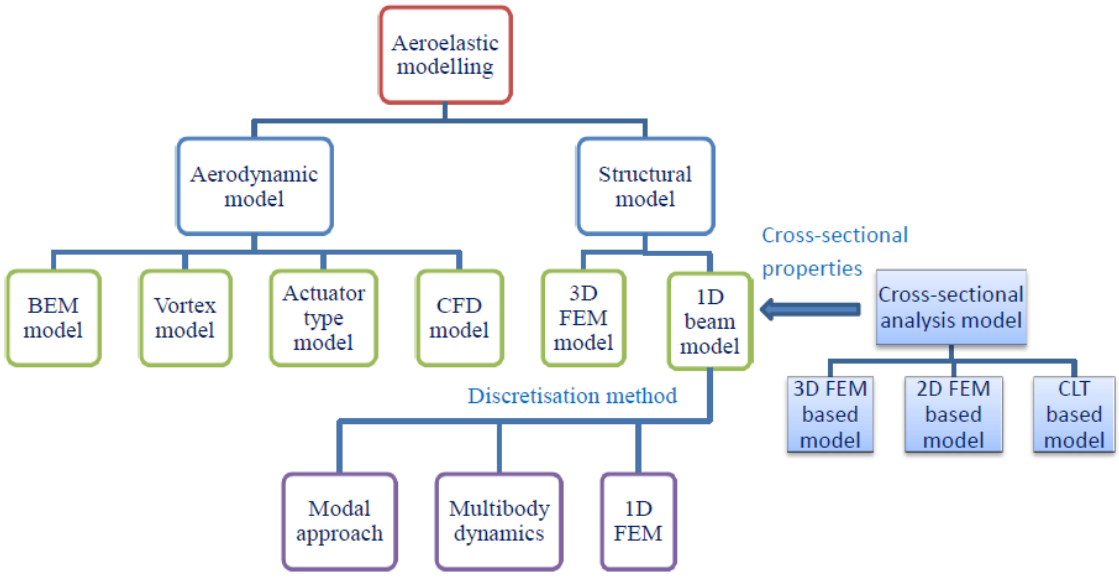

Figure 2.1. Components of aeroelastic modelling of wind turbine blades

This chapter is structured as follows. Sections 2.2 and 2.3 review the aerodynamic models and the structural models, respectively. Section 2.4 reviews cross-sectional analysis models used for extracting cross-sectional properties of wind turbine composite blades for aeroelastic modelling.

2.2. Review of Aerodynamic Models

In order to perform aeroelastic modelling of wind turbine blades, an aerodynamic model should be included to calculate the aerodynamic loads exerted by the airflow passing on the blades. Four types of aerodynamic models have been used in aeroelastic modelling of wind turbine blades, including blade element momentum (BEM) model, vortex model, actuator type model and computational fluid dynamic (CFD) model.

2.2.1. Blade Element Momentum (BEM) Model

Compared to other aerodynamic models, the BEM model is fast and able to provide accurate results when reliable airfoil aerodynamic data are available. For this reason, BEM model has been used for the aerodynamic part by most wind turbine aeroelastic models [42].

The BEM model was originally proposed by Glauert [43] by combining blade element theory and blade momentum theory. The blade element theory discretises the blade into several elements and ignores the mutual influence between two adjacent elements. The aerodynamic loads on each element depend on its local airfoil characteristics, i.e. its lift and drag coefficients. The sum of these loads yields the total loads on the blade. The blade momentum theory introduces axial induction factor a and angular induction factor a' to calculate the induced velocity in the axial and tangential directions, respectively. The induced velocity affects the angle of attack of the blade and therefore influences the aerodynamic loads calculated by the above blade element theory. Combining blade element theory and blade momentum theory provides a solution to obtain the performance parameters of each blade element through an iterative procedure.

The original BEM model has several limitations which are usually found in wind turbine applications. The majority of these limitations have been overcome through introducing empirical corrections borrowed from helicopter applications or based on wind turbine experience.

One of the main limitations of the original BEM model is that it ignores the effects of vortices shedding from the blade tip on the induced velocity. Practically, these effects play a significant role in the induced velocity distribution along the blade, especially the

region near the blade tip. In order to compensate for this deficiency in the BEM model, Prandtl [44] proposed a tip loss correction factor through modelling the wake of the wind turbine as vortex sheets. Prandtl tip loss correction is simple and efficient and also improves the accuracy in the predictions of induced velocity distribution.

Another limitation of the original BEM model is that the model becomes invalid when the axial induction factor a is larger than around 0.4. This occurs for the cases that wind turbines operate at high tip speed ratios, e.g. fixed-speed wind turbines at low wind speeds, as the blade gets into turbulent wake state ($a > 0.5$). For the turbulent wake state, the wind velocity behind the blade calculated based on blade momentum theory becomes negative, which is obviously unreasonable. The original BEM model is incapable of providing reasonable thrust coefficient when the blade is operating at the turbulent wake state. In order to overcome this limitation of the BEM model, several empirical models have been proposed, such as Glauert model [45], Spera model [46], and GH-Bladed model [47]. The comparison of these empirical models in Ref. [48] shows that all these models agree well with experimental data except the Sepra model.

The original BEM model is based on quasi-steady assumption, i.e. the instantaneous aerodynamic loads on a wind turbine blade are assumed to be identical with those which the blade would experience in steady motion at the same instantaneous wind speed and angle of attack. The quasi-steady BEM model can also be expanded to an unsteady model by taking account of unsteady effects, such as dynamic inflow and dynamic stall.

The induced velocities calculated using original BEM model are quasi-steady, which implies the wake is in equilibrium with the inflow. Practically, if the inflow is changed, before a new equilibrium is achieved there exists a time delay, which is a function of rotor diameter and wind speed [42]. Fig. 2.2 depicts the predicted and measured dynamic response on the rotor shaft torque of the Tjaereborg 2MW wind turbine [49] for a sudden change in the pitch angle. At $t = 2\text{s}$, the pitch angle is changed from $0°$ to $3.7°$, reducing the local angle of attack. The rotor shaft torque firstly decreases from 260 to 150 kNm, and then it gradually increases, taking approximately 10s delay to reach a new equilibrium state with value of around 220 kNm. At $t = 32\text{s}$, the pitch angle is adjusted back to $0°$, and a similar time delay in rotor-shaft torque response is observed. Taking account of this time delay needs a dynamic inflow model. Several empirical dynamic inflow models have been developed, such as Øye model [50] and

Pitt-Peters model [51]. The comparison of these models in Ref. [52] shows that all these models agree well with the trends of measurements.

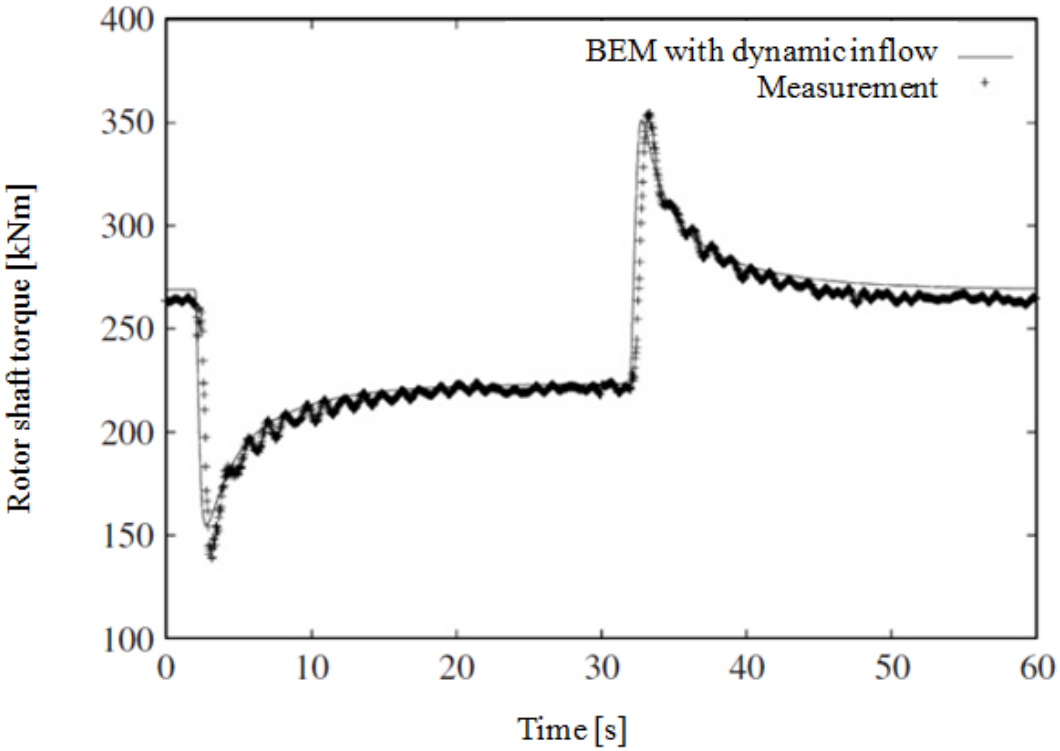

Figure 2.2. Predicted and measured dynamic response on the rotor shaft torque of the Tjaereborg 2MW wind turbine for a sudden change in the pitch angle [42]

Dynamic stall is a phenomenon associated with the separation of the boundary layer. During the dynamic stall, the boundary layer initially separates at the trailing edge, and gradually shifts to leading edge with the increasing angles of attack [20]. The angle of attack of rotating blades changes dynamically due to sudden change in wind, such as wind shear and atmospheric turbulence. The response introduced by changing angle of attack depends on whether the boundary layer is separated and has a time delay. Dynamic stall phenomenon has been evident from the measurement of aerodynamic coefficients on practical wind turbine blades. One example illustrated in Fig. 2.3 is the dynamic stall event measured at the 30% span position of the Combined Experiment Rotor (CER). As can be seen from Fig. 2.3, due to dynamic stall effects, airfoil normal force coefficient C_N changes dynamically with angle of attack and is significantly different from the value measured in static conditions. Several dynamic stall models have been developed, such as Beddoes-Leishman (BL) model [53], ONERA model [54] and Boeing-Vertol (BV) model [55]. The most widely used model is the BL model, which takes account of attached flow, leading edge separation, trailing edge separation,

and unsteady vortex. The BL model was initially developed for calculating the performance of helicopter rotors and has been applied successfully by Harris [56] and Galbraith [57] for predicting the performance of wind turbines.

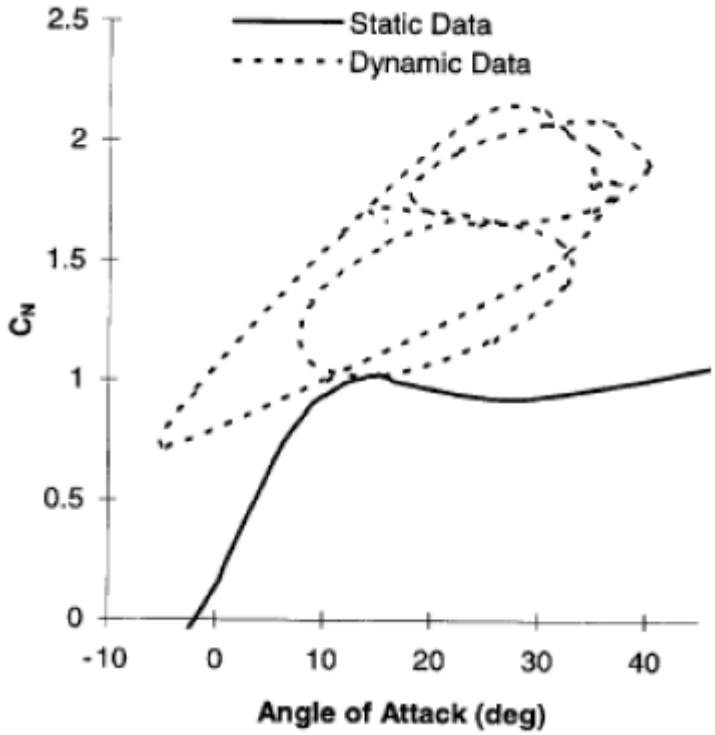

Figure 2.3. Dynamic stall event measured at the 30% span position of the CER [58]

The validity of the BEM model has been extensively established by comparing with experimental data [59]. Because it is simple, efficient and well-proven, the BEM model has become a standard method for analyzing aerodynamic performance of wind turbine blades.

2.2.2. Vortex Model

In order to better model the wake dynamics of wind turbines, the vortex model [60], in which the trailing and shed vorticity in the wake are represented by lifting lines or surfaces, also found applications in aeroelastic models.

The wake in vortex models can be calculated using either prescribed-wake method or free-wake method.

In a prescribed-wake method, the wake shedding from the blade is assumed rigid and described using semi-empirical formulations. The applications of prescribed-wake vortex models in analysing wakes of wind turbine blades can be found in Refs. [61, 62]. The prescribed wake in these models saves computational time but limits their application to steady flow.

A free-wake method, in which the wake can be varied freely both in time and space, is necessary for unsteady flow. Free-wake vortex models have been applied to wind turbine blades to study the unsteady wakes of the blades [63, 64]. The free-wake method used in these models enables them capable of handling complex unsteady flow, e.g. dynamic inflow. However, free-wake method is much more computationally expensive than the prescribed-wake method, and it tends to diverge due to intrinsic singularities of the vortex panels in the developing wake [42].

Compared to the BEM model, vortex models require more computational resources. Additionally, viscous effects are ignored in these models, which limit their application on wind turbines to some extent [42].

2.2.3. Actuator Type Model

In the actuator type model, the blade is represented by a disc/line/surface with distributed loads on the disc/line/surface. Various forms of actuator type model have been developed, which can be classified based on the representation of the blade, namely actuator disc model, actuator line model, and actuator surface model.

The actuator disc model is possibly the earliest model used for studying rotor performance. The classical actuator disc mode, which is derived from 1D momentum theory initially developed by Rankine [65] and Froude [66], is ended up with BEM model [43]. In its general form, however, the actuator disc can also be numerically combined with the Euler or Navier-Stokes equations.

In a numerical actuator disc model, the Euler or Navier-Stokes formulations are typically solved by finite volume or difference scheme, as in a usual CFD calculation. However, the flow around the blades and the geometry of the blades are not resolved. The surface of the blade is replaced by distribution forces acting on the incoming flow.

In the simple case of a uniformly loaded actuator disc, the force acting on the disc is determined by thrust coefficient and reference wind speed, which can be obtained using an iterative procedure [67].

In the case of non-uniformly loaded actuator disc, the force acting on the disc varies along radial location but remains constant over an annulus. Similar to BEM, the local forces on the blades can be calculated using lift and drag coefficients of section airfoil. A relevant issue is the determination of the local angle of attack to find lift and drag coefficients. Shen [68] provided a method to determine the local angle of attack according to information slightly upstream of the blade plane.

Sørensen [69] extended the non-uniformly loaded actuator disc method to the actuator line approach, in which the blade forces was represented using a line with distributed loads. Mikkelsen [70] studied the actuator line approach in detail and applied it in EllipSys3D, a finite volume program for solving incompressible Navier-Stokes formulations [71].

Shen [72, 73] further extended the actuator line approach to the actuator surface method and used it to analyse vertical axis wind turbines. The blade in the actuator surface method was represented by a planar surface. Sibuet Watters and Masson proposed their actuator surface method using a slightly different approach [74-76].

The actuator surface method needs not only lift and drag coefficient of airfoils, but also the skin friction and pressure distribution on the airfoil surface. Dobrev [77] used a linear function which was determined from lift and drag coefficients to represent the pressure distribution in the actuator surface method.

The actuator type models mentioned above should be granted the credit of providing a better insight into the three-dimensional (3D) flow development and the credit of contributing to a better understanding of wake dynamics. However, solving the Navier-Stokes equations is more time-consuming than BEM, and the actuator type models, in which loads on the blade are still calculated based on blade element theory and tabulated airfoil data, does not predict aerodynamic loads more accurately than the BEM model [78].

2.2.4. Computational Fluid Dynamics (CFD) Model

With the advancement of computing resources, CFD has received great attention in recent years. The CFD method solves the governing equations of fluid flow at thousands of positions on and around the blade in an iterative process, which does not require predetermined airfoil aerodynamic data for the calculation. In addition to aerodynamic load calculations, CFD is also a valuable tool to visualize the flow field around the blade, as shown in Fig. 2.4.

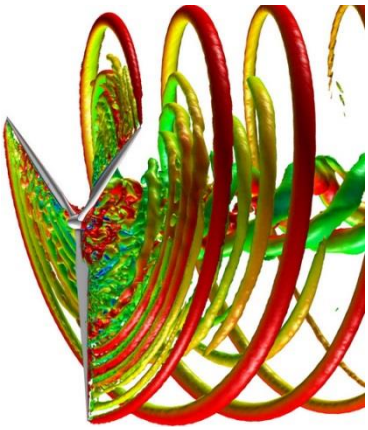

Figure 2.4. Visualised flow field around the blade using CFD [79]

To perform CFD modelling of wind turbine blades, the 3D blade geometry needs to be exactly described in a digitised format. Wind turbine blades often have complex geometric shape with varied spanwise cross-section information, i.e. airfoil shape, chord and twist angle distributions. The 3D blade geometry is generally constructed using computer aided design (CAD) software, such as SolidWorks [80] and UG [81].

Due to the complex geometry of a wind turbine blade, it is quite challenging to generate appropriate mesh for the CFD modelling of the blade. There are three typical types of mesh, including structured mesh, unstructured mesh, and hybrid mesh, as illustrated in Fig. 2.5. Structured mesh has advantages in high resolution, easy convergence and low memory usage. However, it is difficult and time-consuming to generate structured mesh for complex geometries, such as highly twisted blades. The major advantage of unstructured mesh is the ease of mesh generation for complex geometries. However, unstructured mesh consumes more computational time, as it generally results in higher cell count than structured mesh filling the same volume. Hybrid mesh, also known as adaptive mesh, is the combination of structured mesh and unstructured mesh. In hybrid mesh, structured mesh is used for important regions, such as boundary layers, while

unstructured mesh is used elsewhere. Due to the flexibility of hybrid mesh, it has been widely used for the mesh generation of CFD modelling of wind turbine blades [82-84].

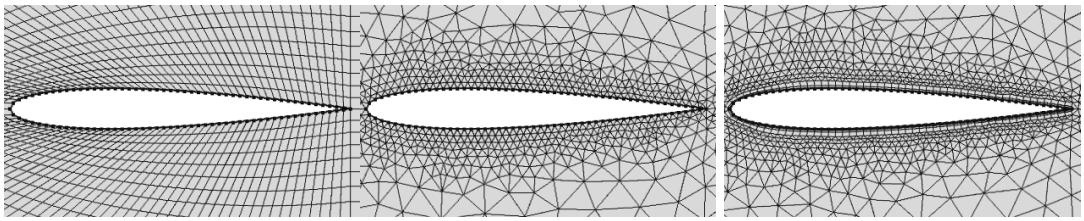

a. Structured mesh b. Unstructured mesh c. Hybrid mesh

Figure 2.5. CFD mesh type

The mathematical fundamentals of CFD are the Navier-Stokes (NS) equations [85], which are the governing equations of fluids derived from the momentum, energy, and continuity conservations.

The discretisation of NS equations can be achieved through three typical discretisation methods, including finite-volume method (FVM), finite-element method (FEM) and finite-difference method (FDM). FVM is a common method used in CFD modelling, as it has advantages in solution speed and memory usage [86]. FEM is mainly utilized in structural analysis, but it can also be applied to fluids. For instance, ANSYS CFX [87], a widely used commercial CFD software package, is based on FEM. Compared to FVM, FEM is much more stable, but it consumes more memory and has slower solution times [88]. FDM is easy to implement, but it is limited to simple grids. Currently, FDM is only utilised in few specialised CFD codes.

Directly solving NS equations, known as direct numerical simulation (DNS), requires huge computational resources, which exceed the capacity of current computers. In order to apply NS equations to solve practical engineering problems on wind turbine blades, some kind of turbulence modelling are required. Currently, turbulence models are mainly derived based on Reynolds Averaged NS equations (RANS) [89], which give approximate time-averaged solutions to NS equations. Various RANS based turbulence models have been used for wind turbine applications, such as $k-\omega$ SST model [90], $k-\varepsilon$ model [91] and Spalart-Allmaras model [92]. Among these models, $k-\omega$ SST model is found the most successful one for both 2D airfoil and 3D blade CFD modelling.

A number of studies have been performed on the CFD modelling of stall-regulated wind turbines, showing that all RANS based turbulence models fail to accurately model the

stalled flow at high angle of attack [42]. Possible solutions to this problem are to use more complicated turbulence modelling approaches, such as 1) large eddy simulations (LES) [93], which retains large eddies and ignore small eddies in solving NS equations; and 2) detached eddy simulations (DES) [94], which is a hybrid method combining RANS and LES. However, both LES and DES are much more computationally costly than RANS, as they require considerably finer computational meshes and the computations have to be carried out with time accurate algorithms [42].

Currently, CFD is still computationally too expensive and not efficient enough for fluid-structure interaction analysis, which is the main obstacle of its industrial applications in aeroelastic modelling [20].

2.3. Review of Structural Models

In order to perform aeroelastic modelling of wind turbine blades, a structural model needs to be included to determine the structural dynamic response of the blade. Structural models used in aeroelastic modelling of wind turbine blades can be roughly categorized into two groups, i.e. 3D finite-element method (FEM) model with shell elements and 1D equivalent beam model with beam elements. In order to discretise the blade into a series of 1D beam elements, three discretisation methods are often used in aeroelastic modelling of wind turbine blades [20], including modal approach, multi-body dynamics (MBD) and 1D finite-element method (FEM).

2.3.1. 3D Finite-element Method (FEM) Model and 1D Beam Model

Wind turbine blade structures can be modelled using either 3D FEM model with shell elements or 1D beam model with beam elements.

2.3.1.1. 3D FEM Model

In 3D FEM model, wind turbine composite blades are generally constructed using 3D composite shell elements, which are capable of describing composite layer characteristics throughout the shell thickness. An example of 3D FEM model of a wind turbine composite blade is illustrated in Fig. 2.6.

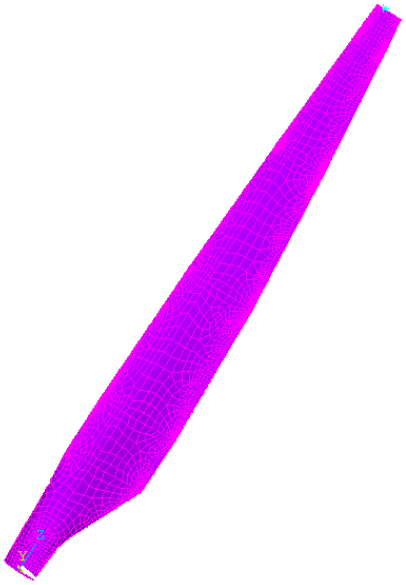

Figure 2.6. 3D FEM model of a wind turbine composite blade

Due to the complicated aerodynamic shape and structural layout of a wind turbine composite blade, generating a 3D FEM model of the blade using general-purpose commercial finite-element packages, such as ANSYS [95] and Abaqus [96], is tedious and time-consuming. In order to facilitate the generation of 3D FEM models of wind turbine blades, Laird developed a specialised tool called NuMAD (Numerical Manufacturing And Design) [97], which is a stand-alone pre-processor for ANSYS. NuMAD provides a user-friendly graphic user interface (GUI), as depicted in Fig. 2.7, for defining the blade geometry information (such as chord and twist angle distributions) and the blade structural layout information (such as shear web locations and composites layup). The output from NuMAD is a series of ANSYS Parametric Design Language (APDL) commands used to generate the 3D FEM model of the blade in ANSYS.

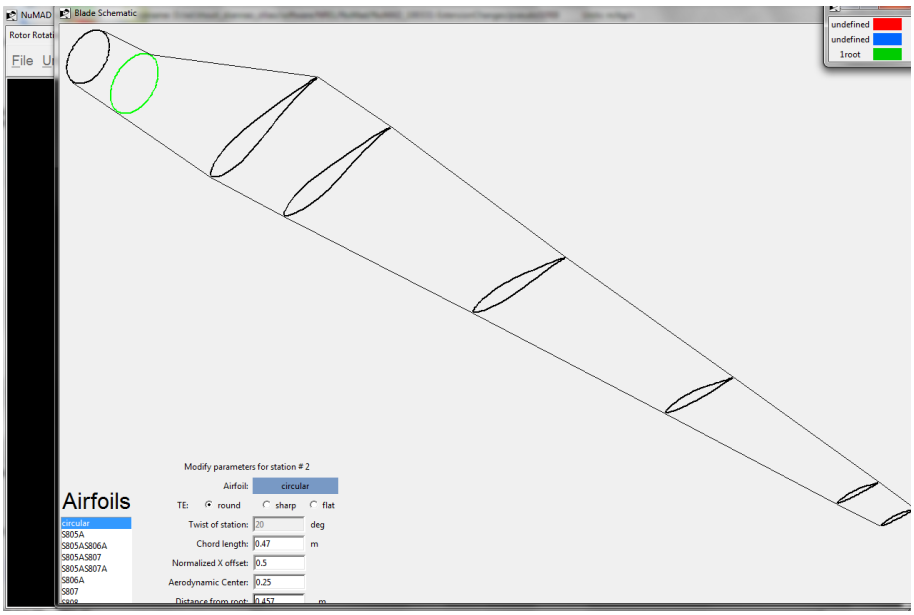

Figure 2.7. GUI of NuMAD

3D FEM is an incredible tool for examining the stress distribution within a blade, which is applicable and valuable for "static" stress analysis. However, 3D FEM is computationally too expensive and this drawback limits its application in aeroelastic modelling, which demands continuous fluid-structure interaction, i.e. interactive aerodynamic loads calculation and structure deflection analysis.

2.3.1.2. 1D Beam Model

Wind turbine blades are slender structures having one of their dimensions significantly larger than the other two. Such structures can be efficiently modelled using beam models. The beam axis is defined along the largest dimension, and a cross-section perpendicular to this axis is considered smoothly varying along the span of the beam. A number of beam models exist and they can be roughly categorised into two groups, i.e. linear beam model and nonlinear beam model.

Two widely used linear beam models are the Euler-Bernoulli beam model [33] and the Timoshenko beam model [98]. The Euler-Bernoulli beam model, also known as classical beam model, deals with slender beams subjected to extensional, torsional, and bending loads. The shear deformation effects are ignored in the model. Timoshenko beam model was developed by Timoshenko in the early 20th century. The model takes account of shear deformation effects, making it more suitable for describing the behaviour of thick and short beams than the Euler-Bernoulli beam model. Regarding

wind turbine blades, which generally have thin and slender structure, Timoshenko beam model does not show much difference from Euler-Bernoulli beam model. Due to its easy implementation, Euler-Bernoulli beam model has been used by most structural models in aeroelastic modelling of wind turbine blades [42].

Both Euler-Bernoulli beam model and Timoshenko beam model contain the assumption of small deflections. However, this assumption is not valid anymore for very flexible blade design because such blades often experience large deflections. Handling large deflections requires a nonlinear beam model, and a number of nonlinear beam models have been proposed. A well-known example is the geometrically exact beam theory (GEBT) [99], in which the deformed beam geometry (i.e. the displacements and rotations of the beam reference line) is represented exactly.

Compared to 3D FEM, the 1D beam model is much fast and saves much computational time and is capable of providing accurate results if constructed properly [100]. Therefore, almost all aeroelastic codes represent the blades as a series of 1D beam elements instead of 3D shell elements [20, 42].

2.3.2. Discretisation Methods of 1D Beam Model

In order to discretise the blade into a series of 1D beam elements, three discretisation methods are often used in aeroelastic modelling of wind turbine blades [20], i.e. modal approach, multi-body dynamics (MBD) and 1D finite-element method (FEM).

2.3.2.1.Modal Approach

In modal approach, the deflection shape of the flexible bodies, such as the blade and tower, is described as a linear combination of a set of mode shapes, which are usually obtained from a finite element pre-processor.

Using mode shapes is an effective way to reduce the number of degrees of freedom (DOFs) and therefore reduce the size of matrices and speed up the computations per time step. Therefore, the modal approach is computationally efficient, resulting in rapid simulation. For this reason, the majority of the present commercial wind turbine

aeroelastic models use the modal approach to calculate the structural dynamics of the blade [101].

However, the flexibility of the modal approach is restricted somewhat by its restraints on the type and number of DOF allowed in the structure. For instance, FLEX5 [27], which is a commercially widely used aeroelastic analysis model based on the modal approach, uses only the initial three or four (two flapwise and one or two edgewise) eigenmodes for the blade.

Another major limitation of the modal approach is that the approach is inherently limited to linear analysis due to its linear assumption, i.e. the deflection shape of the flexible components must be a linear combination of the provided mode shapes. This means that the modal approach is not capable of handling large deflections of the flexible blade.

Additionally, the accuracy of the modal approach greatly depends on the prescribed mode shapes. In order to obtain the mode shapes of the blade, a finite-element based pre-processor is required.

2.3.2.2.Multi-body Dynamics (MBD) Method

In MBD method, the structure is discretised into a number of bodies, which can be either flexible or rigid. These bodies are interconnected by force elements (such as springs) or kinematic constraints (such as joints) [102]. The dynamics of the structure can then be evaluated using equations of motion, which are usually derived from Lagrange's equations or Newtow-Euler equations.

The MBD method benefits from high modelling flexibility due to its capability to generate and couple together arbitrary number of separate bodies in a single dynamic system. Compared to modal approach, the MBD method requires more computational recourses, but it enables an increased number of DOF to be modelled.

2.3.2.3.1D FEM Method

The 1D FEM approach finds approximate solutions of 1D beam problems by the analysis of an assemblage of finite elements, which are interconnected by nodal points. The 1D FEM allows a more comprehensive and accurate deformation description of wind turbine blades, and it only requires slightly more computational resources than the other two discretisation approaches. Therefore, the 1D FEM has been adopted by most of recently developed aeroelastic models of wind turbine blades [42].

2.4. Review of Cross-sectional Models

Wind turbine blades generally are made of composite materials due to their high strength-to-weight ratio and good fatigue performance. To construct the 1D beam model of wind turbine blades for aeroelastic modelling, the cross-sectional properties of the blade, such as mass per unit length and sectional stiffness, are essential information. Fig. 2.8 depicts the structural layout of a typical blade cross-section, including three cells with two shear webs. As can be seen from Fig. 2.8, each cell includes several laminates, each laminate is made up of several plies, and each ply is a composite mat placed at different angles, resulting in a complicated structural topology. Due to the intrinsic nature of composite materials and the complexity of blade structural topologies, it is quite challenging to obtain the cross-sectional properties of a wind turbine blade.

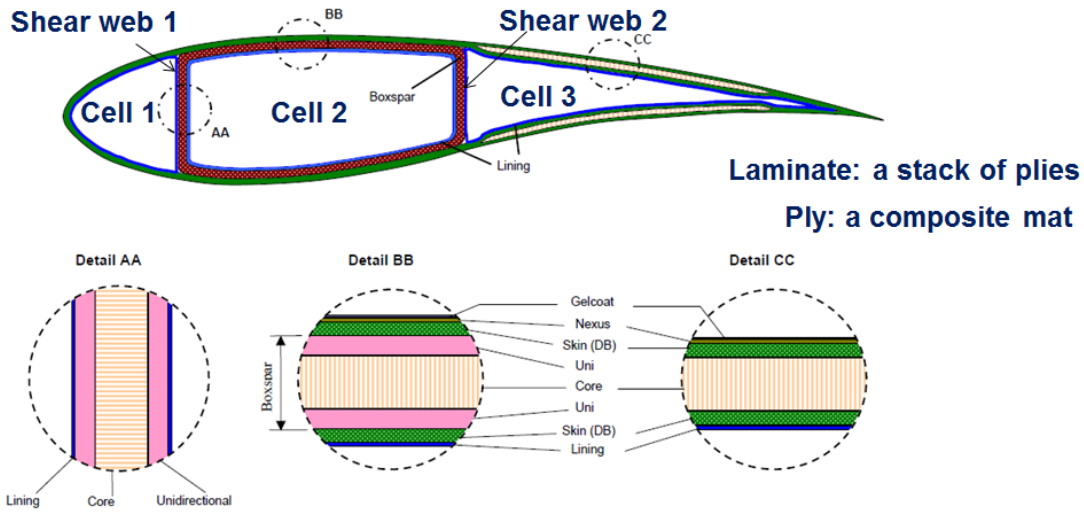

Figure 2.8. Structural layout of a typical blade cross-section [103]

In order to obtain the cross-sectional properties of wind turbine blades, various cross-sectional analysis models have been developed, which can be categorised into three groups, i.e. 3D finite-element method (FEM) based model, 2D FEM based model and classical lamination theory (CLT) based model.

2.4.1. 3D FEM Based Model

The most sophisticated method to extract the cross-sectional properties of wind turbine blades is based on 3D FEM. 3D FEM, despite their ability for accurate stress and displacement analysis, cannot directly yield the cross-sectional properties of wind turbine blades. It relies on computationally complicated post-processing of force-displacement data [104]. One such post-processing tool is BPE (Blade Properties Extractor) [105], which is developed by Sandia National Laboratories and Global Energy Concepts. Currently, BPE is a module of NuMAD (Numerical Manufacturing And Design) [97], which is a windows based pre/post-processor to generate the 3D FEM models of wind turbine blades. BPE applies a series of unit loads at the blade tip and transfers the displacement results of the 3D FEM model of the blade to a series of MATLAB routines, which extract the stiffness matrices for the equivalent beam elements. In principle, BPE should be able to provide the most accurate cross-sectional properties because all 3D information can be captured by the 3D FEM model. However, there are seemingly several challenges facing this method. Firstly, application of loads must be performed carefully to minimize the boundary layer effects. Additionally, the cross-sectional properties estimated by BPE are sensitive to the length of the blade segment, which one chooses to perform the finite-element analysis. Changing the length of the blade segment may even result in a singular stiffness matrix under some extreme situations [106].

2.4.2. 2D FEM Based Model

Several other cross-sectional analysis tools based on 2D finite-element techniques have also been developed. Cesnik and Hodges [107] developed VABS (Variational Asymptotic Beam Sectional analysis) based on variational asymptotic method, which replaces a 3D structural model with a 2D model in terms of an asymptotic series of several small parameters of the structure. Two other examples of applying variational asymptotic method to composite beam analysis can be found in Refs. [108, 109]. VABS

requires a 2D finite-element discretisation of the cross-section to generate its input files, which are the 2D mesh of the cross-section and the corresponding materials. For a practical wind turbine blade made of layers of composites, the generation of VABS input files is very tedious and requires a separate pre-processor called PreVABS [110]. Blasques [111] developed a cross-sectional analysis tool called BECAS (BEam Cross section Analysis Software) based on anisotropic beam theory, which is originally presented by Gianotto et al. [112] for estimating the stiffness and the stresses of inhomogeneous anisotropic beams. Similar to VABS, BECAS also requires a 2D finite-element discretisation of the cross-section. A separate pre-processor called Aifoil2BECAS [113], which is a python program, is needed to generate the input files for BECAS. Currently, the cross-section in Airfoil2BECAS is limited to 8 distinct regions, where layup and thickness information can be assigned.

2.4.3. Classical Lamination Theory (CLT) Based Model

Compared to the finite-element techniques, classical lamination theory (CLT) [114], which is an extension of the classical plate theory [115] to laminated plates, is fast and reasonably accurate. CLT can be used to combine properties and the angle of each ply in a pre-specified stacking sequence to calculate the overall effective performance for a laminate structure. Based on several reasonable assumptions, such as plane stress and linear strain, CLT transfers a complicated 3D elasticity problem to a solvable 2D problem [116]. Among the above assumptions, the assumption 'each ply is under the condition of plane stress' is acceptable for composite blade due to the fact that wind turbine blades are thin-walled structures of composites.

CLT has been widely used for analysing structural performance of composite materials [117, 118]. In terms of composite blades, Bir [104, 119] developed PreComp (Pre-processor for computing Composite blade properties) at National Renewable Energy Laboratory (NREL) based on CLT. PreComp does not need a separate pre-processor to generate the input files, which are the geometric shape and internal structural layout of the blades, and allows an arbitrary number of webs and a general layup of composite laminates. Due to its efficiency, PreComp has been widely used in cross-sectional analysis of wind turbine composite blades [120-122]. However, PreComp ignores the effects of shear webs in the calculation of the torsional stiffness. In other words, if the number of webs on a cross-section is changed, no change in torsional stiffness will be

observed using PreComp. This is invalid for a practical blade cross-section, where the torsional stiffness will be enhanced as the number of shear webs increases.

2.5. Summary

This chapter reviewed the key elements in aeroelastic modelling of wind turbine blades, including aerodynamic models, structural model and cross-sectional analysis models.

For the aerodynamic part of aeroelastic modelling of wind turbine blades, there are four typical types of aerodynamic models, including blade element momentum (BEM) model, vortex model, actuator type model and computational fluid dynamic (CFD) model. Compared to other aerodynamic models, BEM model is fast and able to provide accurate results when reliable airfoil data are available. For this reason, BEM model is chosen as the aerodynamic part of aeroelastic modelling in this thesis.

For the structural part of aeroelastic modelling of wind turbine blades, the blade structure can be modelled using either 3D finite-element method (FEM) model with shell elements or 1D beam model with beam elements. Compared to 3D FEM, 1D beam model is much fast and saves much computational time and is capable of providing accurate results if constructed properly. For this reason, in this thesis, wind turbine blade structure is represented as a series of 1D beam elements instead of 3D shell elements.

In order to discretise the blade into a series of 1D beam elements, three discretisation methods are often used in aeroelastic modelling of wind turbine blades, including modal approach, multi-body dynamics (MBD) and 1D finite-element method (FEM). Compared to the other two discretisation methods, 1D FEM allows a more comprehensive and accurate deformation description of wind turbine blades, and it only requires slightly more computational resources than the other two discretisation methods. Therefore, 1D FEM is adopted for the discretisation of wind turbine blades in this thesis.

To construct the 1D beam model of wind turbine blades for aeroelastic modelling, the cross-sectional properties of the blades, such as mass per unit length and sectional stiffness, are essential information. Due to the intrinsic nature of composite materials

and the complexity of blade structural topologies, obtaining the cross-sectional properties of a wind turbine blade is quite challenging and requires a specialised cross-sectional analysis model. However, existing cross-sectional analysis models for wind turbine blades are either time-consuming or inaccurate. Therefore, it is necessary to develop a cross-sectional model, which is capable of extracting cross-sectional properties of wind turbine blades in a fast and reliable way.

The following Chapter 3 details the development of a cross-sectional analysis model. Chapter 4 and Chapter 5 present the structural model and aerodynamic model, respectively.

CHAPTER 3 BLADE CROSS-SECTIONAL MODELLING

3.1. Introduction

As reviewed in Section 2.3.1, wind turbine blade structures can be modelled using either 3D finite-element method (FEM) model with shell elements or 1D beam model with beam elements. Compared to the 3D FEM model, the 1D beam model is much faster and saves much computational time and is capable of providing reasonable results if constructed properly. Therefore, for the structural part of the aeroelastic modelling in this thesis, the blade is represented as a series of 1D beam elements instead of 3D shell elements.

To construct the 1D beam model of wind turbine blades for aeroelastic modelling, the cross-sectional properties of the blades, such as mass per unit length and sectional stiffness, are essential information. It should be noted that modern wind turbine blades generally are made of composite materials and have complicated structural layout. Due to the intrinsic nature of composite materials and the complexity of blade structural topologies, it is quite challenging to obtain the cross-sectional properties of a wind turbine composite blade.

As reviewed in Section 2.4, three types of models have been proposed for cross-sectional analysis of wind turbine blades, including 3D FEM based model, 2D FEM based model and classical lamination theory (CLT) based model. 3D FEM based model is time-consuming because it relies on computationally complicated post-processing of force-displacement data. 2D FEM based model is not efficient enough since it requires a separate pre-processor to generate its input files. The cross-sectional analysis model PreComp [104, 119], which is based on CLT, is efficient, but it is incapable of predicting torsional stiffness accurately. The torsional stiffness is hard to evaluate because it is significantly affected by shear web effects and warping effects which are difficult to model.

For a closed thin-walled cross-section, Bredt-Batho shear flow theory (BSFT) [123] can be used to determine the torsional stiffness of the cross-section. BSFT is developed based on the assumption that the torsional stress is uniformly distributed across the thickness of the cross-section. Experiments show that this assumption is acceptable for most thin-walled cross-sections [124]. BSFT implicitly includes the dominant warping effects and it can provide reasonable results for the torsional stiffness of the closed thin-walled cross-section [124]. However, the original BSFT is developed for a single-cell cross-section. In order to apply BSFT to a practical wind turbine blade cross-section with shear webs, an extension of BSFT to cover multi-cells is required.

This chapter presents a mathematical model [32], which is capable of accurately and rapidly calculating the cross-sectional properties of wind turbine blades, developed by incorporating CLT with extended Bredt-Batho shear flow theory (EBSFT). Based on the mathematical model, a MATLAB program called CBCSA (Composite Blade Cross-Section Analysis) is developed. In order to validate CBCSA, a series of benchmark tests are performed for isotropic and composite blades as compared with ANSYS, PreComp and experimental data.

The main contents of this chapter have been published in Ref. [32], and more details are provided in this chapter. Additionally, the improvements[1] since the publication are also presented in this chapter.

This chapter is structured as follows. CLT and BSFT are summarised in Sections 3.2 and 3.3, respectively. EBSFT is discussed in Section 3.4. Section 3.5 details the development of a mathematical model for cross-sectional analysis by incorporating CLT with EBSFT. Validations are provided in Section 3.6, followed by a chapter summary in Section 3.7.

[1] Since the publication, improvements have been made to enable CBCSA to output flapwise mass per unit length and edgewise mass per unit length, which are cross-sectional properties required by dynamic analysis.

3.2. CLT

CLT is an extension of the classical plate theory to laminated plates. The main assumptions of CLT are the Kirchhoff hypotheses [114]:

- Straight lines which are perpendicular to the mid-surface before deformation remain straight after deformation.
- The transverse normals are inextensible.
- The transverse normals rotate so that they are always perpendicular to the mid-surface.

The first two assumptions indicate that the transverse displacement is independent of the thickness coordination and the transverse normal strain is zero. The third assumption implies that transverse shear strains are zero. These assumptions are acceptable for thin laminates in most cases [114].

CLT has wide applications including stress and strain analysis of laminate plates. The validity of CLT has been established by comparing with experimental results and the exact solutions of the general elastic problems [125]. In terms of cross-sectional analysis, CLT can be used to calculate the effective engineering constants of angled plies.

The coordinate system used for an angled ply for the cross-sectional analysis using CLT is shown in Fig. 3.1.

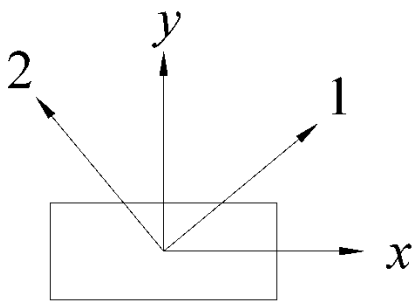

Figure 3.1. Principal material and global coordinates

The directions 1 and 2 constitute principal material coordinates while the directions *x* and *y* constitute global coordinates. The directions 1 and 2 are parallel and perpendicular to the fiber direction, respectively.

The materials considered with CLT are orthotropic. The stress-strain relationship in principal material coordinates for an orthotropic material under plane stress condition can be expressed as:

$$\begin{bmatrix} \varepsilon_1 \\ \varepsilon_2 \\ \gamma_{12} \end{bmatrix} = \begin{bmatrix} S_{11} & S_{12} & 0 \\ S_{12} & S_{22} & 0 \\ 0 & 0 & S_{66} \end{bmatrix} \begin{bmatrix} \sigma_1 \\ \sigma_2 \\ \tau_{12} \end{bmatrix} \tag{3.1}$$

In Eq. (3.1), the components of matrix [S] are calculated by:

$$S_{11} = 1/E_1 \tag{3.2}$$

$$S_{12} = -\nu_{12}/E_1 \tag{3.3}$$

$$S_{22} = 1/E_2 \tag{3.4}$$

$$S_{66} = 1/G_{12} \tag{3.5}$$

where E_1 and E_2 are the Young's modulus along the direction 1 and direction 2, respectively; ν_{12} is the Poisson's ratio and G_{12} is the shear modulus. All of these constants are called engineering constants of a unidirectional ply.

The inverse matrix [*Q*] of the matrix [*S*] in Eq. (3.1) is called reduced stiffness matrix [126], given as follows:

$$\begin{bmatrix} \sigma_1 \\ \sigma_2 \\ \tau_{12} \end{bmatrix} = \begin{bmatrix} Q_{11} & Q_{12} & 0 \\ Q_{12} & Q_{22} & 0 \\ 0 & 0 & Q_{66} \end{bmatrix} \begin{bmatrix} \varepsilon_1 \\ \varepsilon_2 \\ \gamma_{12} \end{bmatrix} \tag{3.6}$$

where:

$$Q_{11} = S_{22}/(S_{11}S_{22} - S_{12}^2) \tag{3.7}$$

$$Q_{12} = -S_{12}/(S_{11}S_{22} - S_{12}^2) \tag{3.8}$$

$$Q_{22} = S_{11}/(S_{11}S_{22} - S_{12}^2) \tag{3.9}$$

$$Q_{66} = 1/S_{66} \tag{3.10}$$

The stress-strain relations in Eq. (3.6) for the principal material coordinates can be transformed into a global coordinate system using:

$$\begin{bmatrix}\sigma_x\\ \sigma_y\\ \tau_{xy}\end{bmatrix}=[T_m]^{-1}[Q][R_m][T_m][R_m]^{-1}\begin{bmatrix}\varepsilon_x\\ \varepsilon_y\\ \gamma_{xy}\end{bmatrix} \tag{3.11}$$

where $[T_m]$ is the transformation matrix, $[Q]$ is the reduced stiffness matrix in Eq. (3.6), $[R_m]$ is the Reuter matrix [126]. $[T_m]$ and $[R_m]$ are respectively defined as:

$$[T_m]=\begin{bmatrix}\cos^2(\alpha_{ply}) & \sin^2(\alpha_{ply}) & -2\sin(\alpha_{ply})\cos(\alpha_{ply})\\ \sin^2(\alpha_{ply}) & \cos^2(\alpha_{ply}) & 2\sin(\alpha_{ply})\cos(\alpha_{ply})\\ \sin(\alpha_{ply})\cos(\alpha_{ply}) & -\sin(\alpha_{ply})\cos(\alpha_{ply}) & \cos^2(\alpha_{ply})-\sin^2(\alpha_{ply})\end{bmatrix} \tag{3.12}$$

$$[R_m]=\begin{bmatrix}1&0&0\\0&1&0\\0&0&2\end{bmatrix} \tag{3.13}$$

where α_{ply} is the ply angle, i.e. the angle between the direction 1 and direction *x* in Fig. 3.1.

The effective engineering constants of an angled ply can be expressed in terms of the engineering constants of a unidirectional ply using the following equations:

$$E_x^{ply}=\frac{1}{\frac{1}{E_1}\cos^4(\alpha_{ply})+\left(\frac{1}{G_{12}}-\frac{2\upsilon_{12}}{E_1}\right)\sin^2(\alpha_{ply})\cos^2(\alpha_{ply})+\frac{1}{E_2}\sin^4(\alpha_{ply})} \tag{3.14}$$

$$G_{xy}^{ply}=\frac{1}{\left[\frac{4}{E_2}+\frac{4+8\upsilon_{12}}{E_1}-\frac{2}{G_{12}}\right]\sin^2(\alpha_{ply})\cos^2(\alpha_{ply})+\frac{\sin^4(\alpha_{ply})+\cos^4(\alpha_{ply})}{G_{12}}} \tag{3.15}$$

where E_x^{ply} and G_{xy}^{ply} are the effective Young's modulus along the direction x (see Fig. 3.1) and effective shear modulus of an angled ply, respectively.

3.3. Bredt-Batho Shear Flow Theory (BSFT)

In the case of a closed thin-walled cross-section, the assumption that the torsional stress τ evenly distributes across the thickness of a segment of the cross-section is acceptable in most situations. The product of the torsional stress τ and the thickness t_c refers to shear flow q_s [124]:

$$q_s=\tau t_c \tag{3.16}$$

Based on the above assumption, a shear flow theory called Bredt-Batho shear flow theory (BSFT) [124] is developed to evaluate stresses and deformations in structures with closed thin-walled cross-section under torsion.

The torsional stiffness *GJ* of the closed thin-walled cross-section (e.g. the cross-section in Fig. 3.2) can be obtained using BSFT:

$$GJ = \frac{4A^{*2}}{\oint \frac{1}{t_c G} ds_c} \tag{3.17}$$

where A^* is the area enclosed by the middle line of the wall , t_c is the thickness of the wall, G is the shear modulus, and s_c is the perimeter coordinate. It is should be noted that the t_c and G can vary along s_c if the cross-section consists of several segments having variable wall thickness and different material properties. In case of varied t_c, shear flow q_s in Eq. (3.16) is also varied.

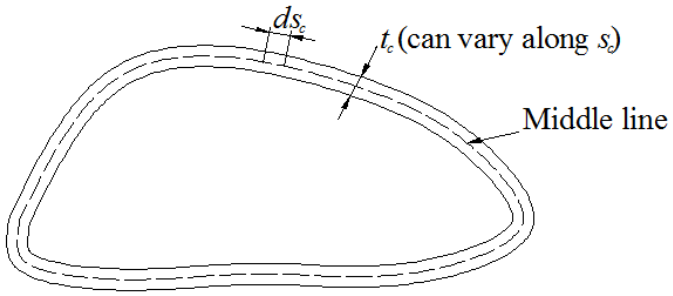

Figure 3.2. Closed thin-walled cross-section

3.4. Extended Bredt-Batho Shear Flow Theory (EBSFT)

The original BSFT mentioned above is developed for a single-cell cross-section, which means no shear webs are included. To apply BSFT in a practical wind turbine blade cross-section with shear webs, an extension of BSFT to cover multi-cell is required.

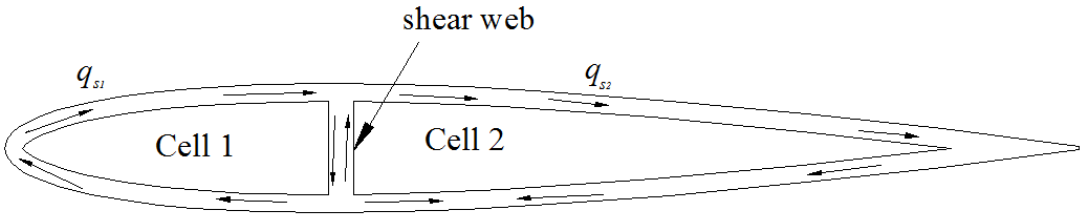

Figure 3.3. Blade cross-section with one shear web

Taking a wind turbine blade cross-section with one shear web in Fig. 3.3 as an example, the torsional moment M_T is expressed as [127]:

$$M_T = 2\left(q_{s1}A_1^* + q_{s2}A_2^*\right) \tag{3.18}$$

where q_{s1} and q_{s2} are the shear flow of cells 1 and 2, respectively; A_1^* and A_2^* are the area enclosed by the middle line of the wall of cells 1 and 2, respectively.

The twist angles (θ_{T1} and θ_{T2}) of cells 1 and 2 are respectively expressed as:

$$\theta_{T1} = \frac{1}{2GA_1^*}\left(q_{s1}\oint_1 ds_c / t_c - q_{s2}\int_{12} ds_c / t_c\right) \tag{3.19}$$

$$\theta_{T2} = \frac{1}{2GA_2^*}\left(q_{s2}\oint_2 ds_c / t_c - q_{s1}\int_{21} ds_c / t_c\right) \tag{3.20}$$

Assuming the twist angles of the two cells are the same, we obtain:

$$\theta_{T1} = \theta_{T2} = \theta_T \tag{3.21}$$

Reformulating Eqs. (3.19) and (3.20), we obtain:

$$\delta_{w11}q_{s1} + \delta_{w12}q_{s2} - 2A_1^*\theta_T = 0 \tag{3.22}$$

$$\delta_{w12}q_{s1} + \delta_{w22}q_{s2} - 2A_2^*\theta_T = 0 \tag{3.23}$$

where δ_w is warping flexibility:

$$\delta_{w11} = \oint_1 \frac{ds_c}{Gt_c} \tag{3.24}$$

$$\delta_{w22} = \oint_2 \frac{ds_c}{Gt_c} \tag{3.25}$$

$$\delta_{w12} = \delta_{w21} = -\int_{12} \frac{ds_c}{Gt_c} \tag{3.26}$$

Eqs. (3.18), (3.22) and (3.23) can also be written in matrix format:

$$M_T = 2\left[A^*\right]^T\left[q_s\right] \tag{3.27}$$

$$\left[\delta_w\right]\left[q_s\right] = 2\theta_T\left[A^*\right] \tag{3.28}$$

where:

$$\left[A^*\right]=\begin{bmatrix}A_1^*\\A_2^*\end{bmatrix} \tag{3.29}$$

$$\left[q_s\right]=\begin{bmatrix}q_{s1}\\q_{s2}\end{bmatrix} \tag{3.30}$$

$$\left[\delta_w\right]=\begin{bmatrix}\delta_{w11}\ \delta_{w12}\\\delta_{w21}\ \delta_{w22}\end{bmatrix} \tag{3.31}$$

The torsional stiffness is given by:

$$GJ=\frac{M_T}{\theta_T} \tag{3.32}$$

Substituting Eqs. (3.27) and (3.28) into Eq. (3.32) gives:

$$GJ=4\left[A^*\right]^T\left[\delta_w\right]^{-1}\left[A^*\right] \tag{3.33}$$

For a wind turbine blade cross-section with arbitrary shear webs, the torsional stiffness can be expressed in the form of Eq. (3.33). For a blade cross-section with two shear webs, $\left[\delta_w\right]$ and $\left[A^*\right]$ becomes:

$$\left[\delta_w\right]=\begin{bmatrix}\delta_{w11} & \delta_{w12} & 0\\\delta_{w21} & \delta_{w22} & \delta_{w23}\\0 & \delta_{w32} & \delta_{w33}\end{bmatrix} \tag{3.34}$$

$$\left[A^*\right]=\begin{bmatrix}A_1^*\\A_2^*\\A_3^*\end{bmatrix} \tag{3.35}$$

3.5. A Mathematical Model for Cross-sectional Analysis by Incorporating CLT and EBSFT

In order to determine the cross-sectional properties of wind turbine blades, all cross-sectional laminates are discretised into many area segments. Each area segment encloses several angled plies. The effective engineering constants of each angled ply are obtained using CLT. A weighting method [128] is used to calculate the equivalent properties of each area segment, the elastic centre and mass centre locations of the cross-section. Firstly, the area moments of inertia of each area segment are calculated with respect to

its local axes and centroid, and then transformed to the elastic axes and centre of the cross-section using transform-axis formula and parallel-axis theorem [129]. Based on the transferred area moments of inertia and calculated equivalent properties of each area segment, the contributions of each area segment to the cross-sectional properties are calculated. The torsional stiffness is obtained using EBSFT while the other cross-sectional properties are obtained by means of adding the contributions of all the area segments. Based on the above strategy, a mathematical model for cross-sectional analysis is developed. The flowchart of the model is shown in Fig. 3.4.

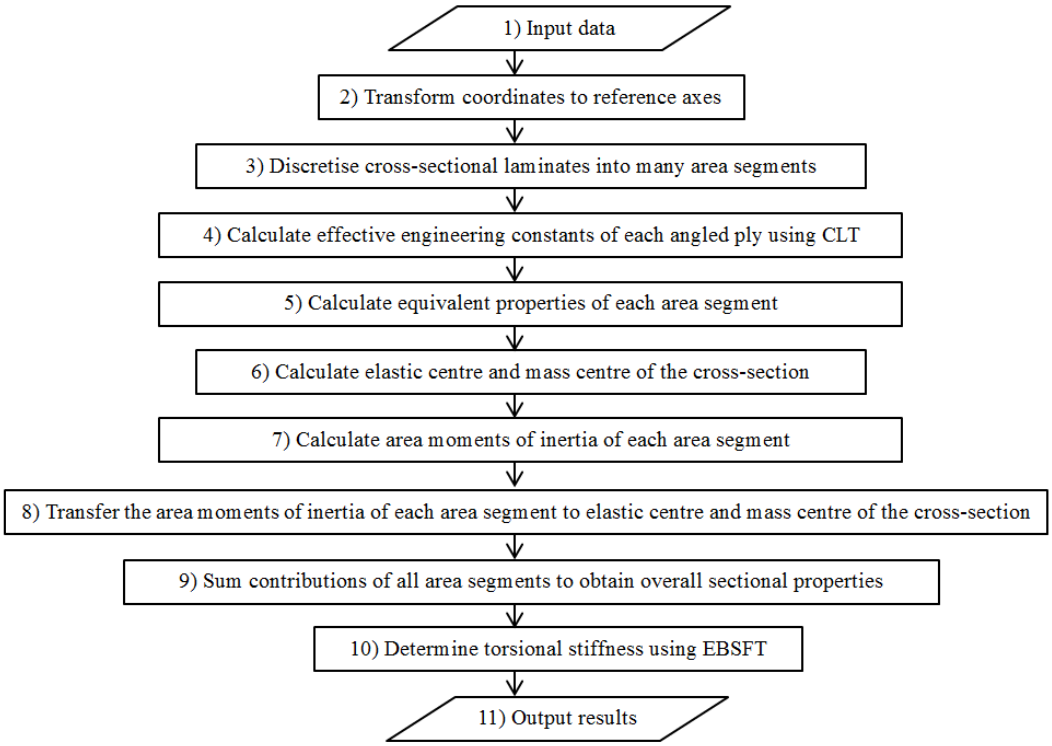

Figure 3.4. Flowchart of the mathematical model

Each step of the flowchart in Fig. 3.4 is detailed as follows:

1) Input data

The model requires cross-sectional external shape (chord, twist angle and airfoil coordinates) and internal laminate layup (laminate schedule, ply angle and material engineering constants) as inputs.

2) Transform coordinates to reference axes

In the cross-sectional analysis, bending stiffness including both flapwise and edgewise stiffness is generally referred to the elastic centre (X_{EC} , Y_{EC}). The flapwise and edgewise mass moments of inertia are generally referred to the mass centre (X_{MC} , Y_{MC}). Both elastic centre and mass centre are measured from the reference axes of the cross-

section, as shown in Fig. 3.5. Therefore, it is necessary to add a step to transfer the input airfoil data to reference axes if the input data refer to different axes.

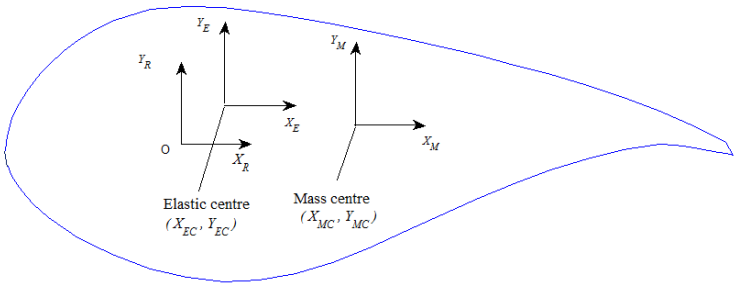

Figure 3.5. Reference axes

As shown in Fig. 3.5, X_R and Y_R are the reference axes; X_E and Y_E are the elastic axes; X_M and Y_M are the mass axes. The directions of X_R and Y_R are parallel and perpendicular to the chord direction of the blade cross-section respectively. The location of reference point O can be specified arbitrarily and usually is identical to the aerodynamic centre of the blade cross-section. Both directions of X_E and X_M are parallel to the reference axis X_R, and both directions of Y_E and Y_M are parallel to the reference axis Y_R.

3) Discretise cross-sectional laminates into many area segments

In this step, all cross-sectional laminates are discretised into many area segments. Each area segment encloses several plies. Taking a typical blade cross-section with one shear web in Fig. 3.6 as an example, the cross-sectional laminates are discretised into 110 area segments and the area segment "ab" encloses three different plies.

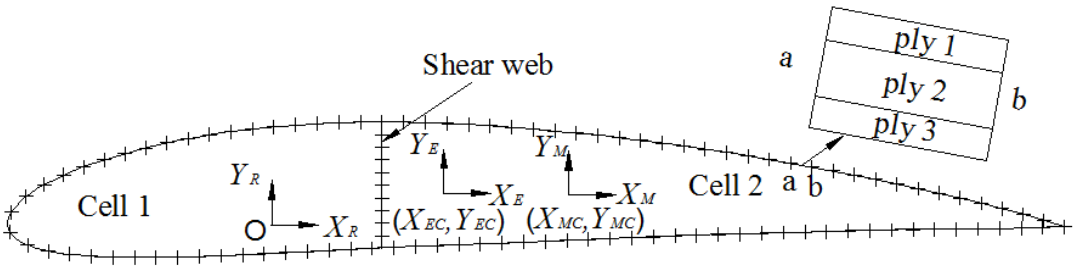

Figure 3.6. Discretisation of a typical blade cross-section with one shear web

4) Calculate effective engineering constants of each angled ply using CLT

In order to achieve better structural performance, some plies are generally placed at an angle. Therefore, it requires a step to obtain the effective engineering constants of angled plies. By giving the engineering constants ($E_1, E_2, G_{12}, \upsilon_{12}$) and ply angle α_{ply},

the effective Young's modulus E_x^{ply} and shear modulus G_{xy}^{ply} of each angled ply are determined using Eqs. (3.14) and (3.15) mentioned in Section 3.2, respectively.

5) Calculate equivalent properties of each area segment

Because each area segment encloses several plies having different material properties, a weighting method is used to represent the non-uniform distribution of materials as a single material having equivalent properties. The actual thickness and area of each segment are maintained. For instance, the equivalent representations of the area segment "ab" in Fig. 3.6 are shown in Fig. 3.7.

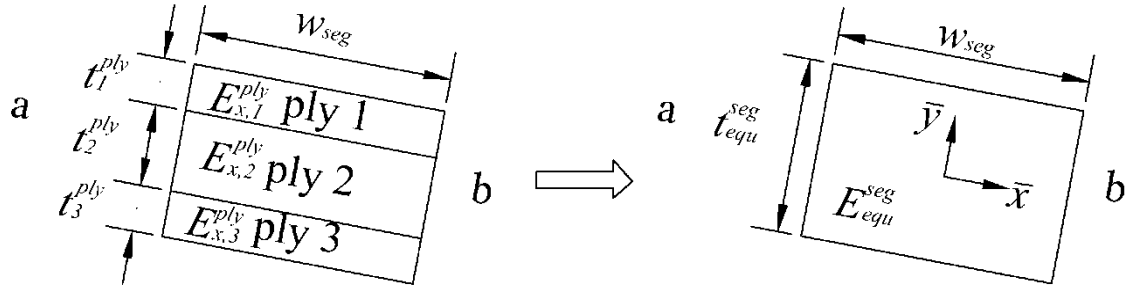

Figure 3.7. Equivalent representations of area segment

According to the weighting method [128], the equivalent Young's modulus E_{equ}^{seg}, thickness t_{equ}^{seg} and area A_{equ}^{seg} of each area segment can be expressed as:

$$E_{equ}^{seg} = \frac{\sum_{i=1}^{m_{ply}} E_{x,i}^{ply} t_i^{ply}}{\sum_{i=1}^{m_{ply}} t_i^{ply}} \tag{3.36}$$

$$t_{equ}^{seg} = \sum_{i=1}^{m_{ply}} t_i^{ply} \tag{3.37}$$

$$A_{equ}^{seg} = \sum_{i=1}^{m_{ply}} A_i^{ply} = \sum_{i=1}^{m_{ply}} t_i^{ply} w_{seg} \tag{3.38}$$

where i indicates the i th ply in an area segment; m_{ply} is the number of plies in an area segment; $E_{x,i}^{ply}$ is the effective Young's modulus of the i th ply; t_i^{ply} and A_i^{ply} are the thickness and area of the i th ply, respectively; w_{seg} is the width of an area segment.

The same method can be used to determine the equivalent density ρ_{equ}^{seg} and equivalent shear modulus G_{equ}^{seg} of each segment by simply replacing the effective Young's modulus $E_{x,i}^{ply}$ in Eq. (3.36) with the density ρ_i^{ply} and effective shear modulus $G_{xy,i}^{ply}$ respectively:

$$\rho_{equ}^{seg} = \frac{\sum_{i=1}^{m_{ply}} \rho_i^{ply} t_i^{ply}}{\sum_{i=1}^{m_{ply}} t_i^{ply}} \tag{3.39}$$

$$G_{equ}^{seg} = \frac{\sum_{i=1}^{m_{ply}} G_{xy,i}^{ply} t_i^{ply}}{\sum_{i=1}^{m_{ply}} t_i^{ply}} \tag{3.40}$$

6) Calculate elastic centre and mass centre of the cross-section

The elastic centre (X_{EC}, Y_{EC}) and mass centre (X_{MC}, Y_{MC}) of the cross-section can also be calculated using weighting method:

$$X_{EC} = \frac{\sum_{I=1}^{N_{seg}} E_{equ}^{seg,I} A_{equ}^{seg,I} \bar{x}_c^{seg,I}}{\sum_{I=1}^{N_{seg}} E_{equ}^{seg,I} A_{equ}^{seg,I}} \tag{3.41}$$

$$Y_{EC} = \frac{\sum_{I=1}^{N_{seg}} E_{equ}^{seg,I} A_{equ}^{seg,I} \bar{y}_c^{seg,I}}{\sum_{I=1}^{N_{seg}} E_{equ}^{seg,I} A_{equ}^{seg,I}} \tag{3.42}$$

$$X_{MC} = \frac{\sum_{I=1}^{N_{seg}} \rho_{equ}^{seg,I} A_{equ}^{seg,I} \bar{x}_c^{seg,I}}{\sum_{I=1}^{N_{seg}} \rho_{equ}^{seg,I} A_{equ}^{seg,I}} \tag{3.43}$$

$$Y_{MC} = \frac{\sum_{I=1}^{N_{seg}} \rho_{equ}^{seg,I} A_{equ}^{seg,I} \bar{y}_c^{seg,I}}{\sum_{I=1}^{N_{seg}} \rho_{equ}^{seg,I} A_{equ}^{seg,I}} \tag{3.44}$$

where I indicates the I th area segment; N_{seg} is the number of area segments; $E_{equ}^{seg,I}$, $A_{equ}^{seg,I}$, and $\rho_{equ}^{seg,I}$ are the equivalent Young's modulus , area and density of the I th

area segment, respectively; $\bar{x}_c^{seg,I}$ and $\bar{y}_c^{seg,I}$ are the centroid coordinates of the I th area segment.

7) Calculate area moments of inertia of each area segment

The area moments of inertia of each area segment with respect to its local axes (e.g. the $\bar{x}-\bar{y}$ axes in Fig. 3.7) can be calculated using an integration scheme:

$$I_{\bar{x}\bar{x}}^{seg} = \int \bar{y}^2 d\bar{x}d\bar{y} \tag{3.45}$$

$$I_{\bar{y}\bar{y}}^{seg} = \int \bar{x}^2 d\bar{x}d\bar{y} \tag{3.46}$$

$$I_{\bar{x}\bar{y}}^{seg} = \int \bar{x}\bar{y} d\bar{x}d\bar{y} \tag{3.47}$$

where $I_{\bar{x}\bar{x}}^{seg}$ and $I_{\bar{y}\bar{y}}^{seg}$ are the area moment of inertia about $\bar{x}$ axis and $\bar{y}$ axis, respectively; $I_{\bar{x}\bar{y}}^{seg}$ is the product of inertia.

8) Transfer the area moments of inertia of each area segment to elastic centre and mass centre of the cross-section

It should be noted that the above calculated area moments of inertia are calculated with respect to the local axes and centroid of each area segment. However, the cross-sectional properties including both flapwise stiffness and edgewise stiffness are generally referred to the elastic axes and elastic centre of the cross-section. The flapwise and edgewise mass moments of inertia are generally referred to the mass axes and mass centre of the cross-section. Therefore, a transformation is necessary. Using the transform-axis formula, the area moments of inertia around the local axes of each area segment can be transferred to that around the axes which are parallel to the elastic axes (X_E, Y_E) of the cross-section:

$$I_{X_E X_E}^{seg} = \frac{I_{\bar{x}\bar{x}}^{seg} + I_{\bar{y}\bar{y}}^{seg}}{2} + \frac{I_{\bar{x}\bar{x}}^{seg} - I_{\bar{y}\bar{y}}^{seg}}{2}\cos 2\varphi_{seg} - I_{\bar{x}\bar{y}}^{seg}\sin 2\varphi_{seg} \tag{3.48}$$

$$I_{Y_E Y_E}^{seg} = \frac{I_{\bar{x}\bar{x}}^{seg} + I_{\bar{y}\bar{y}}^{seg}}{2} - \frac{I_{\bar{x}\bar{x}}^{seg} - I_{\bar{y}\bar{y}}^{seg}}{2}\cos 2\varphi_{seg} + I_{\bar{x}\bar{y}}^{seg}\sin 2\varphi_{seg} \tag{3.49}$$

where φ_{seg} is the angle between the local axes of each area segment and the elastic axes of the cross-section.

Then, using the parallel-axis theorem, the calculated area moments of inertia can be further transferred to elastic centre (X_{EC}, Y_{EC}) of the cross-section:

$$I_{X_E X_E}^{sec} = \left(I_{X_E X_E}^{seg}\right) + A_{equ}^{seg}\left(\bar{x}_c^{seg} - X_{EC}\right)^2 \tag{3.50}$$

$$I_{Y_E Y_E}^{sec} = \left(I_{Y_E Y_E}^{seg}\right) + A_{equ}^{seg}\left(\bar{y}_c^{seg} - Y_{EC}\right)^2 \tag{3.51}$$

Similarly, the area moments of inertia with respect to mass centre (X_{MC}, Y_{MC}) of the cross-section can be obtained using the following equations:

$$I_{X_M X_M}^{sec} = \left(I_{X_M X_M}^{seg}\right) + A_{equ}^{seg}\left(\bar{x}_c^{seg} - X_{MC}\right)^2 \tag{3.52}$$

$$I_{Y_M Y_M}^{sec} = \left(I_{Y_M Y_M}^{seg}\right) + A_{equ}^{seg}\left(\bar{y}_c^{seg} - Y_{MC}\right)^2 \tag{3.53}$$

Noted that mass axes (X_M, Y_M) are parallel to elastic axes (X_E, Y_E). Thus, $I_{X_M X_M}^{seg}$ in Eq. (3.52) and $I_{Y_M Y_M}^{seg}$ in Eq. (3.53) are respectively equal to $I_{X_E X_E}^{seg}$ in Eq. (3.48) and $I_{Y_E Y_E}^{seg}$ in Eq. (3.49).

9) Sum contributions of all area segments to obtain overall sectional properties

The overall cross-sectional properties including axial stiffness EA, flapwise stiffness EI_X, edgewise stiffness EI_Y, mass per unit length μ, flapwise mass moments of inertia $rhoI_X$, and edgewise mass moments of inertia $rhoI_Y$ are obtained by summing the contributions of all area segments:

$$EA = \sum_{I=1}^{N} E_{equ}^{seg,I} A_{equ}^{seg,I} \tag{3.54}$$

$$EI_X = \sum_{I=1}^{N} E_{equ}^{seg,I} I_{X_E X_E}^{sec,I} \tag{3.55}$$

$$EI_Y = \sum_{I=1}^{N} E_{equ}^{seg,I} I_{Y_E Y_E}^{sec,I} \tag{3.56}$$

$$\mu = \sum_{I=1}^{N} \rho_{equ}^{seg,I} A_{equ}^{seg,I} \tag{3.57}$$

$$rhoI_X = \sum_{I=1}^{N} \rho_{equ}^{seg,I} I_{X_M X_M}^{sec,I} \tag{3.58}$$

$$rhoI_Y = \sum_{I=1}^{N} \rho_{equ}^{seg,I} I_{Y_M Y_M}^{sec,I} \tag{3.59}$$

10) Determine torsional stiffness using EBSFT

The torsional stiffness is determined using EBSFT mentioned in Section 4. Taking the blade cross-section with one shear web in Figure 3.6 as an example, having obtained the width w_{seg} (approximate ds_c if the w_{seg} is small enough), equivalent thickness t_{equ}^{seg} and shear modulus G_{equ}^{seg} of each segment in step 5), the components of the warping flexibility matrix $[\delta_w]$ can be calculated using Eqs. (3.24) to (3.26). Then the torsional stiffness is determined using Eq. (3.33).

11) Output results

After all calculations are done, the model will output the cross-sectional properties including axial stiffness EA, flapwise stiffness EI_X, edgewise stiffness EI_Y, torsional stiffness GJ, mass per unit length μ, flapwise mass moments of inertia $rhoI_X$ and edgewise mass moments of inertia $rhoI_Y$.

3.6. Validation

Based on the above mathematical model, a cross-sectional analysis program, which is named as CBCSA (Composite Blade Cross-Section Analysis), is developed using MATLAB. CBCSA allows arbitrary geometric shape and internal structural layout of the blade. It directly extracts the cross-sectional properties of the blade and runs quickly, usually in a fraction of a second. Additionally, the shear web effects and warping effects are taken into account by CBCSA due to the usage of EBSFT in the calculation of torsional stiffness. In order to validate CBCSA, the following benchmark tests are performed.

3.6.1. Case Study A

For the first case study, we compare the performance of CBCSA with analysis done with PreComp for a SERI-8 blade [130]. The stations 4 and 6 of the SERI-8 blade are chosen as examples. The schematic of the cross-section of the SERI-8 blade is shown in Fig. 3.8.

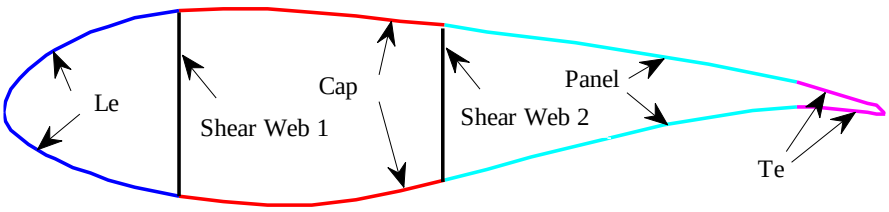

Figure 3.8. Schematic of the cross-section of the SERI-8 blade

The geometric data of the wind turbine blade cross-sections at the stations 4 and 6 are listed in Table 3.1.

Table 3.1. Geometric data [130]

Station#	Chord(m)	Twist angle (degree)	Airfoil
4	1.092	15.7	S807
6	0.665	0.59	S805A

Four materials are used within the structure, labeled Mat, DblBias, Uni and Balsa. The orthotropic material properties used in the model are shown in Table 3.2.

Table 3.2. Material properties [130]

Property	Mat	DblBias	Uni	Balsa
E_1 (GPa)	7.58	11.1	45.8	0.12
E_2 (GPa)	7.58	11.1	10.1	0.12
G_{12} (GPa)	4.00	6.89	6.89	0.02
ν_{12}	0.30	0.39	0.30	0.30
ρ (kg/m^3)	1690	1660	1990	230

The orientation of plies used in [130] is limited to 90°, here our case study also demonstrates the effects of ply angles at 45° and 0°. Ply angles are set in the composites lay-up, as shown in Table 3.3. The composites lay-up in Table 3.3 is used for both stations 4 and 6.

Table 3.3. Composites lay-up [130]

Name	Number of plies	ply angle (deg.)	Ply Name	Thickness (mm)
Le	1	90	Mat	1.21
	4	45	DblBias	1.21
Cap	1	90	Mat	1.21
	6	0	Uni	0.93
Panel	1	90	Mat	1.21
	1	45	DblBias	1.21
	1	0	Balsa	5
	1	45	DblBias	1.21
Shear webs	1	45	DblBias	1.21
1 and 2	1	0	Balsa	8
	1	45	DblBias	1.21
Te	1	90	Mat	1.21
	1	45	DblBias	1.21

Both PreComp and CBCSA are used to calculate the properties of the cross-sections. Calculated cross-sectional properties for station 4 are presented in Fig. 3.9 and Table 3.4, and calculated cross-sectional properties for station 6 are shown in Fig. 3.10 and Table 3.5.

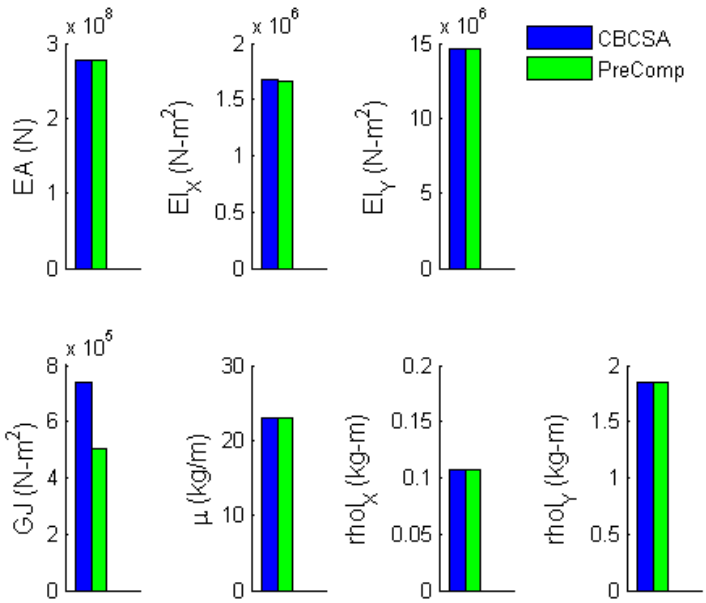

Figure 3.9. Calculated cross-sectional properties of the blade cross-section at station 4

Table 3.4. Calculated cross-sectional properties of the blade cross-section at station 4

Cross-sectional properties	PreComp	CBCSA	%Diff
EA (N)	2.7830E+08	2.7829E+08	0.01
EI_X (N-m^2)	1.6670E+06	1.6692E+06	0.13
EI_Y (N-m^2)	1.4640E+07	1.4641E+07	0.01
GJ (N-m^2)	5.0530E+05	7.3768E+05	45.99
μ (kg/m)	2.2950E+01	2.2952E+01	0.01
$rhoI_X$ (kg-m)	1.0740E-01	1.0738E-01	0.02
$rhoI_Y$ (kg-m)	1.8480E+00	1.8481E+00	0.01

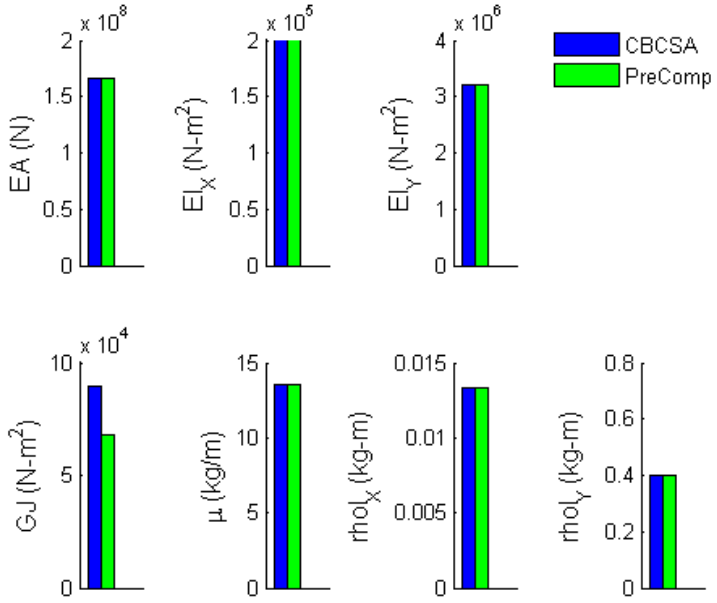

Figure 3.10. Calculated cross-sectional properties of the blade cross-section at station 6

Table 3.5. Calculated cross-sectional properties of the blade cross-section at station 6

Cross-sectional properties	PreComp	CBCSA	%Diff.
EA (N)	1.6580E+08	1.6584E+08	0.02
EI_X (N-m^2)	1.9940E+05	1.9953E+05	0.07
EI_Y (N-m^2)	3.1960E+06	3.1953E+06	0.02
GJ (N-m^2)	6.7830E+04	8.9811E+04	32.41
μ (kg/m)	1.3510E+01	1.3506E+01	0.03
$rhoI_X$ (kg-m)	1.3340E-02	1.3336E-02	0.03
$rhoI_Y$ (kg-m)	4.0030E-01	4.0025E-01	0.01

Figs. 3.9 and 3.10 and Tables 3.4 and 3.5 indicate that the results from CBCSA agree with those from PreComp very well except the torsional stiffness. The torsional stiffness predicted by PreComp is lower than that obtained using CBCAS. Following case studies demonstrate that CBCAS has higher accuracy for the calculation of torsional stiffness than PreComp due to the consideration of the effects of shear webs.

3.6.2. Case Study B

This case study allows comparison of CBCSA with both PreComp and ANSYS for a blade profile with and without shear webs. The first example considered here is an isotropic blade cross-section without a shear web, as shown in Fig. 3.11. The geometric data and material properties of the cross-section are listed in Table 3.6.

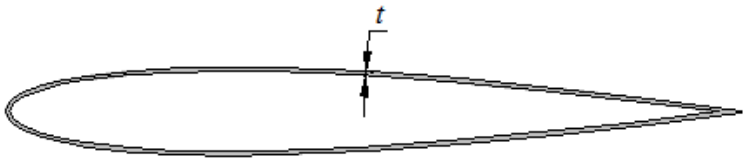

Figure 3.11. Schematic of an isotropic blade cross-section without shear web

Table 3.6. Geometric data and material properties of the isotropic blade cross-section

Properties	Values
E (GPa)	210
ν	0.3
ρ (kg/m^3)	7850
Airfoil	NACA0012
Chord (m)	0.12
t (m)	0.000675

The comparison of cross-sectional properties calculated using CBCAS, PreComp and ANSYS is shown in Fig. 3.12 and Table 3.7, where the relative differences are obtained with respect to the CBCAS results.

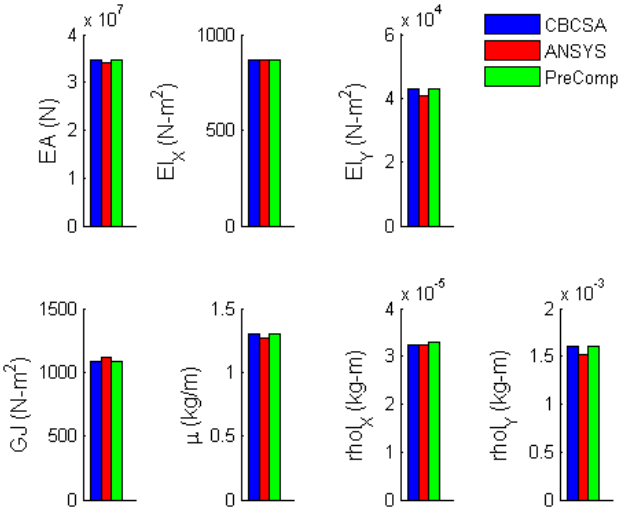

Figure 3.12. Calculated cross-sectional properties of an isotropic blade cross-section without shear web

Table 3.7. Calculated cross-sectional properties of an isotropic blade cross-section without shear web

Cross-sectional properties	CBCAS	PreComp	%Diff. (PreComp)	ANSYS	%Diff. (ANSYS)
EA (N)	3.4721E+07	3.4720E+07	0.01	3.4105E+07	1.77
EI_X (N-m^2)	8.6756E+02	8.6760E+02	0.01	8.6646E+02	0.13
EI_Y (N-m^2)	4.2866E+04	4.2870E+04	0.01	4.0789E+04	4.85
GJ (N-m^2)	1.0848E+03	1.0850E+03	0.02	1.1197E+03	3.22
μ (kg/m)	1.2979E+00	1.2980E+00	0.01	1.2718E+00	2.01
$rhoI_X$ (kg-m)	3.2430E-05	3.2950E-05	1.60	3.2389E-05	0.13
$rhoI_Y$ (kg-m)	1.6024E-03	1.6020E-03	0.02	1.5247E-03	4.85

From Fig. 3.12 and Table 3.7 we can see that the predictions of the CBCAS are in good agreement with PreComp and ANSYS for the isotropic blade cross-section without a shear web.

The next example considered is the isotropic blade with two shear webs, located at 0.2c and 0.5c, as shown in Fig. 3.13.

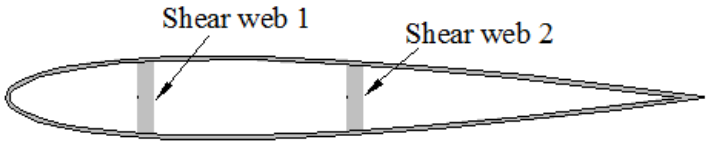

Figure 3.13. Schematic of an isotropic blade cross-section with two shear webs

The thickness of both webs is 0.003m. Other properties of the cross-section remain the same as those used in the first example. The comparison of cross-sectional properties calculated using CBCAS, PreComp and ANSYS is shown in Fig. 3.14 and Table 3.8, where the relative differences are obtained with respect to the ANSYS results.

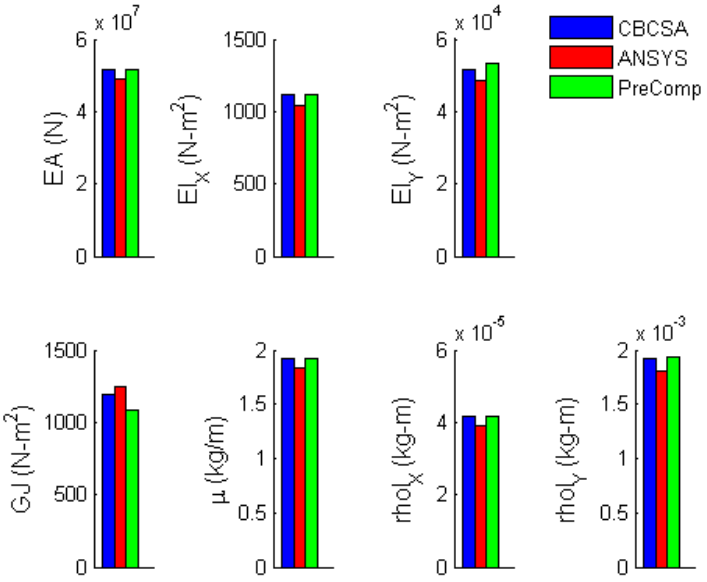

Figure 3.14. Calculated cross-sectional properties of an isotropic blade cross-section with two shear webs

Table 3.8. Calculated cross-sectional properties of an isotropic blade cross-section with two shear webs

Cross-sectional properties	ANSYS	CBCAS	%Diff. (CBCAS)	PreComp	%Diff. (PreComp)
EA (N)	4.9057E+07	5.1396E+07	4.77	5.1400E+07	4.78
EI_X (N-m^2)	1.0439E+03	1.1121E+03	6.53	1.1120E+03	6.52
EI_Y (N-m^2)	4.8368E+04	5.1601E+04	6.68	5.3190E+04	9.97
GJ (N-m^2)	1.2480E+03	1.1871E+03	4.88	1.0850E+03	13.06
μ (kg/m)	1.8304E+00	1.9212E+00	4.96	1.9210E+00	4.95
$rhoI_X$ (kg-m)	3.9022E-05	4.1571E-05	6.53	4.1570E-05	6.53
$rhoI_Y$ (kg-m)	1.8081E-03	1.9280E-03	6.63	1.9290E-03	6.69

A big difference is observed between Tables 3.7 and 3.8, indicating that shear webs significantly affect cross-sectional properties. From Fig. 3.14 and Table 3.8 it can be seen that the results predicted by CBCSA match well with those of ANSYS, with the maximum percentage difference (6.68%) occurring for the edgewise stiffness (EI_Y). It can be observed that for this cross-section with two shear webs, the torsional stiffness predicted by PreComp is exactly the same as the case without shear web mentioned in the previous example. This indicates that PreComp does not account for the effects of shear webs in the calculation of torsional stiffness. Since CBCAS uses EBSFT to determine the torsional stiffness, the effects of shear webs are taken into account. Therefore, CBCAS can provide more realistic torsional stiffness than PreComp.

3.6.3. Case Study C

The final case study aims to verify improved accuracy of torsional stiffness calculation of CBCSA by comparing CBCSA and PreComp with the experimental data [131]. The example considered here is an extension-torsional coupled blade with two-cell cross-section [131], as shown in Fig. 3.15.

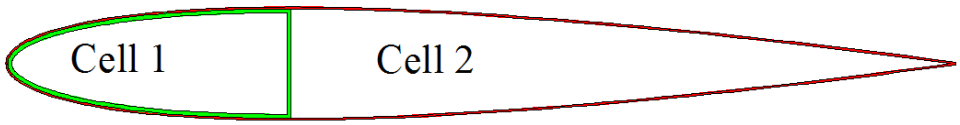

Figure 3.15. Two-cell cross-section

The skin of the cross-section has [15/-15] layups whereas the D-type spar consists of $[0/15]_2$. The geometric data and material properties of the blade are listed in Table 3.9.

Table 3.9. Geometric data and material properties of the blade [131]

Properties	Values
E_1 (GPa)	131
E_2 (GPa)	9.3
G_{12} (GPa)	5.86
ν_{12}	0.4
Airfoil	NACA0012
Length(m)	0.6414
Chord (m)	0.0762
Ply thickness(m)	0.000127

Both CBCSA and PreComp are used to calculate the properties of the cross-section. Predicted values are compared with measured values reported in Ref. [131], as shown in Fig. 3.16 and Table 3.10, where the relative differences are obtained with respect to the experimental data.

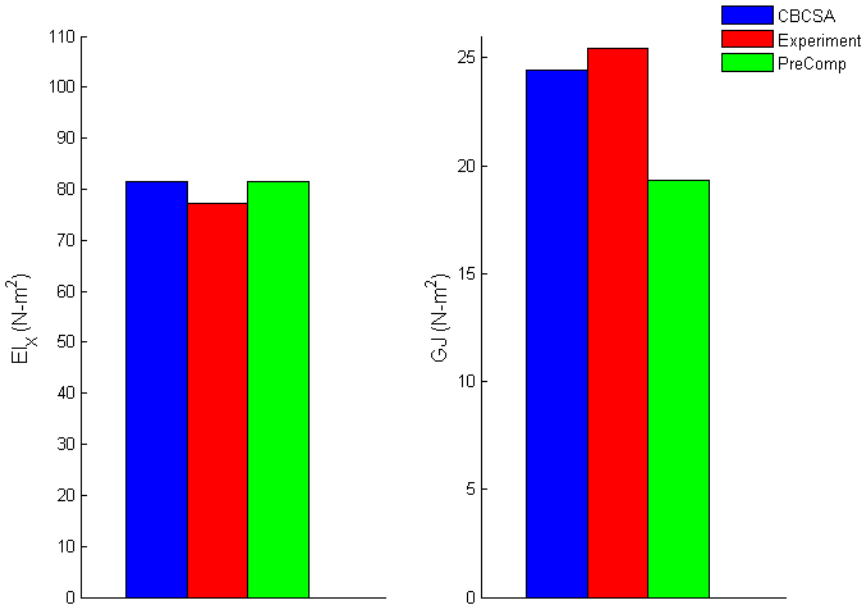

Figure 3.16. Cross-sectional properties of the two-cell cross-section

Table 3.10. Cross-sectional properties of the two-cell cross-section

Cross-sectional properties	Experiment [131]	CBCSA	%Diff (CBCSA)	PreComp	%Diff (PreComp)
EA (N)	-	8.1336E+06	-	8.1340E+06	-
EI_X (N-m^2)	7.7141E+01	8.1449E+01	5.58	8.1531E+01	5.69
EI_Y (N-m^2)	-	3.4529E+03	-	3.4530E+03	-
GJ (N-m^2)	2.5427E+01	2.4443E+01	3.87	1.9330E+01	23.98
μ (kg/m)	-	1.3485E-01	-	1.3480E-01	-
$rhoI_X$ (kg-m)	-	1.4389E-06	-	1.4390E-06	-
$rhoI_Y$ (kg-m)	-	5.8658E-05	-	5.8660E-05	-

From Fig. 3.16 and Table 3.10 we can see that 1) the flapwise stiffness EI_X and torsional stiffness GJ calculated from CBCSA match well with experimental data, with the maximum percentage difference (5.58%) occurring for the flapwise stiffness EI_X; and 2) the torsional stiffness GJ predicted by CBCSA is more accurate than that obtained from PreComp.

3.7. Summary

In this chapter, a mathematical model for accurate and rapid calculation of the cross-sectional properties of wind turbine blades has been developed by incorporating the classical lamination theory (CLT) with the extended Bredt-Batho shear flow theory (EBSFT). A flowchart of the mathematical model, illustrating the detailed procedure for calculating cross-sectional properties of composite blades, is presented. The mathematical model considers both the web effects and warping effects of the blades, and is presented in a code called CBCSA (Composite Blade Cross-Section Analysis), developed using MATLAB. A series of benchmark computational tests are performed for isotropic and composite blades, and the results demonstrate that:

- CBCSA can rapidly extract the cross-sectional properties of the composite blades, usually in a fraction of a second, which is much faster than a 3D finite-element based method.

- Good agreement is achieved in comparison with the data from experiment and finite-element analysis, which indicates CBCSA has sufficient accuracy for the calculation of the cross-sectional properties of the composite blades.
- CBCSA provides a more accurate torsional stiffness calculation than the previously available tool PreComp due to the consideration of the shear web effects by using EBSFT.

The obtained cross-sectional properties of wind turbine composite blades are used as input information to construct the blade structural model, which is presented in Chapter 4.

CHAPTER 4 BLADE STRUCTURAL MODELLING

4.1. Introduction

As discussed in Chapter 2, in order to perform aeroelastic analysis of wind turbine blades, a blade structural model, which determines the blade structural dynamic responses, has to be included. Due to the increasing size and flexibility of large wind turbine blades, the blades often experience large deflections, which introduce significant geometric nonlinearities. In order to take account of geometric nonlinearities, wind turbine blades in this thesis are modelled based on a mixed-form formulation of geometrically exact beam theory (GEBT) [36], which is detailed in this chapter.

The mixed-form formulation of GEBT, which introduces Lagrange multiplier to satisfy the equations of motion with constitutive and kinematic relationships, is capable of handling large deflections, large rotations and geometric nonlinearities. It allows the lowest order of shape functions for all dependent variables, which makes it a viable solution for modelling geometric nonlinearities.

The main contents of this chapter are taken from the manuscript (Appendix G2) submitted for publication in Energy (Elsevier), and more details are provided in this chapter.

This chapter is structured as follows. Section 4.2 describes the main coordinate systems used in blade structural modelling. Section 4.3 presents the equations of motion of nonlinear beam. Section 4.4 derives the mixed variational formula of nonlinear beam by introducing both constitutive and kinematic relationships to the equations of motion, followed by a chapter summary in Section 4.5.

4.2. Coordinate Systems

In order to fully describe the geometry and deflection of a wind turbine blade for aeroelastic modelling, three coordinate systems are adopted, i.e. 1) the global frame,

which aligns with the wind turbine rotor and defines the rotor parameters; 2) the un-deformed blade frame, which aligns with the original blade and defines the blade parameters; and 3) the deformed blade frame, which aligns with the deformed blade. This section illustrates the three coordinate systems and the transformation matrices among them.

4.2.1. Main Coordinate Systems

Three main coordinate systems, i.e. the global frame G, the un-deformed blade frame b and the deformed blade frame B, are chosen for the analysis of wind turbine blades, as shown in Fig. 4.1. The global frame G, having its axes labelled G_1, G_2, and G_3, is rotating along with the wind turbine rotor. Axes G_2 and G_3 are along with and perpendicular to the wind turbine rotor axis, respectively. The un-deformed blade frame b, having its axes labelled b_1, b_2, and b_3, is attached to each un-deformed blade element. Axes b_2 and b_3, located in each un-deformed airfoil plane, are perpendicular and parallel to the chord line of each un-deformed blade element, respectively. The deformed blade frame B, having its axes B_1, B_2, and B_3, is attached to each deformed blade element. Axes B_2 and B_3, located in each deformed airfoil plane, are perpendicular and parallel to the chord line of each deformed blade element, respectively. All the three coordinate systems obey the right hand rule. The details of the three coordinate systems can be found in Appendix A1.

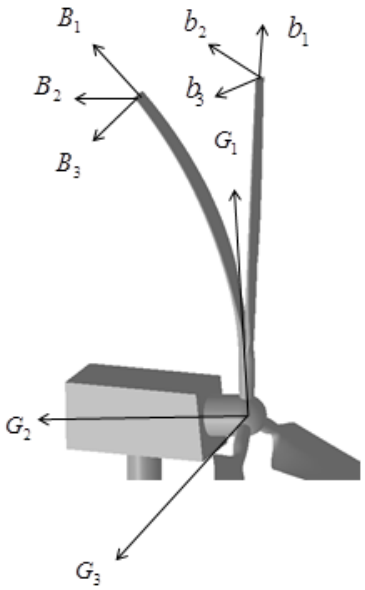

Figure 4.1. Main coordinate systems

4.2.2. Transformation Matrices

A vector given in a frame can be transformed into another frame using transformation matrices. The transformation matrix $\boldsymbol{C}^{bG}$, which transfers vectors from the global frame G into the un-deformed blade frame b, is given by:

$$\boldsymbol{C}^{bG} = \begin{bmatrix} 1 & 0 & 0 \\ 0 & \cos\theta_p & \sin\theta_p \\ 0 & -\sin\theta_p & \cos\theta_p \end{bmatrix} \begin{bmatrix} \cos\beta_1 & -\sin\beta_1 & 0 \\ \sin\beta_1 & \cos\beta_1 & 0 \\ 0 & 0 & 1 \end{bmatrix} \tag{4.1}$$

where β_1 is the rotor cone angle (see Fig. 4.2), the angle between the blade axis and rotor plane; θ_p is the twist angle of each blade element (see Fig. 4.3), the angle between the chord line and the blade reference plane. Obviously, the transformation matrix $\boldsymbol{C}^{bG}$ is time independent, i.e. $\dot{\boldsymbol{C}}^{bG} = 0$.

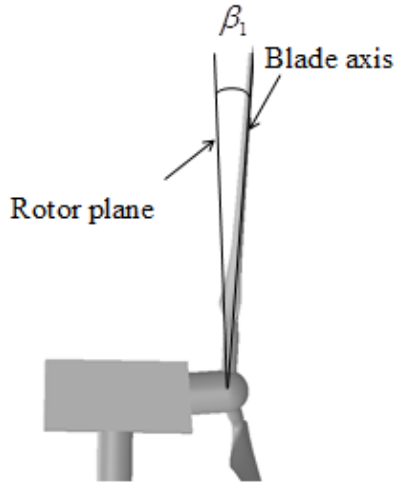

Figure 4.2. Rotor cone angle

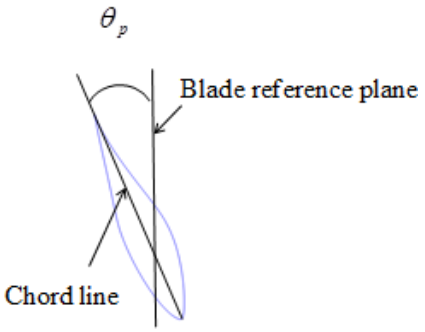

Figure 4.3. Blade-element twist angle

According to Euler's theorem of rigid-body motion [36], any rotational motion can be characterized by the magnitude of rotation β_r and a 3-by-1 unit vector $\boldsymbol{e}$, which describes the rotation axis. On the basis of the Euler's theorem, the transformation

matrix $\boldsymbol{C}^{Bb}$, which transfers vectors from the un-deformed blade frame b into the deformed blade frame B, can be expressed in terms of Rodrigues parameters [36] $\boldsymbol{\theta}$ as:

$$\boldsymbol{C}^{Bb} = \frac{(1-\frac{1}{4}\boldsymbol{\theta}^T\boldsymbol{\theta})\boldsymbol{\Delta} + \frac{1}{2}\boldsymbol{\theta}\boldsymbol{\theta}^T - \tilde{\boldsymbol{\theta}}}{1+\frac{1}{4}\boldsymbol{\theta}^T\boldsymbol{\theta}} \tag{4.2}$$

where T is the transpose symbol; $\boldsymbol{\Delta}$ is the 3-by-3 identity matrix $\begin{bmatrix} 1 & 0 & 0 \\ 0 & 1 & 0 \\ 0 & 0 & 1 \end{bmatrix}$; $\boldsymbol{\theta} = 2\boldsymbol{e}\tan(\beta_r/2)$; $\boldsymbol{e} = [\mathrm{e1} \quad \mathrm{e2} \quad \mathrm{e3}]^T$ and $\boldsymbol{e}^T\boldsymbol{e} = 1$.

Introducing another set of Rodrigues parameters $\boldsymbol{\theta}_G$ such that $\boldsymbol{\theta}_G = \left(\boldsymbol{C}^{bG}\right)^T\boldsymbol{\theta}$, the transformation vector $\boldsymbol{C}^{BG}$, which transfers vectors given in the global frame G into the deformed blade frame B, is obtained by:

$$\boldsymbol{C}^{BG} = \boldsymbol{C}^{bG}\boldsymbol{C} \tag{4.3}$$

where

$$\boldsymbol{C} = \frac{(1-\frac{1}{4}\boldsymbol{\theta}_G^T\boldsymbol{\theta}_G)\boldsymbol{\Delta} + \frac{1}{2}\boldsymbol{\theta}_G\boldsymbol{\theta}_G^T - \tilde{\boldsymbol{\theta}}_G}{1+\frac{1}{4}\boldsymbol{\theta}_G^T\boldsymbol{\theta}_G} \tag{4.4}$$

Having obtained $\boldsymbol{C}^{Bb}$ and $\boldsymbol{C}^{BG}$, the following relations can be easily established:

$$\boldsymbol{C}^{bB} = \left(\boldsymbol{C}^{Bb}\right)^T \tag{4.5}$$

$$\boldsymbol{C}^{GB} = \left(\boldsymbol{C}^{BG}\right)^T \tag{4.6}$$

4.3. Equations of Motion

The geometrically exact equations of motion, which exactly describe the behaviour of an initially curved and twisted beam as a set of mathematical functions in terms of spatial coordinates and time, can be derived from Hamilton's extended principle, kinetic energy and strain energy.

4.3.1. Hamilton's Extended Principle

Hamilton's extended principle is expressed as [36]:

$$\int_{t_1}^{t_2}\int_0^L \left[\delta\left(\boldsymbol{K_E}-\boldsymbol{S_E}\right)+\delta\boldsymbol{W}\right]dx_1 dt=\delta\boldsymbol{A} \tag{4.7}$$

where t_1 and t_2 are arbitrary fixed times; L is the length of the blade; δ is the Lagrangean variation operator for a fixed time; $\boldsymbol{K_E}$ and $\boldsymbol{S_E}$ are the kinetic and strain energy, respectively; $\boldsymbol{\delta W}$ is the virtual work of applied loads; $\boldsymbol{\delta A}$ is the virtual action at the ends of time interval and at the ends of the blade.

4.3.2. Kinetic Energy

The variation of kinetic energy required in Eq. (4.7) can be written as:

$$\delta\boldsymbol{K_E}=\delta\boldsymbol{V_B}^T\boldsymbol{P_B}+\delta\boldsymbol{\Omega_B}^T\boldsymbol{H_B} \tag{4.8}$$

where $\boldsymbol{V_B}$ and $\boldsymbol{\Omega_B}$ are the column matrices that contain linear and angular velocities of the deformed beam reference line measured in the frame B, respectively; $\boldsymbol{P_B}$ and $\boldsymbol{H_B}$ are the column matrices that contain the linear and angular momenta measured in the frame B, respectively. $\delta\boldsymbol{V_B}^T$ and $\delta\boldsymbol{\Omega_B}^T$ can be expressed in terms of the virtual displacement $\overline{\delta\boldsymbol{q}_B}$ and virtual rotation $\overline{\delta\boldsymbol{\psi}_B}$ using the following equations [36]:

$$\delta\boldsymbol{V}_B^T=\overline{\dot{\delta\boldsymbol{q}_B}}^T-\overline{\delta\boldsymbol{q}_B}^T\tilde{\boldsymbol{\Omega}}_B-\overline{\delta\boldsymbol{\psi}_B}^T\tilde{\boldsymbol{V}}_B \tag{4.9}$$

$$\delta\boldsymbol{\Omega}_B^T=\overline{\dot{\delta\boldsymbol{\psi}_B}}^T-\overline{\delta\boldsymbol{\psi}_B}^T\tilde{\boldsymbol{\Omega}}_B \tag{4.10}$$

where the overhead dot denotes the time derivative; the over-head tilde operator $\left(\tilde{\cdot}\right)$ defines a second-order skew-symmetric tensor corresponding to the given vector. For example, given $\boldsymbol{\Omega_B}=\left[\Omega_{B1}\quad\Omega_{B2}\quad\Omega_{B3}\right]^T$, $\tilde{\boldsymbol{\Omega}}_B$ can be expressed as:

$$\tilde{\boldsymbol{\Omega}}_B=\begin{bmatrix}0 & -\Omega_{B3} & \Omega_{B2}\\ \Omega_{B3} & 0 & -\Omega_{B1}\\ -\Omega_{B2} & \Omega_{B1} & 0\end{bmatrix} \tag{4.11}$$

Substituting Eqs. (4.9) and (4.10) into Eq. (4.8) gives:

$$\delta\boldsymbol{K_E}=\left(\overline{\dot{\delta\boldsymbol{q}_B}}^T-\overline{\delta\boldsymbol{q}_B}^T\tilde{\boldsymbol{\Omega}}_B-\overline{\delta\boldsymbol{\psi}_B}^T\tilde{\boldsymbol{V}}_B\right)\boldsymbol{P_B}+\left(\overline{\dot{\delta\boldsymbol{\psi}_B}}^T-\overline{\delta\boldsymbol{\psi}_B}^T\tilde{\boldsymbol{\Omega}}_B\right)\boldsymbol{H_B} \tag{4.12}$$

4.3.3. Strain Energy

The variation of strain energy required in Eq. (4.7) can be written as:

$$\delta \boldsymbol{S}_{\boldsymbol{E}} = \delta \boldsymbol{\gamma}^T \boldsymbol{F}_{\boldsymbol{B}} + \delta \boldsymbol{\kappa}^T \boldsymbol{M}_{\boldsymbol{B}} \tag{4.13}$$

where $\boldsymbol{\gamma}$ and $\boldsymbol{\kappa}$ are the column matrices that contain force and moment strains, respectively; $\boldsymbol{F}_{\boldsymbol{B}}$ and $\boldsymbol{M}_{\boldsymbol{B}}$ are the column matrices that contain the force and moment resultants measured in the frame B, respectively. $\delta \boldsymbol{\gamma}^T$ and $\delta \boldsymbol{\kappa}^T$ can be expressed in terms of the virtual displacement $\overline{\delta \boldsymbol{q}_{\boldsymbol{B}}}$ and virtual rotation $\overline{\delta \boldsymbol{\psi}_{\boldsymbol{B}}}$ using the following equations [36]:

$$\delta \boldsymbol{\gamma}^T = \left(\overline{\delta \boldsymbol{q}_{\boldsymbol{B}}}' \right)^T - \overline{\delta \boldsymbol{q}_{\boldsymbol{B}}}^T \tilde{\boldsymbol{K}}_{\boldsymbol{B}} - \overline{\delta \boldsymbol{\psi}_{\boldsymbol{B}}}^T \left(\tilde{\boldsymbol{e}}_1 + \tilde{\boldsymbol{\gamma}} \right) \tag{4.14}$$

$$\delta \boldsymbol{\kappa}^T = \left(\overline{\delta \boldsymbol{\psi}_{\boldsymbol{B}}}' \right)^T - \overline{\delta \boldsymbol{\psi}_{\boldsymbol{B}}}^T \tilde{\boldsymbol{K}}_{\boldsymbol{B}} \tag{4.15}$$

where $\boldsymbol{K}_{\boldsymbol{B}}$ is the curvature vector for the deformed beam; $\boldsymbol{e}_1 = \begin{bmatrix} 1 & 0 & 0 \end{bmatrix}^T$; the prime symbol $(\,)'$ denotes the spatial derivative.

Substituting Eqs. (4.14) and (4.15) into Eq. (4.13) gives:

$$\delta \boldsymbol{S}_{\boldsymbol{E}} = \left(\left(\overline{\delta \boldsymbol{q}_{\boldsymbol{B}}}' \right)^T - \overline{\delta \boldsymbol{q}_{\boldsymbol{B}}}^T \tilde{\boldsymbol{K}}_{\boldsymbol{B}} - \overline{\delta \boldsymbol{\psi}_{\boldsymbol{B}}}^T \left(\tilde{\boldsymbol{e}}_1 + \tilde{\boldsymbol{\gamma}} \right) \right) \boldsymbol{F}_{\boldsymbol{B}} + \left(\left(\overline{\delta \boldsymbol{\psi}_{\boldsymbol{B}}}' \right)^T - \overline{\delta \boldsymbol{\psi}_{\boldsymbol{B}}}^T \tilde{\boldsymbol{K}}_{\boldsymbol{B}} \right) \boldsymbol{M}_{\boldsymbol{B}} \tag{4.16}$$

4.3.4. Geometrically Exact Equations of Motion

The virtual work of the applied loads appearing in Eq. (4.7) is given by:

$$\delta \boldsymbol{W} = \overline{\delta \boldsymbol{q}_{\boldsymbol{B}}}^T \boldsymbol{f}_{\boldsymbol{B}} + \overline{\delta \boldsymbol{\psi}_{\boldsymbol{B}}}^T \boldsymbol{m}_{\boldsymbol{B}} \tag{4.17}$$

where $\boldsymbol{f}_{\boldsymbol{B}}$ and $\boldsymbol{m}_{\boldsymbol{B}}$ are column matrices that contain applied forces and moments per unit length measured in the frame B, respectively.

Recalling that $\delta \boldsymbol{A}$ in Eq. (4.7) is the virtual action at the ends of the time interval and at the ends of the blade, the mathematical expression of $\delta \boldsymbol{A}$ can be written as:

$$\delta \boldsymbol{A} = \int_0^L \left(\overline{\delta \boldsymbol{q}_{\boldsymbol{B}}}^T \hat{\boldsymbol{P}}_{\boldsymbol{B}} + \overline{\delta \boldsymbol{\psi}_{\boldsymbol{B}}}^T \hat{\boldsymbol{H}}_{\boldsymbol{B}} \right)_{t_1}^{t_2} dx_1 - \int_{t_1}^{t_2} \left(\overline{\delta \boldsymbol{q}_{\boldsymbol{B}}}^T \hat{\boldsymbol{F}}_{\boldsymbol{B}} + \overline{\delta \boldsymbol{\psi}_{\boldsymbol{B}}}^T \hat{\boldsymbol{M}}_{\boldsymbol{B}} \right)_0^L dt \tag{4.18}$$

where the overhead hat denotes the discrete boundary values.

Substituting Eqs. (4.12), (4.16), (4.17) and (4.18) into Eq. (4.7) yields:

$$\begin{aligned}
&\int_{t_1}^{t_2}\int_0^L \Bigg\{ \left(\overline{\dot{\delta \boldsymbol{q}_B}}^T - \overline{\delta \boldsymbol{q}_B}^T \tilde{\boldsymbol{\Omega}}_B - \overline{\delta \boldsymbol{\psi}_B}^T \tilde{\boldsymbol{V}}_B \right) \boldsymbol{P}_B + \left(\overline{\dot{\delta \boldsymbol{\psi}_B}}^T - \overline{\delta \boldsymbol{\psi}_B}^T \tilde{\boldsymbol{\Omega}}_B \right) \boldsymbol{H}_B \\
&\quad - \left(\left(\overline{\delta \boldsymbol{q}_B}' \right)^T - \overline{\delta \boldsymbol{q}_B}^T \tilde{\boldsymbol{K}}_B - \overline{\delta \boldsymbol{\psi}_B}^T \left(\tilde{\boldsymbol{e}}_1 + \tilde{\boldsymbol{\gamma}} \right) \right) \boldsymbol{F}_B - \left(\left(\overline{\delta \boldsymbol{\psi}_B}' \right)^T - \overline{\delta \boldsymbol{\psi}_B}^T \tilde{\boldsymbol{K}}_B \right) \boldsymbol{M}_B \\
&\quad + \overline{\delta \boldsymbol{q}_B}^T \boldsymbol{f}_B + \overline{\delta \boldsymbol{\psi}_B}^T \boldsymbol{m}_B \Bigg\} dx_1 dt \\
&= \int_0^L \left(\overline{\delta \boldsymbol{q}_B}^T \hat{\boldsymbol{P}}_B + \overline{\delta \boldsymbol{\psi}_B}^T \hat{\boldsymbol{H}}_B \right)_{t_1}^{t_2} dx_1 - \int_{t_1}^{t_2} \left(\overline{\delta \boldsymbol{q}_B}^T \hat{\boldsymbol{F}}_B + \overline{\delta \boldsymbol{\psi}_B}^T \hat{\boldsymbol{M}}_B \right)_0^L dt
\end{aligned} \tag{4.19}$$

After integrating Eq. (4.19) by parts with respect to the time to remove the time derivatives of the virtual quantities, one obtains:

$$\begin{aligned}
&\int_{t_1}^{t_2}\int_0^L \Bigg\{ \left(\overline{\delta \boldsymbol{q}_B}' \right)^T \boldsymbol{F}_B + \left(\overline{\delta \boldsymbol{\psi}_B}' \right)^T \boldsymbol{M}_B + \overline{\delta \boldsymbol{q}_B}^T \left(-\tilde{\boldsymbol{K}}_B \boldsymbol{F}_B + \dot{\boldsymbol{P}}_B + \tilde{\boldsymbol{\Omega}}_B \boldsymbol{P}_B \right) \\
&+ \overline{\delta \boldsymbol{\psi}_B}^T \left(-\tilde{\boldsymbol{K}}_B \boldsymbol{M}_B - \left(\tilde{\boldsymbol{e}}_1 + \tilde{\boldsymbol{\gamma}} \right) \boldsymbol{F}_B + \dot{\boldsymbol{H}}_B + \tilde{\boldsymbol{\Omega}}_B \boldsymbol{H}_B + \tilde{\boldsymbol{V}}_B \boldsymbol{P}_B \right) - \overline{\delta \boldsymbol{q}_B}^T \boldsymbol{f}_B - \overline{\delta \boldsymbol{\psi}_B}^T \boldsymbol{m}_B \Bigg\} dx_1 dt \\
&= \int_{t_1}^{t_2} \left(\overline{\delta \boldsymbol{q}_B}^T \hat{\boldsymbol{F}}_B + \overline{\delta \boldsymbol{\psi}_B}^T \hat{\boldsymbol{M}}_B \right)_0^L dt
\end{aligned} \tag{4.20}$$

Eq. (4.20) is the geometrically exact equations of motion of a beam expressed in the frame B. With the help of transformation matrices, the displacement and rotation components can be expressed in global frame G, which are independent of blade geometry and deflection. The details are discussed below.

$\tilde{\boldsymbol{K}}_B$ and $\tilde{\boldsymbol{\Omega}}_B$ in Eq. (4.20) can be expressed in terms of $\boldsymbol{C}^{BG}$ and $\boldsymbol{C}^{GB}$ using [132]:

$$\tilde{\boldsymbol{K}}_B = \boldsymbol{C}^{BG} \left(\boldsymbol{C}^{GB} \right)' \tag{4.21}$$

$$\tilde{\boldsymbol{\Omega}}_B = -\dot{\boldsymbol{C}}^{BG} \boldsymbol{C}^{GB} + \boldsymbol{C}^{BG} \tilde{\boldsymbol{\omega}}_G \boldsymbol{C}^{GB} \tag{4.22}$$

where $\boldsymbol{\omega}_G$ is the column matrix that contains the angular velocity of un-deformed beam reference line measured in frame G.

The virtual displacement $\overline{\delta \boldsymbol{q}_B}$, virtual rotation $\overline{\delta \boldsymbol{\psi}_B}$, linear momentum $\boldsymbol{P}_B$, and angular momentum $\boldsymbol{H}_B$ measured in frame B are related to the virtual displacement $\delta \boldsymbol{u}_G$, virtual rotation $\overline{\delta \boldsymbol{\psi}_G}$, linear momentum $\boldsymbol{P}_G$ and angular momentum $\boldsymbol{H}_G$ measured in frame G by a transformation matrix $\boldsymbol{C}^{BG}$, respectively:

$$\overline{\delta \boldsymbol{q}_B} = \boldsymbol{C}^{BG} \delta \boldsymbol{u}_G \tag{4.23}$$

$$\overline{\delta \boldsymbol{\psi}_B} = \boldsymbol{C}^{BG} \overline{\delta \boldsymbol{\psi}_G} \tag{4.24}$$

$$\boldsymbol{H}_B = \boldsymbol{C}^{BG} \boldsymbol{H}_G \tag{4.25}$$

$$\boldsymbol{P}_B = \boldsymbol{C}^{BG} \boldsymbol{P}_G \tag{4.26}$$

With the help of Eqs. (4.21) ~ (4.26), the following relations can be easily established:

$$\left(\overline{\delta \boldsymbol{q}_B}'\right)^T \boldsymbol{F}_B - \left(\overline{\delta \boldsymbol{q}_B}\right)^T \tilde{\boldsymbol{K}}_B \boldsymbol{F}_B = \left(\delta \boldsymbol{u}_G'\right)^T \boldsymbol{C}^{GB} \boldsymbol{F}_B \tag{4.27}$$

$$\left(\overline{\delta \boldsymbol{\psi}_B}'\right)^T \boldsymbol{M}_B - \left(\overline{\delta \boldsymbol{\psi}_B}\right)^T \tilde{\boldsymbol{K}}_B \boldsymbol{M}_B = \left(\overline{\delta \boldsymbol{\psi}_G}'\right)^T \boldsymbol{C}^{GB} \boldsymbol{M}_B \tag{4.28}$$

$$\boldsymbol{C}^{GB}\left(\dot{\boldsymbol{H}}_B + \tilde{\boldsymbol{\Omega}}_B \boldsymbol{H}_B\right) = \dot{\boldsymbol{H}}_G + \tilde{\boldsymbol{\omega}}_G \boldsymbol{C}^{GB} \boldsymbol{H}_B \tag{4.29}$$

$$\boldsymbol{C}^{GB}\left(\dot{\boldsymbol{P}}_B + \tilde{\boldsymbol{\Omega}}_B \boldsymbol{P}_B\right) = \dot{\boldsymbol{P}}_G + \tilde{\boldsymbol{\omega}}_G \boldsymbol{C}^{GB} \boldsymbol{P}_B \tag{4.30}$$

With the help of Eqs. (4.23) ~ (4.30), Eq. (4.20) can be rewritten in the following form:

$$\begin{aligned}
&\int_{t_1}^{t_2} \int_0^L \Bigg\{ \delta \boldsymbol{u}_G'^T \boldsymbol{C}^{GB} \boldsymbol{F}_B + \left(\overline{\delta \boldsymbol{\psi}_G}'\right)^T \boldsymbol{C}^{GB} \boldsymbol{M}_B + \delta \boldsymbol{u}_G^T \left(\dot{\boldsymbol{P}}_G + \tilde{\boldsymbol{\omega}}_G \boldsymbol{C}^{GB} \boldsymbol{P}_B\right) \\
&+ \overline{\delta \boldsymbol{\psi}_G}^T \left(-\boldsymbol{C}^{GB}\left(\tilde{\boldsymbol{e}}_1 + \tilde{\boldsymbol{\gamma}}\right) \boldsymbol{F}_B + \dot{\boldsymbol{H}}_G + \tilde{\boldsymbol{\omega}}_G \boldsymbol{C}^{GB} \boldsymbol{H}_B + \boldsymbol{C}^{GB} \tilde{\boldsymbol{V}}_B \boldsymbol{P}_B\right) \\
&- \delta \boldsymbol{u}_G^T \boldsymbol{f}_G - \overline{\delta \boldsymbol{\psi}_G}^T \boldsymbol{C}^{GB} \boldsymbol{m}_G \Bigg\} dx_1 dt \\
&= \int_{t_1}^{t_2} \left(\overline{\delta \boldsymbol{u}_G}^T \hat{\boldsymbol{F}}_G + \overline{\delta \boldsymbol{\psi}_G}^T \hat{\boldsymbol{M}}_G\right)_0^L dt
\end{aligned} \tag{4.31}$$

Eq. (4.31) is the geometrically exact equations of motion of a beam expressed in the global frame G.

4.4. Mixed Variational Formula of Nonlinear Beam

Apart from the equations of motion derived in above section, the kinematical and constitutive relations are required in order to have a complete formulation to solve problems in general.

4.4.1. Kinematical Relations

According to Hodges [36], the inverse kinematical relations are given by:

$$\boldsymbol{u}_b' = \boldsymbol{C}^{bB}\left(\boldsymbol{e}_1 + \boldsymbol{\gamma}\right) - \boldsymbol{e}_1 - \tilde{\boldsymbol{k}}_b \boldsymbol{u}_b \tag{4.32}$$

$$\dot{\boldsymbol{u}}_b = \boldsymbol{C}^{bB}\boldsymbol{V}_B - \boldsymbol{v}_b - \tilde{\boldsymbol{\omega}}_b \boldsymbol{u}_b \tag{4.33}$$

$$\boldsymbol{\theta}' = \left(\boldsymbol{\Delta} + \frac{1}{2}\tilde{\boldsymbol{\theta}} + \frac{1}{4}\boldsymbol{\theta}\boldsymbol{\theta}^T\right)\left(\boldsymbol{\kappa} + \boldsymbol{k}_b - \boldsymbol{C}^{Bb}\boldsymbol{k}_b\right) \tag{4.34}$$

$$\dot{\boldsymbol{\theta}} = \left(\boldsymbol{\Delta} + \frac{1}{2}\tilde{\boldsymbol{\theta}} + \frac{1}{4}\boldsymbol{\theta}\boldsymbol{\theta}^T\right)\left(\boldsymbol{\Omega}_B - \boldsymbol{C}^{Bb}\boldsymbol{\omega}_b\right) \tag{4.35}$$

where $\boldsymbol{u}_b$ is the column matrix that contains displacement of the beam reference line measured in the frame b; $\boldsymbol{\theta}$ is the column matrix that contains Rodrigues parameters; $\boldsymbol{k}_b$ is the curvature vector for the un-deformed beam; $\boldsymbol{v}_b$ is the column matrix that contains velocity of the un-deformed beam reference line measured in the frame b; $\boldsymbol{\omega}_b$ is the column matrix that contains angular velocity of the un-deformed beam reference line measured in the frame b.

As it can be seen from Eqs. (4.32) to (4.35), the kinematical relations are nonlinear, taking account of geometric nonlinearities.

4.4.2. Constitutive Relations

For beams having small strain, the constitutive equations are linear. The generalized strain-force relations are given by:

$$\begin{Bmatrix} \boldsymbol{\gamma} \\ \boldsymbol{\kappa} \end{Bmatrix} = \boldsymbol{S}\begin{Bmatrix} \boldsymbol{F}_B \\ \boldsymbol{M}_B \end{Bmatrix} \tag{4.36}$$

where $\boldsymbol{S}$ is the constitutive matrix. The expression of fully coupled constitutive matrix can be found in Refs. [36, 133]. For the sake of simplicity, all coupling terms in constitutive matrix $\boldsymbol{S}$ are ignored, and then it can be then expressed as:

$$\boldsymbol{S} = \begin{bmatrix} 1/EA & 0 & 0 & 0 & 0 & 0 \\ 0 & 1/GK_Y & 0 & 0 & 0 & 0 \\ 0 & 0 & 1/GK_X & 0 & 0 & 0 \\ 0 & 0 & 0 & 1/GJ & 0 & 0 \\ 0 & 0 & 0 & 0 & 1/EI_Y & 0 \\ 0 & 0 & 0 & 0 & 0 & 1/EI_X \end{bmatrix} \tag{4.37}$$

where EA is the axial stiffness; GK_Y and GK_X are the edgewise and flapwise shear stiffness, respectively; GJ is the torsional stiffness; EI_Y and EI_X are the edgewise and

flapwise bending stiffness, respectively. Note that if shear deformation is ignored, $1/GK_Y$ and $1/GK_X$ in Eq. (4.37) become zero.

Similarly, the generalized momentum-velocity relations are given by:

$$\begin{Bmatrix} \boldsymbol{P_B} \\ \boldsymbol{H_B} \end{Bmatrix} = \boldsymbol{I_M} \begin{Bmatrix} \boldsymbol{V_B} \\ \boldsymbol{\Omega_B} \end{Bmatrix} \tag{4.38}$$

where $\boldsymbol{I_M}$ is the mass matrix. If the locus of the mass centre is chosen as reference line, the mass matrix $\boldsymbol{I_M}$ can be expressed as:

$$\boldsymbol{I_M} = \begin{bmatrix} \mu & 0 & 0 & 0 & 0 & 0 \\ 0 & \mu & 0 & 0 & 0 & 0 \\ 0 & 0 & \mu & 0 & 0 & 0 \\ 0 & 0 & 0 & rhoI_X + rhoI_Y & 0 & 0 \\ 0 & 0 & 0 & 0 & rhoI_Y & 0 \\ 0 & 0 & 0 & 0 & 0 & rhoI_X \end{bmatrix} \tag{4.39}$$

where μ is the mass per unit length of the blade element; $rhoI_Y$ and $rhoI_X$ are edgewise and flapwise moments of inertia, respectively.

4.4.3. Closing the Formulation

The inverse kinematical relations Eqs. (4.32), (4.33), (4.34) and (4.35) can be considered to be constraints to Eq.(4.20). These constraints can be introduced with the help of Lagrange multipliers [36]. Thus, the following formulation is obtained:

$$\begin{aligned}
&\int_{t_1}^{t_2}\int_0^L \Bigg\{ \left(\overline{\delta \boldsymbol{q_B}}'\right)^T \boldsymbol{F_B} + \left(\overline{\delta \boldsymbol{\psi_B}}'\right)^T \boldsymbol{M_B} + \overline{\delta \boldsymbol{q_B}}^T \left(-\tilde{\boldsymbol{K}}_{\boldsymbol{B}} \boldsymbol{F_B} + \dot{\boldsymbol{P}}_{\boldsymbol{B}} + \tilde{\boldsymbol{\Omega}}_{\boldsymbol{B}} \boldsymbol{P_B}\right) \\
&+ \overline{\delta \boldsymbol{\psi_B}}^T \left(-\tilde{\boldsymbol{K}}_{\boldsymbol{B}} \boldsymbol{M_B} - (\tilde{\boldsymbol{e}}_1 + \tilde{\boldsymbol{\gamma}}) \boldsymbol{F_B} + \dot{\boldsymbol{H}}_{\boldsymbol{B}} + \tilde{\boldsymbol{\Omega}}_{\boldsymbol{B}} \boldsymbol{H_B} + \tilde{\boldsymbol{V}}_{\boldsymbol{B}} \boldsymbol{P_B}\right) \\
&+ \overline{\delta \boldsymbol{F}}^T \left(\boldsymbol{e}_1 + \tilde{\boldsymbol{k}}_b \boldsymbol{u}_b - \boldsymbol{C}^{bB}(\boldsymbol{e}_1 + \boldsymbol{\gamma})\right) + \overline{\delta \boldsymbol{M}}^T \left(\left(\boldsymbol{\Delta} + \frac{1}{2}\tilde{\boldsymbol{\theta}} + \frac{1}{4}\boldsymbol{\theta}\boldsymbol{\theta}^T\right)\left(\boldsymbol{C}^{Bb}\boldsymbol{k}_b - \boldsymbol{\kappa} - \boldsymbol{k}_b\right)\right) \\
&- \left(\overline{\delta \boldsymbol{F}}'\right)^T \boldsymbol{u}_b - \left(\overline{\delta \boldsymbol{M}}'\right)^T \boldsymbol{\theta} \\
&- \overline{\delta \boldsymbol{P}}^T \left(\boldsymbol{v}_b + \tilde{\boldsymbol{\omega}}_b \boldsymbol{u}_b - \boldsymbol{C}^{bB} \boldsymbol{V_B} + \dot{\boldsymbol{u}}_b\right) - \overline{\delta \boldsymbol{H}}^T \left(\left(\boldsymbol{\Delta} + \frac{1}{2}\tilde{\boldsymbol{\theta}} + \frac{1}{4}\boldsymbol{\theta}\boldsymbol{\theta}^T\right)\left(\boldsymbol{C}^{Bb}\boldsymbol{\omega}_b - \boldsymbol{\Omega_B}\right) + \dot{\boldsymbol{\theta}}\right) \\
&- \overline{\delta \boldsymbol{q_B}}^T \boldsymbol{f_B} - \overline{\delta \boldsymbol{\psi_B}}^T \boldsymbol{m_B} \Bigg\} dx_1 dt \\
&= \int_{t_1}^{t_2} \left(\overline{\delta \boldsymbol{q_B}}^T \hat{\boldsymbol{F}}_{\boldsymbol{B}} + \overline{\delta \boldsymbol{\psi_B}}^T \hat{\boldsymbol{M}}_{\boldsymbol{B}} - \overline{\delta \boldsymbol{F}}^T \hat{\boldsymbol{u}}_b - \overline{\delta \boldsymbol{M}}^T \hat{\boldsymbol{\theta}}\right)_0^L dt
\end{aligned} \tag{4.40}$$

where

$$\overline{\delta \boldsymbol{F}} = \boldsymbol{C}^{bB}\delta \boldsymbol{F}_{\boldsymbol{B}} \tag{4.41}$$

$$\overline{\delta \boldsymbol{M}} = \left(\frac{\boldsymbol{\Delta} + \frac{1}{2}\tilde{\boldsymbol{\theta}}}{1 + \frac{1}{4}\boldsymbol{\theta}^{T}\boldsymbol{\theta}} \right) \delta \boldsymbol{M}_{\boldsymbol{B}} \tag{4.42}$$

$$\overline{\delta \boldsymbol{P}} = \boldsymbol{C}^{bB}\delta \boldsymbol{P}_{\boldsymbol{B}} \tag{4.43}$$

$$\overline{\delta \boldsymbol{H}} = \left(\frac{\boldsymbol{\Delta} + \frac{1}{2}\tilde{\boldsymbol{\theta}}}{1 + \frac{1}{4}\boldsymbol{\theta}^{T}\boldsymbol{\theta}} \right) \delta \boldsymbol{H}_{\boldsymbol{B}} \tag{4.44}$$

Eq. (4.40) is the mixed-form formulation of GEBT expressed in the frame B. The displacement and rotation components can be expressed in global frame G, which are independent of blade geometry and deflection, with the help of transformation matrices. The details will be discussed below.

$\tilde{\boldsymbol{K}}_{\boldsymbol{B}}$ and $\tilde{\boldsymbol{\Omega}}_{\boldsymbol{B}}$ in Eq. (4.40) can be expressed in terms of $\boldsymbol{C}^{BG}$ and $\boldsymbol{C}^{GB}$ using [132]:

$$\tilde{\boldsymbol{K}}_{\boldsymbol{B}} = \boldsymbol{C}^{BG}\left(\boldsymbol{C}^{GB}\right)' \tag{4.45}$$

$$\tilde{\boldsymbol{\Omega}}_{\boldsymbol{B}} = -\dot{\boldsymbol{C}}^{BG}\boldsymbol{C}^{GB} + \boldsymbol{C}^{BG}\tilde{\boldsymbol{\omega}}_{\boldsymbol{G}}\boldsymbol{C}^{GB} \tag{4.46}$$

where $\boldsymbol{\omega}_{\boldsymbol{G}}$ is the column matrix that contains the angular velocity of un-deformed beam reference line measured in frame G.

The virtual displacement $\overline{\boldsymbol{\delta q}_{\boldsymbol{B}}}$, virtual rotation $\overline{\boldsymbol{\delta \psi}_{\boldsymbol{B}}}$, linear momentum $\boldsymbol{P}_{\boldsymbol{B}}$, and angular momentum $\boldsymbol{H}_{\boldsymbol{B}}$ measured in frame B are related to the virtual displacement $\delta \boldsymbol{u}_{\boldsymbol{G}}$, virtual rotation $\overline{\delta \boldsymbol{\psi}_{\boldsymbol{G}}}$, linear momentum $\boldsymbol{P}_{\boldsymbol{G}}$ and angular momentum $\boldsymbol{H}_{\boldsymbol{G}}$ measured in frame G by a transformation matrix $\boldsymbol{C}^{BG}$, respectively:

$$\overline{\delta \boldsymbol{q}_{\boldsymbol{B}}} = \boldsymbol{C}^{BG}\delta \boldsymbol{u}_{\boldsymbol{G}} \tag{4.47}$$

$$\overline{\delta \boldsymbol{\psi}_{\boldsymbol{B}}} = \boldsymbol{C}^{BG}\overline{\delta \boldsymbol{\psi}_{\boldsymbol{G}}} \tag{4.48}$$

$$\boldsymbol{H}_{\boldsymbol{B}} = \boldsymbol{C}^{BG}\boldsymbol{H}_{\boldsymbol{G}} \tag{4.49}$$

$$\boldsymbol{P}_{\boldsymbol{B}} = \boldsymbol{C}^{BG}\boldsymbol{P}_{\boldsymbol{G}} \tag{4.50}$$

With the help of Eqs. (4.45) ~ (4.50), the following relations can be easily established:

$$\left(\overline{\delta \boldsymbol{q}_B}'\right)^T \boldsymbol{F}_B - \left(\overline{\delta \boldsymbol{q}_B}\right)^T \tilde{\boldsymbol{K}}_B \boldsymbol{F}_B = \left(\delta \boldsymbol{u}_G'\right)^T \boldsymbol{C}^{GB} \boldsymbol{F}_B \tag{4.51}$$

$$\left(\overline{\delta \boldsymbol{\psi}_B}'\right)^T \boldsymbol{M}_B - \left(\overline{\delta \boldsymbol{\psi}_B}\right)^T \tilde{\boldsymbol{K}}_B \boldsymbol{M}_B = \left(\overline{\delta \boldsymbol{\psi}_G}'\right)^T \boldsymbol{C}^{GB} \boldsymbol{M}_B \tag{4.52}$$

$$\boldsymbol{C}^{GB}\left(\dot{\boldsymbol{H}}_B + \tilde{\boldsymbol{\Omega}}_B \boldsymbol{H}_B\right) = \dot{\boldsymbol{H}}_G + \tilde{\boldsymbol{\omega}}_G \boldsymbol{C}^{GB} \boldsymbol{H}_B \tag{4.53}$$

$$\boldsymbol{C}^{GB}\left(\dot{\boldsymbol{P}}_B + \tilde{\boldsymbol{\Omega}}_B \boldsymbol{P}_B\right) = \dot{\boldsymbol{P}}_G + \tilde{\boldsymbol{\omega}}_G \boldsymbol{C}^{GB} \boldsymbol{P}_B \tag{4.54}$$

$\tilde{\boldsymbol{k}}_b$ and $\tilde{\boldsymbol{\omega}}_b$ in Eq. (4.40) can be expressed in terms of $\boldsymbol{C}^{bG}$ and $\boldsymbol{C}^{Gb}$ using [132]:

$$\tilde{\boldsymbol{k}}_b = \boldsymbol{C}^{bG}\left(\boldsymbol{C}^{Gb}\right)' \tag{4.55}$$

$$\tilde{\boldsymbol{\omega}}_b = \boldsymbol{C}^{bG} \tilde{\boldsymbol{\omega}}_G \boldsymbol{C}^{Gb} \tag{4.56}$$

Defining $\overline{\delta \boldsymbol{F}_G} = \boldsymbol{C}^{Gb} \overline{\delta \boldsymbol{F}}$, $\overline{\delta \boldsymbol{M}_G} = \boldsymbol{C}^{Gb} \overline{\delta \boldsymbol{M}}$, $\overline{\delta \boldsymbol{P}_G} = \boldsymbol{C}^{Gb} \overline{\delta \boldsymbol{P}}$, $\overline{\delta \boldsymbol{H}_G} = \left(\boldsymbol{\Delta} - \tilde{\boldsymbol{\theta}}/2 + \boldsymbol{\theta}\boldsymbol{\theta}^T/4\right)\overline{\delta \boldsymbol{H}}$, and with the help of Eqs. (4.47) ~ (4.56), Eq. (4.40) can be rewritten in the following form:

$$\begin{aligned}
&\int_{t_1}^{t_2}\int_0^L \Bigg\{ \delta \boldsymbol{u}_G'^T \boldsymbol{C}^{GB} \boldsymbol{F}_B + \left(\overline{\delta \boldsymbol{\psi}_G}'\right)^T \boldsymbol{C}^{GB} \boldsymbol{M}_B + \delta \boldsymbol{u}_G^T \left(\dot{\boldsymbol{P}}_G + \tilde{\boldsymbol{\omega}}_G \boldsymbol{C}^{GB} \boldsymbol{P}_B\right) \\
&+ \overline{\delta \boldsymbol{\psi}_G}^T \left(-\boldsymbol{C}^{GB}\left(\tilde{\boldsymbol{e}}_1 + \tilde{\boldsymbol{\gamma}}\right)\boldsymbol{F}_B + \dot{\boldsymbol{H}}_G + \tilde{\boldsymbol{\omega}}_G \boldsymbol{C}^{GB} \boldsymbol{H}_B + \boldsymbol{C}^{GB} \tilde{\boldsymbol{V}}_B \boldsymbol{P}_B\right) \\
&+ \overline{\delta \boldsymbol{F}_G}^T \left(-\boldsymbol{C}^{GB}\left(\boldsymbol{e}_1 + \boldsymbol{\gamma}\right) + \boldsymbol{C}^{Gb} \boldsymbol{e}_1\right) + \overline{\delta \boldsymbol{M}_G}^T \left(-\left(\Delta + \frac{1}{2}\tilde{\boldsymbol{\theta}}_G + \frac{1}{4}\boldsymbol{\theta}_G \boldsymbol{\theta}_G^T\right)\boldsymbol{C}^{Gb} \boldsymbol{\kappa}\right) \\
&- \left(\overline{\delta \boldsymbol{F}_G}'\right)^T \boldsymbol{u}_G - \left(\overline{\delta \boldsymbol{M}_G}'\right)^T \boldsymbol{\theta}_G \\
&+ \overline{\delta \boldsymbol{P}_G}^T \left(\boldsymbol{C}^{GB} \boldsymbol{V}_B - \boldsymbol{C}^{Gb} \boldsymbol{v}_b - \tilde{\boldsymbol{\omega}}_G \boldsymbol{u}_G - \dot{\boldsymbol{u}}_G\right) + \overline{\delta \boldsymbol{H}_G}^T \left(\boldsymbol{\Omega}_B - \boldsymbol{\omega}_B - \boldsymbol{C}^{bG} \frac{\boldsymbol{\Delta} - \tilde{\boldsymbol{\theta}}_G/2}{1 + \boldsymbol{\theta}_G^T \boldsymbol{\theta}_G/4} \dot{\boldsymbol{\theta}}_G\right) \\
&- \delta \boldsymbol{u}_G^T \boldsymbol{C}^{GB} \boldsymbol{f}_B - \overline{\delta \boldsymbol{\psi}_G}^T \boldsymbol{C}^{GB} \boldsymbol{m}_B \Bigg\} dx_1 dt \\
&= \int_{t_1}^{t_2} \left(\overline{\delta \boldsymbol{u}_G}^T \hat{\boldsymbol{F}}_G + \overline{\delta \boldsymbol{\psi}_G}^T \hat{\boldsymbol{M}}_G - \overline{\delta \boldsymbol{F}_G}^T \hat{\boldsymbol{u}}_G - \overline{\delta \boldsymbol{M}_G}^T \hat{\boldsymbol{\theta}}_G\right)_0^L dt
\end{aligned} \tag{4.57}$$

Eq. (4.57) is the mixed-form formulation of GEBT expressed in the global frame G. In Eq. (4.57), $\boldsymbol{u}_G$, $\boldsymbol{\theta}_G$, $\boldsymbol{F}_B$, $\boldsymbol{M}_B$, $\boldsymbol{P}_B$ and $\boldsymbol{H}_B$ are considered to be the fundamental unknown variables. $\boldsymbol{\gamma}$ and $\boldsymbol{\kappa}$ can be expressed in terms of $\boldsymbol{F}_B$ and $\boldsymbol{M}_B$ using Eq. (4.36). $\boldsymbol{V}_B$ and $\boldsymbol{\Omega}_B$ are related to $\boldsymbol{P}_B$ and $\boldsymbol{H}_B$ through Eq.(4.38). Eq. (4.57) contains all the information needed for the finite-element implementation of the geometrically exact

beam theory. In addition to time-dependent analysis and modal analysis, Eq. (4.57) can also be used for static analysis when all time-dependent variables in Eq. (4.57) are eliminated.

4.5. Summary

In this chapter, a blade structural model based on the mixed-form formulation of GEBT was presented. Three coordinate systems, i.e. the global frame, the un-deformed blade frame and the deformed blade frame, were illustrated and the transformation matrices among them were derived. The geometrically exact equations of motion of an initially curved and twisted beam were derived from Hamilton's extended principle, kinetic energy and strain energy. The geometric nonlinearities are taken into account by nonlinear kinematical relations. The kinematical and constitutive relations were introduced to the equations of motion as constraints with the help of Lagrange multipliers. The resulting mixed-form formulation of GEBT expressed in the deformed blade frame was then transformed into the global frame with the help of transformation matrices.

CHAPTER 5 BLADE LOAD MODELLING

5.1. Introduction

As discussed in Chapter 2, blade load modelling is an essential part for aeroelastic analysis of wind turbine blades. In order to perform reliable aeroelastic analysis of wind turbine blades, the loads on the blades need to be accurately modelled.

This chapter summarises the methods used for blade load modelling. The most important sources of loads on wind turbine blades are aerodynamic loads, which are exerted by the airflow passing the blades. As reviewed in Chapter 2, compared to other aerodynamic models, the BEM model is fast and is capable of providing accurate results. For this reason, the BEM model is chosen in this thesis to calculate the aerodynamic loads. In order to accurately predict unsteady aerodynamic loads, the BEM model used in this thesis is extended to an unsteady aerodynamic model through combining with the Beddoes-Leishman (BL) dynamic stall model. In addition to aerodynamics loads, the gravity loads, which are introduced by the gravity of the blades, and the centrifugal loads, which are caused by the rotation of the blades, are also important sources of loads on the blades. The sum of aerodynamic loads, gravity loads and centrifugal loads yields the applied loads, which are applied on the blade structure as distributed loads. Fig.5.1 illustrates the relationship among the loads on a wind turbine blade.

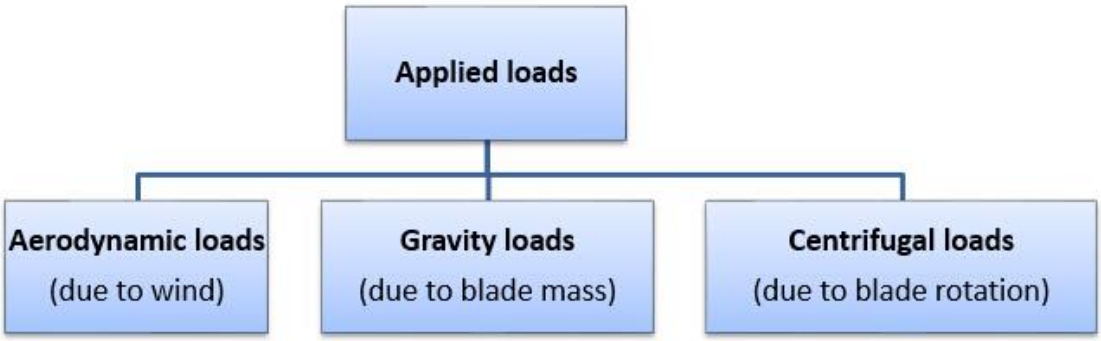

Figure 5.1. Loads on a wind turbine blade

The main contents of this chapter are taken from the manuscript (Appendix G2) submitted for publication in Energy (Elsevier), and the improvements [2] since the submission are also presented in this chapter.

This chapter is structured as follows. Section 5.2 introduces the aerodynamic load calculation based on combining the BEM model with the BL dynamic stall model. The gravity loads and centrifugal loads are summarised in Sections 5.3 and 5.4, respectively. Section 5.5 illustrates the applied loads, followed by a chapter summary in Section 5.6.

5.2. Aerodynamic Loads

In this thesis, the aerodynamic loads are calculated based on combining the BEM model with the BL dynamic stall model. The BEM model with both tip loss correction and wake state consideration is briefly summarised in Section 5.2.1. The main equations and nomenclatures involved in the BEM model can be found in Appendix B. The BL dynamic stall model is illustrated in Section 5.2.2, followed by a flowchart in Section 5.2.3 illustrating the combination of the BEM model and the BL dynamic stall model.

5.2.1. BEM Model

The BEM model was developed through the combination of blade element theory and blade momentum theory. The blade element theory discretises the blade into several elements and ignores the mutual influence between two adjacent elements. The aerodynamic loads on each element are dependent on its local airfoil characteristics, i.e. its lift and drag coefficients. The sum of these loads yields the total loads on the blade. The blade momentum theory introduces the axial induction factor a and angular induction factor a' to calculate the induced velocity in the axial and tangential directions, respectively. The induced velocity will affect the angle of attack of the blade and therefore influence the aerodynamic loads calculated by the above blade element theory. Combining blade element theory with blade momentum theory provides a solution to obtain the performance parameters of each blade element, such as axial induction factor a and angular induction factor a', through an iterative procedure, which is summarised below [39, 134]:

[2] Since the submission, improvements have been made to extend the BEM model to an unsteady aerodynamic model by combining it with the BL dynamic stall model.

1) Use an estimate to obtain the initial axial induction factor a and angular induction factor a'. In this study, zero initial values are used for both axial induction factor a and angular induction factor a':

$$a_1 = 0 \tag{5.1}$$

$$a'_1 = 0 \tag{5.2}$$

2) Start the iterative procedure for the *j*th iteration. For the first iteration ($j = 1$), follow step 1. Calculate the relative wind angle φ_j and the Prandtl tip loss factor $F_{tip-loss,j}$:

$$\varphi_j = \arctan\left(\frac{(1-a_j)V_0 + v_{op}}{(1+a'_j)\Omega r + v_{ip}}\right) \tag{5.3}$$

$$F_{tip-loos,j} = \left(\frac{2}{\pi}\right)\cos^{-1}\left[\exp\left(-\left(\frac{(B_N/2)[1-(r/R)]}{(r/R)\sin\varphi_j}\right)\right)\right] \tag{5.4}$$

where v_{op} and v_{ip} are respectively the out-of-plane and in-plane velocities of the blade element (see Fig. B.2 in Appendix B); v_{op} and v_{ip} are generally ignored in a typical BEM model, but they are considered in this thesis to take account of blade motions in the calculation of aerodynamic loads; V_0 is the upcoming wind velocity on each blade element; Ω is the rotor rotational speed; r is the distance from the blade element to the rotor centre; B_N is the number of blades; R is the blade radius. In this study, V_0 and r are calculated based on the deformed blade geometry to take account of the blade deflection in the calculation of aerodynamic loads.

The Prandtl tip loss factor $F_{tip-loss,j}$ in Eq. (5.4) is used to take account of the influence of vortices shedding from the blade tip on the induced velocity. From Eq. (5.4) we can see that the Prandtl tip loss factor is always between 0 and 1.

3) Determine the local angle of attack of the blade element:

$$\alpha_j = \varphi_j - \theta_p \tag{5.5}$$

where θ_p is the twist angle of each blade element (see Fig. 4.3), previously defined in Section 4.2.2.

Then obtain the lift coefficient $C_{l,j}$ and drag coefficient $C_{d,j}$ from the airfoil lift and drag coefficient curves against the angle of attack.

4) Update the axial induction factor a and angular induction factor a' for the next iteration, considering the drag effects:

$$a_{j+1} = \frac{1}{\left[1 + \frac{4F_{tip-loss,j}\sin^2(\varphi_j)}{\sigma'(C_{l,j}\cos\varphi_j + C_{d,j}\sin\varphi_j)}\frac{1}{H}\right]} \tag{5.6}$$

$$a'_{j+1} = \frac{1}{\frac{4F_{tip-loss,j}\sin\varphi_j\cos\varphi_j}{\sigma'(C_{l,j}\sin\varphi_j - C_{d,j}\cos\varphi_j)} - 1} \tag{5.7}$$

The parameter σ' in Eq. (5.6) is the local solidity, defined by:

$$\sigma' = B_N c / 2\pi r \tag{5.8}$$

where c is the chord of the blade element.

The parameter H in Eq. (5.6) is used for the situation when large axial induction factor occurs. When the axial induction factor a is greater than 0.5, wind turbine blades get into turbulent wake state, and the expression of thrust coefficient [134]:

$$C_T = 4a(1-a) \tag{5.9}$$

needs to be replaced by the empirical expression [135]:

$$C_T = 0.6 + 0.61a + 0.79a^2 \tag{5.10}$$

To obtain a better transition, the above empirical model is used for the situation that a is greater than 0.3539 rather than 0.5 [135]. The parameter H is defined as [135]:

$$\text{for } a_{j+1} \le 0.3539, H = 1.0 \tag{5.11}$$

$$\text{for } a_{j+1} > 0.3539, H = \frac{4a(1-a)}{(0.6 + 0.61a + 0.79a^2)} \tag{5.12}$$

The above process is repeated until the deviation between the new and previous induction factors is within an acceptable tolerance. Then confirm the local relative wind angle φ, tip loss factor $F_{tip-loss}$, angle of attack α, lift coefficient C_l and drag coefficient C_d for each blade element.

Having determined the above performance parameters for each blade element, the normal force per unit length $\mathrm{d}F_N$ and tangential force per unit length $\mathrm{d}F_T$ on each blade element (see Fig. B.2 in Appendix B) are respectively calculated by:

$$\mathrm{d}F_N = F_{tip-loss}\,\tfrac{1}{2}\rho U_{rel}^2 (C_l\cos\varphi + C_d\sin\varphi)c \tag{5.13}$$

$$\mathrm{d}F_T = F_{tip-loss}\,\frac{1}{2}\rho U_{\mathrm{rel}}^2 (C_l\sin\varphi - C_d\cos\varphi)c \tag{5.14}$$

where ρ is the air density, U_{rel} is the relative wind velocity.

The above aerodynamic loads on each blade element are calculated with respect to the deformed blade frame B and can be stored in the aerodynamic-force vector $\boldsymbol{F}_{\boldsymbol{aero}}^{\boldsymbol{B}}$:

$$\boldsymbol{F}_{\boldsymbol{aero}}^{\boldsymbol{B}} = \begin{bmatrix} 0 \\ dF_N \\ dF_T \end{bmatrix} \tag{5.15}$$

Fig. 5.2 presents the flowchart of the aerodynamic load calculation based on the BEM model.

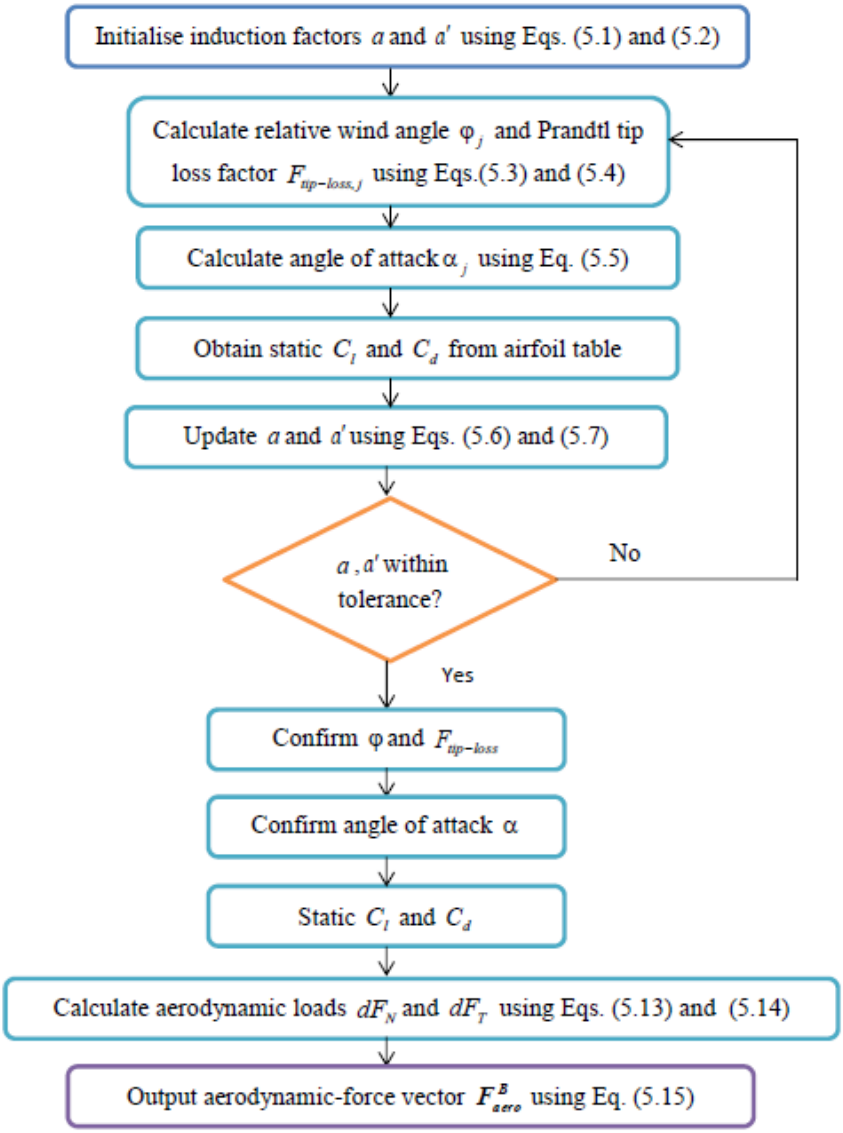

Figure 5.2. Flowchart of aerodynamic load calculation based on the BEM model

5.2.2. Beddoes-Leishman (BL) Dynamic Stall Model

The BEM model illustrated in the above section is based on quasi-steady assumption. However, practical aerodynamic loads are unsteady due to sudden change in wind, such as wind shear and atmospheric turbulence. In order to take account of the unsteady effects, a dynamic stall model is required.

Dynamic stall is a phenomenon associated with the separation of the boundary layer. During the dynamic stall, the boundary layer initially separates at the trailing edge, and gradually shifts to leading edge with the increasing angles of attack [20]. The angle of attack of rotating blades changes dynamically due to sudden change in wind, such as wind shear and atmospheric turbulence. The response introduced by changing angle of attack is dependent on whether the boundary layer is separated and will have a time delay.

In order to take account of dynamic stall effects in aerodynamic load calculation, the BL dynamic stall model [53] is used in this thesis. Even though dynamic stall process comprises various intrinsically related phenomena, Beddoes and Leishman managed to decompose it into three distinct models, i.e. 1) an attached flow model, which calculates the unsteady attached force coefficients; 2) a separated flow model, which uses the force coefficients obtained in the attached flow model as input to recalculate the force coefficients through taking account of unsteady separated flow effects, such as pressure lag, viscous lag and unsteady trailing edge separation point; 3) a vortex lift model, which adds the vortex contribution to the results from the separated flow model, yielding the total unsteady force coefficients on the airfoil.

5.2.2.1. Attached Flow Model

For unsteady attached flow, the normal force coefficient on an airfoil can be split into two components, i.e. a circulatory component and an impulsive component, which are considered separately in the attached flow model.

- **Circulatory Component**

According to Ref. [53], the circulatory normal force coefficient $C_{N,n}^{C}$ resulted from an accumulating series of time step inputs in the angle of attack can be calculated by:

$$C_{N,n}^{C} = C_{Na}\alpha_{E,n} \tag{5.16}$$

where n denotes the n th time step, C_{Na} is the static C_N curve slope near zero lift, $\alpha_{E,n}$ is the equivalent angle of attack at the n th time step. $\alpha_{E,n}$ can be expressed as :

$$\alpha_{E,n} = \alpha_n - X_n - Y_n \tag{5.17}$$

where α_n is the angle of attack at the n th time step. X_n and Y_n in Eq. (5.17) are deficiency functions at the n th time step, respectively defined as:

$$X_n = X_{n-1}e^{-A_3\Delta S} + A_1\Delta a_n e^{-A_3\Delta S/2} \tag{5.18}$$

$$Y_n = Y_{n-1}e^{-A_4\Delta S} + A_2\Delta a_n e^{-A_4\Delta S/2} \tag{5.19}$$

where Δa_n is the change in angle of attack at the n th time step, i.e. $\Delta a_n = \alpha_n - \alpha_{n-1}$; A_1, A_2, A_3 and A_4 are empirical constants. As given in Ref. [136], the suggested values for these constant are:

$A_1 = 0.3$, $A_2 = 0.7$, $A_3 = 0.14$, $A_4 = 0.53$.

ΔS in Eq. (5.18) is the dimensionless time and can be expressed in terms of relative wind speed U_{rel}, time interval Δt and chord c using the following equation:

$$\Delta S = \frac{U_{rel}\Delta t}{c/2} \tag{5.20}$$

- **Impulsive Component**

For an airfoil undergoing rapid motion, there exists an impulsive force due to local pressure variations. The impulsive normal force coefficient $C_{N,n}^{I}$ can be calculated using [53]:

$$C_{N,n}^{I} = \frac{3c}{U_{rel}}\left(\frac{\Delta\alpha_n}{\Delta t} - D_n\right) \tag{5.21}$$

D_n in Eq. (5.21) is another deficiency function, defined as:

$$D_n = D_{n-1} e^{\frac{-\Delta t}{K_a T_I}} + \left(\frac{\Delta\alpha_n - \Delta\alpha_{n-1}}{\Delta t} \right) e^{\frac{-\Delta t}{2K_a T_I}} \tag{5.22}$$

where $\Delta\alpha_{n-1}$ is the change in angle of attack at the $n-1$ th time step, i.e. $\Delta\alpha_{n-1} = \alpha_{n-1} - \alpha_{n-2}$; K_a is a function of Mach number, and for incompressible flow it becomes a constant with suggested value of 0.75 given in Ref. [136]. T_I in Eq. (5.22) is the non-circulatory time constant, defined as:

$$T_I = \frac{c}{a_s} \tag{5.23}$$

where a_s is the speed of sound.

- **Total Attached Flow Normal Force Coefficient**

The total unsteady attached-flow normal force coefficient $C_{N,n}^P$ is obtained by summing the circulatory normal force coefficient $C_{N,n}^C$ and the impulsive normal force coefficient $C_{N,n}^I$:

$$C_{N,n}^P = C_{N,n}^C + C_{N,n}^I \tag{5.24}$$

5.2.2.2. Separated Flow Model

The relationship between static normal force coefficient C_N and the dimensionless suction side separation point position f can be established using Kirchoff theory [53]:

$$C_N = C_{Na} \left(\frac{1+\sqrt{f}}{2} \right)^2 (\alpha - \alpha_0) \tag{5.25}$$

where α is the angle of attack; α_0 is the angle of attack for zero lift; f is measured from the leading edge, meaning that $f = 0$ when the flow is fully separated and $f = 1$ when the flow is entirely attached.

Inverting Eq. (5.25) and using airfoil's static characteristic yields separation point position f as a function of angle of attack α, obtaining $f(\alpha)$.

For unsteady flow, there exists a time delay in the leading edge pressure response with respect to the attached flow normal force coefficient $C_{N,n}^{P}$. In order to take account of the time delay, another deficiency function $D_{P,n}$ is introduced in the calculation of the normal force coefficient $C'_{N,n}$:

$$C'_{N,n} = C_{N,n}^{P} - D_{P,n} \tag{5.26}$$

$D_{P,n}$ in Eq. (5.26) can be expressed as:

$$D_{P,n} = D_{P,n-1} e^{\frac{-\Delta S}{T_P}} + \left(C_{N,n}^{P} - C_{N,n-1}^{P}\right) e^{\frac{-\Delta S}{2T_P}} \tag{5.27}$$

where T_P is the pressure-lag time constant. As given in Ref. [136], the suggested value of T_P is 1.5.

In order to obtain effective separation point f'_n, another effective angle of attack $\alpha_{f,n}$ is introduced, defined as:

$$\alpha_{f,n} = \frac{C'_{N,n} - C_{N_0}}{C_{Na}} \tag{5.28}$$

where C_{N_0} is the normal force coefficient at zero angle of attack.

Having obtained the effective angle of attack $\alpha_{f,n}$, the effective separation point f'_n is then obtained from the static separation point characteristic:

$$f'_n = f\left(\alpha_{f,N}\right) \tag{5.29}$$

It should be noted that there exists a time delay in the boundary layer's response for unsteady conditions. This unsteady effect can be taken into account by applying a first order lag to the effective separation point:

$$f''_n = f'_n - D_{f,n} \tag{5.30}$$

where $D_{f,n}$ is another deficiency function, defined by:

$$D_{f,n} = D_{f,n-1} e^{\frac{-\Delta S}{T_f}} + \left(f'_n - f'_{n-1}\right) e^{\frac{-\Delta S}{2T_f}} \tag{5.31}$$

T_f in Eq.(5.31) is the viscous-lag time constant. As given in Ref. [136], the suggested value of T_f is 5.

At last, the unsteady normal force coefficient $C_{N,n}^f$ accounting for both pressure lag and viscous lag can be calculated with the effective unsteady edge separation point f'' using the Kirchhoff relation [53]:

$$C_{N,n}^f = C_{Na}\left(\frac{1+\sqrt{f_n''}}{2}\right)^2 \alpha_{Eq,n} + C_{N,n}^I \tag{5.32}$$

5.2.2.3. Vortex Lift Model

In this model, the contribution of vortex lift to the unsteady normal force coefficient is calculated. The vortex lift contribution is only calculated when the following condition is satisfied:

$$\tau_{v,n} < T_{vl} \tag{5.33}$$

where T_{vl} is an empirical time constant, with suggested value of 5 given in Ref. [136].

$\tau_{v,n}$ in Eq. (5.33) is the vortex time parameter, defined as:

$$\tau_{v,n} = \tau_{v,n-1} + \frac{dt}{c/2} V_{rel}\, 0.45, \text{ if } C'_{N,n} > C_{N,I} \tag{5.34}$$

$$\tau_{v,n} = 0, \text{ if } C'_{N,n} < C_{N,I} \wedge \Delta\alpha_n > 0 \tag{5.35}$$

where $C_{N,I}$ is the critical value of normal coefficient. According to Ref. [136], $C_{N,I}$ can be assumed to be the maximum static normal coefficient.

The vortex lift $C_{V,n}$ is obtained using the following equation:

$$C_{V,n} = C_{N,n}^C\left(1 - K_{N,n}\right) \tag{5.36}$$

where $C_{N,n}^C$ is the circulatory normal force coefficient (see Eq. (5.16)); $K_{N,n}$ is defined as:

$$K_{N,n} = \frac{\left(1+\sqrt{f_n''}\right)^2}{4} \tag{5.37}$$

Then, the total accumulated vortex contribution $C_{N,n}^{V}$ is obtained using the following equation:

$$C_{N,n}^{V} = C_{N,n-1}^{V} e^{\frac{-\Delta S}{T_v}} + \left(C_{V,n} - C_{V,n-1}\right)\left(\frac{-\Delta S}{2T_v}\right) \tag{5.38}$$

where T_v is the vortex delay constant. As given in Ref. [136], the suggested value of T_v is 6.

5.2.2.4. Model Outputs and Flowchart

The total unsteady normal force coefficient $C_{N,n}$ is obtained by summing the unsteady separated term $C_{N,n}^{f}$ and the vortex lift term $C_{N,n}^{V}$:

$$C_{N,n} = C_{N,n}^{f} + C_{N,n}^{V} \tag{5.39}$$

According to Ref. [53], the unsteady tangential force coefficient $C_{C,n}$ can be obtained using:

$$C_{C,n} = \eta C_{Na} \alpha_{E,n}^{2} \sqrt{f_n''} \tag{5.40}$$

where η is the recovery factor, which is used to account for the fact that the airfoil usually does not realize all of the tangential pressure obtained in potential flow. η can be attained empirically from static airfoil aerodynamic data, and its typical value is 0.95 [53].

Having obtained the unsteady normal force coefficient $C_{N,n}$ and unsteady tangential force coefficient $C_{C,n}$, the unsteady lift coefficient $C_{l,n}$ and unsteady drag coefficient $C_{d,n}$ can be respectively obtained using the following equations:

$$C_{l,n} = C_{N,n}\cos(\varphi) + C_{C,n}\sin(\varphi) \tag{5.41}$$

$$C_{d,n} = C_{N,n}\sin(\varphi) - C_{C,n}\sin(\varphi) \tag{5.42}$$

In order to illustrate the calculation process, a flowchart of the BL dynamic stall model is presented in Fig. 5.3, showing an open loop system.

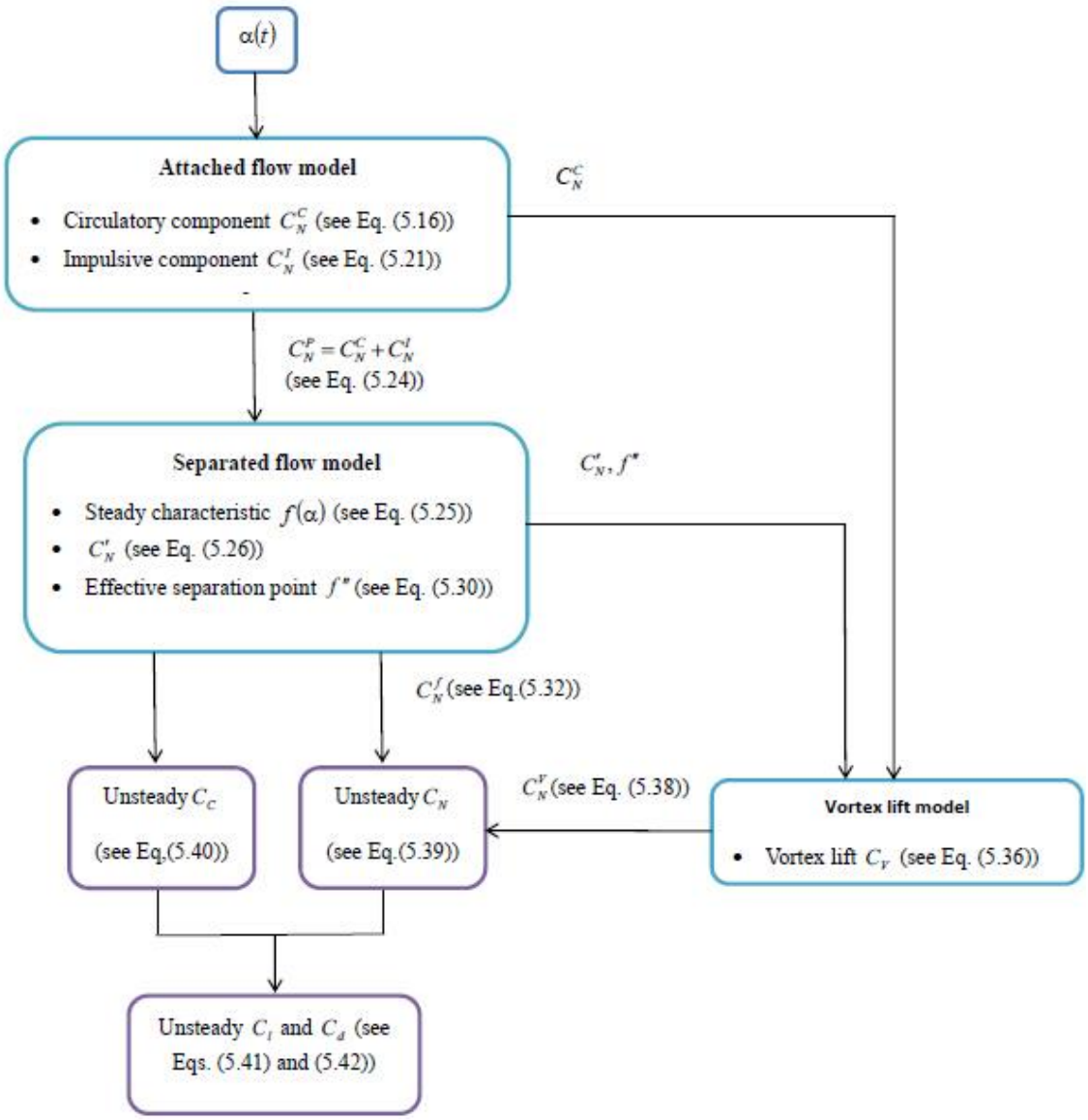

Figure 5.3. Flowchart of the BL dynamic stall model

5.2.3. Flowchart of Aerodynamic Load Calculation Based on Combining the BEM Model with the BL Dynamic Stall Model

The BEM model presented in Section 5.2.1 can be extend to an unsteady aerodynamic model by combining with the BL dynamic stall model presented in Section 5.2.2. Through slightly modifying the flowchart presented in Fig. 5.2, the flowchart of the aerodynamic load calculation based on combing the BEM model with the BL dynamic stall model is illustrated in Fig. 5.4.

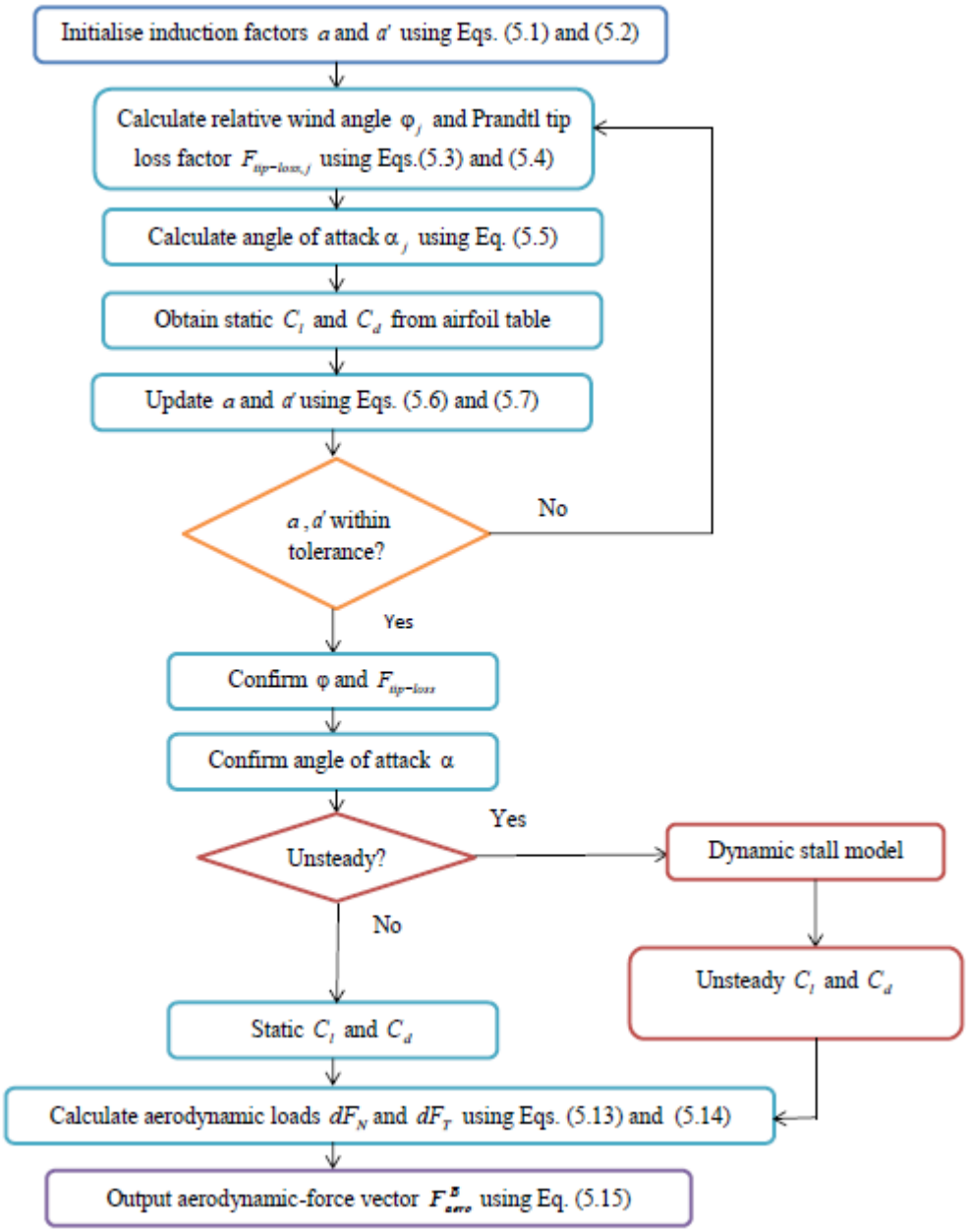

Figure 5.4. Flowchart of aerodynamic load calculation based on combining the BEM model with the BL dynamic stall model

5.3. Gravity Loads

For large wind turbine blades, gravity is an important source of loading. Taking account of the tilt angle β_2 (see Fig. 5.5), the angle between the shaft and the horizontal axis, and the azimuth angle β_3 (see Fig. 5.6), the position of the blade in the circumferential direction of the wind turbine rotor axis, the gravity-force vector $\boldsymbol{F}_g^G$ of a blade element with respect to the global frame G is given by:

$$\boldsymbol{F}_{\boldsymbol{g}}^{\boldsymbol{G}} = \begin{bmatrix} \cos\beta_3 & 0 & -\sin\beta_3 \\ 0 & 1 & 0 \\ \sin\beta_3 & 0 & \cos\beta_3 \end{bmatrix} \begin{bmatrix} \cos\beta_2 & \sin\beta_2 & 0 \\ -\sin\beta_2 & \cos\beta_2 & 0 \\ 0 & 0 & 1 \end{bmatrix} \begin{bmatrix} -g\mu \\ 0 \\ 0 \end{bmatrix} \tag{5.43}$$

where g is the gravity constant , μ is the mass per unit length of each blade element.

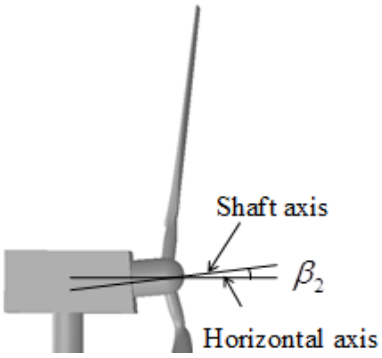

Figure 5.5. Tilt angle

Figure 5.6. Azimuth angle

The force vector $\boldsymbol{F}_{\boldsymbol{g}}^{\boldsymbol{G}}$ with respect to the global frame G can be transformed into the deformed blade frame B using the following equation:

$$\boldsymbol{F}_{\boldsymbol{g}}^{\boldsymbol{B}} = \boldsymbol{C}^{\boldsymbol{BG}} \boldsymbol{F}_{\boldsymbol{g}}^{\boldsymbol{G}} \tag{5.44}$$

where $\boldsymbol{C}^{\boldsymbol{BG}}$ is the transformation matrix (see Eq. 4.3), previously defined in Section 4.2.2.

5.4. Centrifugal Loads

Due to the rotation of the wind turbine blades, centrifugal loads have to be considered. Taking account of the azimuth angle β_3, the centrifugal-force vector $\boldsymbol{F}_{\boldsymbol{c}}^{\boldsymbol{G}}$ of a blade element with respect to the global frame G is given by:

$$\boldsymbol{F}_c^G = \begin{bmatrix} \cos\beta_3 & 0 & -\sin\beta_3 \\ 0 & 1 & 0 \\ \sin\beta_3 & 0 & \cos\beta_3 \end{bmatrix} \begin{bmatrix} r\,\Omega^2\,\mu \\ 0 \\ 0 \end{bmatrix} \tag{5.45}$$

The force vector $\boldsymbol{F}_c^G$ can be transformed into the deformed blade frame B using the following equation:

$$\boldsymbol{F}_c^B = \boldsymbol{C}^{BG}\boldsymbol{F}_c^G \tag{5.46}$$

5.5. Applied Loads

Having obtained the aerodynamic force $\boldsymbol{F}_{aero}^B$, gravity force $\boldsymbol{F}_g^B$ and centrifugal force $\boldsymbol{F}_c^B$ on each blade element, the applied force $\boldsymbol{F}_{AL}^B$ on each blade element is obtained by summing these forces (in vector form):

$$\boldsymbol{F}_{AL}^B = \boldsymbol{F}_{aero}^B + \boldsymbol{F}_g^B + \boldsymbol{F}_c^B \tag{5.47}$$

5.6. Summary

This chapter presented the methods used for calculating the main sources of loads on a wind turbine blade, i.e. 1) aerodynamic loads, which are contributed by the wind passing the blade; 2) gravity loads, which are introduced by the gravity of the blade; and 3) centrifugal loads, which are caused by the rotation of the blade. The aerodynamic loads were calculated based on combining the BEM model with the BL dynamic stall model. The calculated aerodynamic loads, gravity loads and centrifugal loads were stored in a vector form and transformed to the deformed blade frame with the help of transformation matrices. The applied loads were then obtained by summing these load vectors.

Chapter 6 presents the implementation of the nonlinear aeroelastic model by coupling the blade structural model and blade load model.

CHAPTER 6 IMPLEMENTATION OF THE NONLINEAR AEROELASTIC MODEL

6.1. Introduction

The blade structural model and blade load model have been presented in Chapters 4 and 5, respectively. The blade structural model is based on a mixed-form formulation of geometrically exact beam theory (GEBT), which can be used for static analysis, time-dependent analysis and modal analysis. The blade load model takes account of aerodynamic loads, gravity loads and centrifugal loads. This chapter details the implementation of the nonlinear aeroelastic model by coupling the blade structural model and blade load model. The strategies for applying the nonlinear aeroelastic model to four types of studies, i.e. static analysis, modal analysis, time-dependent analysis and stability analysis, are also presented in this chapter.

COMSOL Multiphysics [137] is used to achieve the implementation. The choice is mainly based on the fact that COMSOL Multiphysics 1) allows equation-based modelling, e.g. the chance to define a partial differential equation (PDE) by its weak form using COMSOL 1D Weak Form PDE module; 2) enables MATLAB functions in model settings definition, such as boundary conditions and material properties; and 3) provides interfaces between its graphical user interface (GUI) and MATLAB, which enables direct use of MATLAB scripts in building COMSOL model.

This chapter is structured as follows. Section 6.2 presents the strategy used for coupling the blade structural modelling module and the blade load modelling module to yield a nonlinear aeroelastic model; Section 6.3 addresses the strategies for applying the nonlinear aeroelastic model to four types of studies, including static analysis, modal analysis, time-dependent analysis and stability analysis; And Section 6.4 summarises the findings of this chapter.

6.2. Coupling Strategy

Based on the methods presented in Chapter 5, a blade load modelling module is developed using MATLAB to calculate the applied forces $\boldsymbol{F}_{AL}^{B}$ (see Eq. (5.47)). The blade load modelling module takes account of the aerodynamic loads (calculated based on combing the BEM model and the BL dynamic stall model), gravity loads and centrifugal loads, as presented in Chapter 5. GEBT is not available in COMSOL Multiphysics, but COMSOL Multiphysics allows equation-based modelling, e.g. the chance to define a partial differential equation (PDE) by its weak form. The mixed-form formulation of GEBT (see Eq. (4.57)) is implemented using COMSOL 1D Weak Form PDE module, yielding a blade structural modelling module.

In order to facilitate illustration, Eq. (5.47) for the applied forces $\boldsymbol{F}_{AL}^{B}$ and Eq. (4.57) for the mixed-form formualtion of GEBT are respectively rewritten below:

$$\boldsymbol{F}_{AL}^{B} = \boldsymbol{F}_{aero}^{B} + \boldsymbol{F}_{g}^{B} + \boldsymbol{F}_{c}^{B} \tag{6.1}$$

$$\begin{aligned}
&\int_{t_1}^{t_2}\int_{0}^{L}\Big\{\delta\boldsymbol{u}_G'^{T}\boldsymbol{C}^{GB}\boldsymbol{F}_B+\left(\overline{\delta\boldsymbol{\psi}_G}'\right)^{T}\boldsymbol{C}^{GB}\boldsymbol{M}_B+\delta\boldsymbol{u}_G^{T}\left(\dot{\boldsymbol{P}}_G+\tilde{\boldsymbol{\omega}}_G\boldsymbol{C}^{GB}\boldsymbol{P}_B\right)\\
&+\overline{\delta\boldsymbol{\psi}_G}^{T}\left(-\boldsymbol{C}^{GB}\left(\tilde{\boldsymbol{e}}_1+\tilde{\boldsymbol{\gamma}}\right)\boldsymbol{F}_B+\dot{\boldsymbol{H}}_G+\tilde{\boldsymbol{\omega}}_G\boldsymbol{C}^{GB}\boldsymbol{H}_B+\boldsymbol{C}^{GB}\tilde{\boldsymbol{V}}_B\boldsymbol{P}_B\right)\\
&+\overline{\delta\boldsymbol{F}_G}^{T}\left(-\boldsymbol{C}^{GB}\left(\boldsymbol{e}_1+\boldsymbol{\gamma}\right)+\boldsymbol{C}^{Gb}\boldsymbol{e}_1\right)+\overline{\delta\boldsymbol{M}_G}^{T}\left(-\left(\Delta+\frac{1}{2}\tilde{\boldsymbol{\theta}}_G+\frac{1}{4}\boldsymbol{\theta}_G\boldsymbol{\theta}_G^{T}\right)\boldsymbol{C}^{Gb}\boldsymbol{\kappa}\right)\\
&-\left(\overline{\delta\boldsymbol{F}_G}'\right)^{T}\boldsymbol{u}_G-\left(\overline{\delta\boldsymbol{M}_G}'\right)^{T}\boldsymbol{\theta}_G\\
&+\overline{\delta\boldsymbol{P}_G}^{T}\left(\boldsymbol{C}^{GB}\boldsymbol{V}_B-\boldsymbol{C}^{Gb}\boldsymbol{v}_b-\tilde{\boldsymbol{\omega}}_G\boldsymbol{u}_G-\dot{\boldsymbol{u}}_G\right)+\overline{\delta\boldsymbol{H}_G}^{T}\left(\boldsymbol{\Omega}_B-\boldsymbol{\omega}_B-\boldsymbol{C}^{bG}\frac{\Delta-\tilde{\boldsymbol{\theta}}_G/2}{1+\boldsymbol{\theta}_G^{T}\boldsymbol{\theta}_G/4}\dot{\boldsymbol{\theta}}_G\right)\\
&-\delta\boldsymbol{u}_G^{T}\boldsymbol{C}^{GB}\boldsymbol{f}_B-\overline{\delta\boldsymbol{\psi}_G}^{T}\boldsymbol{C}^{GB}\boldsymbol{m}_B\Big\}dx_1dt\\
&=\left(\overline{\delta\boldsymbol{u}_G}^{T}\hat{\boldsymbol{F}}_G+\overline{\delta\boldsymbol{\psi}_G}^{T}\hat{\boldsymbol{M}}_G-\overline{\delta\boldsymbol{F}_G}^{T}\hat{\boldsymbol{u}}_G-\overline{\delta\boldsymbol{M}_G}^{T}\hat{\boldsymbol{\theta}}_G\right)_0^{L}
\end{aligned} \tag{6.2}$$

All variables in Eqs. (6.1) and (6.2) have been defined in Chapters 5 and 4, respectively.

In Eq. (6.2), $\boldsymbol{u}_G$, $\boldsymbol{\theta}_G$, $\boldsymbol{F}_B$, $\boldsymbol{M}_B$, $\boldsymbol{P}_B$ and $\boldsymbol{H}_B$ are considered to be the fundamental unknown variables, i.e. dependent variables. $\boldsymbol{\gamma}$ and $\boldsymbol{\kappa}$ can be expressed in terms of $\boldsymbol{F}_B$ and $\boldsymbol{M}_B$ using Eq. (4.36). $\boldsymbol{V}_B$ and $\boldsymbol{\Omega}_B$ are related to $\boldsymbol{P}_B$ and $\boldsymbol{H}_B$ through Eq.(4.38). In

order to facilitate illustration, Eqs. (4.36) and Eq. (4.38) are respectively rewritten below:

$$\begin{Bmatrix} \boldsymbol{\gamma} \\ \boldsymbol{\kappa} \end{Bmatrix} = \boldsymbol{S} \begin{Bmatrix} \boldsymbol{F}_B \\ \boldsymbol{M}_B \end{Bmatrix} \tag{6.3}$$

$$\begin{Bmatrix} \boldsymbol{P}_B \\ \boldsymbol{H}_B \end{Bmatrix} = \boldsymbol{I}_M \begin{Bmatrix} \boldsymbol{V}_B \\ \boldsymbol{\Omega}_B \end{Bmatrix} \tag{6.4}$$

where $\boldsymbol{S}$ is the constitutive matrix (see Eq. (4.37)), $\boldsymbol{I}_M$ is the mass matrix (see Eq.(4.39)). $\boldsymbol{S}$ and $\boldsymbol{I}_M$ contains cross-sectional properties, such as flapwise stiffness and mass per unit length. Theses cross-sectional properties are used as the input data to define a beam element, and each beam element is allowed to have diffferent cross-sectional properties.

All parameters in Eq. (6.2) are defined as 1) global variables, such as time, which are applied to the entire model and do not depend on the geometry; or 2) local variables, such as cross-sectional properties, which vary along the blade span. Eq. (6.2) is in its weakest possible form, which means the lowest order of shape functions can be used. Therefore, linear (first-order) Lagrange element is used for the discretisation of dependent variables (u_G, $\boldsymbol{\theta}_G$, $\boldsymbol{F}_B$, $\boldsymbol{M}_B$, $\boldsymbol{P}_B$ and $\boldsymbol{H}_B$). The combination of blade load modelling module and blade structural modelling module is achieved by replacing $\boldsymbol{f}_B$ in Eq. (6.2) with $\boldsymbol{F}_{AL}^{B}$ (see Eq. (6.1)) calculated using MATLAB program.

6.3. Types of Studies

The implemented nonlinear aeroelastic model can be used for four types of studies, including static analysis, modal analysis, time-dependent analysis and stability analysis, as illustrated in Fig. 6.1.

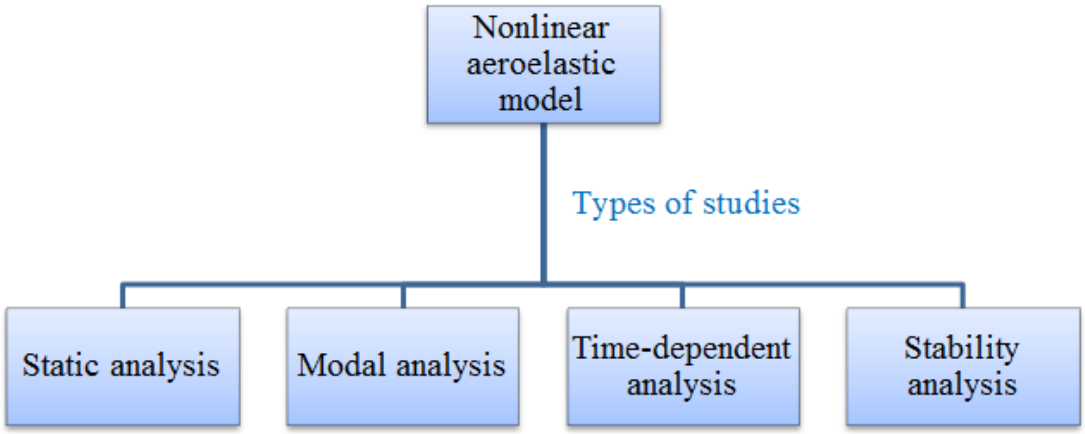

Figure 6.1. Types of studies for the nonlinear aeroelastic model

Each type of study in Fig. 6.1 is detailed below.

6.3.1. Static Analysis

For the static analysis, the type of study in COMSOL is set to *Stationary*, and Eq. (6.2) is reduced to the following form by neglecting all time-dependent variables (i.e. $\boldsymbol{P}_B$, $\boldsymbol{H}_B$, $\dot{\boldsymbol{P}}_G$ and $\dot{\boldsymbol{H}}_G$):

$$
\begin{aligned}
&\int_0^L \Big\{ \delta \boldsymbol{u}_G'^T \boldsymbol{C}^{GB} \boldsymbol{F}_B + \left(\overline{\delta \boldsymbol{\psi}_G}' \right)^T \boldsymbol{C}^{GB} \boldsymbol{M}_B \\
&+ \overline{\delta \boldsymbol{\psi}_G}^T \left(-\boldsymbol{C}^{GB} \left(\tilde{\boldsymbol{e}}_1 + \tilde{\boldsymbol{\gamma}} \right) \boldsymbol{F}_B \right) \\
&+ \overline{\delta \boldsymbol{F}_G}^T \left(-\boldsymbol{C}^{GB} \left(\boldsymbol{e}_1 + \boldsymbol{\gamma} \right) + \boldsymbol{C}^{Gb} \boldsymbol{e}_1 \right) + \overline{\delta \boldsymbol{M}_G}^T \left(-\left(\Delta + \frac{1}{2} \tilde{\boldsymbol{\theta}}_G + \frac{1}{4} \boldsymbol{\theta}_G \boldsymbol{\theta}_G^T \right) \boldsymbol{C}^{Gb} \boldsymbol{\kappa} \right) \\
&- \left(\overline{\delta \boldsymbol{F}_G}' \right)^T \boldsymbol{u}_G - \left(\overline{\delta \boldsymbol{M}_G}' \right)^T \boldsymbol{\theta}_G \\
&- \delta \boldsymbol{u}_G^T \boldsymbol{C}^{GB} \boldsymbol{F}_{AL}^B - \overline{\delta \boldsymbol{\psi}_G}^T \boldsymbol{C}^{GB} \boldsymbol{m}_B \Big\} dx_1 \\
&= \left(\overline{\delta \boldsymbol{u}_G}^T \hat{\boldsymbol{F}}_G + \overline{\delta \boldsymbol{\psi}_G}^T \hat{\boldsymbol{M}}_G - \overline{\delta \boldsymbol{F}_G}^T \hat{\boldsymbol{u}}_G - \overline{\delta \boldsymbol{M}_G}^T \hat{\boldsymbol{\theta}}_G \right) \Big|_0^L
\end{aligned}
\tag{6.5}
$$

In Eq. (6.5), $\boldsymbol{u}_G$, $\boldsymbol{\theta}_G$, $\boldsymbol{F}_B$, $\boldsymbol{M}_B$ are considered to be the fundamental unknown variables. $\boldsymbol{F}_{AL}^B$ is the applied forces (see Eq. 6.1) calculated using MALTAB program.

6.3.2. Modal Analysis

For the modal analysis, also known as eigenfrequency analysis, the type of study in COMSOL is set to *Eigenfrequency*. The mathematic equations involved in the modal analysis are briefly summarised in Appendix C.

6.3.3. Time-dependent Analysis

For the time-dependent analysis, the type of study in COMSOL is set to *Time Dependent*. The generalized-alpha method [137], which is an implicit and second-order accurate method with a parameter alpha to control the numerical time step, is used for time-stepping scheme. In generalized-alpha method, the time step can be set manually, which provides the flexibility for controlling the convergence and computational time.

The computational scheme of the nonlinear aeroelastic model for time-dependent analysis can be divided into the following major steps:

1. Read input file. The main input parameters of the model are 1) the blade structural properties, such as flapwise stiffness and mass per unit length; and 2) the blade aerodynamic data, such as airfoil aerodynamic data, chord and twist angle distributions. These parameters are stored in a .txt file which can be read by MATLAB function.
2. Construct blade geometry using a series of 1D elements. The blade is represented as a series of 1D elements and each element is allowed to have different cross-sectional properties, such as flapwise stiffness and mass per unit length [32].
3. Initialise the dependent variables, such as $\boldsymbol{u}_G$ and $\boldsymbol{\theta}_G$, and global variables, such as time.
4. Perform blade load modelling using MATLAB function to calculate the applied loads, including aerodynamic loads (based on combining the BEM model with the BL dynamic stall model), gravity loads and centrifugal loads.
5. Apply the loads on the blade and perform blade structural modelling based on the mixed-form formulation of GEBT to calculate the deflections of the blade.
6. Go back to step 4 to update the applied loads according to the feedback of blade deflections and global variables.

7. If the current simulation time is less than total simulation time, repeat steps 5-6 using current solution as the initial values for the subsequent steps; otherwise, end the simulation and output results.

The flowchart of the nonlinear aeroelastic model for time-dependent analysis is shown in Fig. 6.2.

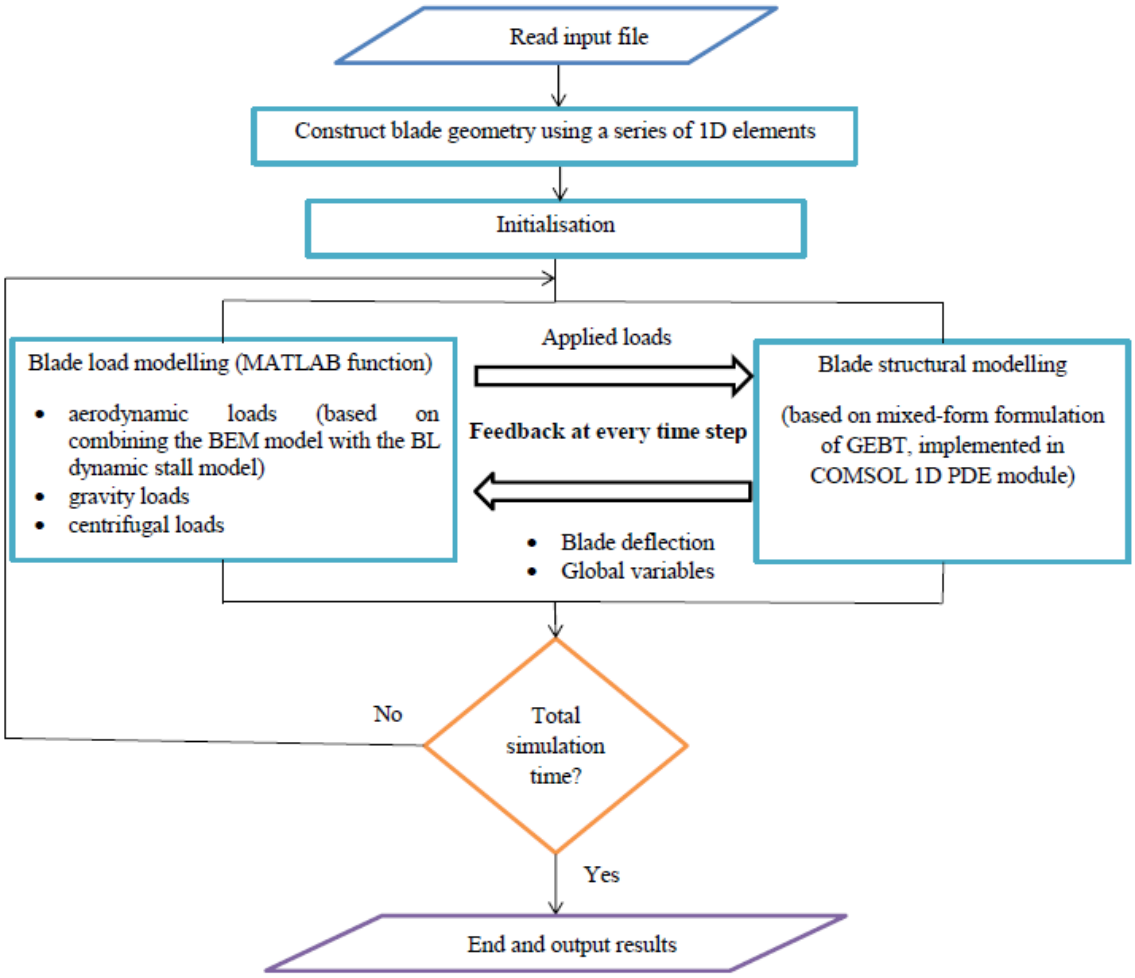

Figure 6.2. Flowchart of the nonlinear aeroelastic model for time-dependent analysis

6.3.4. Stability Analysis

The main objective of stability analysis of wind turbine blades is to check the aeroelastic stability of the blade by examining the damping ratio of the blade. The damping ratio is a sum of structural damping ratio and aerodynamic damping ratio. The stability analysis in this thesis is based on the direct eigenanalysis approach. This approach is useful for modal-interaction dominated instabilities. It is efficient and capable of accurately capturing all participant modes. Fig. 6.3 illustrates the flowchart

of the stability analysis based on the direct eigenanalysis approach. Based on the flowchart, a stability analysis module is developed using MATLAB.

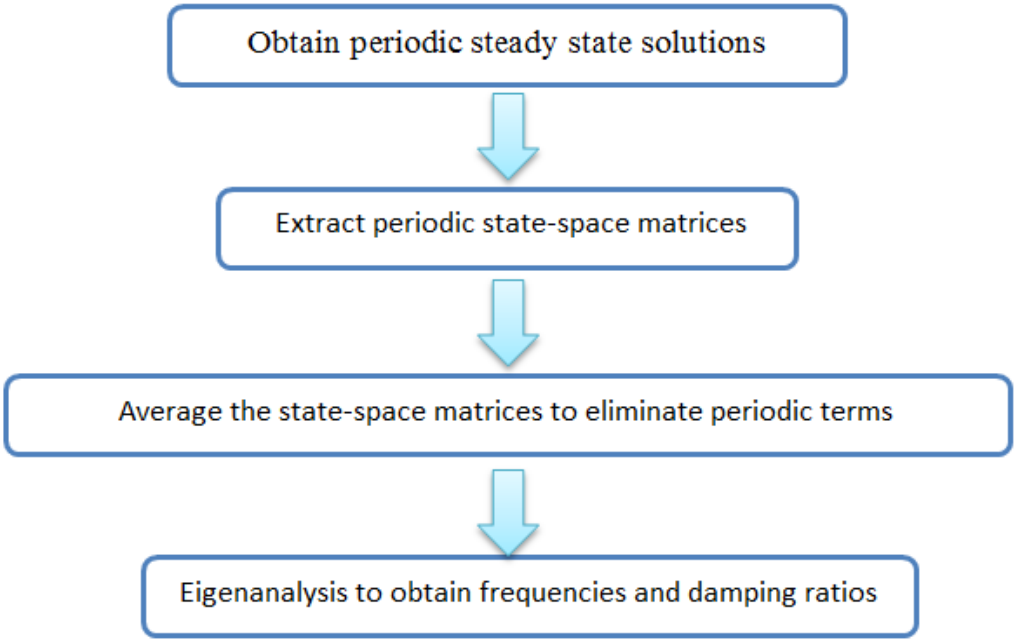

Figure 6.3. Flowchart of stability analysis based on direct eigenanalysis approach

Each step of the flowchart in Fig. 6.3 is detailed below.

6.3.4.1. Obtain Periodic Steady-state Solutions

The first step is to determine a linearisation point, also known as an equilibrium point, to linearise the nonlinear aeroelastic model. For a time-dependent nonlinear system, the steady-state solution is generally chosen as the linearisation point. For a rotating wind turbine blade, this linearisation point is periodic, i.e. the steady-state solutions depend on the rotor azimuth position. This periodicity is driven by applied loads (the sum of aerodynamic loads, gravity loads and centrifugal loads), which depend on the rotor azimuth position. In COMSOL, the periodic steady-state solutions can be obtained through performing a series of steady-state analysis by changing rotor azimuth position.

6.3.4.2. Extract Periodic State-space Matrices

Once a periodic steady-state solution has been obtained, the solution is then chosen as a linearisation position to extract the system matrices, including the mass matrix $\boldsymbol{M}$, the damping matrix $\boldsymbol{C}$, the stiffness matrix $\boldsymbol{K}$ and the load matrix $\boldsymbol{F}$. These system

matrices can be used to find the state-space representation of the nonlinear aeroelastic model. The state-space modelling is briefly summarised below.

The general second-order system equations are in the following form:

$$\boldsymbol{M}\ddot{\boldsymbol{x}} + \boldsymbol{C}\dot{\boldsymbol{x}} + \boldsymbol{K}\boldsymbol{x} = \boldsymbol{F} \tag{6.6}$$

where $\boldsymbol{x}$ is a vector containing dependent variables. For a wind turbine blade, $\boldsymbol{x}$ is also known as degrees of freedom (DOFs) vector. For instance, if a blade is discretised into a series of blade elements connected by nodes, the length of vector $\boldsymbol{x}$ at each node is six, i.e. three translation DOFs and three rotation DOFs.

In order to derive the state space equations, the following equation is introduced:

$$\boldsymbol{M}\dot{\boldsymbol{x}} - \boldsymbol{M}\dot{\boldsymbol{x}} = 0 \tag{6.7}$$

Combining Eqs. (6.6) and (6.7) in one equation yields:

$$\boldsymbol{A}\dot{\boldsymbol{z}} + \boldsymbol{B}\boldsymbol{z} = \boldsymbol{E} \tag{6.8}$$

where $\boldsymbol{z}$ is the state-space vector. $\boldsymbol{A}$, $\boldsymbol{B}$, $\boldsymbol{E}$ and $\boldsymbol{z}$ in Eq. (6.8) are respectively given by:

$$\boldsymbol{A} = \begin{bmatrix} \boldsymbol{C} & \boldsymbol{M} \\ \boldsymbol{M} & 0 \end{bmatrix} \tag{6.9}$$

$$\boldsymbol{B} = \begin{bmatrix} \boldsymbol{K} & 0 \\ 0 & -\boldsymbol{M} \end{bmatrix} \tag{6.10}$$

$$\boldsymbol{E} = \begin{bmatrix} \boldsymbol{F} \\ 0 \end{bmatrix} \tag{6.11}$$

$$\boldsymbol{z} = \begin{bmatrix} \boldsymbol{x} \\ \dot{\boldsymbol{x}} \end{bmatrix} \tag{6.12}$$

Eq. (6.8) can be rewritten as a standard form of the state-space:

$$\dot{\boldsymbol{z}} = \boldsymbol{A}_{sys}\boldsymbol{z} + \boldsymbol{B}_{sys}\boldsymbol{u} \tag{6.13}$$

where $\boldsymbol{A}_{sys}$ is the state-space matrix of the system, $\boldsymbol{B}_{sys}$ is the input matrix of the system, $\boldsymbol{u}$ is the input vector. $\boldsymbol{A}_{sys}$ and $\boldsymbol{B}_{sys}$ in Eq. (6.13) are respectively given by:

$$\boldsymbol{A}_{sys} = \begin{bmatrix} 0 & \boldsymbol{I} \\ -\boldsymbol{M}^{-1}\boldsymbol{K} & -\boldsymbol{M}^{-1}\boldsymbol{C} \end{bmatrix} \tag{6.14}$$

$$\boldsymbol{B}_{sys} = \begin{bmatrix} 0 \\ \boldsymbol{M}^{-1}\boldsymbol{F} \end{bmatrix} \tag{6.15}$$

In summary, having obtained the mass matrix $\boldsymbol{M}$, the damping matrix $\boldsymbol{C}$, the stiffness matrix $\boldsymbol{K}$ and the load matrix $\boldsymbol{F}$, the state-space matrix $\boldsymbol{A}_{sys}$ and the input matrix $\boldsymbol{B}_{sys}$ can be respectively calculated using Eqs. (6.14) and (6.15).

6.3.4.3. Average the State-space Matrices to Eliminate Periodic Terms

Due to the rotation of wind turbine blades, the steady-state solutions are periodic, resulting in periodic state-space matrices. A direct eigenanalysis on the periodic state-space matrices yields periodic eigenvalues, which are physically meaningless. In order to eliminate the periodic terms, it is necessary to average the state-space matrices obtained at different rotor azimuth positions. The averaged state-space matrix $\boldsymbol{A}_{sys}^{avg}$ can be obtained using the following equation:

$$\boldsymbol{A}_{sys}^{avg} = \frac{\sum_{i=1}^{N_A} \boldsymbol{A}_{sys,i}}{N_A} \tag{6.16}$$

where $\boldsymbol{A}_{sys,i}$ is the static-space matrix obtained at ith azimuth position, N_A is the total number of azimuth positions.

6.3.4.4. Eigenanalysis to Obtain Frequencies and Damping Ratios

In this step, eigenanalysis on averaged state-space matrix $\boldsymbol{A}_{sys}^{avg}$ is performed, yielding N pairs of eigenvalues and N eigenvectors, where N is the total number of degrees of freedom. Each pair of eigenvalues $\lambda_{1,2}$ is generally in the following form:

$$\lambda_{1,2} = N_R \pm N_I i \tag{6.17}$$

where N_R is the real part number and N_I is the imaginary part number.

Each pair eigenvalues $\lambda_{1,2}$ can also be written as the following form (see Eq. C.9 in Appendix C):

$$\lambda_{1,2} = -\xi\omega \pm \omega\sqrt{\xi^2 - 1} \tag{6.18}$$

where ξ is the damping ratio, ω is the un-damped frequency. It should be noted that the steady-state solutions obtained in Section 6.3.4.1 vary with wind speeds because

aerodynamic loads depend on wind speeds. Therefore, eigenvalues $\lambda_{1,2}$, damping ratio ξ and un-damped frequency ω in Eq. (6.18) also change with wind speed.

Through comparing Eqs. (6.17) and (6.18), the un-damped frequency ω and damping ratio ξ can be respectively expressed in terms of N_R and N_I using the following equations:

$$\omega = \sqrt{N_R^2 + N_I^2} \tag{6.19}$$

$$\xi = \frac{N_R}{\sqrt{N_R^2 + N_I^2}} \tag{6.20}$$

Having obtained the un-damped frequency ω and the damping ratio ξ , the damped frequency ω_D is calculated by:

$$\omega_D = \omega\sqrt{1-\xi^2} \tag{6.21}$$

It should be noted that damped frequency ω_D in Eq. (6.21) also varies with wind speed because both un-damped frequency ω and the damping ratio ξ change with wind speed.

The unit of both un-damped frequency ω and damped frequency ω_D is rad/s and can be transformed to Hz using the following equations:

$$f_{Hz} = \frac{\omega}{2\pi} \tag{6.22}$$

$$f_{D,Hz} = \frac{\omega_D}{2\pi} \tag{6.23}$$

where f_{Hz} and $f_{D,Hz}$ are the un-damped and damped frequencies in Hz, respectively.

The eigenvectors provide the corresponding mode shapes, which are essential information to identify stability modes.

6.4. Summary

In this chapter, the implementation of the nonlinear aeroelastic model using COMSOL Multiphysics was presented. A blade load modelling module was developed using

MATLAB based on the methods presented in Chapter 5. The blade load modelling module takes account of aerodynamic loads, gravity loads and centrifugal loads. Based on the mixed-form formulation of GEBT presented in Chapter 4, a blade structural modelling module was established using COMSOL 1D Weak Form PDE module. The strategy used for coupling the blade load modelling module and blade structural modelling module to yield a nonlinear aeroelastic model was presented. The implemented nonlinear aeroelastic model can be used for four types of studies, i.e. static analysis, modal analysis, time-dependent analysis and stability analysis. The strategy used for each type of study was discussed.

Chapter 7 presents the validation of the nonlinear aeroelastic model by a series of benchmark calculation tests.

CHAPTER 7 VALIDATION OF THE NONLINEAR AEROELASTIC MODEL

7.1. Introduction

A nonlinear aeroelastic model, called NAM_WTB (Nonlinear Aeroelastic Model for Wind Turbine Blades), is developed based on the strategy presented in Chapter 6. In order to validate the NAM_WTB, a series of benchmark calculation tests are performed, which are presented in this chapter.

The main components of the NAM_WTB, i.e. the aerodynamic part and the structural part, are validated first, followed by a case study to validate the aeroelastic simulation results.

Section 7.2 presents the validation of the aerodynamic part of the NAM_WTB. The components of the aerodynamic part of NAM_WTB, i.e. the BEM model and the BL dynamic stall model, are validated separately through two case studies. In the first case study, the BEM model in NAM_WTB is validated against WT_Perf [138], which is an existing widely used BEM-based aerodynamic code. A wind turbine blade with rotor radius of 13.757m is chosen as an example. In this case study, the dynamic stall effects are ignored. In the second case study, the BL dynamic stall model in NAM_WTB is validated against experimental 2D unsteady aerodynamic data. S809 and S814 airfoils, which are two widely used wind turbine dedicated airfoils, are chosen as examples.

Section 7.3 presents the validation of the structural part of the NAM_WTB. Two case studies have been performed for the validation. In the first case study, an experimentally large-deflection cantilever beam is chosen as an example. The static tip deflections of the cantilever beam calculated using the structural part of the NAM_WTB are compared with experimental results obtained in the laboratory. The COMSOL Euler-Bernoulli beam model, which is a widely used linear beam model, is also used in this case study for comparison purpose. In the second case study, a practical wind turbine blade is chosen. The natural frequencies calculated using the structural part of the NAM_WTB are validated against measured values.

Section 7.4 presents the validation of the aeroelastic simulation results of the NAM_WTB against FAST [26], which is an existing well-known aeroelastic code. A 10m-diameter rotor R&D wind turbine is chosen as the case study. In this case study, in addition to aerodynamic loads, the gravity loads and centrifugal loads are also taken into account, and the blade is considered flexible. Moreover, dynamic stall effects are taken into account.

Finally, a chapter summary is presented in Section 7.5.

7.2. Validation of the Aerodynamic Part of NAM_WTB

The aerodynamic part of the NAM_WTB comprises two components, i.e. the BEM model and the BL dynamic stall model. The two components of the aerodynamic part of the NAM_WTB are validated separately through two case studies. In the first case study, the BEM model of the NAM_WTB is validated against WT_Perf [138], which is an existing widely used BEM-based aerodynamic code. A wind turbine blade with rotor radius of 13.757m, which is a representative of medium-size wind turbine blades, is chosen in the case study. In this case study, the dynamic stall effects are ignored. In the second case study, the BL dynamic stall model of the NAM_WTB is validated against experimental 2D unsteady aerodynamic data, and S809 and S814 airfoils, which are widely used wind turbine dedicated airfoils, are chosen in the case study.

7.2.1. BEM Model Validation

In this case study, the BEM model in the NAM_WTB is validated against WT_Perf [138], which is a wind turbine aerodynamic performance predictor developed by Andrew Platt at National Renewable Energy Laboratory (NREL) based on BEM. The wind turbine model used in this case study is the AWT-27CR2 wind turbine, which is a two-bladed research wind turbine, and the main parameters of the wind turbine are summarised in Table 7.1.

Table 7.1. Main parameters of the AWT-27CR2 wind turbine

Parameters	Values
Rated power (kW)	300
Number of blades	2
Rotor radius (m)	13.757
Rated rotor speed (rpm)	53.333
Cone angle (deg.)	7
Tilt angle (deg.)	0

The chord and twist angle distributions of the AWT-27CR2 wind turbine blade are depicted in Fig.7.1. The corresponding numerical values can be found in Appendix D. The details of the AWT-27CR2 wind turbine, such as its airfoil aerodynamic data, can be found from the test file of WT_Perf [138].

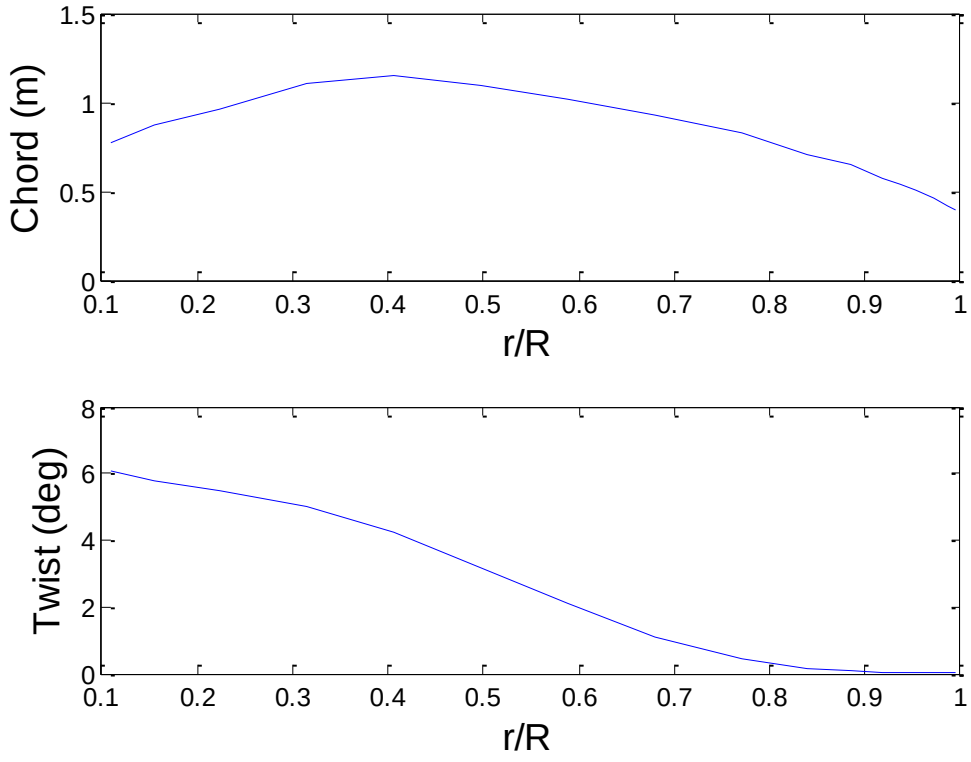

Figure 7.1. Chord and twist angle distributions of the AWT-27CR2 wind turbine blade

Both NAM_WTB and WT_Perf are used to predict the aerodynamic performance of the AWT-27CR2 wind turbine. In this case, both yaw angle and pitch angle are $0°$, and the rotor speed is at rated value (53.333rpm). For the sake of simplicity, the gravity loads and centrifugal loads of the blade are ignored, and the blade is assumed rigid, i.e. no deflections are considered in the calculation of the aerodynamic performance.

Additionally, dynamic stall effects are ignored in this case study. Figs. 7.2, 7.3 and 7.4 respectively show the comparisons of the axial induction factor, angular induction factor and normal force distributions along the wind turbine blade at free stream wind speed of 15m/s.

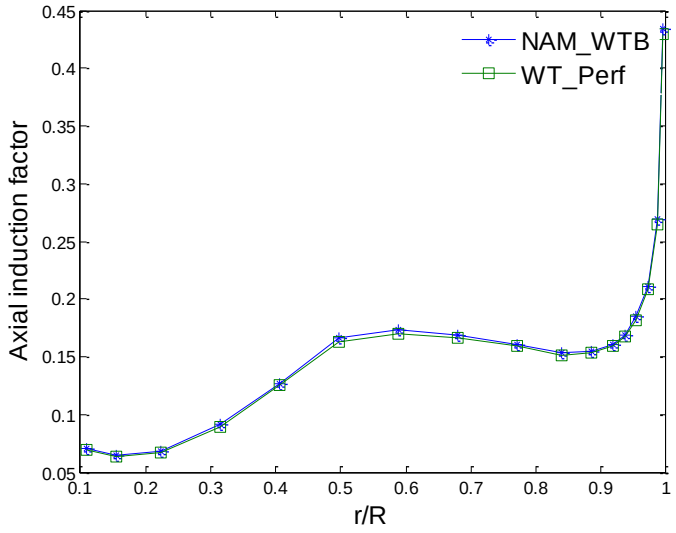

Figure 7.2. Calculated axial induction factor distribution at wind speed of 15m/s

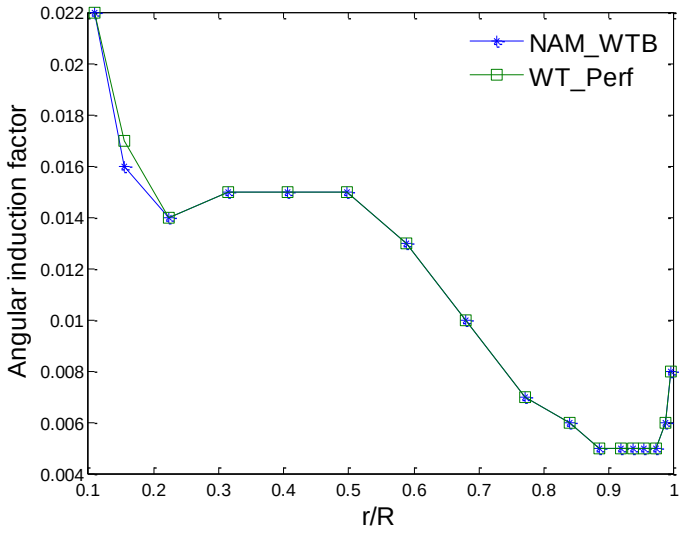

Figure 7.3. Calculated angular induction factor distribution at wind speed of 15m/s

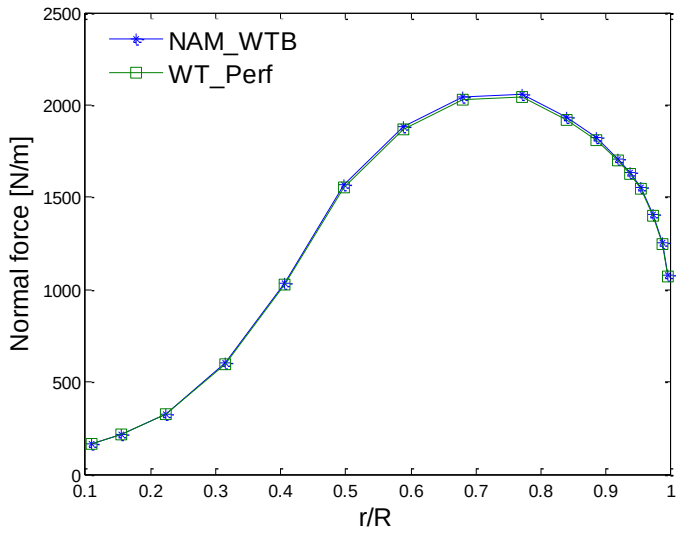

Figure 7.4. Calculated normal force distribution at wind speed of 15m/s

The results in Figs. 7.2, 7.3 and 7.4 demonstrate that the calculated axial induction factor, angular induction factor and normal force distributions along the wind turbine blade from NAM_WTB agree with those from WT_Perf very well. This means that the BEM model in the NAM_WTB can be utilized for aerodynamic loads predictions of wind turbine blades.

7.2.2. Dynamic Stall Model Validation

In this case study, the BL dynamic stall model, a component of the aerodynamic part of the NAM_WTB, is validated against experimental 2D unsteady aerodynamic data. The examples used in this case study are the S809 and S814 airfoils, which are widely used wind turbine dedicated airfoils. The geometries of S809 and S814 airfoils are depicted in Fig. 7.5.

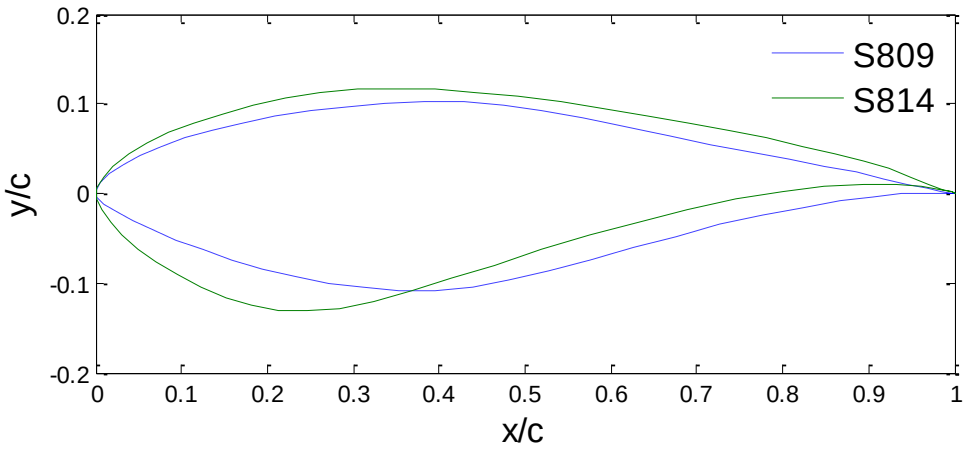

Figure 7.5. Geometries of S809 and S814 airfoils

The aerodynamic measurements of S809 and S814 airfoils, such as measured lift and drag coefficients, are available from the Ohio State University (OSU) database [139]. In this case study, the Reynolds number is set to 1E6, and the angle of attack α varies sinusoidally with an oscillation frequency 1.2Hz and 10° amplitude around 14° mean AOA[3].

The BL dynamic stall model in the NAM_WTB is used to predict the instantaneous unsteady normal force coefficient C_N of the S809 and S814 airfoils. In this case, the airfoil oscillates in torsional mode only, and both flapping motion and bending-torsion coupling motion are ignored. The comparison between the predicted unsteady values, static measurements and unsteady measurements for the S809 and S814 airfoils are shown in Figs. 7.6 and 7.7, respectively.

[3] In the OSU unsteady aerodynamic database, the angle of attack (AOA) amplitude is 5° or 10°, and the mean AOA is 8°, 14° or 20°.

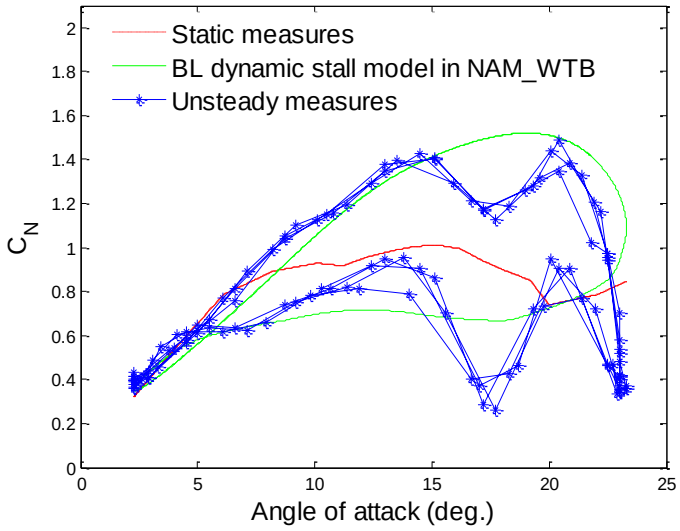

Figure 7.6. Normal force coefficient of S809 airfoil

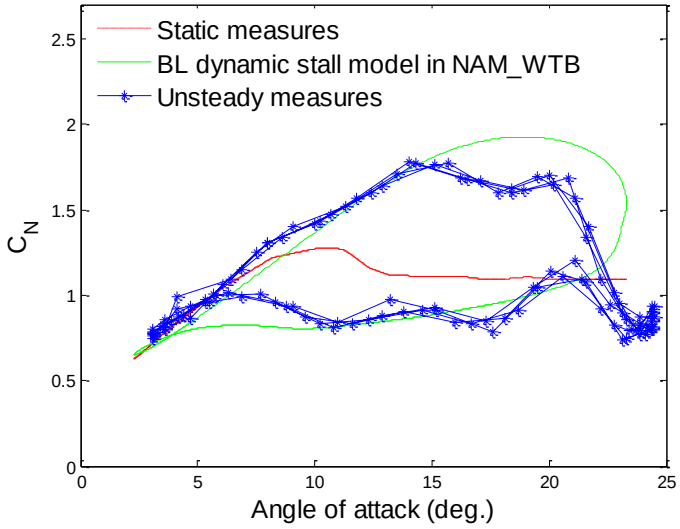

Figure 7.7. Normal force coefficient of S814 airfoil

From Figs. 7.6 and 7.7 we can see that 1) the static measurements show significant difference from the unsteady measurements; 2) the results from the BL dynamic stall model in the NAM_WTB show reasonable agreement with the unsteady measurements.

It can also be noticed that there are two values of C_N at each angle of attack for dynamic stall case, and the higher value of C_N occurs when angle of attack is increasing. This is a consequence of the dynamic stall phenomenon. As it can be seen from Figs. 7.6 and 7.7, starting from the point of minimum angle of attack, the unsteady C_N follows the static C_N until the static C_N reduces due to increasing trailing edge separation (i.e. the static stall). The unsteady C_N, however, continues increasing almost

linearly until a breakdown, occurring when the leading edge vortex has travelled past the airfoil trailing edge. At the breakdown point, massive flow are separated and the unsteady C_N drops to levels far below the typical values of the static C_N curve. There is a time delay to recover more regular behavior, and the unsteady C_N remains below the static C_N for most of the remaining cycle.

This case study demonstrates that the BL dynamic stall model in the NAM_WTB can be utilized for predicting unsteady airfoil aerodynamic coefficients.

7.3. Validation of the Structural Part of NAM_WTB

In order to validate the structural part of the NAM_WTB, two case studies have been performed. The first case study compares both the structural part of the NAM_WTB and the COMSOL Euler-Bernoulli beam model with experimental results obtained in laboratory. In this case study, the static deflections of an experimentally large-deflection cantilever beam are investigated, and the details of the experiment are presented. In the second case study, the modal analysis results from structural part of the NAM_WTB are validated against the experimental data, and a practical wind turbine blade is chosen as an example.

7.3.1. Static Deflection of Large-deflection Beam

This case study aims to verify the accuracy of the structural part of the NAM_WTB and demonstrate its nonlinear capability by comparing both the structural part of the NAM_WTB and the COMSOL Euler-Bernoulli beam model with experimental results obtained in the laboratory. The example used here is an experimentally large-deflection cantilever beam. Fig. 7.8 depicts the photograph of the experimental system, which is made up of a steel beam, fixed at one end and loaded at the free end. A vertical ruler is used to measure the vertical deflection of the beam at the free end. The length of the beam is 0.48m and it has a uniform rectangular cross-section of width 0.02m and height 0.0012m.

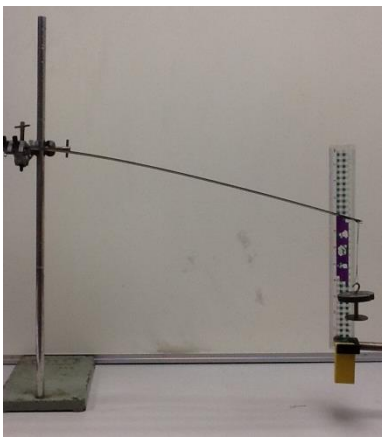

Figure 7.8. Experimentally cantilever beam

Both the NAM_WTB and COMSOL Euler-Bernoulli beam model are used to numerically calculate the tip deflection of the cantilever beam. The value of Young's modulus used in the numerical calculation is 2.0E11Pa (typical value of Young's modulus for steel). The weight of the beam, 0.87N, is taken into account in the numerical calculation by applying a uniform distribution load over its entire length with the value of 1.81N/m. Six values of tip load, i.e. 0, 1.176, 2.156, 3.136, 4.116 and 5.096N, are used for both experimental test and numerical calculation. The comparison between the predicted vertical tip deflection and measured values are shown in Fig. 7.9 and Table 7.2, where relative differences are obtained with respect to the measured values.

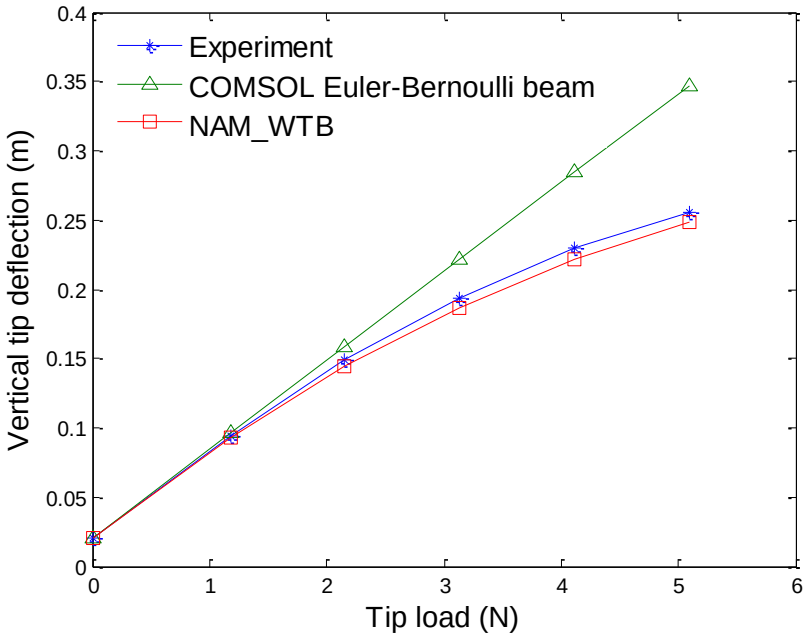

Figure 7.9. Tip deflection of the cantilever beam

Table 7.2. Tip deflection of the cantilever beam

Tip load (N)	Vertical tip deflection (m)			%Diff. (COMSOL Euler-Bernoulli beam)	%Diff (NAM_WTB)
	Experiment	COMSOL Euler-Bernoulli beam	NAM_WTB		
0	0.0200	0.0206	0.0205	3.00	2.50
1.176	0.0940	0.0961	0.0926	2.23	1.49
2.156	0.1490	0.1588	0.1444	6.58	3.09
3.136	0.1930	0.2216	0.1870	14.82	3.11
4.116	0.2300	0.2843	0.2213	23.61	3.78
5.096	0.2550	0.3470	0.2486	36.08	2.51

From Fig. 7.9 and Table 7.2 we can see that 1) the tip deflections calculated using COMSOL Euler-Bernoulli beam model increase linearly and do not coincide with experimental data for the cases when the tip loads are over 3.136N, with maximum percentage difference of 36.08% occurring when the tip load is 5.096N; 2) the tip deflections predicted using the NAM_WTB increases nonlinearly and show good agreement with experimental data for all cases, with the maximum percentage difference 3.78% occurring when the tip load is 4.116N; 3) the COMSOL Euler-Bernoulli beam model overestimates tip deflections when large deflections occur because it fails to capture geometric nonlinearities.

This case study clearly demonstrates that 1) the NAW_WTB is capable of handling geometric nonlinearities arising from large deflections; 2) when the deflection is small, the error introduced by linear assumptions, e.g. the assumption adopted in the COMSOL Euler-Bernoulli beam model, can be ignored; however, when large deflection occurs, the error introduced by linear assumptions should be quantified.

7.3.2. Modal Analysis of Truncated RB70 Blade

This case study aims to validate the modal analysis results from the structural part of the NAM_WTB against experimental data. The example used here is the truncated RB70 wind turbine blade [140], which has been subjected to the eigenmode validation within

the STABTOOL-3 research project [141]. The chord and twist angle distributions of the truncated RB70 wind turbine blade are depicted in Fig. 7.10.

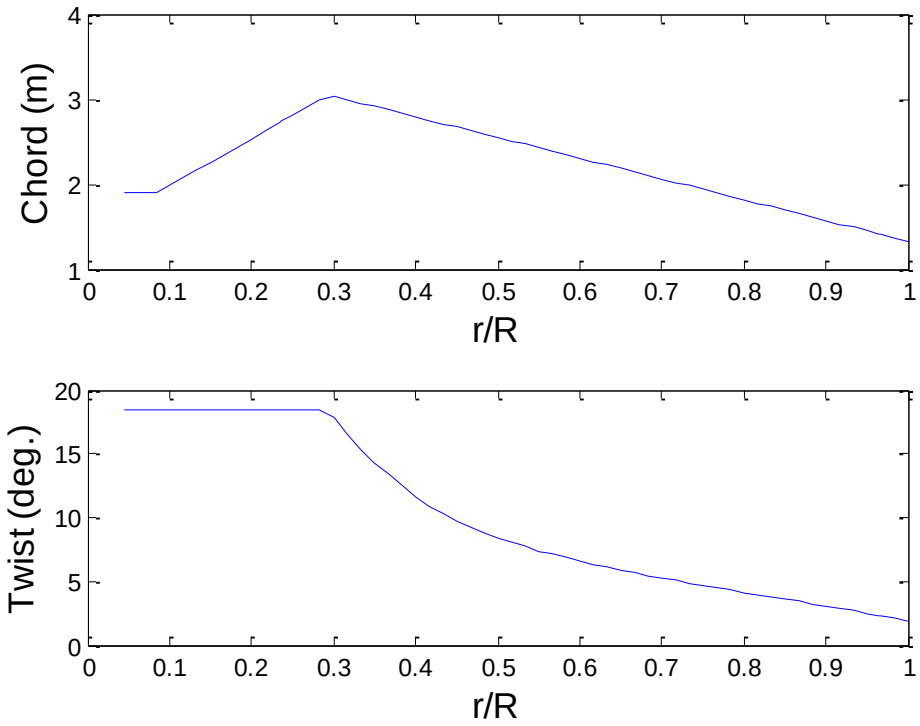

Figure 7.10. Chord and twist angle distributions of the truncated RB70 wind turbine blade

The distributions of bending stiffness and mass per unit length of the truncated RB70 wind turbine blade are respectively shown in Figs. 7.11 and 7.12, and its details can be found in Ref. [140].

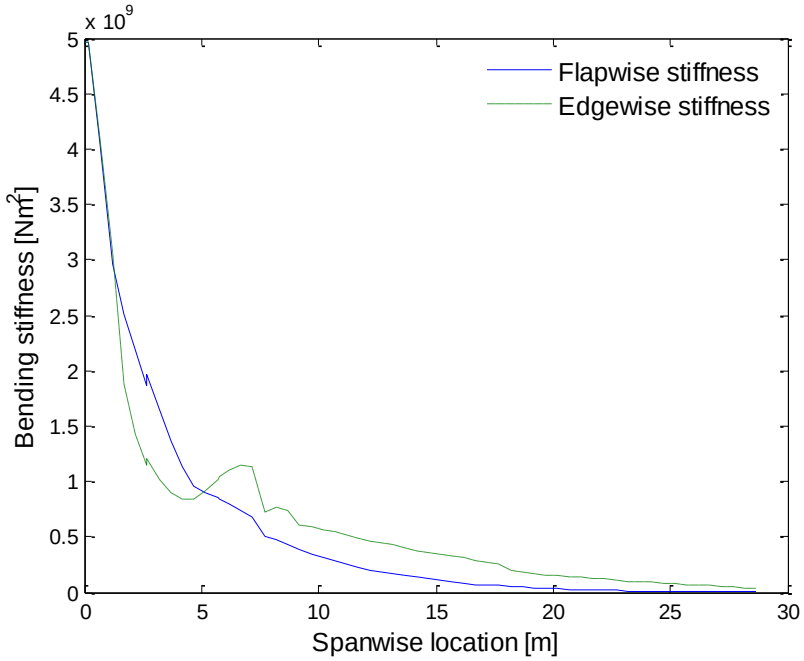

Figure 7.11. Bending stiffness distribution of the truncated RB70 wind turbine blade

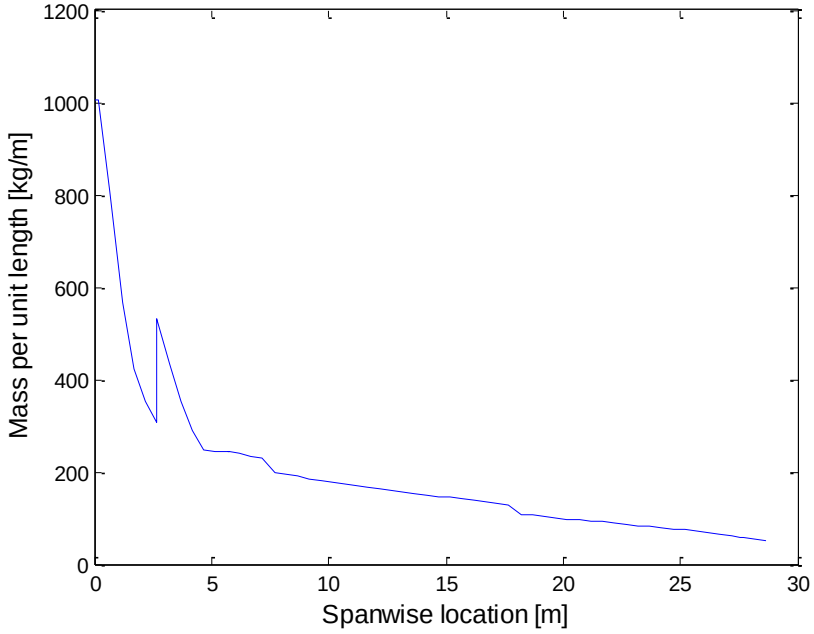

Figure 7.12. Mass per unit length distribution of the truncated RB70 wind turbine blade

NAM_WTB is used to perform modal analysis of the truncated RB70 blade. The fundamental mathematic equations involved in the modal analysis can be found in Appendix C. In this case study, the blade is non-rotating and free-vibration (no loads on the blade). The predicted values are compared with measured values reported in Ref.

[142] as shown in Fig. 7.13 and Table 7.3, where the relative differences are observed with respect to the measured values.

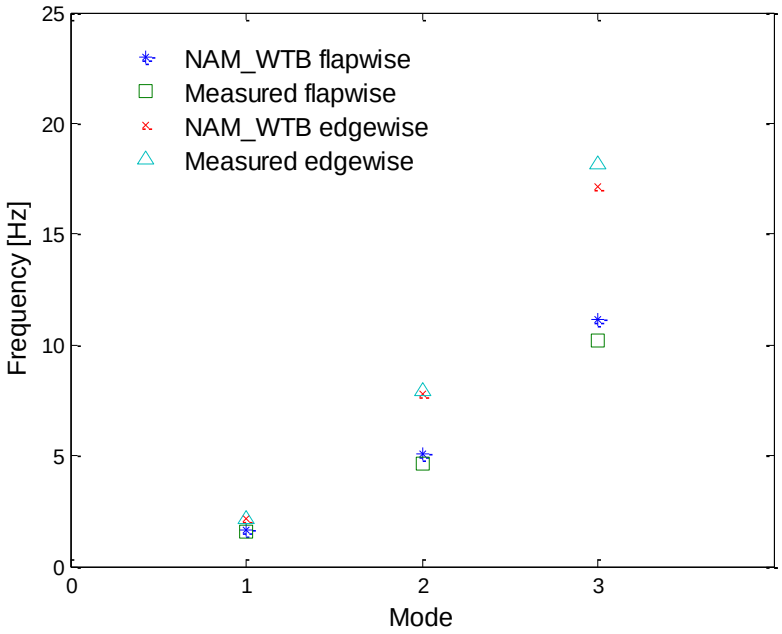

Figure 7.13. Flapwise and edgewise mode frequencies of the truncated RB70 wind turbine blade

Table 7.3. Flapwise and edgewise mode frequencies of the truncated RB70 wind turbine blade

Mode frequencies	Measured values [142]	NAM_WTB	Diff. (%)
1st flapwise (Hz)	1.582	1.637	3.48
2nd flapwise (Hz)	4.630	5.061	9.31
3rd flapwise (Hz)	10.199	11.152	9.34
1st edgewise (Hz)	2.174	2.173	0.05
2nd edgewise (Hz)	7.962	7.772	2.39
3rd edgewise (Hz)	18.138	17.133	5.54

As can be seen from Fig. 7.13 and Table 7.3, the flapwise and edgewise blade mode frequencies calculated from the NAM_WTB match well with the experimental data, with the maximum percentage difference (9.34%) occurring for the 3rd flapwise mode.

This case study not only further validates the structural part of the NAM_WTB, but also demonstrates that representing wind turbine blades as a series of 1D beam elements provides reasonable accuracy if the beam model is constructed properly.

7.4. Validation of Aeroelastic Simulation Results of NAM_WTB

This case study aims to validate the NAM_WTB against FAST [26], which is a widely used linear aeroelastic code developed by NREL based on combining BEM with modal approach. The wind turbine model used in this case study is NREL Phase VI wind turbine [143], which is a 10m-diameter rotor research wind turbine. The main parameters of the turbine are listed in Table 7.4.

Table 7.4. Main parameters of the NREL Phase VI wind turbine

Parameters	Values
Rated power (kW)	20
Number of blades	2
Rotor radius (m)	5.029
Rotor speed (rpm)	71.9
Cone angle (deg.)	0
Tilt angle (deg.)	0

The chord and twist angle distributions of NREL Phase VI wind turbine blade are depicted in Fig. 7.14, and its details can be found in Ref. [143] and Appendix E.

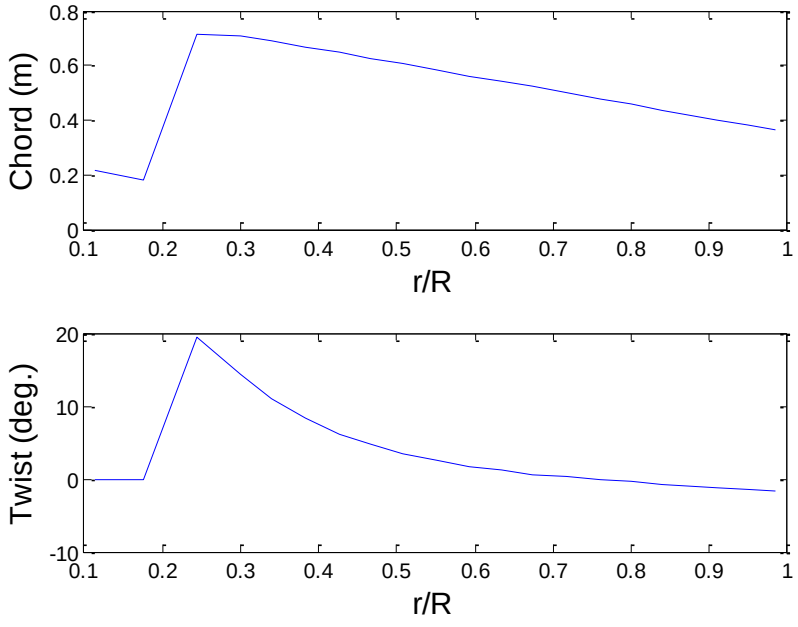

Figure 7.14. Chord and twist angle distributions of the NREL Phase VI wind turbine blade

Both NAM_WTB and FAST are used to perform aeroelastic modelling of NREL Phase VI rotor. In this case, yaw angle, pitch angle and rotor speed are $0°$, $4.815°$ and 71.9rpm, respectively. The gravity loads and centrifugal loads are taken into account, and the blade is considered flexible. Additionally, dynamic stall effects are considered. The calculated blade root load and blade tip deflection at free stream wind speed of 10m/s are shown in Figs. 7.15 and 7.16 respectively.

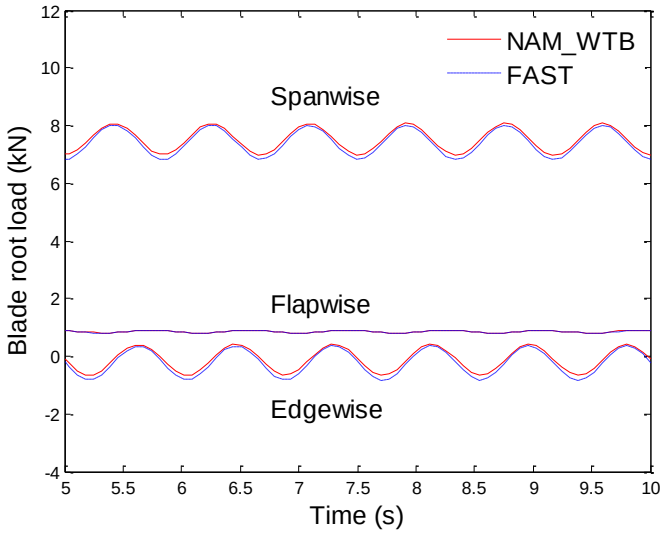

Figure 7.15. Calculated blade root load at wind speed 10m/s

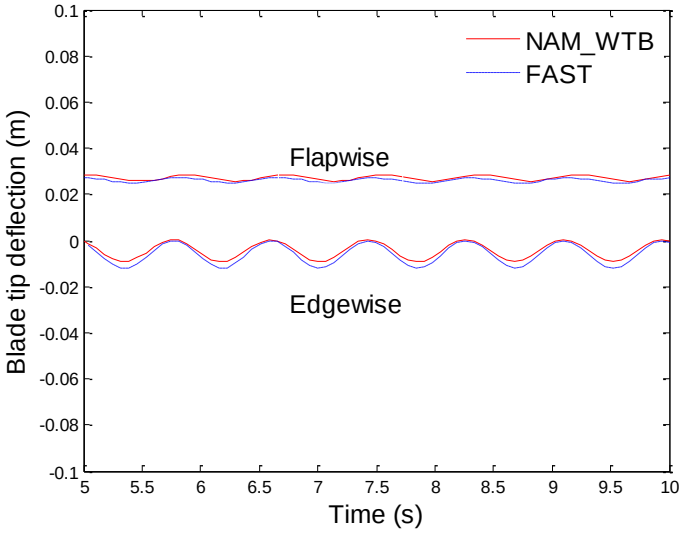

Figure 7.16. Calculated blade tip deflection at wind speed 10m/s

Figs. 7.15 and 7.16 demonstrate that the results from NAM_WTB show good agreement with those from FAST for this case study. Fig. 7.16 also indicates that the tip deflection of the blade used in this case study is very small due to the quite stiff blade design of the NREL Phase VI wind turbine. This case study demonstrates that both NAM_WTB and FAST work well for small deflections.

7.5. Summary

In this chapter, the nonlinear aeroelastic model NAM_WTB was validated by a series of benchmark calculation tests. The key components of the NAM_WTB, i.e. the aerodynamic part (based on combining the BEM model and the BL dynamic stall model) and the structural part (based on a mixed-form formulation of GEBT) were validated separately. Then a case study was performed to validate the aeroelastic simulation results.

Close agreement with existing widely used BEM-based aerodynamic code WT_perf confirms the validity of the BEM model in the NAM_WTB for aerodynamic load prediction for wind turbine blades. Additionally, the predicted unsteady aerodynamic coefficients from the BL dynamic stall model in the NAM_WTB showed good agreement with experimental data. This further confirms the capability of the aerodynamic part of the NAM_WTB for unsteady aerodynamic load calculation.

Close agreement with experimental data for large beam deflections demonstrates the capability of the structural part of NAM_WTB to handle geometric nonlinearities when compared with COMSOL Euler-Bernoulli beam model. Moreover, close agreement with experimental data for the modal analysis of a practical wind turbine blade further validates the structural part of the NAM_WTB. It also demonstrates that representing the blades as a series of 1D beam elements provides reasonable accuracy if the beam model is constructed properly.

The aeroelastic simulation results of NAM_WTB were validated against the well-known aeroelastic code FAST. In this case study, the blade deflections are very small, and the results of NAM_WTB are consistent with the results of linear aeroelastic code FAST, which indicates geometric nonlinearities can be ignored for small blade deflections.

Chapter 8 presents the application of NAM_WTB, including the aeroelastic simulation of a parked wind turbine blade and the stability analysis of the blade.

CHAPTER 8 APPLICATION OF THE NONLINEAR AEROELASTIC MODEL

8.1. Introduction

In Chapter 7, NAM_WTB (Nonlinear Aeroelastic Model for Wind Turbine Blades) has been validated through a series of case studies. This chapter presents the application of NAM_WTB on aeroelastic modelling of large wind turbine blades.

The wind turbine model used in this chapter is the WindPACT 1.5MW wind turbine [144], which is a reference wind turbine created by NREL. NAM_WTB is applied to simulate the parked WindPACT 1.5MW wind turbine blade and to perform stability analysis of the blade.

This chapter is structured as follows. Section 8.2 introduces the WindPACT 1.5MW wind turbine. Section 8.3 presents the application of NAM_WTB on the aeroelastic simulation of the parked WindPACT 1.5MW wind turbine blade. Section 8.4 presents the application of NAM_WTB on the stability analysis of the WindPACT 1.5MW wind turbine blade, followed by a chapter summary in Section 8.5.

8.2. WindPACT 1.5MW Wind Turbine

WindPACT 1.5MW wind turbine [144] is a reference wind turbine designed by NREL for the Wind Partnership for Advanced Component Technologies (WindPACT) project between years 2000 and 2002. In the WindPACT project, the effects of the main wind turbine components (such as blades and generator) on the cost of energy (COE) have been investigated. The ultimate goal of the WindPACT project is to identify technology improvements to reduce the COE of wind turbines in low-wind-speed sites. The details of WindPACT project can be found in Ref. [145].

WindPACT 1.5MW wind turbine is a three-bladed horizontal-axis wind turbine. Its main parameters are summarised in Table 8.1.

Table 8.1. Main parameters of the WindPACT 1.5MW wind turbine

Parameters	Values
Rated power (MW)	1.5
Number of blades	3
Rotor radius (m)	35
Cone angle (deg.)	0
Tilt angle (deg.)	5

The chord and twist angle distributions of the WindPACT 1.5MW wind turbine blade are shown in Fig. 8.1 and Table 8.2, and its structural properties can be found in Appendix F.

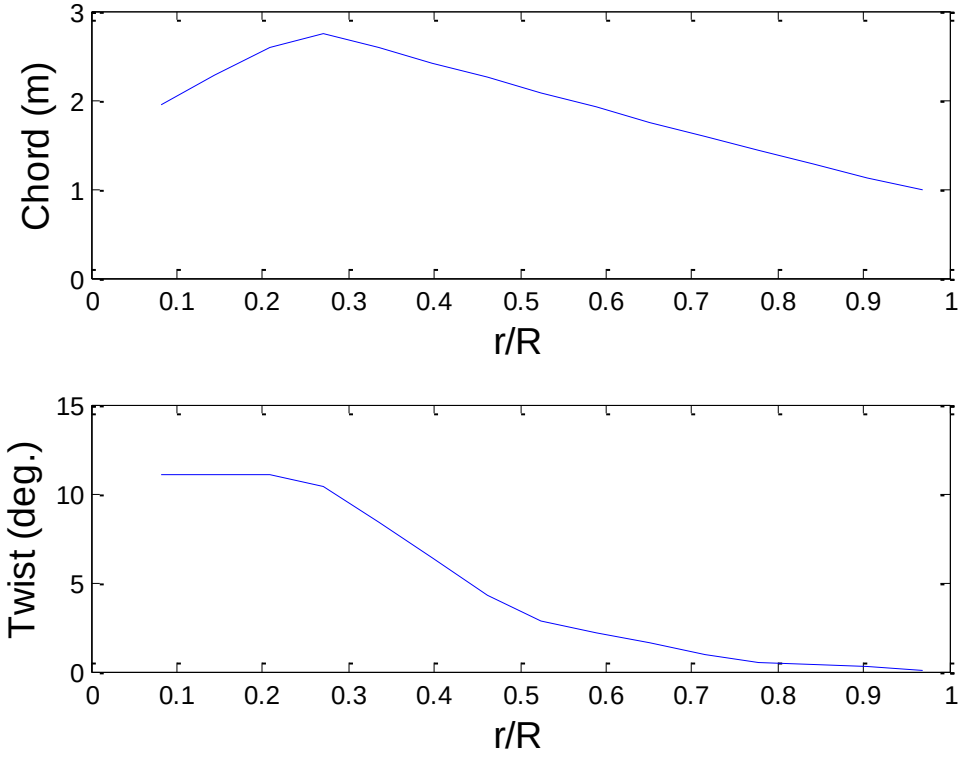

Figure 8.1. Chord and twist angle distributions of WindPACT 1.5MW wind turbine blade

Table 8.2. Chord ant twist angle distributions of the WindPACT 1.5MW wind turbine blade

r (m)	Chord c (m)	Twist angle θ_p (deg.)	Airfoil
2.858	1.949	11.1	cylinder
5.075	2.269	11.1	S818
7.292	2.589	11.1	S818
9.508	2.743	10.41	S818
11.725	2.578	8.38	S818
13.942	2.412	6.35	S818
16.158	2.247	4.33	S818
18.375	2.082	2.85	S825
20.592	1.916	2.22	S825
22.808	1.751	1.58	S825
25.025	1.585	0.95	S825
27.242	1.427	0.53	S825
29.458	1.278	0.38	S825
31.675	1.129	0.23	S826
33.892	0.98	0.08	S826

8.3. Aeroelastic Simulation of Parked WindPACT 1.5MW Wind Turbine Blade

This case study aims to investigate the effects of large blade deflections on the aeroelastic modelling of wind turbine blades. Both NAM_WTB and FAST are used to perform aeroelastic modelling of the parked WindPACT 1.5MW wind turbine blade. In this case study, the rotor rotational speed, yaw angle and blade pitch angle are 0rpm, $0°$ and $2°$, respectively. For the sake of simplicity, the dynamic stall effects are ignored. Additionally, in order to investigate the large deflection effects, the flapwise stiffness of the WindPACT 1.5MW wind turbine blade in this case study is adjusted by a factor of 0.2 to make the blade more flexible.

The calculated flapwise tip deflections at free-stream wind speeds between 15m/s and 50m/s are depicted in Fig. 8.2. For comparison purposes, Fig. 8.2 also presents the results from a linear aeroelastic model, BEM_COMSOL-Euler-Bernoulli-beam, which is based on combining BEM and COMSOL Euler-Bernoulli beam model and is

implemented by replacing the structural part of NAM_WTB with COMSOL Euler-Bernoulli beam model.

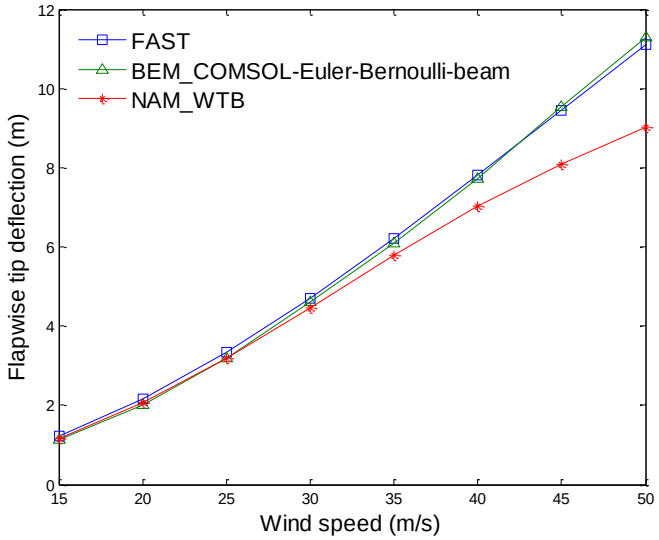

Figure 8.2. Calculated flapwise tip deflection

Fig. 8.2 clearly shows that 1) the results from BEM_COMSOL-Euler-Bernoulli-beam show good agreement with the results from FAST for all cases; 2) for this case study, when wind speed below 30m/s, the results from NAM_WTB show good agreement with the results from FAST; 3) as wind speed further increases, the difference between NAM_WTB and FAST gets larger, with maximum percentage difference 23%, which occurs for the case study when the wind speed achieves 50m/s, and the blade tip deflection predicted by NAM_WTB is less than that predicted by FAST.

It should be noted that the only difference between BEM_COMSOL-Euler-Bernoulli-beam and NAM_WTB is that the former one uses the COMSOL Euler-Bernoulli beam model for the structural part while the latter one uses GEBT. As demonstrated in the previous case study (see Section 7.3.1) of the experimentally large-deflection cantilever beam, COMSOL Euler-Bernoulli beam model overestimates tip deflections when large deflections occur because it fails to capture geometric nonlinearities. Since NAM_WTB uses GEBT for the structural part, the effects of geometric nonlinearities are taken into account. Therefore, NAM_WTB can provide more reliable aeroelastic modelling than linear aeroelastic models, such as FAST and BEM_COMSOL-Euler-Bernoulli-beam, for the cases when large deflections occur. No general conclusion can be drawn, but in this case study it seems like geometric nonlinearities are to be expected when the ratio

of blade deflection to blade radius exceeds 12% (corresponding to wind speed of 30m/s in this case study).

This case study clearly demonstrates that when the blade deflection is small, the errors introduced by small deflection assumptions, e.g. the assumption adopted in FAST, can be ignored. However, as the blade deflection increases, the errors introduced by these assumptions should be quantified.

8.4. Stability Analysis of WindPACT 1.5MW Wind Turbine Blade

In this case study, the stability behaviour of the WindPACT 1.5MW wind turbine blade is investigated. The WindPACT 1.5MW wind turbine blade is simulated at different operating points, which are defined by free-stream wind speed, blade pitch angle and rotor rotational speed. The rated wind speed of WindPACT 1.5MW wind turbine blade is 11.5m/s. At wind speeds above the rated wind speed, the blade pitch angle increases while the rotor rotational speed is held constant at the rated value (20rpm) to maintain rated power output. In order to investigate the effects of rotor rotational speed on the stability behaviour of the blade, two operating conditions are considered, i.e. 1) operating condition A, in which the rotor rotational speed is held constant at the rated value; and 2) operating condition B, in which the roror rotational speed is held constant at 40rpm (double of the rated value). In this case study, the simulation wind speeds are 12, 15, 18, 21, 24 and 27, and the corresponding rotor rotational speed and blade pitch angle under both operating conditions A and B are shown in Figure 8.3.

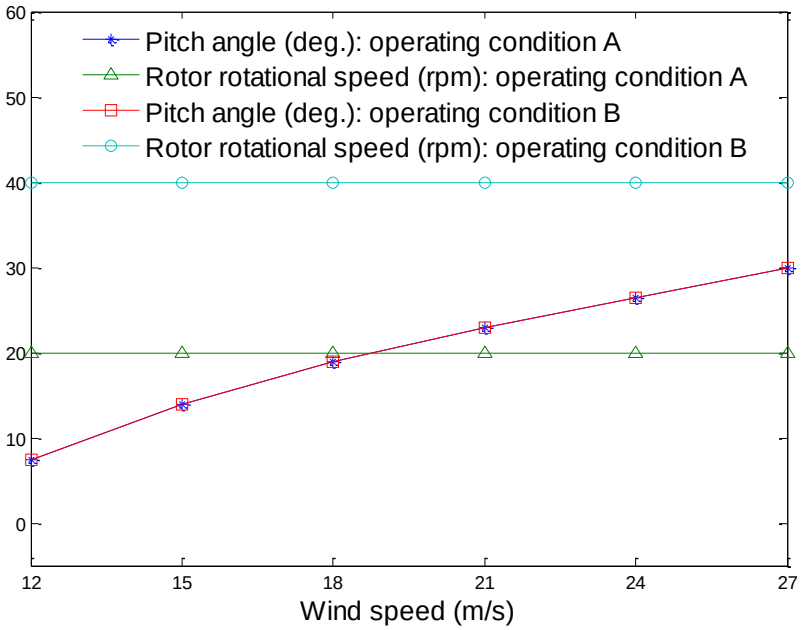

Figure 8.3. Rotor rotational speed and blade pitch angle against wind speed

Based on the method presented in Section 6.3.4, NAM_WTB is used to calculate the damped frequencies and damping ratios of the WindPACT 1.5MW wind turbine blade operating under both conditions A and B. The resulting damped frequency and damping ratio distributions for both flapwise and edgewise modes are shown in Figs. 8.4 and 8.5, respectively.

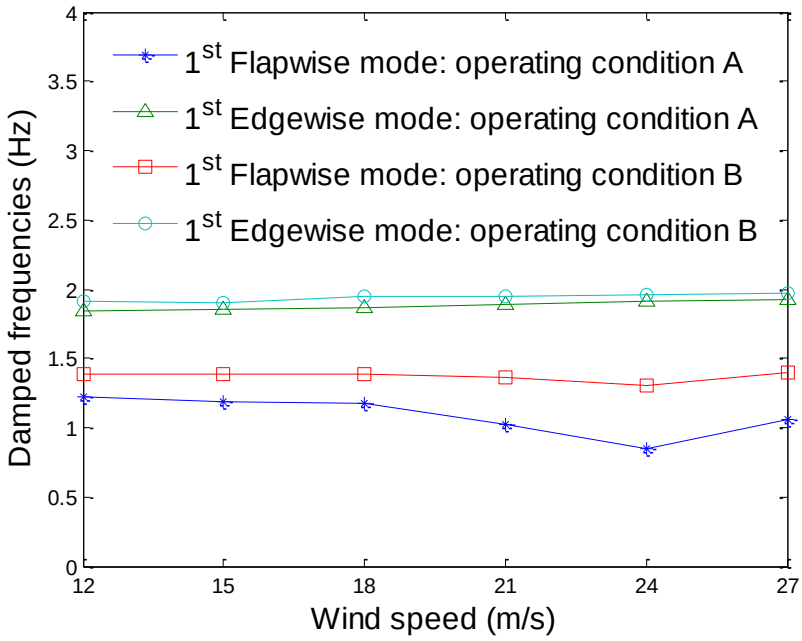

Figure 8.4. Damped frequencies of WindPACT 1.5MW wind turbine blade

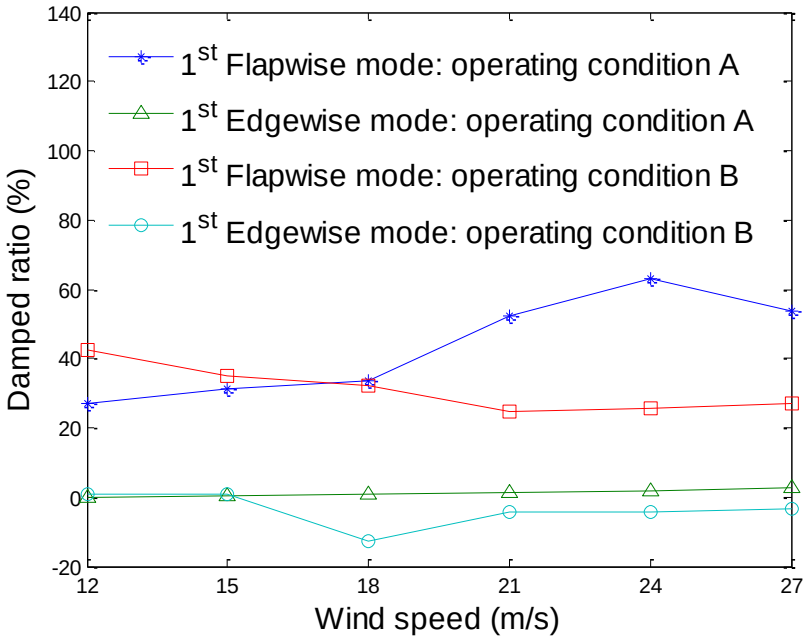

Figure 8.5. Damping ratio of WindPACT 1.5MW wind turbine blade

As can be seen from Figs. 8.4 and 8.5, under both operating condition A (rotor rotational speed is 20rpm) and operating condition B (rotor rotational speed is 40rpm), it is observed that 1) both the damped frequencies and amping ratio fo the 1st edgewise mode are insensitive to the wind speed; 2) damped frequencies of the 1st flapwise model decreases gradually as wind speed goes up, reaching lowest value at wind speed 24m/s; 3) damping ratio of the 1st edgewise mode is much lower than the damping ratio of the 1st flapwise mode, indicating that edgewise instability is more like to occur than flapwise instability.

Figs. 8.4 and 8.5 also show that 1) the damped frequencies under operating condition B are higher than those under operating condition A, indicating that the damped frequency is increased with rotor rotational speed; 2) the damping ratio of the 1st edgewise mode under operating condition B becomes negative at wind speeds above 15m/s, indicating that improper rotor rotational speed (40rpm in this case) can result in edgewise instability.

8.5. Summary

In this chapter, the nonlinear aeroelastic model NAM_WTB was applied to simulate the parked WindPACT 1.5MW wind turbine blade and to perform aeroelastic stability analysis of the blade.

Taking account of geometric nonlinearities resulted from large blade deflections, significantly reduced tip deflection based on the presented NAM_WTB code is observed comparing with the linear aeroelastic code FAST. This difference in deflection could be vital for blade designers. No general conclusion can be drawn, but in the presented case study it seems like geometric nonlinearities are to be expected when the ratio of blade deflection to blade radius exceeds 12%.

The stability behaviour of the WindPAC 1.5MW wind turbine blade was investigated. NAM_WTB was used to calculate the damped frequencies and damping ratios of both 1^{st} flapwise and 1^{st} edgewise modes of the blade. Results show that damping ratio of the 1^{st} edgewise mode is much lower than the damping ratio of the 1^{st} flapwise mode, indicating that edgewise instability is more likely to occur than flapwise instability. It is also demonstrated that improper rotor rotational speeds can result in edgewise instability.

Next chapter presents the conclusions of the thesis and summarises the recommendations for future work.

CHAPTER 9 CONCLUSIONS AND FUTURE RESEARCH

This thesis presents the research on nonlinear aeroelastic modelling of large wind turbine composite blades. The conclusions of the thesis are presented in Section 9.1, and the recommendations for future works are presented in Section 9.2.

9.1. Conclusions

With the increasing size and flexibility of large wind turbine blades, aeroelasticity has become a significant subject in wind turbine blade design. In the development of large wind turbines, there have been some examples of commercial wind turbine blades suffering from instability problems due to aeroelasticity. Those examples have heightened the need for aeroelastic modelling of wind turbine blades.

In order to provide a reliable and efficient aeroelastic modelling of large wind turbine blades, this project have developed 1) a cross-sectional model, which can extract cross-sectional properties of wind turbine blade in a reliable and efficient way; and 2) a nonlinear aeroelastic model, which is capable of handling large blade deflections.

The cross-sectional analysis model has been developed by incorporating the classical lamination theory (CLT) with the extended Bredt-Batho shear flow theory (EBSFT). The cross-sectional analysis model considers both the web effects and warping effects of the blades, and is presented in a code called CBCSA (Composite Blade Cross-Section Analysis), developed using MATLAB. A series of benchmark computational tests have been performed for isotropic and composite blades. The results demonstrate that

1. CBCSA can rapidly extract the cross-sectional properties of the composite blades, usually in a fraction of a second, which is much faster than a 3D finite-element based method.
2. Good agreement is achieved in comparison with the data from experiment and finite-element analysis, which indicates CBCSA has sufficient accuracy for the calculation of the cross-sectional properties of the composite blades.

3. CBCSA provides a more accurate torsional stiffness calculation than previously available tool PreComp due to the consideration of the shear web effects by using EBSFT.

Additionally, a nonlinear aeroelastic model for large wind turbine blades has been developed by combining 1) a blade structural model, which is based on a mixed-form formulation of geometrically exact beam theory (GEBT), taking account of geometric nonlinearities; and 2) a blade load model, which includes gravity loads, centrifugal loads and aerodynamic loads. The aerodynamic loads are calculated based on combining the blade element momentum (BEM) model with the Beddoes-Leishman (BL) dynamic stall model. The nonlinear aeroelastic model takes account of large blade deflections, and is presented in a code called NAM_WTB (Nonlinear Aeroelastic Model for Wind Turbine Blades) based on COMSOL Multiphysics. NAM_WTB discretises the wind turbine blade into a series of 1D elements using 1D finite-element approach, which is computationally more efficient than 3D finite-element approaches. Validated by a series of benchmark computational tests, the nonlinear aeroelastic model was applied to the aeroelastic analysis of the parked WindPACT 1.5MW baseline wind turbine and to the stability analysis of the blade. The following conclusions can be drawn:

a) Close agreement with existing widely used BEM-based aerodynamic code WT_Perf confirms the validity of the BEM model in the aerodynamic part of NAM_WTB for aerodynamic load prediction for wind turbine blades.
b) Good agreement with unsteady airfoil experimental data confirms the validity of the BL dynamic stall model in the aerodynamic part of NAM_WTB for unsteady aerodynamic load predictions.
c) Good agreement (with maximum percentage difference of 3.78%) is achieved in comparison with the data from experiment of a large-deflection cantilever beam, which indicates the NAM_WTB is capable of handling geometric nonlinearities resulted from large deflections.
d) Good agreement (with maximum percentage difference of 9.34%) is achieved in comparison with the data from modal experiment of a practical wind turbine blade, which further validates the structural part of NAM_WTB. It also demonstrates that representing the blade as a series of 1D beam elements provides reasonable accuracy if the beam model is constructed properly.

e) In case of small deflections, the results of the NAM_WTB are consistent with the results of the linear aeroelastic code FAST, which indicates geometric nonlinearities can be ignored for small blade deflections.

f) Taking account of geometric nonlinearities resulted from large blade deflections, significantly reduced tip deflection based on the presented NAM_WTB code is observed comparing with the linear aeroelastic code FAST. This difference in deflection could be vital for blade designers.

g) No general conclusion can be drawn, but in the presented case study it seems like geometric nonlinearities are to be expected when the ratio of blade deflection to blade radius exceeds 12%.

h) In the presented case study on the stability analysis of a large wind turbine blade, the calculated damping ratio of the 1st edgewise model is much lower than the calculated damping ratio of the 1st flapwise mode, indicating that edgewise instability is more likely to occur than flapwise instability. It is also demonstrated that improper rotor rotational speeds can result in edgewise instability.

9.2. Recommendations for Future Research

It is recommended that future research work be undertaken in the following areas:

- To apply the cross-sectional analysis model CBCSA and the nonlinear aeroelastic model NAM_WTB to the optimisation of the blade structural layout with the consideration of aeroelastic effects.
- To conduct aeroelastic experiments to provide more available experimental data for the benchmark test of the nonlinear aeroelastic model.
- To extend the nonlinear aeroelastic model to a nonlinear aero-hydro-elastic model for offshore wind turbine applications by introducing a reliable hydrodynamic model to take account of hydrodynamic loads in offshore environment.

REFERENCES

[1] B. N. E. Finance, "Global trends in renewable energy investment 2011," *UNEP United Nations Environment Programme and Bloomberg New Energy Finance,* 2011.

[2] M. Z. Jacobson and M. A. Delucchi, "A path to sustainable energy by 2030," *Scientific American,* vol. 301, pp. 58-65, 2009.

[3] L. Fried, S. Shukla, and S. Sawyer, "Global Wind Report: annual market update 2013," *Global Wind Energy Council,* 2014.

[4] "http://vestas.com/en/products_and_services/turbines/v164-8_0-mw#!power-curve-and-aep; accessed 09-March-2014."

[5] J. Peeringa, R. Brood, O. Ceyhan, W. Engels, and G. d. Winkel, "Upwind 20 MW Wind Turbine Pre-Design," *ECN, Paper No. ECN-E–11-017,* 2011.

[6] "http://commons.wikimedia.org/wiki/File:Wind_turbine_size_increase_1980-2011.png; accessed 04-July-2014."

[7] T. Moeller, "Blade cracks signal new stress problem," *WindPower Monthly,* vol. 25, 1997.

[8] D. Cox, H. C. Curtiss Jr, J. Edwards, K. Hall, D. A. Peters, R. Scanlan, *et al.*, *A modern course in aeroelasticity* vol. 116: Springer, 2006.

[9] A. Collar, "The expanding domain of aeroelasticity," *Journal of the Royal Aeronautical Society,* vol. 50, pp. 613-636, 1946.

[10] J. R. Wright and J. E. Cooper, *Introduction to aircraft aeroelasticity and loads* vol. 20: John Wiley & Sons, 2008.

[11] (02 June). Available: http://en.wikipedia.org/wiki/Aeroelasticity#cite_note-Hodges-5

[12] A. Collar, "The first fifty years of aeroelasticity," *Aerospace,* vol. 5, pp. 12-20, 1978.

[13] W. Turbines, "Part 1: Design Requirements, IEC 61400-1," ed: International Electrotechnical Commission: Geneva, Switzerland, 2005.

[14] M. L. Buhl Jr and A. Manjock, "A comparison of wind turbine aeroelastic codes used for certification," in *44th AIAA Aerospace Sciences Meeting and Exhibit, 9–12 January 2006, Reno, NV, AIAA Meeting Papers on Disc*, 2006, pp. 2006-786.

[15] R. L. Bisplinghoff, *Aeroelasticity*: Addison-Wesley Publishing Company, Inc. Cambrige, 1995.

[16] L. P. Kollár and G. S. Springer, *Mechanics of composite structures*: Cambridge university press, 2003.

[17] S. J. Guo, J. Bannerjee, and C. Cheung, "The effect of laminate lay-up on the flutter speed of composite wings," *Proceedings of the Institution of Mechanical Engineers, Part G: Journal of Aerospace Engineering,* vol. 217, pp. 115-122, 2003.

[18] S. Guo, W. Cheng, and D. Cui, "Aeroelastic tailoring of composite wing structures by laminate lay-up optimization (TN)," *AIAA Journal*, pp. 3146-3150, 2006.

[19] S. Guo, "Aeroelastic optimization of an aerobatic aircraft wing structure," *Aerospace Science and Technology*, vol. 11, pp. 396-404, 2007.

[20] P. Zhang and S. Huang, "Review of aeroelasticity for wind turbine: Current status, research focus and future perspectives," *Frontiers in Energy*, vol. 5, pp. 419-434, 2011.

[21] H. Stiesdal, "Extreme wind loads on stall regulated wind turbines," in *Proceedings of the 16th British Wind Energy Association Conference*, 1994, pp. 101-106.

[22] C. Anderson, H. Heerkes, and R. Yemm, "The use of blade-mounted dampers to eliminate edgewise stall vibration," in *EWEC-CONFERENCE-*, 1999, pp. 207-211.

[23] J. Thirstrup Petersen, H. Aagaard Madsen, A. Björck, P. Enevoldsen, S. Øye, H. Ganander, *et al.*, *Prediction of dynamic loads and induced vibrations in stall*, 1998.

[24] H. Aagaard Madsen, J. Thirstrup Petersen, A. Björck, H. Ganander, D. Winkelaar, A. Brand, *et al.*, "Prediction of dynamic loads and induced vibrations in stall STALLVIB. Final report," ed: Risø National Laboratory, 1998.

[25] A. S. Elliott and A. D. Wright, "ADAMS/WT: an industry-specific interactive modelling interface for wind turbine analysis," in *The Energy-Sources Technology Conference, New Orleans, LA, USA, 01/23-26/94*, 1994, pp. 111-122.

[26] J. M. Jonkman and M. L. Buhl Jr, "FAST user's guide," *Golden, CO: National Renewable Energy Laboratory*, 2005.

[27] S. Øye, "FLEX 5 User Manual," *Danske Techniske Hogskole*, 1999.

[28] V. A. V. a. S.G.Voutsinas, "Gast: A general aerodynamic and structural prediction tool for wind turbines," presented at the European union wind energy conference, Dublin, Ireland, 1996.

[29] E. Bossanyi, "GH Bladed user manual," *Garrad Hassan and Partners Ltd*, 2009.

[30] T. Larsen, "How 2 HAWC2, the user's manual," *Risø Report, Risø*, 2009.

[31] C. Lindenburg, "PHATAS release'APR-2005'user's manual," Report ECN-I–05-005, ECN2005.

[32] L. Wang, X. Liu, L. Guo, N. Renevier, and M. Stables, "A mathematical model for calculating cross-sectional properties of modern wind turbine composite blades," *Renewable Energy*, vol. 64, pp. 52-60, 2014.

[33] O. Bauchau and J. Craig, "Euler-Bernoulli beam theory," in *Structural Analysis*, ed: Springer, 2009, pp. 173-221.

[34] E. Petrov and M. Geradin, "Finite element theory for curved and twisted beams based on exact solutions for three-dimensional solids Part 1: Beam concept and geometrically exact nonlinear formulation," *Computer methods in applied mechanics and engineering*, vol. 165, pp. 43-92, 1998.

[35] R. Palacios and C. E. Cesnik, "Structural models for flight dynamic analysis of very flexible aircraft," *Daedalus Boston*, pp. 1-17, 2009.

[36] D. H. Hodges, *Nonlinear composite beam theory*: American Institute of Aeronautics and Astronautics, 2006.

[37] M. J. Patil, D. H. Hodges, and C. E. S. Cesnik, "Nonlinear aeroelasticity and flight dynamics of high-altitude long-endurance aircraft," *Journal of Aircraft*, vol. 38, pp. 88-94, 2001.

[38] L. Wang, X. Liu, N. Renevier, M. Stables, and G. M. Hall, "Nonlinear aeroelastic modelling for wind turbine blades based on blade element momentum theory and geometrically exact beam theory," *Energy*, vol. 76, pp. 487-501, 2014.

[39] X. Liu, L. Wang, and X. Tang, "Optimized linearization of chord and twist angle profiles for fixed-pitch fixed-speed wind turbine blades," *Renewable Energy*, vol. 57, pp. 111-119, 2013.

[40] L. Wang, X. Tang, and X. Liu, "Optimized chord and twist angle distributions of wind turbine blade considering Reynolds number effects," in *Internation conference on Wind Energy: Materials, Engineering and Policies (WEMEP)*, Bits Pilani Hyderabad Campus (India), 2012.

[41] L. Wang, X. Tang and X. Liu, "Blade design optimisation for fixed-pitch fixed-speed wind turbines," *ISRN Renewable Energy*, vol. 2012, 2012.

[42] M. O. L. Hansen, J. N. Sørensen, S. Voutsinas, N. Sørensen, and H. A. Madsen, "State of the art in wind turbine aerodynamics and aeroelasticity," *Progress in Aerospace Sciences*, vol. 42, pp. 285-330, 2006.

[43] H. Glauert, "Airplane propellers," *Aerodynamic theory*, vol. 4, pp. 169-360, 1935.

[44] O. Vries, "Fluid dynamic aspects of wind energy conversion," DTIC Document1979.

[45] H. Glauert, *The analysis of experimental results in the windmill brake and vortex ring states of an airscrew*: HM Stationery Office, 1926.

[46] C. Crawford, "Re-examining the precepts of the blade element momentum theory for coning rotors," *Wind Energy*, vol. 9, pp. 457-478, 2006.

[47] E. Bossanyi, "GH Bladed–Theory Manual, Version 3.81," *Garrad Hassan and Partners*, p. 16, 2008.

[48] X. Tang, "Aerodynamic design and analysis of small horizontal axis wind turbine blades," University of Central Lancashire, 2012.

[49] S. Øye, "Tjæreborg wind turbine (Esbjerg) Structural dynamics data," *VK–186, Dept. of Fluid Mechanics, Technical University of Denmark: Lyngby*, 1991.

[50] S. Øye, "Tjæreborg wind turbine: Dynamic flow measurement," *AFM Notat VK*, vol. 233, 1992.

[51] D. M. Pitt and D. A. Peters, "Theoretical prediction of dynamic-inflow derivatives," *Vertica*, vol. 5, pp. 21-34, 1981.

[52] H. Snel, J. Schepers, and S. E. C. Nederland, *Joint investigation of dynamic inflow effects and implementation of an engineering method*: Netherlands Energy Research Foundation ECN, 1995.

[53] J. Leishman and T. Beddoes, "A Semi-Empirical Model for Dynamic Stall," *Journal of the American Helicopter Society*, vol. 34, pp. 3-17, 1989.

[54] C. Tran and D. Petot, "Semi-empirical model for the dynamic stall of airfoils in view of the application to the calculation of responses of a helicopter blade in forward flight," 1980.

[55] F. Tarzanin, "Prediction of control loads due to blade stall," *Journal of the American Helicopter Society*, vol. 17, pp. 33-46, 1972.

[56] A. Harris, "The role of unsteady aerodynamics in vertical axis wind turbines," 1990.

[57] R. McD, "Galbraith, AJ Niven, and FN Coton,"Aspects of unsteady aerodynamics in wind turbines,"" *Wind Eng*, vol. 14, pp. 286-99, 1990.

[58] K. G. Pierce, "Wind turbine load prediction using the beddoes-leishman model for unsteady aerodynamics and dynamic stall," The University of Utah, 1996.

[59] J. Tangler, "Comparison of wind turbine performance prediction and measurement," *Journal of solar energy engineering*, vol. 104, pp. 84-88, 1982.

[60] L. M. Milne-Thomson, *Theoretical aerodynamics*: Courier Dover Publications, 1966.

[61] J. Gould and S. Fiddes, "Computational methods for the performance prediction of HAWTS," *Journal of Wind Engineering and Industrial Aerodynamics*, vol. 39, pp. 61-72, 1992.

[62] D. Kocurek, "Lifting surface performance analysis for horizontal axis wind turbines," *NASA STI/Recon Technical Report N*, vol. 87, p. 29946, 1987.

[63] A. Afjeh and T. Keith, "A simplified free wake method for horizontal-axis wind turbine performance prediction," *Journal of fluids engineering*, vol. 108, pp. 400-406, 1986.

[64] A. Zervos, S. Huberson, and A. Hemon, "Three-dimensional free wake calculation of wind turbine wakes," *Journal of Wind Engineering and Industrial Aerodynamics*, vol. 27, pp. 65-76, 1988.

[65] W. J. M. Rankine and I. o. N. Architects, *On the mechanical principles of the action of propellers*, 1865.

[66] R. Froude, "On the part played in propulsion by differences of fluid pressure," *Transactions of the Institute of Naval Architects*, vol. 30, pp. 390-405, 1889.

[67] J. Prospathopoulos, E. Politis, K. Rados, and P. Chaviaropoulos, "Enhanced CFD Modelling of Wind Turbine Wakes," *Wind Turbine Wakes*, p. 3, 2009.

[68] W. Z. Shen, M. O. L. Hansen, and J. N. Sørensen, "Determination of the angle of attack on rotor blades," *Wind Energy*, vol. 12, pp. 91-98, 2009.

[69] J. N. SØRENSEN and W. Z. Shen, "Numerical modeling of wind turbine wakes," *Journal of fluids engineering*, vol. 124, pp. 393-399, 2002.

[70] R. Mikkelsen, "Actuator disc methods applied to wind turbines," Technical University of Denmark, 2003.

[71] J. Michelsen, "Basis3D-a platform for development of multiblock PDE solvers," *Report AFM 92*, vol. 5, 1992.

[72] W. Z. Shen, J. N. Sørensen, and J. Zhang, "Actuator surface model for wind turbine flow computations," 2007.

[73] W. Z. Shen, J. H. Zhang, and J. N. Sørensen, "The actuator surface model: a new Navier–Stokes based model for rotor computations," *Journal of Solar Energy Engineering*, vol. 131, p. 011002, 2009.

[74] C. Leclerc and C. Masson, "Toward blade-tip vortex simulation with an actuator-lifting surface model," *AIAA paper*, vol. 667, p. 2004, 2004.

[75] C. Sibuet Watters and C. Masson, "Recent advances in modeling of wind turbine wake vortical structure using a differential actuator disk theory," 2007, p. 2037.

[76] C. Sibuet Watters and C. Masson, "Modeling of lifting-device aerodynamics using the actuator surface concept," *International journal for numerical methods in fluids*, vol. 62, pp. 1264-1298, 2010.

[77] I. Dobrev, F. Massouh, and M. Rapin, "Actuator surface hybrid model," 2007, p. 012019.

[78] F. Rasmussen, M. H. Hansen, K. Thomsen, T. J. Larsen, F. Bertagnolio, J. Johansen, *et al.*, "Present status of aeroelasticity of wind turbines," *Wind Energy*, vol. 6, pp. 213-228, 2003.

[79] "http://www.nvidia.ru/object/nvidia-tesla-acusolve-press-20100527-ru.html; accessed 05-June-2014."

[80] S. U. s. Manual, "version SP3. 1," *Dassault Systemes, Sureness, France*, 2005.

[81] Unigraphics, "Unigraphics User's Guide," ed: version, 2000.

[82] H. Bijl, A. Van Zuijlen, and A. Van Mameren, "Validation of adaptive unstructured hexahedral mesh computations of flow around a wind turbine airfoil," *International journal for numerical methods in fluids*, vol. 48, pp. 929-945, 2005.

[83] A. Van Zuijlen, H. Bijl, G. Dufour, and A. Van Mameren, "Evaluation of adaptive, unstructured CFD calculations of the flow around the DU91 airfoil," 2003.

[84] T. J. Carrigan, B. H. Dennis, Z. X. Han, and B. P. Wang, "Aerodynamic shape optimization of a vertical-axis wind turbine using differential evolution," *ISRN Renewable Energy*, vol. 2012, 2012.

[85] R. Temam, *Navier--Stokes Equations*: American Mathematical Soc., 1984.

[86] S. Patankar, *Numerical heat transfer and fluid flow*: CRC Press, 1980.

[87] C. ANSYS, "ANSYS CFX," *Reference Guide. Release*, vol. 13, 2010.

[88] K. H. Huebner, D. L. Dewhirst, D. E. Smith, and T. G. Byrom, *The finite element method for engineers*: John Wiley & Sons, 2008.

[89] P. Durbin and B. Reif, "Reynolds Averaged Navier–Stokes Equations," *Statistical Theory and Modeling for Turbulent Flows, Second Edition, Second Edition,* pp. 45-56.

[90] F. R. Menter, "Improved two-equation k-omega turbulence models for aerodynamic flows," *NASA STI/Recon Technical Report N,* vol. 93, p. 22809, 1992.

[91] C. Lam and K. Bremhorst, "A modified form of the k-ε model for predicting wall turbulence," *Journal of Fluids Engineering,* vol. 103, pp. 456-460, 1981.

[92] P. SPALART and S. ALLMARAS, "A one-equation turbulence model for aerodynamic flows," 1992.

[93] P. Sagaut and D. Drikakis, "Large Eddy Simulation," *Encyclopedia of Aerospace Engineering,* 2010.

[94] A. Travin, M. Shur, M. Strelets, and P. Spalart, "Detached-eddy simulations past a circular cylinder," *Flow, Turbulence and Combustion,* vol. 63, pp. 293-313, 2000.

[95] G. J. De Salvo, R. W. Gorman, and M. C. Imgrund, *ANSYS: Engineering Analysis System. User's Manual*: Swanson Analysis Systems, Incorporated, 1987.

[96] Hibbitt, Karlsson, and Sorensen, *ABAQUS/Standard user's manual* vol. 1: Hibbitt, Karlsson & Sorensen, 2001.

[97] D. L. Laird and T. D. Ashwill, "Introduction to NuMAD: A numerical manufacturing and design tool," Sandia National Labs., Albuquerque, NM (United States)1997.

[98] D. Thomas, J. Wilson, and R. Wilson, "Timoshenko beam finite elements," *Journal of Sound and Vibration,* vol. 31, pp. 315-330, 1973.

[99] D. H. Hodges, "Geometrically exact, intrinsic theory for dynamics of curved and twisted anisotropic beams," *AIAA journal,* vol. 41, pp. 1131-1137, 2003.

[100] D. J. Malcolm and D. L. Laird, "Modeling of blades as equivalent beams for aeroelastic analysis," in *2003 ASME Wind Energy Symposium AIAA/ASME*, 2003, pp. 293-303.

[101] A. Cordle, "State-of-the-art in design tools for floating offshore wind turbines," *Deliverable D4,* vol. 3, 2010.

[102] A. A. Shabana, *Dynamics of multibody systems*: Cambridge university press, 2013.

[103] G. S. Bir and P. G. Migliore, *Preliminary structural design of composite blades for two- and three-blade rotors*: National Renewable Energy Laboratory, 2004.

[104] G. Bir, "User's Guide to PreComp (Pre-Processor for Computing Composite Blade Properties)," National Renewable Energy Laboratory (NREL)2006.

[105] M. David and L. Daniel, "Identification and Use of Blade Physical Properties," in *43rd AIAA Aerospace Sciences Meeting and Exhibit*, ed: American Institute of Aeronautics and Astronautics, 2005.

[106] D. J. Malcolm and D. L. Laird, "Extraction of equivalent beam properties from blade models," *Wind Energy,* vol. 10, pp. 135-157, 2007.

[107] C. E. S. Cesnik and D. H. Hodges, "VABS: a new concept for composite rotor blade cross-sectional modeling," *Journal of the American Helicopter Society*, vol. 42, pp. 27-38, 1997.

[108] V. Berdichevsky, E. Armanios, and A. Badir, "Theory of anisotropic thin-walled closed-cross-section beams," *Composites Engineering*, vol. 2, pp. 411-432, 1992.

[109] E. A. Armanios and A. M. Badir, "Free vibration analysis of anisotropic thin-walled closed-section beams," *AIAA journal*, vol. 33, pp. 1905-1910, 1995.

[110] H. Chen and W. Yu, "Manual of PreVABS," Utah State University2008.

[111] J. P. Blasques, "User's Manual for BECAS," Technical University of Denmark2012.

[112] V. Giavotto, M. Borri, P. Mantegazza, G. Ghiringhelli, V. Carmaschi, G. Maffioli, *et al.*, "Anisotropic beam theory and applications," *Computers & Structures*, vol. 16, pp. 403-413, 1983.

[113] R. D. Bitsche, "Airfoil2BECAS: A preprocessor for the cross-section analysis software BECAS," Technical University of Denmark2012.

[114] J. N. Reddy, *Mechanics of laminated composite plates and shells: theory and analysis*: CRC, 2003.

[115] S. Timoshenko, S. Woinowsky-Krieger, and S. Woinowsky, *Theory of plates and shells* vol. 2: McGraw-hill New York, 1959.

[116] R. M. Jones, *Mechanics of composite materials*: CRC Press, 1998.

[117] J. Lee and S. Lee, "Flexural–torsional behavior of thin-walled composite beams," *Thin-walled structures*, vol. 42, pp. 1293-1305, 2004.

[118] J. Lee, S. E. Kim, and K. Hong, "Lateral buckling of I-section composite beams," *Engineering Structures*, vol. 24, pp. 955-964, 2002.

[119] G. Bir and P. Migliore, "Preliminary structural design of composite blades for two-and three-blade rotors," National Renewable Energy Laboratory2004.

[120] M. Sessarego, K. Dixon, D. Rival, and D. Wood, "A hybrid multi-objective evolutionary algorithm for wind-turbine blade optimization," *Engineering Optimization*, pp. 1-20, 2014.

[121] F. Zhou, H. Mahfuz, G. M. Alsenas, and H. P. Hanson, "Design and Analysis of Composite Ocean Current Turbine Blades Using NREL Codes," in *ASME 2012 International Mechanical Engineering Congress and Exposition*, 2012, pp. 255-261.

[122] L. Zwang and W. Energy, "Boundary Layer Suction on a Horizontal Axis Wind Turbine," *Delf University of Technology*, 2009.

[123] L. Librescu and O. Song, *Thin-walled composite beams: theory and application* vol. 131: Springer, 2006.

[124] W. D. Pilkey, *Analysis and design of elastic beams*: Wiley Online Library, 2002.

[125] J. M. Berthelot, *Composite materials: mechanical behavior and structural analysis*: Springer Verlag, 1999.

[126] A. K. Kaw, *Mechanics of composite materials* vol. 29: CRC press, 2006.

[127] M. Shama, *Torsion and Shear Stresses in Ships*: Springer, 2010.

[128] O. Bauchau and J. I. Craig, "Aerospace Structural Analysis," *Georgia Institute of Technology, Atlanta, GA*, 2002.

[129] F. P. Beer and E. R. Johnston, *Vector mechanics for engineers* vol. 1: Tata McGraw-Hill Education, 1988.

[130] D. L. Laird and S. N. Laboratories, *NuMAD User's Manual*: Sandia National Laboratories, 2001.

[131] R. Chandra and I. Chopra, "Structural behavior of two-cell composite rotor blades with elastic couplings," *AIAA Journal*, vol. 30, pp. 2914-2921, 1992.

[132] W. Yu and M. Blair, "GEBT: A general-purpose nonlinear analysis tool for composite beams," *Composite Structures*, vol. 94, pp. 2677-2689, 2012.

[133] J. Banerjee, S. Guo, and W. Howson, "Exact dynamic stiffness matrix of a bending-torsion coupled beam including warping," *Computers & structures*, vol. 59, pp. 613-621, 1996.

[134] J. Manwell, J. McGowan, and A. Rogers, *Wind energy explained: theory, design and application*, 2nd ed.: Wiley, 2009.

[135] E. Bossanyi, "GH bladed theory manual," *GH & Partners Ltd*, 2003.

[136] R. B. dos Santos Pereira, "Validating the Beddoes-Leishman Dynamic Stall Model in the Horizontal Axis Wind Turbine Environment," Master Thesis, Lisbon's Instituto Superior Técnico, 2010.

[137] C. Multiphysics, "4.3 User's Guide," ed: COMSOL, 2012.

[138] M. L. Buhl, "WT_Perf user's guide," *National Renewable Energy Laboratory*, 2004.

[139] "OSU Wind-Tunnel Test Data," https://wind.nrel.gov/airfoils/OSU_data/data/, accessed 12-June-2014.

[140] C. Lindenburg, M. Hansen, and E. Politis, "Structural Pitch for a Pitch-to-vane Controlled Wind Turbine Rotor," 2004.

[141] T. van Holten, et al., "Aeroelastic Tools to Assess the Stability of Large Wind Turbines,Final Report STABTOOL Phase III," *FM&P-02-004,TU-Delft*, June 2002.

[142] C. Lindenburg, "Bladmode; program for rotor blade mode analysis," *Wind Energy*, vol. 2011, p. 2010, 2012.

[143] M. M. Hand, D. Simms, L. Fingersh, D. Jager, and J. Cotrell, *Unsteady aerodynamics experiment phase VI: test configuration and available data campaigns*: National Renewable Energy Laboratory, 2001.

[144] D. Malcolm, A. Hansen, and G. E. Concepts, *WindPACT Turbine Rotor Design Study: June 2000--June 2002*: National Renewable Energy Laboratory, 2006.

[145] *http://www.nrel.gov/wind/windpact.html; accessed 28-July-2014*.

APPENDIX A MAIN COORDINATE SYSTEMS AND DEGREES OF FREEDOME OF BLADES

This appendix presents the main coordinate system and degrees of freedom of wind turbine blades.

A1. Main Coordinate Systems

Three main coordinate systems, i.e. the global frame G, the un-deformed blade frame b and the deformed blade frame B, are chosen for the analysis of wind turbine blades, as shown in Fig. A.1.

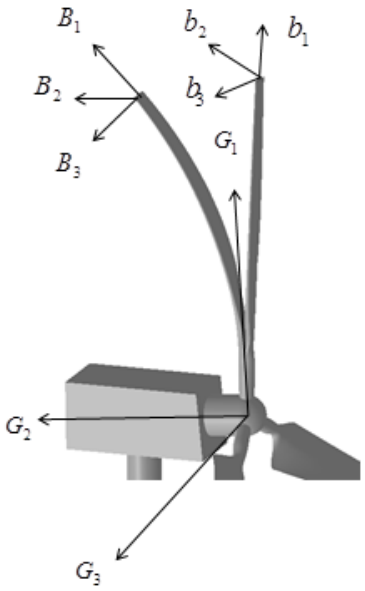

A.1. Main coordinate systems

The details of the three main coordinates systems are presented below.

- **Global frame** G

Origin: at hub centre (intersection of blade and shaft axes).

Axis G_1: Perpendicular to Axes G_2 and G_3, to give a right-handed co-ordinate system.

Axis G_2: along with the wind turbine rotor axis, and pointing towards the tower.

Axis G_3: perpendicular to the wind turbine rotor axis.

- **Un-deformed blade frame** b

Origin: at each un-deformed blade section.

Axis b_1: Perpendicular to Axes b_2 and b_3, to give a right-handed co-ordinate system.

Axis b_2: located in each un-deformed airfoil plane, and perpendicular to the chord line of each un-deformed blade element.

Axis b_3: located in each un-deformed airfoil plane, and parallel to the chord line of each un-deformed blade element.

- **Deformed blade frame** B

Origin: at each deformed blade section

Axis B_1: Perpendicular to Axes B_2 and B_3, to give a right-handed co-ordinate system.

Axis B_2: located in each deformed airfoil plane, and perpendicular to the chord line of each deformed blade element.

Axis B_3: located in each deformed airfoil plane, and parallel to the chord line of each deformed blade element.

A2. Degrees of Freedom of Blades

Fig. A.2 depicts the typical three degrees of freedom (DOFs) of a blade, i.e. torsional (pitch), flapwise (flap) and edgewise (lag) DOFs. The torsional (pitch) DOF refers to the freedom of movement of the blade about the blade pitch axis. The flapwise (flap) DOF refers to the freedom of movement of the blade out of rotor rotational plane. The edgewise (lag) DOF refers to the freedom of movement of the blade in the rotor rotational plane.

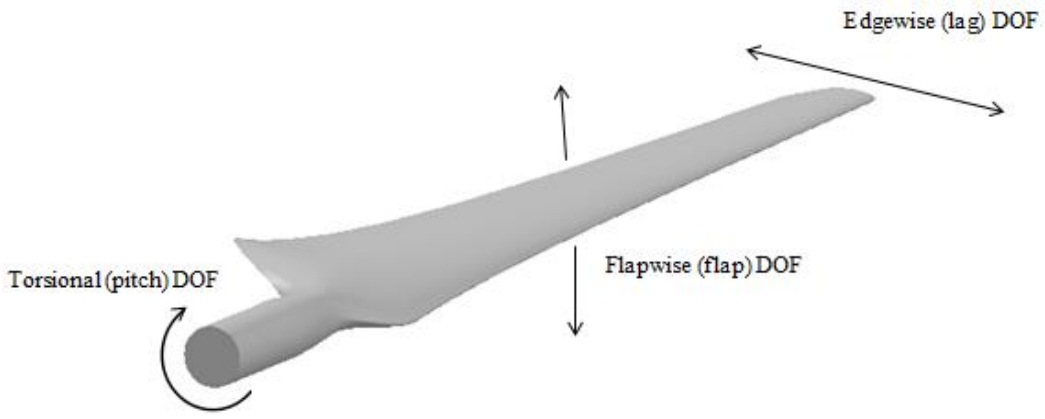

A.2. Degrees of freedom of a blade

APPENDIX B BLADE ELEMENT MOMENTUM THEORY

This appendix presents the fundamental equations involved in the blade element momentum (BEM) theory, which is a combination of the blade momentum theory and the blade element theory.

B1. Blade Momentum Theory

The expression of aerodynamic forces on wind turbine blades can be derived from blade momentum theory, which is developed based on the following main assumptions:

- The fluid is incompressible and homogenous.
- Both far upstream static pressure and far downstream static pressure are equal to undisturbed atmospheric static pressure.

Fig. A.1 depicts a schematic of the parameters involved in the blade momentum theory. In Fig. B.1, numbers 1, 2, 3, 4 respectively denote sections at far upstream, just in front of rotor plane, just behind rotor plane, and far downstream. It is assumed that 1) ω, the angular velocity imparted to the flow stream by the rotating blade, is small when compared to Ω, the rotor angular velocity; and 2) far upstream pressure p_1 is equal to far downstream pressure p_4. The following analysis is based upon the use of an annular stream tube with a radius r and a thickness dr, resulting in a cross-sectional area $2\pi r dr$ (see Fig. B.1).

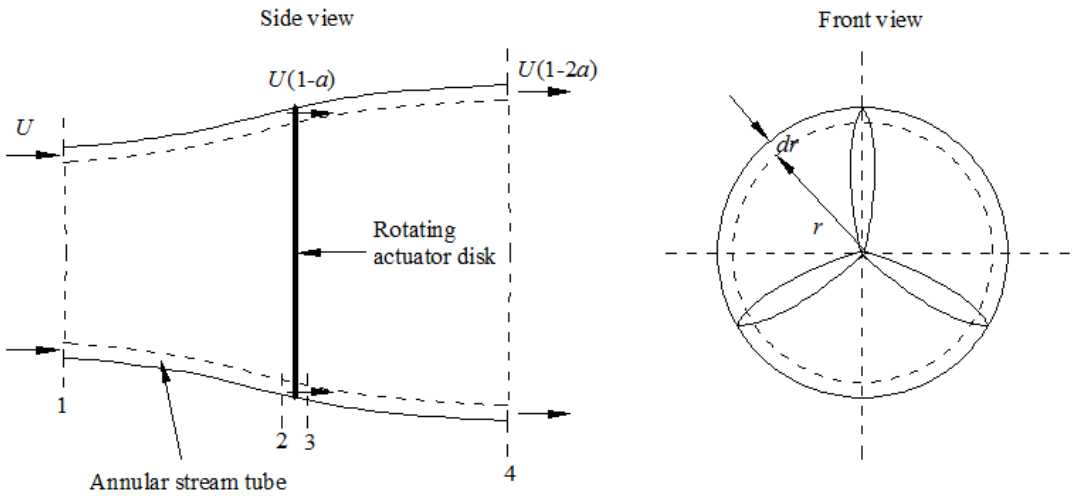

Figure B.1. Rotor geometry

The mass flow rate along the annular element is determined by:

$$d\dot{m} = \rho 2\pi r dr U(1-a) \tag{B.1}$$

where ρ is the air density; U is far upstream wind speed; a is the axial induction factor, the fractional reduction in axial wind velocity between the free stream and rotor plane.

The linear momentum of the annular element at Sections 1 and 4 (see Fig. B.1) are $d\dot{m}U$ and $d\dot{m}U(1-2a)$, respectively. Applying the conservation of linear momentum to the annular element yields the expression of the thrust on it:

$$dT = \rho U^2 4a(1-a)\pi r dr \tag{B.2}$$

Similarly, the expression of the torque on the annular element can be obtained by applying the conservation of angular momentum to the element. It should be noted that the angular velocity of the airflow relative to the rotor increases from Ω to $\Omega+\omega$. According to conservation of angular momentum, the torque equals the rate of change of angular momentum of the control volume:

$$dQ = d\dot{m}((\Omega+\omega)r)(r) - d\dot{m}(\Omega r)(r) = \rho 2\pi r dr U(1-a)(\omega r)(r) \tag{B.3}$$

Defining the angular induction factor a' as $\frac{\omega}{2\Omega}$ and substituting it into Eq. (B.3) yields:

$$dQ = 4a'(1-a)\rho U\pi r^3 \Omega dr \tag{B.4}$$

Thus, from the blade momentum theory, the thrust dT and torque dQ on an annular element are respectively defined by Eqs. (B.2) and (B.4) as a function of axial induction factor a and tangential induction factor a'.

B2. Blade Element Theory

The expression of aerodynamic forces on wind turbine blades can also be derived from blade element theory. The blade element theory discretizes the blade into several elements with the following assumptions:

- Elements are independent and no aerodynamic mutual influence between two adjacent elements.
- The aerodynamic loads on each element are solely dependent on its local airfoil characteristics, i.e. its lift and drag coefficients.

Fig. B.2 depicts the relationships of the various velocities, angles and forces at the blade section. In Fig. B.2, U_{rel} is the relative wind velocity; φ is the angle of relative wind, the angle between the relative wind and the plane of blade rotation; α is the angle of attack, the angle between the relative wind and the chord line of the section; θ_P is the section pitch angle, the angle between the chord line of the section and the plane of blade rotation; θ_{P0} is the pitch angle at blade tip, the angle between the chord line of the blade tip and the plane of blade rotation; θ_T is the twist angle, the angle between the chord line of the section and the chord line of the blade tip; dF_T is the tangential force one the section, which is tangential to the plane of blade rotation; dF_N is the normal force on the section, which is normal to the plane of blade rotation; dF_D is the drag force on the section, which is parallel to the relative wind speed; and dF_L is the lift force on the section, which is perpendicular to the relative wind speed.

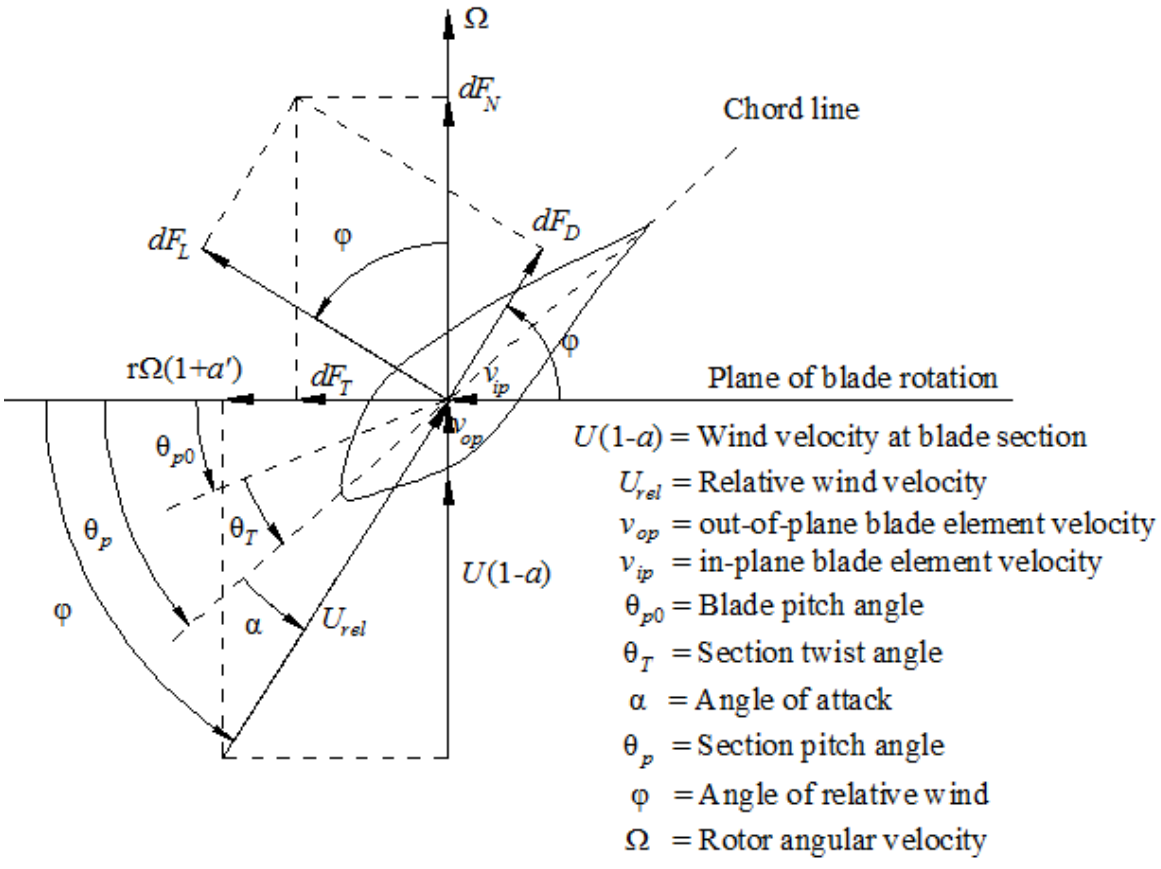

Figure B.2. Various velocities, angles, and forces at blade section

From Fig. B.2, the following relationships are established:

$$\varphi = \theta_P + \alpha \tag{B.5}$$

$$\tan(\varphi) = \frac{(1-a)U + v_{op}}{(1+a')\Omega r + v_{ip}} \tag{B.6}$$

$$U_{rel} = \frac{U(1-a)}{\sin(\varphi)} \tag{B.7}$$

v_{op} and v_{ip} in Eq. (B.6) respectively are out-of-plane and in-plane blade element velocities, and they are generally ignored if the blade element motion is small. If v_{op} and v_{ip} are ignored, Eq. (B.6) becomes:

$$\tan(\varphi) = \frac{(1-a)U}{(1+a')\Omega r} \tag{B.8}$$

According to airfoil theory, the lift force dF_L and drag force dF_D on the section are respectively calculated using the following equations:

$$dF_L = \frac{1}{2}\rho U_{rel}^2 C_l c dr \tag{B.9}$$

$$dF_D = \frac{1}{2}\rho U_{rel}^2 C_d c dr \tag{B.10}$$

where C_l and C_d are the lift and drag coefficients of the airfoil section, respectively; c is the chord length of the section.

The normal force dF_N and tangential force dF_T can be obtained by projecting the lift force dF_L and drag force dF_D on the normal and tangential directions (see Fig. B.2):

$$dF_N = dF_L \cos(\varphi) + dF_D \sin(\varphi) \tag{B.11}$$

$$dF_T = dF_L \sin(\varphi) - dF_D \cos(\varphi) \tag{B.12}$$

Substituting Eqs. (B.9) and (B.10) into Eqs. (B.11) and (B.12), and with the help of Eq.(B.7), one obtains:

$$dF_N = \frac{1}{2}\rho \frac{U^2(1-a)^2}{\sin^2(\varphi)}\left[C_l \cos(\varphi) + C_d \sin(\varphi)\right] c dr \tag{B.13}$$

$$dF_T = \frac{1}{2}\rho \frac{U^2(1-a)^2}{\sin^2(\varphi)}\left[C_l \cos(\varphi) - C_d \sin(\varphi)\right] c dr \tag{B.14}$$

If the rotor has B blades, the thrust force dT and the torque dQ on the section at a distance r from the rotor centre are respectively calculated by:

$$dT = BdF_N \tag{B.15}$$

$$dQ = BrdF_T \tag{B.16}$$

Substituting Eqs. (B.13) and (B.14) into Eqs. (B.15) and (B.16) yields:

$$dT = \sigma'\pi\rho\frac{U^2(1-a)^2}{\sin^2(\varphi)}\left[C_l\cos(\varphi)+C_d\sin(\varphi)\right]rdr \tag{B.17}$$

$$dQ = \sigma'\pi\rho\frac{U^2(1-a)^2}{\sin^2(\varphi)}\left[C_l\cos(\varphi)+C_d\sin(\varphi)\right]r^2dr \tag{B.18}$$

where σ' is the local solidity, defined as

$$\sigma' = B_N c/2\pi r \tag{B.19}$$

Thus, from the blade element theory, the thrust force and torque on an annular rotor element can be expressed using Eqs.(B.17) and (B.18), respectively.

B3. Combination of Blade Momentum Theory and Blade Element Theory

The performance parameters of each blade element, such as axial induction factor a and tangential induction factor a', can be obtained by combining the blade element theory with the blade momentum theory.

Equating Eq. (B.2), the thrust force expression from blade momentum theory, to Eq. (B.17), the thrust force expression from blade element theory, one obtains the following expression for axial induction factor a:

$$a = \frac{1}{1+\dfrac{4\sin^2(\varphi)}{\sigma\left[C_l\cos(\varphi)+C_d\sin(\varphi)\right]}} \tag{B.20}$$

Similarly, equating Eq. (B.4), the torque expression from blade momentum theory, to Eq. (B.18), the torque expression from blade element theory, one obtains the following expression for tangential induction factor a':

$$a' = \frac{1}{\frac{4\sin(\varphi)\cos(\varphi)}{\sigma[C_l \sin(\varphi) - C_d \cos(\varphi)]} - 1} \tag{B.21}$$

APPENDIX C MODAL ANALYSIS

This appendix summarises the mathematic equations involved in the modal analysis of a free-vibration system. A spring damper system with one degree of freedom, as illustrated in Fig. C.1, is chosen as an example.

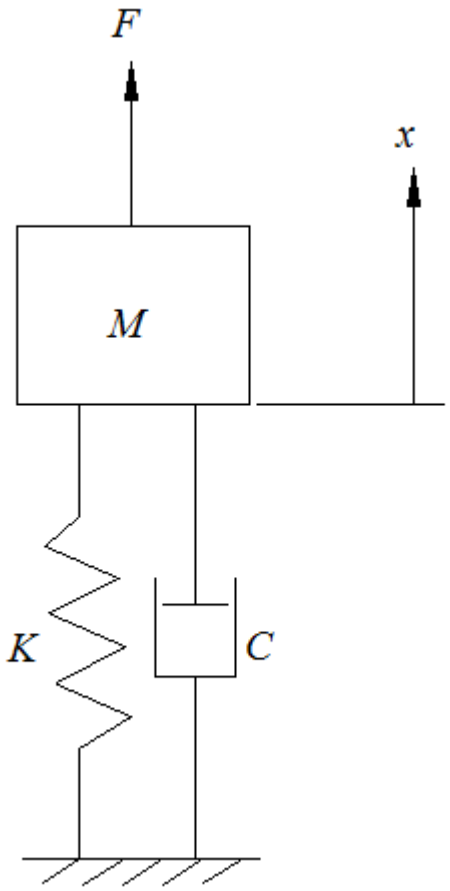

Figure C.1. A spring damper system with one degree of freedom

The governing equation for the system in Fig. C.1 can be written in a general matrix form:

$$M\ddot{x}(t)+C\dot{x}(t)+Kx(t)=F \tag{C.1}$$

where M , C and K are the mass, damping and stiffness of the system, respectively; F is the applied load of the system; $\boldsymbol{x}$ is the dependent variable of the system.

Dropping the applied load F in Eq. (C.1) yields the governing equation of a free-vibration system:

$$M\ddot{x}(t)+C\dot{x}(t)+Kx(t)=0 \tag{C.2}$$

The solution of Eq. (C.2) can be found by assuming it has the following type of solution:

$$x(t) = X(t)e^{\lambda t} \tag{C.3}$$

Substituting Eq. (C.3) into Eq. (C.2) gives:

$$\left(M\lambda^2 + C\lambda + K\right)X(t)e^{\lambda t} = 0 \tag{C.4}$$

Eq. (C.4) must hold for every value of t, resulting in:

$$\left(M\lambda^2 + C\lambda + K\right) = 0 \tag{C.5}$$

Solving Eq. (C.5) yields two solutions for λ:

$$\lambda_{1,2} = -\frac{C}{2M} \pm \frac{1}{2M}\sqrt{C^2 - 4KM} \tag{C.6}$$

As can be seen from Eq. C.6, the solutions for λ can be real or complex numbers, depending on the sign of $C^2 - 4KM$.

There are three possibilities for the sign of $C^2 - 4KM$. The first case is that $C^2 - 4KM$ is greater than zero. In this case, both λ_1 and λ_2 are negative real numbers. The second case is that $C^2 - 4KM$ equals zero, resulting in both λ_1 and λ_2 are the same negative real number. The last case is that $C^2 - 4KM$ is less than zero. In this case, λ_1 and λ_2 will be a complex conjugate pair.

Damping ratio ξ is defined by:

$$\xi = \frac{C}{C_r} = \frac{C}{2M\omega} \tag{C.7}$$

where C_r is the critical damping coefficient; ω is the un-damped natural frequency, defined by:

$$\omega = \sqrt{\frac{K}{M}} \tag{C.8}$$

With the help of Eq. (C.7), Eq. (C.6) can be written as:

$$\lambda_{1,2} = -\xi\omega \pm \omega\sqrt{\xi^2 - 1} \tag{C.9}$$

The solutions for λ are also in the following form:

$$\lambda_{1,2} = A_1 \pm A_2 i \tag{C.10}$$

where A_1 is the real part number and A_2 is the imaginary number.

Through comparing Eqs. (C.9) and (C.10), the un-damped frequency ω and damping ratio ξ can be expressed in terms of A_1 and A_2 using the following equations:

$$\omega = \sqrt{A_1^2 + A_2^2} \tag{C.11}$$

$$\xi = \frac{A_1}{\sqrt{A_1^2 + A_2^2}} \tag{C.12}$$

Having obtained the un-damped frequency ω and the damping ratio ξ , the damped frequency ω_D is calculated by:

$$\omega_D = \omega\sqrt{1-\xi^2} \tag{C.13}$$

The unit of both un-damped frequency ω and damped frequency ω_D is rad/s and can be transformed to Hz using the following equations:

$$f_{Hz} = \frac{\omega}{2\pi} \tag{C.14}$$

$$f_{D,Hz} = \frac{\omega_D}{2\pi} \tag{C.15}$$

where f_{Hz} and $f_{D,Hz}$ are the un-damped and damped frequencies in Hz, respectively.

The values of X in Eq. (C.4), which correspond to each eigenvalue, are called eigenvectors and can be obtained by substituting calculated eigenvalues λ back to Eq. (C.4).

APPENDIX D AWT-27CR2 WIND TURBINE BLADE CONFIGURATION

In this appendix, the chord and twist angle distributions of the AWT-27CR2 wind turbine blade are listed in Table D.1.

Table D.1. The chord and twist angle distributions of the AWT-27CR2 wind turbine blade

r (m)	Chord (m)	Twist angle (deg.)
1.498	0.774	6.1
2.127	0.869	5.764
3.07	0.962	5.47
4.327	1.108	4.996
5.585	1.148	4.208
6.842	1.089	3.172
8.099	1.015	2.086
9.356	0.931	1.117
10.614	0.83	0.424
11.557	0.711	0.122
12.185	0.646	0.076
12.625	0.576	0.048
12.877	0.538	0.041
13.128	0.501	0.033
13.38	0.459	0.023
13.568	0.414	0.012
13.694	0.392	0.006

APPENDIX E NREL PHASE VI WIND TURBINE BLADE CONFIGURATION

In this appendix, the geometry shape data (i.e. chord and twist angle distributions) of the NREL Phase VI wind turbine blade are listed in Table E.1, and the cross-sectional properties of the blade are listed in Table E.2.

Table E.1. Chord ant twist angle distributions of the NREL Phase VI wind turbine blade

r (m)	Chord c (m)	Twist angle θ_p (deg.)	Airfoil
0.568	0.219	0	cylinder
0.88	0.181	-0.098	cylinder
1.232	0.714	19.423	S809
1.509	0.711	14.318	S809
1.71	0.691	10.971	S809
1.928	0.668	8.244	S809
2.146	0.647	6.164	S809
2.347	0.627	4.689	S809
2.548	0.606	3.499	S809
2.766	0.584	2.478	S809
2.984	0.561	1.686	S809
3.185	0.542	1.115	S809
3.386	0.522	0.666	S809
3.604	0.499	0.267	S809
3.822	0.478	-0.079	S809
4.023	0.457	-0.381	S809
4.224	0.437	-0.679	S809
4.4	0.419	-0.933	S809
4.576	0.401	-1.184	S809
4.778	0.381	-1.466	S809
4.954	0.363	-1.711	S809

Table E.2a. Cross-sectional properties of NREL Phase VI wind turbine blade (part 1)

r (m)	axial stiffness EA (N)	flapwise stiffness EI_X (Nm^2)	edgewise stiffness EI_Y (Nm^2)	Torsional stiffness GJ (Nm^2)
0.568	1.46E+09	2.90E+06	1.12E+06	3.60E+06
0.88	4.02E+08	7.24E+05	2.80E+05	4.21E+05
1.232	4.06E+08	5.88E+05	1.14E+06	3.01E+06
1.509	3.84E+08	5.04E+05	1.15E+06	2.89E+06
1.71	3.65E+08	4.47E+05	1.10E+06	2.68E+06
1.928	3.58E+08	4.00E+05	1.08E+06	2.48E+06
2.146	3.54E+08	3.64E+05	1.05E+06	2.29E+06
2.347	3.21E+08	3.09E+05	8.32E+05	1.63E+06
2.548	2.94E+08	2.64E+05	7.33E+05	1.46E+06
2.766	2.68E+08	2.24E+05	6.40E+05	1.30E+06
2.984	2.48E+08	1.94E+05	5.58E+05	1.15E+06
3.185	2.35E+08	1.73E+05	4.93E+05	1.03E+06
3.386	2.18E+08	1.49E+05	4.32E+05	9.10E+05
3.604	2.00E+08	1.25E+05	3.72E+05	7.94E+05
3.822	1.82E+08	1.04E+05	3.18E+05	6.89E+05
4.023	1.66E+08	8.59E+04	2.70E+05	5.97E+05
4.224	1.51E+08	7.17E+04	2.33E+05	5.20E+05
4.4	1.37E+08	5.96E+04	1.99E+05	4.54E+05
4.576	1.24E+08	4.97E+04	1.71E+05	3.97E+05
4.778	1.09E+08	3.91E+04	1.41E+05	3.35E+05
4.954	9.69E+07	3.13E+04	1.18E+05	2.86E+05

Table E.2b. Cross-sectional properties of NREL Phase VI wind turbine blade (part 2)

r (m)	mass per unit length μ (kg/m)	flapwise mass moments of inertia $rhoI_X$ (kgm)	edgewise mass moments of inertia $rhoI_Y$ (kgm)
0.568	49.933	0.067	0.067
0.88	10.233	0.04	0.04
1.232	15.88	0.038	0.461
1.509	15.634	0.034	0.452
1.71	15.118	0.031	0.422
1.928	14.781	0.028	0.397
2.146	14.512	0.026	0.372
2.347	12.372	0.02	0.277
2.548	11.744	0.017	0.247
2.766	11.136	0.015	0.218
2.984	10.634	0.013	0.191
3.185	10.254	0.012	0.169
3.386	9.79	0.01	0.149
3.604	9.313	0.009	0.129
3.822	8.851	0.008	0.111
4.023	8.414	0.006	0.096
4.224	8.01	0.006	0.083
4.4	7.651	0.005	0.072
4.576	7.291	0.004	0.062
4.778	6.888	0.003	0.052
4.954	6.536	0.003	0.044

APPENDIX F WindPACT 1.5MW WIND TURBINE BLADE CONFIGURATION

In this appendix, the geometry shape data (i.e. chord and twist angle distribution) of the WindPACT 1.5MW wind turbine blade are listed in Table F.1, and the cross-sectional properties of the blade are listed in Table F.2.

Table F.1. Chord ant twist angle distributions of the WindPACT 1.5MW wind turbine blade

r (m)	Chord c (m)	Twist angle θ_p (deg.)	Airfoil
2.858	1.949	11.1	cylinder
5.075	2.269	11.1	S818
7.292	2.589	11.1	S818
9.508	2.743	10.41	S818
11.725	2.578	8.38	S818
13.942	2.412	6.35	S818
16.158	2.247	4.33	S818
18.375	2.082	2.85	S825
20.592	1.916	2.22	S825
22.808	1.751	1.58	S825
25.025	1.585	0.95	S825
27.242	1.427	0.53	S825
29.458	1.278	0.38	S825
31.675	1.129	0.23	S826
33.892	0.98	0.08	S826

Table F.2a. Cross-sectional properties of WindPACT 1.5MW wind turbine blade (part 1)

r (m)	axial stiffness EA (N)	flapwise stiffness EI_X (Nm^2)	edgewise stiffness EI_Y (Nm^2)	Torsional stiffness GJ (Nm^2)
2.858	2.63E+09	1.11E+09	1.14E+09	3.84E+08
5.075	2.57E+09	7.97E+08	9.76E+08	2.46E+08
7.292	2.51E+09	4.82E+08	8.12E+08	1.09E+08
9.508	2.41E+09	2.57E+08	6.66E+08	1.80E+07
11.725	2.24E+09	2.07E+08	5.52E+08	1.53E+07
13.942	2.08E+09	1.56E+08	4.38E+08	1.27E+07
16.158	1.91E+09	1.06E+08	3.25E+08	1.01E+07
18.375	1.71E+09	6.89E+07	2.37E+08	7.80E+06
20.592	1.45E+09	5.27E+07	1.89E+08	6.08E+06
22.808	1.19E+09	3.66E+07	1.41E+08	4.36E+06
25.025	9.31E+08	2.05E+07	9.25E+07	2.63E+06
27.242	7.12E+08	1.03E+07	5.93E+07	1.51E+06
29.458	5.43E+08	7.39E+06	4.46E+07	1.13E+06
31.675	3.73E+08	4.52E+06	2.99E+07	7.50E+05
33.892	2.03E+08	1.66E+06	1.52E+07	3.70E+05

Table F.2b. Cross-sectional properties of WindPACT 1.5MW wind turbine blade (part 2)

r (m)	mass per unit length μ (kg/m)	flapwise mass moments of inertia $rhoI_X$ (kgm)	edgewise mass moments of inertia $rhoI_Y$ (kgm)
2.858	180.854	75.72	80.337
5.075	183.682	49.881	79.563
7.292	1.87E+02	24.043	78.79
9.508	1.84E+02	6.576	73.957
11.725	1.71E+02	5.206	61.317
13.942	1.59E+02	3.835	48.676
16.158	1.46E+02	2.464	36.037
18.375	1.31E+02	1.501	26.218
20.592	1.11E+02	1.162	20.726
22.808	9.19E+01	0.822	15.233
25.025	7.26E+01	0.484	9.74
27.242	5.62E+01	0.264	6.029
29.458	4.34E+01	0.194	4.521
31.675	3.06E+01	0.124	3.011
33.892	1.78E+01	0.054	1.502

APPENDIX G AUTHOR PUBLICATIONS

G1. Paper 1

Lin Wang, Xiongwei Liu, Lianggang Guo, Nathalie Renevier, and Matthew Stables, "A mathematical model for calculating cross-sectional properties of modern wind turbine composite blades," *Renewable Energy* 64 (2014): 52-60.

Renewable Energy 64 (2014) 52–60

Contents lists available at ScienceDirect

Renewable Energy

journal homepage: www.elsevier.com/locate/renene

A mathematical model for calculating cross-sectional properties of modern wind turbine composite blades

Lin Wang [a], Xiongwei Liu [b,*], Lianggang Guo [c], Nathalie Renevier [a], Matthew Stables [a]

[a] School of Computing, Engineering and Physical Sciences, University of Central Lancashire, Preston PR1 2HE, UK
[b] Sustainable Engineering, University of Cumbria, Energus, Workington CA14 4JW, UK
[c] State Key Laboratory of Solidification Processing, Northwestern Polytechnical University (NWPU), Xi'an 710072, PR China

ARTICLE INFO

Article history:
Received 28 May 2013
Accepted 28 October 2013
Available online

Keywords:
Wind turbine blade
Cross-sectional analysis
Composite
Mathematical model
Classical lamination theory (CLT)
Extended Bredt-Batho shear flow theory (EBSFT)

ABSTRACT

A wind turbine blade generally has complex structures including several layers of composite materials with shear webs. It is essential but also inherently difficult to accurately and rapidly calculate the cross-sectional properties of a complex composite blade for the structural dynamics and aeroelasticity analysis of the blade. In this paper, a novel mathematical model for calculating the cross-sectional properties of composite blades has been developed by incorporating classical lamination theory (CLT) with extended Bredt-Batho shear flow theory (EBSFT). The mathematical model considers the shear web effects and warping effects of composite blades thus greatly improves the accuracy of torsional stiffness calculation compared with the results from direct use of 3D laminate theories. It also avoids complicated post-processing of force-displacement data from computationally expensive 3D finite-element analysis (FEA) thus considerably improves the computational efficiency. A Matlab program was developed to verify the accuracy and efficiency of the mathematical model and a series of benchmark calculation tests were undertaken. The results show that good agreement is achieved comparing with the data from experiment and FEA, and improved accuracy of torsional stiffness calculation due to consideration of the shear web effects is observed comparing with an existing cross-sectional analysis code PreComp.

1. Introduction

Modern wind turbine blades generally are made of thin-walled shells with composite materials. Cross-sectional properties of the thin-walled shells, such as mass per unit length and sectional stiffness, of the composite blade are essential information for the structural dynamics and aeroelasticity analysis of the wind turbine blade, which is often represented as one-dimensional (1D) beam elements instead of three-dimensional (3D) shell elements [1]. However, due to the intrinsic nature of composite materials and the complexity of blade structural topologies, it is quite challenging to obtain the cross-sectional properties of a wind turbine blade.

Various methods have been proposed for calculating the cross-sectional properties of wind turbine blades, ranging from complicated finite-element techniques and 3D laminate theories to the simple two-dimensional (2D) lamination theory. The most sophisticated method to extract the cross-sectional properties of wind turbine blades is based on 3D finite-element techniques. 3D finite-element techniques, despite their ability for accurate stress and displacement analysis, cannot directly yield the cross-sectional properties of wind turbine blades. It relies on computationally complicated post-processing of force-displacement data [2]. One such post-processing tool is BPE (Blade Properties Extractor) [3], which is developed by Sandia National Laboratories and Global Energy Concepts. Currently, BPE is a module of NuMAD (Numerical Manufacturing And Design) [4], which is a windows based pre/post-processor to generate the 3D finite-element models of wind turbine blades. BPE applies a series of unit loads at the blade tip and transfers the displacement results of the 3D finite-element model of the blade to a series of MATLAB routines, which extract the stiffness matrices for the equivalent beam elements. In principle, BPE should be able to provide the most accurate cross-sectional properties because all 3D information can be captured by the 3D finite-element model. However, there are seemingly several challenges facing this method. Firstly, application of loads must be performed carefully to minimize the boundary layer effects. Additionally, the cross-sectional properties estimated by BPE are sensitive to the length of the blade segment, which one chooses to

* Corresponding author. Tel.: +44 (0)1900 605665x1069.
E-mail addresses: Xiongwei.Liu@Cumbria.ac.uk, xiongweiliu@263.net (X. Liu).

0960-1481/$ – see front matter
http://dx.doi.org/10.1016/j.renene.2013.10.046

perform the finite-element analysis. Changing the length of the blade segment may even result in a singular stiffness matrix under some extreme situations [5].

Several other cross-sectional analysis tools based on 2D finite-element techniques have also been developed. Cesnik and Hodges [6] developed VABS (Variational Asymptotic Beam Sectional analysis) based on variational asymptotic method, which replaces a 3D structural model with a 2D model in terms of an asymptotic series of several small parameters of the structure. VABS requires a 2D finite-element discretization of the cross-section to generate its input files, which are the 2D mesh of the cross-section and the corresponding materials. For a practical wind turbine blade made of layers of composites, the generation of VABS input files is very tedious and requires a separate pre-processor called PreVABS [7]. Recently, Blasques [8] developed a cross-sectional analysis tool called BECAS based on anisotropic beam theory, which is originally presented by Gianotto et al. [9] for estimating the stiffness and the stresses of inhomogeneous anisotropic beams. Similar to VABS, BECAS also requires a 2D finite-element discretization of the cross-section. A separate pre-processor called Airfoil2BECAS [10], which is a python program, is needed to generate the input files for BECAS. Currently, the cross-section in Airfoil2BECAS is limited to 8 distinct regions, where layup and thickness information can be assigned.

Researchers have tried to obtain structural properties directly using 3D laminate theories. However, these theories cannot accurately estimate the torsional stiffness, which is overestimated by as much as 50–80 times using these theories [2]. The torsional stiffness is hard to evaluate because it is significantly affected by shear web effects and warping effects, which are difficult to model. This is particularly true for wind turbine blades, which commonly use asymmetrical cross-sections with several shear webs.

Compared to the finite-element techniques and 3D laminate theories, classical lamination theory (CLT) [11], which is an extension of the classical plate theory [12] to laminated plates, is fast and reasonably accurate. CLT can be used to combine properties and the angle of each ply in a pre-specified stacking sequence to calculate the overall effective performance for a laminate structure. Based on several reasonable assumptions, such as plane stress and linear strain, CLT transfers a complicated 3D elasticity problem to a solvable 2D problem [13]. Among the above assumptions, the assumption "each ply is under the condition of plane stress" is acceptable for composite blade due to the fact that wind turbine blades are thin-walled structures of composites.

CLT has been widely used for analyzing structural performance of composite materials [14,15]. In terms of composite blades, Bir [2,16] developed PreComp (Pre-processor for computing Composite blade properties) at National Renewable Energy Laboratory (NREL) based on CLT. PreComp does not need a separate pre-processor to generate the input files, which are the geometric shape and internal structural layout of the blade, and allows an arbitrary number of webs and a general layup of composite laminates. However, PreComp ignores the effects of shear webs in the calculation of the torsional stiffness. In other words, if the number of webs on a cross-section is changed, no change in torsional stiffness will be observed using PreComp. This is invalid for a practical blade cross-section, where the torsional stiffness will be enhanced as the number of shear webs increases.

For a closed thin-walled cross-section, Bredt-Batho shear flow theory (BSFT) [17] can be used to determine the torsional stiffness of the cross-section. BSFT is developed based on the assumption that the torsional stress is uniformly distributed across the thickness of the cross-section. Experiments show that this assumption is acceptable for most thin-walled cross-sections [18]. BSFT implicitly includes the dominant warping effects and it can provide reasonable results for the torsional stiffness of the closed thin-walled cross-section [18]. However, the original BSFT is developed for a single-cell cross-section. In order to apply BSFT to a practical wind turbine blade cross-section with shear webs, an extension of BSFT to cover multi-cells is required.

This paper attempts to incorporate CLT with an extended Bredt-Batho shear flow theory (EBSFT) [19] to develop a mathematical model, which extracts the cross-sectional properties of wind turbine blades in a fast and reliable way. Based on the mathematical model, a Matlab program is developed. In order to validate the developed program, a series of benchmark tests are performed for isotropic and composite blades as compared with ANSYS, PreComp and experimental data.

This paper is structured as follows. CLT and BSFT are summarized in Sections 2 and 3 respectively. EBSFT is discussed in Section 4. Section 5 details the development of a new mathematical model for cross-sectional analysis by incorporating CLT with EBSFT. Results and discussions are provided in Section 6, followed by a conclusion in Section 7.

2. Classical lamination theory (CLT)

CLT is an extension of the classical plate theory to laminated plates. The main assumptions of CLT are the Kirchhoff hypotheses [11]:

- Straight lines which are perpendicular to the mid-surface before deformation remain straight after deformation.
- The transverse normals are inextensible.
- The transverse normals rotate so that they are always perpendicular to the mid-surface.

The first two assumptions indicate that the transverse displacement is independent of the thickness coordination and the transverse normal strain is zero. The third assumption implies that transverse shear strains are zero. These assumptions are acceptable for thin laminates in most cases [11].

CLT has wide applications including stress and strain analysis of laminate plates. The validity of CLT has been established by comparing with experimental results and the exact solutions of the general elastic problems [20]. In terms of cross-sectional analysis, CLT can be used to calculate the effective engineering constants of angled plies.

The coordinate system used for an angled ply for the cross-sectional analysis using CLT is shown in Fig. 1.

The directions 1 and 2 constitute principal material coordinates while the directions x and y constitute global coordinates. The directions 1 and 2 are parallel and perpendicular to the fiber direction respectively.

The materials considered with CLT are orthotropic. The stress–strain relationship in principal material coordinates for an orthotropic material under plane stress condition can be expressed as:

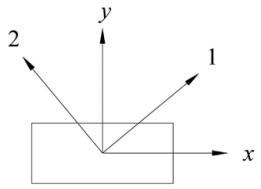

Fig. 1. Principal material and global coordinates.

$$\begin{bmatrix} \varepsilon_1 \\ \varepsilon_2 \\ \gamma_{12} \end{bmatrix} = \begin{bmatrix} S_{11} & S_{12} & 0 \\ S_{12} & S_{22} & 0 \\ 0 & 0 & S_{66} \end{bmatrix} \begin{bmatrix} \sigma_1 \\ \sigma_2 \\ \tau_{12} \end{bmatrix} \tag{1}$$

In Eq. (1), the components of matrix [S] are calculated by:

$$S_{11} = 1/E_1 \tag{2}$$

$$S_{12} = -\nu_{12}/E_1 \tag{3}$$

$$S_{22} = 1/E_2 \tag{4}$$

$$S_{66} = 1/G_{12} \tag{5}$$

where,E_1 and E_2 are the Young's modulus along the direction 1 and direction 2, respectively; ν_{12} is the Poisson's ratio and G_{12} is the shear modulus. All of these constants are called engineering constants of a unidirectional ply.

The inverse matrix [Q] of the matrix [S] in Eq. (1) is called reduced stiffness matrix [21], given as follows:

$$\begin{bmatrix} \sigma_1 \\ \sigma_2 \\ \tau_{12} \end{bmatrix} = \begin{bmatrix} Q_{11} & Q_{12} & 0 \\ Q_{12} & Q_{22} & 0 \\ 0 & 0 & Q_{66} \end{bmatrix} \begin{bmatrix} \varepsilon_1 \\ \varepsilon_2 \\ \gamma_{12} \end{bmatrix} \tag{6}$$

where:

$$Q_{11} = S_{22}/\left(S_{11}S_{22} - S_{12}^2\right) \tag{7}$$

$$Q_{12} = -S_{12}/\left(S_{11}S_{22} - S_{12}^2\right) \tag{8}$$

$$Q_{22} = S_{11}/\left(S_{11}S_{22} - S_{12}^2\right) \tag{9}$$

$$Q_{66} = 1/S_{66} \tag{10}$$

The stress–strain relations in Eq. (6) for the principal material coordinates can be transformed into a global coordinate system using:

$$\begin{bmatrix} \sigma_x \\ \sigma_y \\ \tau_{xy} \end{bmatrix} = [T]^{-1}[Q][R][T][R]^{-1} \begin{bmatrix} \varepsilon_x \\ \varepsilon_y \\ \gamma_{xy} \end{bmatrix} \tag{11}$$

where, [T] is the transformation matrix, [Q] is the reduced stiffness matrix in Eq. (6), [R] is the Reuter matrix [21]. [T] and [R] are defined as:

$$[T] = \begin{bmatrix} \cos^2(\alpha) & \sin^2(\alpha) & -2\sin(\alpha)\cos(\alpha) \\ \sin^2(\alpha) & \cos^2(\alpha) & 2\sin(\alpha)\cos(\alpha) \\ \sin(\alpha)\cos(\alpha) & -\sin(\alpha)\cos(\alpha) & \cos^2(\alpha) - \sin^2(\alpha) \end{bmatrix} \tag{12}$$

$$[R] = \begin{bmatrix} 1 & 0 & 0 \\ 0 & 1 & 0 \\ 0 & 0 & 2 \end{bmatrix} \tag{13}$$

where, α is the ply angle, i.e. the angle between the direction 1 and direction x in Fig. 1.

The effective engineering constants of an angled ply can be expressed in terms of the engineering constants of a unidirectional ply using the following equations:

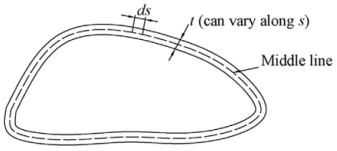

Fig. 2. Closed thin-walled cross-section.

$$E_x^{\text{ply}} = \frac{1}{\frac{1}{E_1}\cos^4(\alpha) + \left(\frac{1}{G_{12}} - \frac{2\nu_{12}}{E_1}\right)\sin^2(\alpha)\cos^2(\alpha) + \frac{1}{E_2}\sin^4(\alpha)} \tag{14}$$

$$G_{xy}^{\text{ply}} = \frac{1}{\left[\frac{4}{E_2} + \frac{4+8\nu_{12}}{E_1} - \frac{2}{G_{12}}\right]\sin^2(\alpha)\cos^2(\alpha) + \frac{\sin^4(\alpha)+\cos^4(\alpha)}{G_{12}}} \tag{15}$$

where, E_x^{ply} and G_{xy}^{ply} are the effective Young's modulus along the direction x (Fig. 1) and effective shear modulus of an angled ply, respectively.

3. Bredt-Batho shear flow theory (BSFT)

In the case of a closed thin-walled cross-section, the assumption that the torsional stress τ evenly distributes across the thickness of the cross-section is acceptable in most situations. The product of the torsional stress τ and the thickness t refers to shear flow [18]:

$$q = \tau t \tag{16}$$

Based on the above assumption, a shear flow theory called Bredt-Batho shear flow theory (BSFT) [18] is developed to evaluate stresses and deformations in structures with closed thin-walled cross-section under torsion.

The torsional stiffness GJ of the closed thin-walled cross-section (e.g. the cross-section in Fig. 2) can be obtained using BSFT:

$$\text{GJ} = \frac{4A^{*2}}{\oint \frac{1}{tG} ds} \tag{17}$$

where, A^* is the area enclosed by the middle line of the wall, t is the thickness of the wall, G is the shear modulus, and s is the perimeter coordinate. It is should be noted that the t and G can vary along s if the cross-section consists of several segments having variable wall thickness and different material properties.

4. Extended Bredt-Batho shear flow theory (EBSFT)

The original BSFT mentioned above is developed for a single-cell cross-section, which means no shear webs are included. To apply BSFT in a practical wind turbine blade cross-section with shear webs, an extension of BSFT to cover multi-cell is required.

Taking a wind turbine blade cross-section with one shear web in Fig. 3 as an example, the torsional moment M is expressed as [19]:

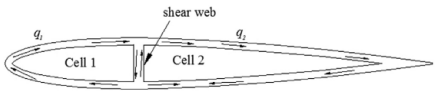

Fig. 3. Blade cross-section with one shear web.

$$M = 2\left(q_1 A_1^* + q_2 A_2^*\right) \tag{18}$$

where, q_1 and q_2 are the shear flow of cells 1 and 2, respectively; A_1^* and A_2^* are the area enclosed by the middle line of the wall of cells 1 and 2, respectively.

The twist angles (θ_1 and θ_2) of cells 1 and 2 are respectively expressed as:

$$\theta_1 = \frac{1}{2GA_1^*}\left(q_1 \oint_1 \mathrm{d}s/t - q_2 \int_{12} \mathrm{d}s/t\right) \tag{19}$$

$$\theta_2 = \frac{1}{2GA_2^*}\left(q_2 \oint_2 \mathrm{d}s/t - q_1 \int_{21} \mathrm{d}s/t\right) \tag{20}$$

Assuming the twist angles of the two cells are the same, we obtain:

$$\theta_1 = \theta_2 = \theta \tag{21}$$

Reformulating Eqs. (19) and (20), we obtain:

$$\delta_{11} q_1 + \delta_{12} q_2 - 2A_1^* \theta = 0 \tag{22}$$

$$\delta_{12} q_1 + \delta_{22} q_2 - 2A_2^* \theta = 0 \tag{23}$$

where δ is warping flexibility:

$$\delta_{11} = \oint_1 \frac{\mathrm{d}s}{Gt} \tag{24}$$

$$\delta_{22} = \oint_2 \frac{\mathrm{d}s}{Gt} \tag{25}$$

$$\delta_{12} = \delta_{21} = -\int_{12} \frac{\mathrm{d}s}{Gt} \tag{26}$$

The Eqs. (18), (22) and (23) can also be written in matrix format:

$$M = 2\left[A^*\right]^T [q] \tag{27}$$

$$[\delta][q] = 2\theta\left[A^*\right] \tag{28}$$

where:

$$\left[A^*\right] = \begin{bmatrix} A_1^* \\ A_2^* \end{bmatrix} \tag{29}$$

$$[q] = \begin{bmatrix} q_1 \\ q_2 \end{bmatrix} \tag{30}$$

$$[\delta] = \begin{bmatrix} \delta_{11} & \delta_{12} \\ \delta_{21} & \delta_{22} \end{bmatrix} \tag{31}$$

The torsional stiffness is given by:

$$\mathrm{GJ} = \frac{M}{\theta} \tag{32}$$

Substituting Eqs. (27) and (28) into Eq. (32) gives:

$$\mathrm{GJ} = 4\left[A^*\right]^T [\delta]^{-1}\left[A^*\right] \tag{33}$$

For a wind turbine blade cross-section with arbitrary shear webs, the torsional stiffness can be expressed in the form of Eq. (33). For a blade cross-section with two shear webs, $[\delta]$ and $[A^*]$ becomes:

$$[\delta] = \begin{bmatrix} \delta_{11} & \delta_{12} & 0 \\ \delta_{21} & \delta_{22} & \delta_{23} \\ 0 & \delta_{32} & \delta_{33} \end{bmatrix} \tag{34}$$

$$\left[A^*\right] = \begin{bmatrix} A_1^* \\ A_2^* \\ A_3^* \end{bmatrix} \tag{35}$$

5. A new mathematical model for cross-sectional analysis by incorporating CLT and EBSFT

In order to determine the cross-sectional properties of wind turbine blades, all cross-sectional laminates are discretised into many area segments. Each area segment encloses several angled plies. The effective engineering constants of each angled ply are obtained using CLT. A weighting method [22] is used to calculate the equivalent properties of each area segment and the elastic center location of the cross-section. Firstly, the area moments of inertia of each area segment are calculated with respect to its local axes and centroid, and then transformed to the elastic axes and center of the cross-section using transform-axis formula and parallel-axis theorem [23]. Based on the transferred area moments of inertia and calculated equivalent properties of each area segment, the contributions of each area segment to the cross-sectional properties are calculated. The torsional stiffness is obtained using EBSFT while the other cross-sectional properties are obtained by means of adding the contributions of all the area segments. Based on the above strategy, a mathematical model for cross-sectional analysis is developed. The flow chart of the model is shown in Fig. 4.

Each step of the flow chart in Fig. 4 is detailed as follows:

1) Input data

The model requires cross-sectional external shape (chord, twist and airfoil coordinates) and internal laminate layup (laminate schedule, ply angle and material engineering constants) as inputs.

2) Transform coordinates to reference axes

In the cross-sectional analysis, bending stiffness including both flapwise and edgewise stiffness is generally referred to the elastic center (X_E, Y_E), of which the location is measured from the reference axes of the cross-section, as shown in Fig. 5. Therefore, it is necessary to add a step to transfer the input airfoil data to reference axes if the input data refer to different axes.

As shown in Fig. 5, X_R and Y_R are the reference axes while X and Y are the elastic axes. The directions of X_R and Y_R are parallel and perpendicular to the chord direction of the blade cross-section respectively. The location of reference point O can be specified arbitrarily and usually is identical to the aerodynamic center of the blade cross-section. The directions of X and Y are parallel to the reference axes X_R and Y_R, respectively.

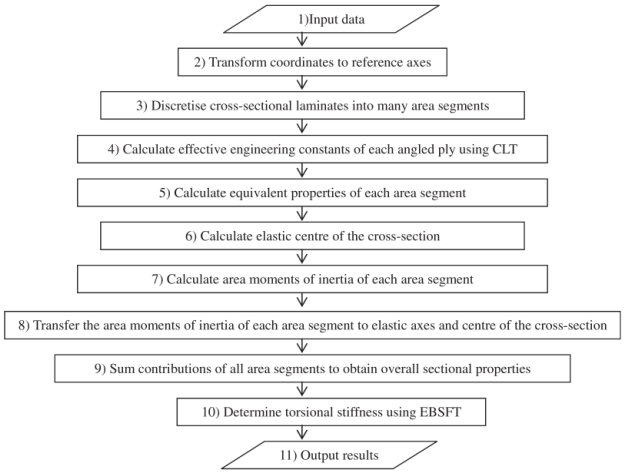

Fig. 4. Flow chart of the mathematical model.

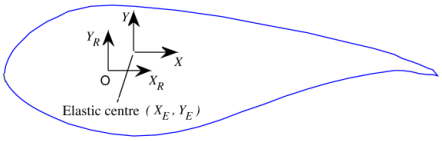

Fig. 5. Reference axes.

3) Discretize cross-sectional laminates into many area segments

In this step, all cross-sectional laminates are discretised into many area segments. Each area segment encloses several plies. Taking a typical blade cross-section with one shear web in Fig. 6 as an example, the cross-sectional laminates are discretised into 110 area segments and the area segment "ab" encloses three different plies.

4) Calculate effective engineering constants of each angled ply using CLT

In order to achieve better structural performance, some plies are generally placed at an angle. Therefore, it requires a step to obtain the effective engineering constants of angled plies. By giving the engineering constants $(E_1, E_2, G_{12}, v_{12})$ and ply angle α, the effective Young's modulus E_x^{ply} and shear modulus G_{xy}^{ply} of each angled ply are determined using Eqs. (14) and (15) mentioned in Section 2 respectively.

5) Calculate equivalent properties of each area segment

Because each area segment encloses several plies having different material properties, a weighting method is used to represent the non-uniform distribution of materials as a single material having equivalent properties. The actual thickness and area of each segment are maintained. For instance, the equivalent representations of the area segment "ab" in Fig. 6 are shown in Fig. 7.

The equivalent Young's modulus $E_{\text{equ}}^{\text{seg}}$, thickness $t_{\text{equ}}^{\text{seg}}$ and area $A_{\text{equ}}^{\text{seg}}$ of each area segment can be expressed as:

$$E_{\text{equ}}^{\text{seg}} = \frac{\sum_{i=1}^{m} E_{x,i}^{\text{ply}} t_i^{\text{ply}}}{\sum_{i=1}^{m} t_i^{\text{ply}}} \tag{36}$$

$$t_{\text{equ}}^{\text{seg}} = \sum_{i=1}^{m} t_i^{\text{ply}} \tag{37}$$

$$A_{\text{equ}}^{\text{seg}} = \sum_{i=1}^{m} A_i^{\text{ply}} = \sum_{i=1}^{m} t_i^{\text{ply}} w_{\text{seg}} \tag{38}$$

where i indicates the ith ply in an area segment, m is the number of plies in an area segment, $E_{x,i}^{\text{ply}}$ is the effective Young's modulus of the

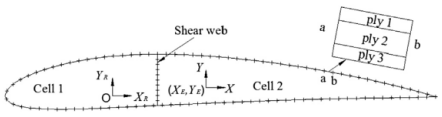

Fig. 6. Discretization of a typical blade cross-section with one shear web.

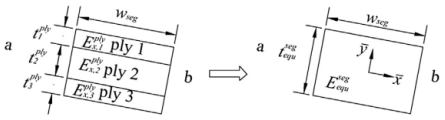

Fig. 7. Equivalent representations of area segment.

ith ply, t_i^{ply} and A_i^{ply} are the thickness and area of the ith ply respectively, w_{seg} is the width of an area segment.

The same method can be used to determine the equivalent density ρ_{equ}^{seg} and equivalent shear modulus G_{equ}^{seg} of each segment by simply replacing the effective Young's modulus $E_{x,i}^{ply}$ in Eq. (36) with the density ρ_i^{ply} and effective shear modulus $G_{xy,i}^{ply}$ respectively:

$$\rho_{equ}^{seg} = \frac{\sum_{i=1}^{m} \rho_i^{ply} t_i^{ply}}{\sum_{i=1}^{m} t_i^{ply}} \tag{39}$$

$$G_{equ}^{seg} = \frac{\sum_{i=1}^{m} G_{xy,i}^{ply} t_i^{ply}}{\sum_{i=1}^{m} t_i^{ply}} \tag{40}$$

6) Calculate elastic center of the cross-section

The elastic center (X_E, Y_E) of the cross-section can also be calculated using weighting method:

$$X_E = \frac{\sum_{I=1}^{N} E_{equ}^{seg,I} A_{equ}^{seg,I} \bar{x}_c^{seg,I}}{\sum_{I=1}^{N} E_{equ}^{seg,I} A_{equ}^{seg,I}} \tag{41}$$

$$Y_E = \frac{\sum_{I=1}^{N} E_{equ}^{seg,I} A_{equ}^{seg,I} \bar{y}_c^{seg,I}}{\sum_{I=1}^{n} E_{equ}^{seg,I} A_{equ}^{seg,I}} \tag{42}$$

where I indicates the Ith area segment, N is the number of area segments, $E_{equ}^{seg,I}$ and $A_{equ}^{seg,I}$ are the equivalent Young's modulus and area of the Ith area segment respectively, $\bar{x}_c^{seg,I}$ and $\bar{y}_c^{seg,I}$ are the centroid coordinates of the Ith area segment.

7) Calculate area moments of inertia of each area segment

The area moments of inertia of each area segment with respect to its local axes (e.g. the $\bar{x}-\bar{y}$ axes in Fig. 7) can be calculated using an integration scheme:

$$I_{\bar{x}\bar{x}}^{seg} = \int \bar{y}^2 d\bar{x}d\bar{y} \tag{43}$$

$$I_{\bar{y}\bar{y}}^{seg} = \int \bar{x}^2 d\bar{x}d\bar{y} \tag{44}$$

$$I_{\bar{x}\bar{y}}^{seg} = \int \bar{x}\bar{y} d\bar{x}d\bar{y} \tag{45}$$

where $I_{\bar{x}\bar{x}}^{seg}$ and $I_{\bar{y}\bar{y}}^{seg}$ are the area moment of inertia about $\bar{x}$ axis and $\bar{y}$ axis respectively, $I_{\bar{x}\bar{y}}^{seg}$ is the product of inertia.

8) Transfer the area moments of inertia of each area segment to elastic axes and center of the cross-section

It should be noted that the above calculated area moments of inertia are calculated with respect to the local axes and centroid of each area segment. However, the cross-sectional properties including both flapwise stiffness and edgewise stiffness are generally referred to the elastic axes and center of the cross-section. Therefore, a transformation is necessary. Using the transform-axis formula, the area moments of inertia around the local axes of each area segment can be transferred to that around the axes which are parallel to the elastic axes of the cross-section:

$$I_{XX}^{seg} = \frac{I_{\bar{x}\bar{x}}^{seg} + I_{\bar{y}\bar{y}}^{seg}}{2} + \frac{I_{\bar{x}\bar{x}}^{seg} - I_{\bar{y}\bar{y}}^{seg}}{2} \cos 2\varphi - I_{\bar{x}\bar{y}}^{seg} \sin 2\varphi \tag{46}$$

$$I_{YY}^{seg} = \frac{I_{\bar{x}\bar{x}}^{seg} + I_{\bar{y}\bar{y}}^{seg}}{2} - \frac{I_{\bar{x}\bar{x}}^{seg} - I_{\bar{y}\bar{y}}^{seg}}{2} \cos 2\varphi + I_{\bar{x}\bar{y}}^{seg} \sin 2\varphi \tag{47}$$

where φ is the angle between the local axes of each area segment and the elastic axes of the cross-section.

Then, using the parallel-axis theorem, the calculated area moments of inertia can be further transferred to elastic center (X_E, Y_E) of the cross-section:

$$I_{XX}^{sec} = (I_{XX}^{seg}) + A_{equ}^{seg} (\bar{x}_c^{seg} - X_E)^2 \tag{48}$$

$$I_{YY}^{sec} = (I_{XX}^{seg}) + A_{equ}^{seg} (\bar{y}_c^{seg} - Y_E)^2 \tag{49}$$

9) Sum contributions of all area segments to obtain overall sectional properties

The overall cross-sectional properties including axial stiffness EA, flapwise stiffness EI_X, edgewise stiffness EI_Y and mass per unit length μ are obtained by summing the contributions of all area segments:

$$EA = \sum_{I=1}^{N} E_{equ}^{seg,I} A_{equ}^{seg,I} \tag{50}$$

$$EI_X = \sum_{I=1}^{N} E_{equ}^{seg,I} I_{XX}^{sec,I} \tag{51}$$

$$EI_Y = \sum_{I=1}^{N} E_{equ}^{seg,I} I_{YY}^{sec,I} \tag{52}$$

$$\mu = \sum_{I=1}^{N} \rho_{equ}^{seg,I} A_{equ}^{seg,I} \tag{53}$$

10) Determine torsional stiffness using EBSFT

The torsional stiffness is determined using EBSFT mentioned in Section 4. Taking the blade cross-section with one shear web in Fig. 6 as an example, having obtained the width w_{seg} (approximate ds if the w_{seg} is small enough), equivalent thickness t_{equ}^{seg} and shear modulus G_{equ}^{seg} of each segment in step 5), the components of the warping flexibility matrix $[\delta]$ can be calculated using Eqs. (24)–(26). Then the torsional stiffness is determined using Eq. (33).

11) Output results

After all calculations are done, the model will output the cross-sectional properties including axial stiffness EA, flapwise stiffness EI_X, edgewise stiffness EI_Y, mass per unit length μ and torsional stiffness GJ.

6. Results and discussion

Based on the above mathematical model, a cross-sectional analysis program, which is named as CBCSA (Composite Blade Cross-Section Analysis), is developed using Matlab. CBCSA allows arbitrary geometric shape and internal structural layout of the blade. It directly extracts the cross-sectional properties of the blade

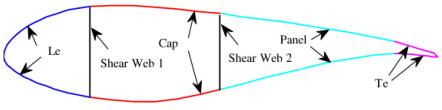

Fig. 8. Schematic of the cross-section of the SERI-8 blade.

Table 1
Geometric data [24].

Station#	Chord (m)	Twist (°)	Airfoil
4	1.092	15.7	S807
6	0.665	0.59	S805A

and runs fast, usually in a fraction of a second. Additionally, the shear web effects and warping effects are taken into account by CBCSA due to the usage of EBSFT in the calculation of torsional stiffness. In order to validate CBCSA, the following benchmark tests are performed.

6.1. Case study A

For the first case study, we compare the performance of CBCSA with analysis done with PreComp for a SERI-8 blade [24]. The stations 4 and 6 of the SERI-8 blade are chosen as examples. The schematic of the cross-section of the SERI-8 blade is shown in Fig. 8.

The geometric data of the wind turbine blade cross-sections at the stations 4 and 6 is shown in Table 1.

Four materials are used within the structure, labeled Mat, DblBias, Uni and Balsa. The orthotropic material properties used in the model are shown in Table 2.

The orientation of plies used in Ref. [24] is limited to 90°, here our case study also demonstrates the effects of ply angles at 45° and 0°. Ply angles are set in the composites lay-up, as shown in Table 3. The composites lay-up in Table 3 is used for both stations 4 and 6.

Table 2
Material properties [24].

Property	Mat	DblBias	Uni	Balsa
E_1 (GPa)	7.58	11.1	45.8	0.12
E_2 (GPa)	7.58	11.1	10.1	0.12
G_{12} (GPa)	4.00	6.89	6.89	0.02
ν_{12}	0.30	0.39	0.30	0.30
ρ (kg/m^3)	1690	1660	1990	230

Table 3
Composites lay-up [24].

Name	Number of plies	Ply angle (degree)	Ply name	Thickness (mm)
Le	1	90	Mat	1.21
	4	45	DblBias	1.21
Cap	1	90	Mat	1.21
	6	0	Uni	0.93
Panel	1	90	Mat	1.21
	1	45	DblBias	1.21
	1	0	Balsa	5
	1	45	DblBias	1.21
Shear webs	1	45	DblBias	1.21
1 and 2	1	0	Balsa	8
	1	45	DblBias	1.21
Te	1	90	Mat	1.21
	1	45	DblBias	1.21

Table 4
Calculated cross-sectional properties of the blade cross-section at station 4.

Cross-sectional properties	PreComp	CBCSA	%Diff
EA (N)	2.7830E+08	2.7829E+08	0.01
EI_X (N-m^2)	1.6670E+06	1.6692E+06	0.13
EI_Y (N-m^2)	1.4640E+07	1.4641E+07	0.01
GJ (N-m^2)	5.0530E+05	7.3768E+05	45.99
μ (kg/m)	2.2950E+01	2.2952E+01	0.01

Table 5
Calculated cross-sectional properties of the blade cross-section at station 6.

Cross-sectional properties	PreComp	CBCSA	%Diff.
EA (N)	1.6580E+08	1.6584E+08	0.02
EI_X (N-m^2)	1.9940E+05	1.9953E+05	0.07
EI_Y (N-m^2)	3.1960E+06	3.1953E+06	0.02
GJ (N-m^2)	6.7830E+04	8.9811E+04	32.41
μ (kg/m)	1.3510E+01	1.3506E+01	0.03

Both PreComp and CBCSA are used to calculate the properties of the cross-sections. Resulting cross-sectional properties for stations 4 and 6 are presented in Tables 4 and 5, respectively.

Tables 4 and 5 indicate that the results from CBCSA agree with those from PreComp very well except the torsional stiffness. The torsional stiffness predicted by PreComp is lower than that obtained using CBCAS. Following case studies demonstrate that CBCAS has higher accuracy for the calculation of torsional stiffness than PreComp due to the consideration of the effects of shear webs.

6.2. Case study B

This case study allows comparison of CBCSA with both PreComp and ANSYS for a blade profile with and without shear webs. The first example considered here is an isotropic blade cross-section without a shear web, as shown in Fig. 9. The geometric data and material properties of the cross-section are listed in Table 6.

The comparison of cross-sectional properties calculated using CBCAS, PreComp and ANSYS is shown in Table 7, where the relative differences are obtained with respect to the CBCAS results.

From Table 7 we can see that the predictions of the CBCAS are in good agreement with PreComp and ANSYS for the isotropic blade cross-section without a shear web.

The next example considered is the isotropic blade with two shear webs, located at 0.2c and 0.5c, as shown in Fig. 10.

The thickness of both webs is 0.003 m. Other properties of the cross-section remain the same as those used in the first example.

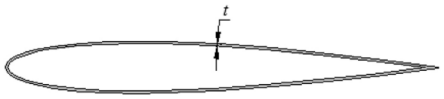

Fig. 9. Schematic of an isotropic blade cross-section without shear web.

Table 6
Geometric data and material properties of the isotropic blade cross-section.

Properties	Values
E (GPa)	210
ν	0.3
ρ (kg/m^3)	7850
Airfoil	NACA0012
Chord (m)	0.12
t (m)	0.000675

Table 7
Calculated cross-sectional properties of an isotropic blade cross-section without shear web.

Cross-sectional properties	CBCAS	PreComp	%Diff. (PreComp)	ANSYS	%Diff. (ANSYS)
EA (N)	3.4721E+07	3.4720E+07	0.01	3.4105E+07	1.77
EI_X (N-m^2)	8.6756E+02	8.6760E+02	0.01	8.6646E+02	0.13
EI_Y (N-m^2)	4.2866E+04	4.2870E+04	0.01	4.0789E+04	4.85
GJ (N-m^2)	1.0848E+03	1.0850E+03	0.02	1.1197E+03	3.22
μ (kg/m)	1.2979E+00	1.2980E+00	0.01	1.2718E+00	2.01

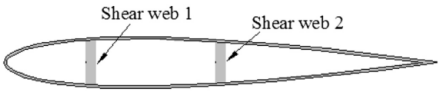

Fig. 10. Schematic of an isotropic blade cross-section with two shear webs.

The comparison of cross-sectional properties calculated using CBCAS, PreComp and ANSYS is shown in Table 8, where the relative differences are obtained with respect to the ANSYS results.

From Table 8 it can be seen that the results predicted by CBCSA match well with those of ANSYS, with the maximum percentage difference (6.68%) occurring for the edgewise stiffness (EI_Y). It can be observed that for this cross-section with two shear webs, the torsional stiffness predicted by PreComp is exactly the same as the case without shear web mentioned in the previous example. This indicates that PreComp does not account for the effects of shear webs in the calculation of torsional stiffness. Since CBCAS uses EBSFT to determine the torsional stiffness, the effects of shear webs are taken into account. Therefore, CBCAS can provide more realistic torsional stiffness than PreComp.

6.3. Case study C

The final case study aims to verify improved accuracy of torsional stiffness calculation of CBCSA by comparing CBCSA and PreComp with the experimental data [25]. The example considered here is an extension-torsional coupled blade with two-cell cross-section [25], as shown in Fig. 11.

The skin of the cross-section has $[15/-15]$ layups whereas the D-type spar consists of $[0/15]_2$. The geometric data and material properties of the blade are listed in Table 9.

Both CBCSA and PreComp are used to calculate the properties of the cross-section. Predicted values are compared with measured values reported in Ref. [25], as shown in Table 10.

Table 8
Calculated cross-sectional properties of an isotropic blade cross-section with two shear webs.

Cross-sectional properties	ANSYS	CBCAS	%Diff. (CBCAS)	PreComp	%Diff. (PreComp)
EA (N)	4.9057E+07	5.1396E+07	4.77	5.1400E+07	4.78
EI_X (N-m^2)	1.0439E+03	1.1121E+03	6.53	1.1120E+03	6.52
EI_Y (N-m^2)	4.8368E+04	5.1601E+04	6.68	5.3190E+04	9.97
GJ (N-m^2)	1.2480E+03	1.1871E+03	4.88	1.0850E+03	13.06
μ (kg/m)	1.8304E+00	1.9212E+00	4.96	1.9210E+00	4.95

Fig. 11. Two-cell cross-section.

Table 9
Geometric data and material properties of the blade [25].

Properties	Values
E_1 (GPa)	131
E_2 (GPa)	9.3
G_{12} (GPa)	5.86
ν_{12}	0.4
Airfoil	NACA0012
Length (m)	0.6414
Chord (m)	0.0762
Ply thickness (m)	0.000127

From Table 10 we can see that a good correlation is achieved between CBCSA and experimental data. The torsional stiffness predicted by CBCSA is more accurate than that obtained from PreComp.

7. Conclusion

In this work, a novel mathematical model and method for accurate and rapid calculation of the cross-sectional properties of wind turbine blades has been developed by incorporating the classical lamination theory (CLT) with the extended Bredt-Batho shear flow theory (EBSFT). The mathematical model considers both the web effects and warping effects of the blades, and is presented in a code called CBCSA (Composite Blade Cross-Section Analysis), developed using Matlab. A series of benchmark computational tests are performed for isotropic and composite blades, and the results demonstrate that:

1) CBCSA can rapidly extract the cross-sectional properties of the composite blades, usually in a fraction of a second, which is much faster than a finite-element method.
2) Good agreement is achieved in comparison with the data from experiment and finite-element analysis, which indicates CBCSA has sufficient accuracy for the calculation of the cross-sectional properties of the composite blades.
3) CBCSA provides a more accurate torsional stiffness calculation than previously available tool PreComp due to the consideration of the shear web effects by using EBSFT.

It is believed that CBCSA can be used as a useful pre-processor, which can accurately and rapidly calculate the cross-sectional

Table 10
Cross-sectional properties of the two-cell cross-section.

Cross-sectional properties	Experiment [25]	CBCSA	%Error (CBCSA)	PreComp	%Error (PreComp)
EA (N)	–	8.1336E+06	–	8.1340E+06	–
EI_X (N-m^2)	7.7141E+01	8.1449E+01	5.58	8.1531E+01	5.69
EI_Y (N-m^2)	–	3.4529E+03	–	3.4530E+03	–
GJ (N-m^2)	2.5427E+01	2.4443E+01	3.87	1.9330E+01	23.98
μ (kg/m)	–	1.3485E-01	–	1.3480E-01	–

properties of modern wind turbine blades made from composites, thus providing important information for both structural dynamics and aeroelasticity analysis of the blades, and also for topological structure optimization of the blades.

References

[1] David M, Daniel L. Modeling of blades as equivalent beams for aeroelastic analysis. In: 41st aerospace sciences meeting and exhibit. American Institute of Aeronautics and Astronautics; 2003.
[2] Bir G. User's guide to PreComp (pre-processor for computing composite blade properties). National Renewable Energy Laboratory (NREL); 2006.
[3] David M, Daniel L. Identification and use of blade physical properties. In: 43rd AIAA aerospace sciences meeting and exhibit. American Institute of Aeronautics and Astronautics; 2005.
[4] Laird DL, Ashwill TD. Introduction to NuMAD: a numerical manufacturing and design tool. Albuquerque, NM (United States): Sandia National Labs; 1997.
[5] Malcolm DJ, Laird DL. Extraction of equivalent beam properties from blade models. Wind Energy 2007;10:135–57.
[6] Cesnik CES, Hodges DH. VABS: a new concept for composite rotor blade cross-sectional modeling. J Am Helicopter Soc 1997;42:27–38.
[7] Chen H, Yu W. Manual of PreVABS. Utah State University; 2008.
[8] Blasques JP. User's manual for BECAS. Technical University of Denmark; 2012.
[9] Giavotto V, Borri M, Mantegazza P, Ghiringhelli G, Carmaschi V, Maffioli G, et al. Anisotropic beam theory and applications. Comput Structures 1983;16:403–13.
[10] Bitsche RD. Airfoil2BECAS: a preprocessor for the cross-section analysis software BECAS. Technical University of Denmark; 2012.
[11] Reddy JN. Mechanics of laminated composite plates and shells: theory and analysis. CRC; 2003.
[12] Timoshenko S, Woinowsky-Krieger S, Woinowsky S. Theory of plates and shells. New York: McGraw-hill; 1959.
[13] Jones RM. Mechanics of composite materials. Hemisphere Pub; 1999.
[14] Lee J, Lee S. Flexural–torsional behavior of thin-walled composite beams. Thin-walled Struct 2004;42:1293–305.
[15] Lee J, Kim SE, Hong K. Lateral buckling of I-section composite beams. Eng Structures 2002;24:955–64.
[16] Bir G, Migliore P. Preliminary structural design of composite blades for two- and three-blade rotors. National Renewable Energy Laboratory; 2004.
[17] Librescu L, Song O. Thin-walled composite beams: theory and application. Springer; 2006.
[18] Pilkey WD. Analysis and design of elastic beams. Wiley Online Library; 2002.
[19] Shama M. Torsion and shear stresses in ships. Springer; 2010.
[20] Berthelot JM. Composite materials: mechanical behavior and structural analysis. Springer Verlag; 1999.
[21] Kaw AK. Mechanics of composite materials. CRC Press; 2006.
[22] Bauchau O, Craig JI. Aerospace structural analysis. Atlanta, GA: Georgia Institute of Technology; 2002.
[23] Beer FP, Johnston ER. Vector mechanics for engineers. Tata McGraw-Hill Education; 1988.
[24] Laird DL, Laboratories SN. NuMAD user's manual. Sandia National Laboratories; 2001.
[25] Chandra R, Chopra I. Structural behavior of two-cell composite rotor blades with elastic couplings. AIAA J 1992;30:2914–21.

G2. Paper 2

Lin Wang, Xiongwei Liu, Nathalie Renevier, Matthew Stables, and George M. Hall, "Nonlinear aeroelastic modelling for wind turbine blades based on blade element momentum theory and geometrically exact beam theory ," *Energy* 76 (2014): 487-501.

Energy xxx (2014) 1–15

Contents lists available at ScienceDirect

Energy

journal homepage: www.elsevier.com/locate/energy

Nonlinear aeroelastic modelling for wind turbine blades based on blade element momentum theory and geometrically exact beam theory

Lin Wang [a], Xiongwei Liu [b, *], Nathalie Renevier [a], Matthew Stables [a], George M. Hall [a]

[a] School of Computing, Engineering and Physical Sciences, University of Central Lancashire, Preston PR1 2HE, UK
[b] Sustainable Engineering, University of Cumbria, Energus, Workington CA14 4JW, UK

ARTICLE INFO

Article history:
Received 25 March 2014
Received in revised form
6 August 2014
Accepted 11 August 2014
Available online xxx

Keywords:
Wind turbine blade
Nonlinear
Aeroelastic model
Large blade deflections
BEM (Blade element momentum)
GEBT (Geometrically exact beam theory)

ABSTRACT

Due to the increasing size and flexibility of large wind turbine blades, accurate and reliable aeroelastic modelling is playing an important role for the design of large wind turbines. Most existing aeroelastic models are linear models based on assumption of small blade deflections. This assumption is not valid anymore for very flexible blade design because such blades often experience large deflections. In this paper, a novel nonlinear aeroelastic model for large wind turbine blades has been developed by combining BEM (blade element momentum) theory and mixed-form formulation of GEBT (geometrically exact beam theory). The nonlinear aeroelastic model takes account of large blade deflections and thus greatly improves the accuracy of aeroelastic analysis of wind turbine blades. The nonlinear aeroelastic model is implemented in COMSOL Multiphysics and validated with a series of benchmark calculation tests. The results show that good agreement is achieved when compared with experimental data, and its capability of handling large deflections is demonstrated. Finally the nonlinear aeroelastic model is applied to aeroelastic modelling of the parked WindPACT 1.5 MW baseline wind turbine, and reduced flapwise deflection from the nonlinear aeroelastic model is observed compared to the linear aeroelastic code FAST (Fatigue, Aerodynamics, Structures, and Turbulence).

1. Introduction

In the past decade, wind energy has received tremendous attention from the public, politicians and energy industry due to its potential to tackle the energy security and climate change, and wind turbine technology has experienced great advancement. The power rating of wind turbines has gone up to 8 MW recently [1], and the potential of 10–20 MW wind turbine is being investigated [2]. The increasing size of large wind turbines introduces several new technical challenges, and one of the major challenges facing wind turbine designers today is the aeroelastic effect of the wind turbine blades, which is caused by the interaction between the aerodynamic loads on the blades and the structural dynamics of the blades [3]. Specifically, during the operation of a wind turbine, the blades experience deformation due to aerodynamic loads exerted by the airflow passing the blades. The deformed blade affects, in turn, the flow field around the blade, which in return influences the aerodynamic loads on the blade. The interaction between the aerodynamic loads and structural deformation may result in aeroelastic problems, such as flapwise instability, edgewise instability and flutter, which can be devastating to the blades and wind turbine [4]. Therefore, developing a reliable and efficient aeroelastic model to investigate aeroelastic characterisation of wind turbine blades is of great importance for the development of large wind turbines.

Due to the fact that the aeroelastic effects are introduced by the interaction between the aerodynamic loads and structural deformation, an aeroelastic model should contain an aerodynamic part to calculate the aerodynamic loads and a structural part to determine the structural dynamic responses.

For the aerodynamic part, four types of aerodynamic models have been used in aeroelastic modelling of wind turbine blades, including BEM (blade element momentum) model, lifting panel and vortex model, actuator line model and CFD (computational fluid dynamic) model. The BEM model, which is the combination of blade element theory and blade momentum theory, was originally proposed by Glauert [5] and then improved by several researchers through introducing corrections, such as Prandtl's tip

* Corresponding author. Tel.: +44 (0)7553109009; fax: +44 (0)1524842337.
E-mail addresses: Xiongwei.Liu@Cumbria.ac.uk, xiongweiliu@263.net (X. Liu).

http://dx.doi.org/10.1016/j.energy.2014.08.046
0360-5442/

Please cite this article in press as: Wang L, et al., Nonlinear aeroelastic modelling for wind turbine blades based on blade element momentum theory and geometrically exact beam theory, Energy (2014), http://dx.doi.org/10.1016/j.energy.2014.08.046

Nomenclature

a,a'	axial and angular induction factors, respectively
b_1,b_2,b_3	orthonormal triad of un-deformed blade frame b
B_1,B_2,B_3	orthonormal triad of deformed blade frame B
c	chord
C_l,C_d	lift and drag coefficients, respectively
C_T	thrust coefficient
$\boldsymbol{C^{bG}}$,$\boldsymbol{C^{Gb}}$,$\boldsymbol{C^{bB}}$,$\boldsymbol{C^{Bb}}$,$\boldsymbol{C^{GB}}$,$\boldsymbol{C^{BG}}$	transformation matrices between frames
dF_N, dF_T	blade-element normal and tangential forces per unit length, respectively
$\boldsymbol{e}$	unit vector describing the rotation axis
$\boldsymbol{e}_1$	$[1 \quad 0 \quad 0]^T$
$\boldsymbol{f_B}$	column matrix that contains applied forces per unit length measured in frame B
$\boldsymbol{F_B}$,$\boldsymbol{F_G}$	column matrices that contain the force resultants measured in frames B and G, respectively
$F_{\text{tip}-\text{loss}}$	Prandtl tip loss factor
$\boldsymbol{F_c^G}$,$\boldsymbol{F_c^B}$	centrifugal-load vector with respect to frames G and B, respectively
$\boldsymbol{M_B}$,$\boldsymbol{M_G}$	column matrices that contain the moment resultants measured in frames B and G, respectively
$\boldsymbol{P_B}$,$\boldsymbol{P_G}$	column matrices that contain the linear momentum measured in frames B and G, respectively
r	distance from blade element to the rotor centre
R	blade radius
$\boldsymbol{S}$	constitutive matrix
$\boldsymbol{S_E}$	strain energy
t_1,t_2	arbitrary fixed times
T	transpose symbol
$\boldsymbol{u_b}$	column matrix that contains displacement of beam reference line measured in frame b
U_{rel}	relative wind speed
$\boldsymbol{v_b}$	column matrix that contains linear velocity of the un-deformed beam reference line measured in frame b
$\boldsymbol{V_B}$,$\boldsymbol{V_G}$	column matrices that contain linear velocities of deformed beam reference line measured in frames B and G, respectively
EA,GJ	axial and torsional stiffness, respectively
$\boldsymbol{\theta}$,$\boldsymbol{\theta_G}$	Rodrigues parameters
θ_p	twist angle of each blade element
ρ	air density
σ'	local solidity
B_N	number of blade
$\boldsymbol{F_g^G}$,$\boldsymbol{F_g^B}$	gravity-load vector with respect to frames G and B, respectively
$\boldsymbol{F_{\text{aero}}^B}$	aerodynamic-load vector
$\boldsymbol{F_{\text{AL}}^B}$	applied-load vector
g	gravity constant
G_1,G_2,G_3	orthonormal triad of global frame G
$\boldsymbol{H_G}$,$\boldsymbol{H_B}$	column matrices that contain the angular momentum measured in frames G and B, respectively
i_2,i_3	flapwise and edgewise moments of inertia, respectively
$\boldsymbol{I_M}$	mass matrix
$\boldsymbol{k_b}$	curvature vector for the un-deformed beam
$\boldsymbol{K_B}$	curvature vector for the deformed beam
$\boldsymbol{K_E}$	kinetic energy
L	length of the blade
$\boldsymbol{m_B}$	column matrix that contains applied moments per unit length measured in frame B
EI_2,EI_3	edgewise and flapwise bending stiffness, respectively
GK_2,GK_3	edgewise and flapwise shear stiffness, respectively
α	angle of attack
β_1,β_2,β_3	cone angle, tilt angle, azimuth angle, respectively
β_r	magnitude of rotation
δ	Lagrangean variation
$\delta\boldsymbol{A}$	virtual action at the ends of time interval and at the ends of the blade
$\overline{\delta\boldsymbol{q_B}}$,$\delta\boldsymbol{u_G}$	virtual displacement measured in frames B and G, respectively
$\delta\boldsymbol{W}$	virtual work of applied loads
$\overline{\delta\psi_B}$,$\overline{\delta\psi_G}$	virtual rotation measured in frames B and G, respectively
φ	angle of relative wind
$\boldsymbol{\gamma}$,$\boldsymbol{\kappa}$	column matrices that contain force and momentum strains, respectively
μ	mass per unit length of each blade element
$\boldsymbol{\omega_b}$,$\boldsymbol{\omega_G}$	column matrices that contain angular velocity of the un-deformed beam reference line measured in frames b and G, respectively
Ω	rotor rotational speed
$\boldsymbol{\Omega_B}$,$\boldsymbol{\Omega_G}$	column matrices that contain angular velocities of deformed beam reference line measured in frames B and G, respectively
$(\tilde{\cdot})$	defines a second-order, skew-symmetric tensor corresponding to the given vector

loss correction [6] and thrust coefficient correction [7]. Compared to other aerodynamic models, the BEM model is fast (i.e. efficient) and able to provide accurate results (i.e. reliable) when reliable airfoil aerodynamic data are available. For this reason, BEM model has been used for the aerodynamic part by most aeroelastic codes [4]. In order to better model the wake dynamics of wind turbines, the lifting panel and vortex model [8], in which the trailing and shed vorticity in the wake are represented by lifting lines or surfaces, also found applications in aeroelastic codes. However, this model tends to diverge due to intrinsic singularities of the vortex panels in the developing wake [9]. The actuator line model, in which the blade is represented by a line with distributed loads on the line and the flow field around the blade is governed by Navier–Stokes equations, was originally developed by Sørensen [10] for improving the accuracy of the wake modelling. However, solving the Navier–Stokes equations is more time-consuming than BEM, and the actuator line model, in which the distributed loads on the blade are calculated based on blade element theory and tabulated airfoil data, does not predict aerodynamic loads more accurately than the BEM model [11]. With the advancement of computing resources, CFD has received great attention in recent years. The CFD method solves the governing equations of fluid flow at thousands of positions on and around the blade in an iterative process, which does not require predetermined airfoil's aerodynamic data for the calculation. However, the CFD method is incapable of providing reliable results when high angle of attack occurs [12], which limits its application in aeroelastic modelling of certain types of wind turbines, e.g. stall-controlled turbines. Additionally, the CFD method is still computationally too expensive and not efficient enough for fluid-structure interaction analysis, which is the major barrier of its application in aeroelastic modelling [13]. Concerning computational accuracy and efficiency,

Please cite this article in press as: Wang L, et al., Nonlinear aeroelastic modelling for wind turbine blades based on blade element momentum theory and geometrically exact beam theory, Energy (2014), http://dx.doi.org/10.1016/j.energy.2014.08.046

the BEM model is chosen as the aerodynamic part of aeroelastic modelling in this study.

For the structural part, wind turbine blades can be modelled using either 3D (three-dimensional) FEM (finite-element method) with shell elements or 1D (one-dimensional) equivalent beam model with beam elements. The 3D FEM is an incredible tool for examining the stress distribution within a blade, which is applicable and valuable for "static" stress analysis. However, the 3D FEM is computationally too expensive and this drawback limits its application in aeroelastic modelling, which demands continuous fluid-structure interaction, i.e. interactive aerodynamic loads calculation and structure deflection analysis. Compared to the 3D FEM, the 1D beam model is much fast and saves much computational time and is capable of providing reasonable accuracy, which is only slightly less accurate than 3D FEM [14]. For this reason, in the present study, wind turbine blade structure is represented as a series of 1D beam elements instead of 3D shell elements. The 1D beam elements are characterised by cross-sectional properties, e.g. sectional stiffness, which can be obtained using cross-sectional analysis tools, such as VABS [15], PreComp [16] and CBCSA [17].

In order to discretise the blade into a series of 1D beam elements, three methods are often used in aeroelastic modelling of wind turbine blades [13]: modal approach, MBD (multi-body dynamics) and 1D FEM (finite-element method). The modal approach, in which the blade deflection shape is described as a linear combination of a few shape functions, is computationally efficient due to the simple way of reducing the number of degrees of freedom. The MBD method, which connects different rigid parts through springs and hinges, is computationally more expensive than the modal approach. The 1D FEM approach finds approximate solutions of 1D beam problems by the analysis of an assemblage of finite elements, which are interconnected by nodal points. The 1D FEM allows a more comprehensive and accurate deformation description of wind turbine blades, and it only requires slightly more computational resources than the other two discretisation approaches. Therefore, the 1D FEM is adopted for the discretization of wind turbine blades in this study.

There are several aeroelastic models available today for wind turbine blades, such as PHATAS (Program for Horizontal Axis wind Turbine Analysis Simulation) [18], FAST (Fatigue, Aerodynamics, Structures, and Turbulence) [19] and GH (Garrad Hassan)-Bladed [20]. Almost all of them are linear models based on assumption of small blade deflections, and do not take account of large deflection effects on modelling responses and loads [13]. However, with the increasing size and flexibility of large wind turbine blades, this assumption is not valid anymore because the blades often experience large deflections, which introduce significant geometric nonlinearities. Therefore, developing a nonlinear aeroelastic model to take account of geometric nonlinearities is essential for accurate aeroelastic modelling of large wind turbine blades.

So far, only few nonlinear aeroelastic models have been developed. One example is HAWC2 (Horizontal Axis Wind turbine simulation Code 2nd generation) [21], which is an in-house nonlinear aeroelastic model developed by DTU (Technical University of Denmark). The aerodynamic model of HAWC2 is based on BEM and its structural model is based on a MBD formulation where each body is a linear Timoshenko beam element, which is an extension of Euler-Bernoulli beam element [22] to cover shear deformation. The geometric nonlinearities are captured by the MBD formulation, in which the flexible blades are modelled, for example, by 40 bodies each. However, if only one body per blade is used, HAWC2 will become a linear model because the Timoshenko beam model in each body is linear. In other words, the results of HAWC2 are sensitive to the number of bodies, which one chooses to model the flexible blade. Additionally, HAWC2 contains assumption that relative displacement between two adjacent bodies is small and it assumes some simplifications for the kinematic equations, which introduces uncertainties in its results.

An alternative way to handle the geometric nonlinearities is the GEBT (geometrically exact beam theory) [23], in which the deformed beam geometry, i.e. the displacements and rotations of the beam reference line, is represented exactly. Various nonlinear formulations have been proposed for GEBT, which can be classified on the basis of solution methodology, namely displacement-based formulation, strain-based formulation and mixed-form formulation [24]. The main differences between these formulations are the definition of the independent variables and the treatment of the rotation of the beam reference line in the solution. The displacement-based formulation defines the displacements and rotations of the beam reference line as the irreducible set of independent variables, which include high order nonlinearities. The main advantage of this formulation is that the displacement constraints can be easily applied. However, the solution of this formulation demands high computational cost due to its high order nonlinearities. In order to solve the geometrically nonlinear beam problems more efficiently, an alternative way is the strain-based formulation, which uses the strains and curvatures of the beam reference line as the primary variables to represent the beam deformation. A more efficient way to solve the geometrically nonlinear beams is to use the mixed-form formulation proposed by Hodges [25], which introduces Lagrange multipliers to satisfy the equations of motion with constitutive and kinematic relationships. The mixed-from formulation allows the lowest order of shape functions for all independent variables, which makes it a viable solution for modelling geometric nonlinearities, and it has been widely used for flexible aircraft wings [26].

The similarities between the aircraft wings and wind turbine blades, i.e. both of them are long, slender and flexible structures, provide us with the possibility to borrow the aeroelastic modelling techniques from aircraft applications for wind turbine blades. To the best of the authors' knowledge, the combination of BEM and GEBT for aeroelastic modelling of wind turbine blades has not been found in the literature. This paper attempts to combine BEM with the mixed-form formulation of GEBT proposed by Hodges [25] to develop a nonlinear aeroelastic model, which takes account of large blade deflections. An aerodynamic model is developed using MATLAB based on BEM theory with both Prandtl's tip loss correction [6] and thrust coefficient correction [27]. A blade structural model is established based on the mixed-form formulation of GEBT [25] and discretised by a 1D finite-element scheme using COMSOL Multiphysics [28]. The coupling of the blade aerodynamic model and structural model is implemented in COMSOL Multiphysics. The resulting nonlinear aeroelastic model is validated by a series of benchmark tests as compared with FAST and experimental data, and applied to aeroelastic modelling of the parked WindPACT 1.5 MW baseline wind turbine [29], a representative of megawatt-class horizontal-axis wind turbines.

This paper is structured as follows. Section 2 describes the main coordinate systems used in this study. Section 3 introduces the aerodynamic loads calculation based on BEM. The gravity loads and centrifugal loads are summarised in Section 4, and the applied loads are illustrated in Section 5. Section 6 details the blade structural model based on a mixed formulation of GEBT. Section 7 illustrates the implementation of the nonlinear aeroelastic model in COMSOL Multiphysics. Results and discussions are provided in Section 8, followed by a conclusion in Section 9.

2. Coordinate systems

In order to fully describe the geometry and deflection of a wind turbine blade for aeroelastic modelling, this paper adopts three

Please cite this article in press as: Wang L, et al., Nonlinear aeroelastic modelling for wind turbine blades based on blade element momentum theory and geometrically exact beam theory, Energy (2014), http://dx.doi.org/10.1016/j.energy.2014.08.046

coordinate systems, i.e. the global frame, which aligns with the wind turbine rotor and defines the rotor parameters; the un-deformed blade frame, which aligns with the original blade and defines the blade parameters; and the deformed blade frame, which aligns with the deformed blade. This section illustrates the three coordinate systems and the transformation matrices among them.

2.1. Main coordinate systems

Three main coordinate systems, i.e. the global frame G, the un-deformed blade frame b and the deformed blade frame B, are chosen for the analysis of wind turbine blades, as shown in Fig. 1. The global frame G, having its axes labelled G_1, G_2, and G_3, is rotating along with the wind turbine rotor. Axes G_2 and G_3 are along with and perpendicular to the wind turbine rotor axis, respectively. The un-deformed blade frame b, having its axes labelled b_1, b_2, and b_3, is attached to each un-deformed blade element. Axes b_2 and b_3, located in each un-deformed airfoil plane, are perpendicular and parallel to the chord line of each un-deformed blade element, respectively. The deformed blade frame B, having its axes B_1, B_2, and B_3, is attached to each deformed blade element. Axes B_2 and B_3, located in each deformed airfoil plane, are perpendicular and parallel to the chord line of each deformed blade element, respectively. All the three coordinate systems obey the right hand rule.

2.2. Transformation matrices

A vector given in a frame can be transformed into another frame using transformation matrices. The transformation matrix $\boldsymbol{C^{bG}}$, which transfers vectors from the global frame G into the un-deformed blade frame b, is given by:

$$\boldsymbol{C^{bG}} = \begin{bmatrix} 1 & 0 & 0 \\ 0 & \cos\theta_p & \sin\theta_p \\ 0 & -\sin\theta_p & \cos\theta_p \end{bmatrix} \begin{bmatrix} \cos\beta_1 & -\sin\beta_1 & 0 \\ \sin\beta_1 & \cos\beta_1 & 0 \\ 0 & 0 & 1 \end{bmatrix} \tag{1}$$

where β_1 is the rotor cone angle (see Fig. 2a), the angle between the blade axis and rotor plane; θ_p is the twist angle of each blade element (see Fig. 2b), the angle between the chord line and the blade reference plane. Obviously, the transformation matrix $\boldsymbol{C^{bG}}$ is time independent, i.e. $\dot{\boldsymbol{C}}^{\boldsymbol{bG}} = 0$.

According to Euler's theorem of rigid-body motion [25], any rotational motion can be characterized by the magnitude of rotation β_r and a 3-by-1 unit vector $\boldsymbol{e}$, which describes the rotation axis. On the basis of the Euler's theorem, the transformation matrix $\boldsymbol{C^{Bb}}$, which transfers vectors from the un-deformed blade frame b into the deformed blade frame B, can be expressed in terms of Rodrigues parameters [25] $\boldsymbol{\theta}$ as:

$$\boldsymbol{C^{Bb}} = \frac{\left(1 - \frac{1}{4}\boldsymbol{\theta}^T\boldsymbol{\theta}\right)\Delta + \frac{1}{2}\boldsymbol{\theta}\boldsymbol{\theta}^T - \tilde{\boldsymbol{\theta}}}{1 + \frac{1}{4}\boldsymbol{\theta}^T\boldsymbol{\theta}} \tag{2}$$

where T is the transpose symbol; $\boldsymbol{\Delta}$ is the 3-by-3 identity matrix $\begin{bmatrix} 1 & 0 & 0 \\ 0 & 1 & 0 \\ 0 & 0 & 1 \end{bmatrix}$; $\boldsymbol{\theta} = 2\boldsymbol{e}\tan(\beta_r/2)$; $\boldsymbol{e} = [\,\mathrm{e1} \quad \mathrm{e2} \quad \mathrm{e3}\,]^T$ and $\boldsymbol{e}^T\boldsymbol{e} = 1$.

Introducing another set of Rodrigues parameters $\boldsymbol{\theta_G}$ such that $\boldsymbol{\theta_G} = (\boldsymbol{C^{bG}})^T\boldsymbol{\theta}$, the transformation vector $\boldsymbol{C^{BG}}$, which transfers vectors given in the global frame G into the deformed blade frame B, is obtained by:

$$\boldsymbol{C^{BG}} = \boldsymbol{C^{bG}}\boldsymbol{C} \tag{3}$$

where

$$\boldsymbol{C} = \frac{\left(1 - \frac{1}{4}\boldsymbol{\theta_G^T}\boldsymbol{\theta_G}\right)\Delta + \frac{1}{2}\boldsymbol{\theta_G}\boldsymbol{\theta_G^T} - \tilde{\boldsymbol{\theta}}_{\boldsymbol{G}}}{1 + \frac{1}{4}\boldsymbol{\theta_G^T}\boldsymbol{\theta_G}} \tag{4}$$

Having obtained $\boldsymbol{C^{Bb}}$ and $\boldsymbol{C^{BG}}$, the following relations can be easily established:

$$\boldsymbol{C^{bB}} = \left(\boldsymbol{C^{Bb}}\right)^T \tag{5}$$

$$\boldsymbol{C^{GB}} = \left(\boldsymbol{C^{BG}}\right)^T \tag{6}$$

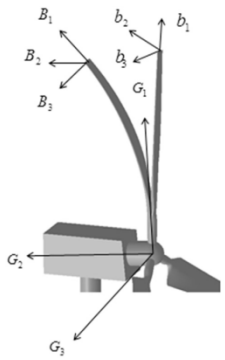

Fig. 1. Main coordinate systems.

3. Aerodynamic loads

In this study, the aerodynamic loads are calculated based on BEM theory, which has been widely used in industrial practice to predict aerodynamic loads on wind turbine blades.

BEM theory was developed through the combination of blade element theory and blade momentum theory. The blade element theory discretises the blade into several elements and ignores the mutual influence between two adjacent elements. The aerodynamic loads on each element are dependent on its local airfoil characteristics, i.e. its lift and drag coefficients. The sum of these loads yields the total loads on the blade. The blade momentum theory introduces the axial induction factor a and angular induction factor a' to calculate the induced velocity in the axial and tangential directions, respectively. The induced velocity will affect the angle of attack of the blade thereby influencing the aerodynamic loads calculated by the above blade element theory. Combining blade element theory and blade momentum theory provides a solution to obtain the performance parameters of each blade element, such as axial induction factor a and angular induction factor a', through an iterative procedure, which is summarized below [30,31]:

1) Use an estimate to obtain the initial axial induction factor a and angular induction factor a'. In this study, zero initial values are used for both axial induction factor a and angular induction factor a':

Please cite this article in press as: Wang L, et al., Nonlinear aeroelastic modelling for wind turbine blades based on blade element momentum theory and geometrically exact beam theory, Energy (2014), http://dx.doi.org/10.1016/j.energy.2014.08.046

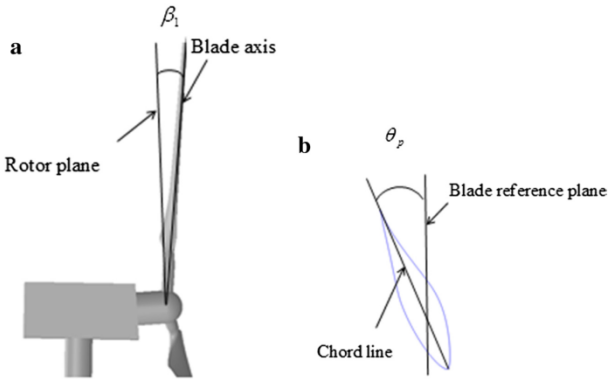

Fig. 2. a. Rotor cone angle. b. blade-element twist angle.

$$a_1 = 0 \tag{7}$$

$$a'_1 = 0 \tag{8}$$

2) Start the iterative procedure for the jth iteration. For the first iteration ($j = 1$), follow step 1. Calculate the relative wind angle φ_j and the Prandtl tip loss factor $F_{\text{tip}\_\text{loss},j}$:

$$\varphi_j = \arctan\left(\frac{(1-a_j)V_0 + v_{\text{op}}}{(1+a'_1)\Omega r + v_{\text{ip}}}\right) \tag{9}$$

$$F_{\text{tip-loos},j} = \left(\frac{2}{\pi}\right)\cos^{-1}\left[\exp\left(-\left(\frac{(B_N/2)[1-(r/R)]}{(r/R)\sin\varphi_j}\right)\right)\right] \tag{10}$$

where v_{op} and v_{ip} are the blade element velocities, and they are generally ignored if the blade motion is small; V_0 is the upcoming wind velocity on each blade element; Ω is the rotor rotation speed; r is the distance from the blade element to the rotor centre; B_N is the number of blade; R is the blade radius. In this study, V_0 and r are calculated based on the deformed blade geometry to take account of the blade deflection in the calculation of aerodynamic loads.

The Prandtl tip loss factor $F_{\text{tip}\_\text{loss},j}$ in Eq. (10) is used to take account of the influence of vortices shedding from the blade tip on the induced velocity. From Eq. (10) we can see that the Prandtl tip loss factor is always between 0 and 1.

3) Determine the local angle of attack of the blade element:

$$\alpha_j = \varphi_j - \theta_p \tag{11}$$

Then obtain the lift coefficient $C_{l,j}$ and drag coefficient $C_{d,j}$ from the airfoil lift and drag coefficient curve against the angle of attack.

4) Update the axial induction factor a and angular induction factor a' for the next iteration, considering the drag effects:

$$a_{j+1} = \frac{1}{\left[1 + \frac{4F_{\text{tip}-\text{loss},j}\sin^2(\varphi_j)}{\sigma'(C_{l,j}\cos\varphi_j + C_{d,j}\sin\varphi_j)}\frac{1}{H}\right]} \tag{12}$$

$$a'_{j+1} = \frac{1}{\frac{4F_{\text{tip}-\text{loss},j}\sin\varphi_j\cos\varphi_j}{\sigma'(C_{l,j}\sin\varphi_j - C_{d,j}\cos\varphi_j)} - 1} \tag{13}$$

The parameter σ' in Eq. (12) is the local solidity, defined by:

$$\sigma' = B_N c/2\pi r \tag{14}$$

where c is the chord of the blade element.

The parameter H in Eq. (12) is used for the situation when large axial induction factor occurs. When the axial induction factor a is greater than 0.5, the expression of thrust coefficient [30]:

$$C_T = 4a(1-a) \tag{15}$$

needs to be replaced by the empirical expression [27]:

$$C_T = 0.6 + 0.61a + 0.79a^2 \tag{16}$$

To obtain a better transition, the above empirical model is used for the situation that a is greater than 0.3539 rather than 0.5 [27].

The parameter H is defined as [27]:

$$\text{for } a_{j+1} \le 0.3539,\ H = 1.0 \tag{17}$$

$$\text{for } a_{j+1} > 0.3539,\ H = \frac{4a(1-a)}{(0.6 + 0.61a + 0.79a^2)} \tag{18}$$

The above process is repeated until the deviation between the new and previous induction factors is within an acceptable

Please cite this article in press as: Wang L, et al., Nonlinear aeroelastic modelling for wind turbine blades based on blade element momentum theory and geometrically exact beam theory, Energy (2014), http://dx.doi.org/10.1016/j.energy.2014.08.046

tolerance. Then confirm the local relative wind angle ϕ, tip loss factor $F_{\text{tip}-\text{loss}}$, angle of attack α, lift coefficient C_l, and drag coefficient C_d for each blade element.

Having determined the above performance parameters for each blade element, the normal force per unit length $\mathrm{d}F_N$ and tangential force per unit length $\mathrm{d}F_T$ on each blade element are respectively calculated by:

$$\mathrm{d}F_N = F_{\text{tip}-\text{loss}}\frac{1}{2}\rho U_{\text{rel}}^2\Big(C_l\cos\varphi + C_d\sin\varphi\Big)c \tag{19}$$

$$\mathrm{d}F_T = F_{\text{tip}-\text{loss}}\frac{1}{2}\rho U_{\text{rel}}^2\Big(C_l\sin\varphi - C_d\cos\varphi\Big)c \tag{20}$$

where ρ is the air density, U_{rel} is the relative wind velocity.

The above aerodynamic loads on each blade element are calculated with respect to the deformed blade frame B and can be stored in the aerodynamic-load vector $\boldsymbol{F}_{\mathbf{aero}}^{\boldsymbol{B}}$:

$$\boldsymbol{F}_{\mathbf{aero}}^{\boldsymbol{B}} = \begin{bmatrix} 0 \\ \mathrm{d}F_N \\ \mathrm{d}F_T \end{bmatrix} \tag{21}$$

4. Gravity loads and centrifugal loads

In addition to aerodynamic loads, the gravity loads and centrifugal loads on each blade element should be taken into account in the calculation of the applied loads, which are applied on the deformed blade structure as distributed loads.

4.1. Gravity loads

For large wind turbine blades, gravity is an important source of loading. Taking account of the tilt angle β_2 (see Fig. 3a), the angle between the shaft and the horizontal axis, and the azimuth angle β_3 (see Fig. 3b), the position of the blade in the circumferential direction of the wind turbine rotor axis, the gravity-load vector $\boldsymbol{F}_{\boldsymbol{g}}^{\boldsymbol{G}}$ of a blade element with respect to the global frame G is given by:

$$\boldsymbol{F}_{\boldsymbol{g}}^{\boldsymbol{G}} = \begin{bmatrix} \cos\beta_3 & 0 & -\sin\beta_3 \\ 0 & 1 & 0 \\ \sin\beta_3 & 0 & \cos\beta_3 \end{bmatrix}\begin{bmatrix} \cos\beta_2 & \sin\beta_2 & 0 \\ -\sin\beta_2 & \cos\beta_2 & 0 \\ 0 & 0 & 1 \end{bmatrix}\begin{bmatrix} -g\mu \\ 0 \\ 0 \end{bmatrix} \tag{22}$$

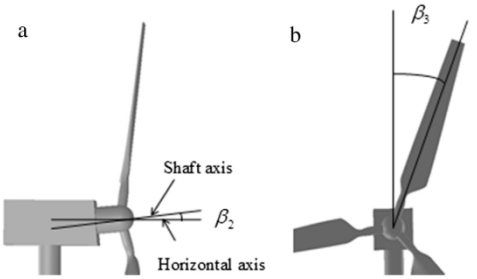

Fig. 3. a. Tilt angle. b. Azimuth angle.

where g is the gravity constant, μ is the mass per unit length of each blade element.

In this study, loads will be applied on the deformed blade structure. Therefore, the load vector $\boldsymbol{F}_{\boldsymbol{g}}^{\boldsymbol{G}}$ with respect to the global frame G needs to be transformed into the deformed blade frame B using the following equation:

$$\boldsymbol{F}_{\boldsymbol{g}}^{\boldsymbol{B}} = \boldsymbol{C}^{\boldsymbol{BG}}\boldsymbol{F}_{\boldsymbol{g}}^{\boldsymbol{G}} \tag{23}$$

4.2. Centrifugal loads

Due to the rotation of the wind turbine blades, centrifugal loads have to be considered. Taking account of the azimuth angle β_3, the centrifugal-load vector $\boldsymbol{F}_{\boldsymbol{c}}^{\boldsymbol{G}}$ of a blade element with respect to the global frame G is given by:

$$\boldsymbol{F}_{\boldsymbol{c}}^{\boldsymbol{G}} = \begin{bmatrix} \cos\beta_3 & 0 & -\sin\beta_3 \\ 0 & 1 & 0 \\ \sin\beta_3 & 0 & \cos\beta_3 \end{bmatrix}\begin{bmatrix} r\Omega^2\,\mu \\ 0 \\ 0 \end{bmatrix} \tag{24}$$

The load vector $\boldsymbol{F}_{\boldsymbol{c}}^{\boldsymbol{G}}$ can be transformed into the deformed blade frame B using the following equation:

$$\boldsymbol{F}_{\boldsymbol{c}}^{\boldsymbol{B}} = \boldsymbol{C}^{\boldsymbol{BG}}\boldsymbol{F}_{\boldsymbol{c}}^{\boldsymbol{G}} \tag{25}$$

5. Applied loads

Having obtained the aerodynamic load $\boldsymbol{F}_{\boldsymbol{aero}}^{\boldsymbol{B}}$, gravity load $\boldsymbol{F}_{\boldsymbol{g}}^{\boldsymbol{B}}$ and centrifugal load $\boldsymbol{F}_{\boldsymbol{c}}^{\boldsymbol{B}}$ on each blade element, the applied load $\boldsymbol{F}_{\boldsymbol{AL}}^{\boldsymbol{B}}$ on each blade element is obtained by summing these loads (in vector form):

$$\boldsymbol{F}_{\mathbf{AL}}^{\boldsymbol{B}} = \boldsymbol{F}_{\mathbf{aero}}^{\boldsymbol{B}} + \boldsymbol{F}_{\boldsymbol{g}}^{\boldsymbol{B}} + \boldsymbol{F}_{\boldsymbol{c}}^{\boldsymbol{B}} \tag{26}$$

6. Structural model

To perform aeroelastic analysis of wind turbine blades, a structural model, which determines the blade structural dynamic responses, has to be included. In this study, wind turbine blades are modelled based on a mixed-form formulation of GEBT (geometrically exact beam theory), which will be detailed in this section.

6.1. Equations of motion

The geometrically exact equations of motion, which exactly describe the behaviour of an initially curved and twisted beam as a set of mathematical functions in terms of spatial coordinates and time, can be derived from Hamilton's extended principle, kinetic energy and strain energy.

6.1.1. Hamilton's extended principle

Hamilton's extended principle is expressed as [25]:

$$\int_{t_1}^{t_2}\int_0^L [\delta(\boldsymbol{K}_{\boldsymbol{E}} - \boldsymbol{S}_{\boldsymbol{E}}) + \delta\boldsymbol{W}]\mathrm{d}x_1\mathrm{d}t = \delta\boldsymbol{A} \tag{27}$$

where t_1 and t_2 are arbitrary fixed times; L is the length of the blade; δ is the Lagrangean variation operator for a fixed time; $\boldsymbol{K}_{\boldsymbol{E}}$

Please cite this article in press as: Wang L, et al., Nonlinear aeroelastic modelling for wind turbine blades based on blade element momentum theory and geometrically exact beam theory, Energy (2014), http://dx.doi.org/10.1016/j.energy.2014.08.046

and $\boldsymbol{S_E}$ are the kinetic and strain energy, respectively; $\boldsymbol{\delta W}$ is the virtual work of applied loads; $\boldsymbol{\delta A}$ is the virtual action at the ends of time interval and at the ends of the blade.

6.1.2. Kinetic energy

The variation of kinetic energy required in Eq. (27) can be written as:

$$\delta \boldsymbol{K_E} = \delta \boldsymbol{V_B^T} \boldsymbol{P_B} + \delta \boldsymbol{\Omega_B^T} \boldsymbol{H_B} \tag{28}$$

where $\boldsymbol{V_B}$ and $\boldsymbol{\Omega_B}$ are the column matrices that contain linear and angular velocities of the deformed beam reference line measured in the frame B, respectively; $\boldsymbol{P_B}$ and $\boldsymbol{H_B}$ are the column matrices that contain the linear and angular momenta measured in the frame B, respectively. $\delta \boldsymbol{V_B^T}$ and $\delta \boldsymbol{\Omega_B^T}$ can be expressed in terms of the virtual displacement $\overline{\delta \boldsymbol{q_B}}$ and virtual rotation $\overline{\delta \boldsymbol{\psi_B}}$ using the following equations [25]:

$$\delta \boldsymbol{V_B^T} = \overline{\dot{\delta \boldsymbol{q_B}}}^{\,T} - \overline{\delta \boldsymbol{q_B}}^{\,T} \tilde{\boldsymbol{\Omega}}_{\boldsymbol{B}} - \overline{\delta \boldsymbol{\psi_B}}^{\,T} \tilde{\boldsymbol{V}}_{\boldsymbol{B}} \tag{29}$$

$$\delta \boldsymbol{\Omega_B^T} = \overline{\dot{\delta \boldsymbol{\psi_B}}}^{\,T} - \overline{\delta \boldsymbol{\psi_B}}^{\,T} \tilde{\boldsymbol{\Omega}}_{\boldsymbol{B}} \tag{30}$$

where the overhead dot denotes the time derivative; the overhead tilde operator $\tilde{(\cdot)}$ defines a second-order, skew-symmetric tensor corresponding to the given vector. For example, given $\boldsymbol{\Omega_B} = [\,\Omega_{B1} \quad \Omega_{B2} \quad \Omega_{B3}\,]^T$, $\tilde{\boldsymbol{\Omega}}_{\boldsymbol{B}}$ can be expressed as:

$$\tilde{\boldsymbol{\Omega}}_{\boldsymbol{B}} = \begin{bmatrix} 0 & -\Omega_{B3} & \Omega_{B2} \\ \Omega_{B3} & 0 & -\Omega_{B1} \\ -\Omega_{B2} & \Omega_{B1} & 0 \end{bmatrix} \tag{31}$$

Substituting Eqs. (29) and (30) into Eq. (28) gives:

$$\begin{aligned} \delta \boldsymbol{K_E} = & \left(\overline{\dot{\delta \boldsymbol{q_B}}}^{\,T} - \overline{\delta \boldsymbol{q_B}}^{\,T} \tilde{\boldsymbol{\Omega}}_{\boldsymbol{B}} - \overline{\delta \boldsymbol{\psi_B}}^{\,T} \tilde{\boldsymbol{V}}_{\boldsymbol{B}} \right) \boldsymbol{P_B} \\ & + \left(\overline{\dot{\delta \boldsymbol{\psi_B}}}^{\,T} - \overline{\delta \boldsymbol{\psi_B}}^{\,T} \tilde{\boldsymbol{\Omega}}_{\boldsymbol{B}} \right) \boldsymbol{H_B} \end{aligned} \tag{32}$$

6.1.3. Strain energy

The variation of strain energy required in Eq. (27) can be written as:

$$\delta \boldsymbol{S_E} = \delta \boldsymbol{\gamma}^T \boldsymbol{F_B} + \delta \boldsymbol{\kappa}^T \boldsymbol{M_B} \tag{33}$$

where $\boldsymbol{\gamma}$ and $\boldsymbol{\kappa}$ are the column matrices that contain force and moment strains, respectively; $\boldsymbol{F_B}$ and $\boldsymbol{M_B}$ are the column matrices that contain the force and moment resultants measured in the frame B, respectively. $\delta \boldsymbol{\gamma}^T$ and $\delta \boldsymbol{\kappa}^T$ can be expressed in terms of the virtual displacement $\overline{\delta \boldsymbol{q_B}}$ and virtual rotation $\overline{\delta \boldsymbol{\psi_B}}$ using the following equations [25]:

$$\delta \boldsymbol{\gamma}^T = \left(\overline{\delta \boldsymbol{q_B}}' \right)^T - \overline{\delta \boldsymbol{q_B}}^{\,T} \tilde{\boldsymbol{K}}_{\boldsymbol{B}} - \overline{\delta \boldsymbol{\psi_B}}^{\,T} (\tilde{\boldsymbol{e}}_1 + \tilde{\boldsymbol{\gamma}}) \tag{34}$$

$$\delta \boldsymbol{\kappa}^T = \left(\overline{\delta \boldsymbol{\psi_B}}' \right)^T - \overline{\delta \boldsymbol{\psi_B}}^{\,T} \tilde{\boldsymbol{K}}_{\boldsymbol{B}} \tag{35}$$

where $\boldsymbol{K_B}$ is the curvature vector for the deformed beam; $\boldsymbol{e}_1 = [\,1 \quad 0 \quad 0\,]^T$; the prime symbol $()'$ denotes the spatial derivative.

Substituting Eqs. (34) and (35) into Eq. (33) gives:

$$\begin{aligned} \delta \boldsymbol{S_E} = & \left(\left(\overline{\delta \boldsymbol{q_B}}' \right)^T - \overline{\delta \boldsymbol{q_B}}^{\,T} \tilde{\boldsymbol{K}}_{\boldsymbol{B}} - \overline{\delta \boldsymbol{\psi_B}}^{\,T} (\tilde{\boldsymbol{e}}_1 + \tilde{\boldsymbol{\gamma}}) \right) \boldsymbol{F_B} \\ & + \left(\left(\overline{\delta \boldsymbol{\psi_B}}' \right)^T - \overline{\delta \boldsymbol{\psi_B}}^{\,T} \tilde{\boldsymbol{K}}_{\boldsymbol{B}} \right) \boldsymbol{M_B} \end{aligned} \tag{36}$$

6.1.4. Geometrically exact equations of motion

The virtual work of the applied loads appearing in Eq. (27) is given by:

$$\delta \boldsymbol{W} = \overline{\delta \boldsymbol{q_B}}^{\,T} \boldsymbol{f_B} + \overline{\delta \boldsymbol{\psi_B}}^{\,T} \boldsymbol{m_B} \tag{37}$$

where $\boldsymbol{f_B}$ and $\boldsymbol{m_B}$ are column matrices that contain applied forces and moments per unit length measured in the frame B, respectively.

Recalling that $\delta \boldsymbol{A}$ in Eq. (27) is the virtual action at the ends of the time interval and at the ends of the blade, the mathematical expression of $\delta \boldsymbol{A}$ can be written as:

$$\delta \boldsymbol{A} = \int_0^L \left(\overline{\delta \boldsymbol{q_B}}^{\,T} \widehat{\boldsymbol{P}}_{\boldsymbol{B}} + \overline{\delta \boldsymbol{\psi_B}}^{\,T} \widehat{\boldsymbol{H}}_{\boldsymbol{B}} \right) \Big|_{t_1}^{t_2} \mathrm{d}x_1 - \int_{t_1}^{t_2} \left(\overline{\delta \boldsymbol{q_B}}^{\,T} \widehat{\boldsymbol{F}}_{\boldsymbol{B}} + \overline{\delta \boldsymbol{\psi_B}}^{\,T} \widehat{\boldsymbol{M}}_{\boldsymbol{B}} \right) \Big|_0^L \mathrm{d}t \tag{38}$$

where the overhead hat denotes the discrete boundary values.

Substituting Eqs. (32) and (36)–(38) into Eq. (27) yields:

$$\begin{aligned} & \int_{t_1}^{t_2} \int_0^L \Bigg\{ \left(\overline{\dot{\delta \boldsymbol{q_B}}}^{\,T} - \overline{\delta \boldsymbol{q_B}}^{\,T} \tilde{\boldsymbol{\Omega}}_{\mathbf{B}} - \overline{\delta \boldsymbol{\psi_B}}^{\,T} \tilde{\mathbf{V}}_{\mathbf{B}} \right) \mathbf{P}_{\mathbf{B}} + \left(\overline{\dot{\delta \boldsymbol{\psi_B}}}^{\,T} \right. \\ & \left. - \overline{\delta \boldsymbol{\psi_B}}^{\,T} \tilde{\boldsymbol{\Omega}}_{\boldsymbol{B}} \right) \boldsymbol{H_B} - \left(\left(\overline{\delta \boldsymbol{q_B}}' \right)^T - \overline{\delta \boldsymbol{q_B}}^{\,T} \tilde{\mathbf{K}}_{\mathbf{B}} - \overline{\delta \boldsymbol{\psi_B}}^{\,T} (\tilde{\boldsymbol{e}}_1 + \tilde{\boldsymbol{\gamma}}) \right) \boldsymbol{F_B} \\ & - \left(\left(\overline{\delta \boldsymbol{\psi_B}}' \right)^T - \overline{\delta \boldsymbol{\psi_B}}^{\,T} \tilde{\boldsymbol{K}}_{\boldsymbol{B}} \right) \boldsymbol{M_B} + \overline{\delta \boldsymbol{q_B}}^{\,T} \boldsymbol{f_B} + \overline{\delta \boldsymbol{\psi_B}}^{\,T} \boldsymbol{m_B} \Bigg\} \mathrm{d}x_1 \mathrm{d}t \\ & = \int_0^L \left(\overline{\delta \boldsymbol{q_B}}^{\,T} \widehat{\boldsymbol{P}}_{\boldsymbol{B}} + \overline{\delta \boldsymbol{\psi_B}}^{\,T} \widehat{\boldsymbol{H}}_{\boldsymbol{B}} \right) \Big|_{t_1}^{t_2} \mathrm{d}x_1 - \int_{t_1}^{t_2} \left(\overline{\delta \boldsymbol{q_B}}^{\,T} \widehat{\boldsymbol{F}}_{\boldsymbol{B}} + \overline{\delta \boldsymbol{\psi_B}}^{\,T} \widehat{\boldsymbol{M}}_{\boldsymbol{B}} \right) \Big|_0^L \mathrm{d}t \end{aligned} \tag{39}$$

After integrating Eq. (39) by parts with respect to the time to remove the time derivatives of the virtual quantities, one obtains:

$$\begin{aligned} & \int_{t_1}^{t_2} \int_0^L \Bigg\{ \left(\overline{\delta \boldsymbol{q_B}}' \right)^T \boldsymbol{F_B} + \left(\overline{\delta \boldsymbol{\psi_B}}' \right)^T \boldsymbol{M_B} + \overline{\delta \boldsymbol{q_B}}^{\,T} \Big(- \tilde{\boldsymbol{K}}_{\boldsymbol{B}} \boldsymbol{F_B} \\ & + \dot{\boldsymbol{P}}_{\boldsymbol{B}} + \tilde{\boldsymbol{\Omega}}_{\boldsymbol{B}} \boldsymbol{P_B} \Big) + \overline{\delta \boldsymbol{\psi_B}}^{\,T} \Big(- \tilde{\boldsymbol{K}}_{\boldsymbol{B}} \boldsymbol{M_B} - (\tilde{\boldsymbol{e}}_1 + \tilde{\boldsymbol{\gamma}}) \boldsymbol{F_B} + \dot{\boldsymbol{H}}_{\boldsymbol{B}} \\ & + \tilde{\boldsymbol{\Omega}}_{\boldsymbol{B}} \boldsymbol{H_B} + \tilde{\boldsymbol{V}}_{\boldsymbol{B}} \boldsymbol{P_B} \Big) - \overline{\delta \boldsymbol{q_B}}^{\,T} \boldsymbol{f_B} - \overline{\delta \boldsymbol{\psi_B}}^{\,T} \boldsymbol{m_B} \Bigg\} \mathrm{d}x_1 \mathrm{d}t \\ & = \int_{t_1}^{t_2} \left(\overline{\delta \boldsymbol{q_B}}^{\,T} \widehat{\boldsymbol{F}}_{\boldsymbol{B}} + \overline{\delta \boldsymbol{\psi_B}}^{\,T} \widehat{\boldsymbol{M}}_{\boldsymbol{B}} \right) \Big|_0^L \mathrm{d}t \end{aligned} \tag{40}$$

Eq. (40) is the geometrically exact equations of motion of a beam expressed in the frame B.

6.2. Mixed variational formula of nonlinear beam

Apart from the equations of motion derived in above section, the kinematical and constitutive relations are required in order to have a complete formulation to solve problems in general.

Please cite this article in press as: Wang L, et al., Nonlinear aeroelastic modelling for wind turbine blades based on blade element momentum theory and geometrically exact beam theory, Energy (2014), http://dx.doi.org/10.1016/j.energy.2014.08.046

6.2.1. Kinematical relations

According to Hodges [25], the inverse kinematical relations are given by:

$$\boldsymbol{u}_{\boldsymbol{b}}' = \boldsymbol{C}^{\boldsymbol{bB}}(\boldsymbol{e}_1 + \boldsymbol{\gamma}) - \boldsymbol{e}_1 - \tilde{\boldsymbol{k}}_{\boldsymbol{b}}\boldsymbol{u}_{\boldsymbol{b}} \tag{41}$$

$$\dot{\boldsymbol{u}}_{\boldsymbol{b}} = \boldsymbol{C}^{\boldsymbol{bB}}\boldsymbol{V}_{\boldsymbol{B}} - \boldsymbol{v}_{\boldsymbol{b}} - \tilde{\omega}_{\boldsymbol{b}}\boldsymbol{u}_{\boldsymbol{b}} \tag{42}$$

$$\boldsymbol{\theta}' = \left(\Delta + \frac{1}{2}\tilde{\boldsymbol{\theta}} + \frac{1}{4}\boldsymbol{\theta}\boldsymbol{\theta}^T\right)\left(\boldsymbol{\kappa} + \boldsymbol{k}_{\boldsymbol{b}} - \boldsymbol{C}^{\boldsymbol{Bb}}\boldsymbol{k}_{\boldsymbol{b}}\right) \tag{43}$$

$$\dot{\boldsymbol{\theta}} = \left(\Delta + \frac{1}{2}\tilde{\boldsymbol{\theta}} + \frac{1}{4}\boldsymbol{\theta}\boldsymbol{\theta}^T\right)\left(\boldsymbol{\Omega}_{\boldsymbol{B}} - \boldsymbol{C}^{\boldsymbol{Bb}}\boldsymbol{\omega}_{\boldsymbol{b}}\right) \tag{44}$$

where $\boldsymbol{u_b}$ is the column matrix that contains displacement of the beam reference line measured in the frame b; $\boldsymbol{\theta}$ is the column matrix that contains Rodrigues parameters; $\boldsymbol{k_b}$ is the curvature vector for the un-deformed beam; $\boldsymbol{v_b}$ is the column matrix that contains velocity of the un-deformed beam reference line measured in the frame b; $\boldsymbol{\omega_b}$ is the column matrix that contains angular velocity of the un-deformed beam reference line measured in the frame b.

6.2.2. Constitute relations

For beams having small strain, the constitutive equations are linear. The generalized strain-force relations are given by:

$$\begin{Bmatrix} \boldsymbol{\gamma} \\ \boldsymbol{\kappa} \end{Bmatrix} = \boldsymbol{S}\begin{Bmatrix} \boldsymbol{F}_{\boldsymbol{B}} \\ \boldsymbol{M}_{\boldsymbol{B}} \end{Bmatrix} \tag{45}$$

where $\boldsymbol{S}$ is the constitutive matrix. If all coupling terms are ignored, the constitutive matrix $\boldsymbol{S}$ can be expressed as:

$$\boldsymbol{S} = \begin{bmatrix} 1/\mathrm{EA} & 0 & 0 & 0 & 0 & 0 \\ 0 & 1/\mathrm{GK}_2 & 0 & 0 & 0 & 0 \\ 0 & 0 & 1/\mathrm{GK}_3 & 0 & 0 & 0 \\ 0 & 0 & 0 & 1/\mathrm{GJ} & 0 & 0 \\ 0 & 0 & 0 & 0 & 1/\mathrm{EI}_2 & 0 \\ 0 & 0 & 0 & 0 & 0 & 1/\mathrm{EI}_3 \end{bmatrix} \tag{46}$$

where EA is the axial stiffness; GK_2 and GK_3 are the edgewise and flapwise shear stiffness, respectively; GJ is the torsional stiffness; EI_2 and EI_3 are the edgewise and flapwise bending stiffness, respectively. Note that if shear deformation is ignored, $1/\mathrm{GK}_2$ and $1/\mathrm{GK}_3$ in Eq. (46) become zero.

Similarly, the generalized momentum–velocity relations are given by:

$$\begin{Bmatrix} \boldsymbol{P}_{\boldsymbol{B}} \\ \boldsymbol{H}_{\boldsymbol{B}} \end{Bmatrix} = \boldsymbol{I}_{\boldsymbol{M}}\begin{Bmatrix} \boldsymbol{V}_{\boldsymbol{B}} \\ \boldsymbol{\Omega}_{\boldsymbol{B}} \end{Bmatrix} \tag{47}$$

where $\boldsymbol{I_M}$ is the mass matrix. If the locus of the mass centre is chosen as reference line, the mass matrix $\boldsymbol{I_M}$ can be expressed as:

$$\boldsymbol{I}_{\boldsymbol{M}} = \begin{bmatrix} \mu & 0 & 0 & 0 & 0 & 0 \\ 0 & \mu & 0 & 0 & 0 & 0 \\ 0 & 0 & \mu & 0 & 0 & 0 \\ 0 & 0 & 0 & i_2 + i_3 & 0 & 0 \\ 0 & 0 & 0 & 0 & i_2 & 0 \\ 0 & 0 & 0 & 0 & 0 & i_3 \end{bmatrix} \tag{48}$$

where μ is the mass per unit length of the blade element; i_2 and i_3 are edgewise and flapwise moments of inertia, respectively.

6.2.3. Closing the formulation

The inverse kinematical relations Eqs. (41)–(44) can be considered to be constraints to Eq. (40). These constraints can be introduced with the help of Lagrange multipliers [25]. Thus, the following formulation is obtained:

$$\begin{aligned}
&\int_{t_1}^{t_2}\int_0^L \Big\{ \left(\overline{\delta \boldsymbol{q}_{\boldsymbol{B}}}'\right)^T \boldsymbol{F}_{\boldsymbol{B}} + \left(\overline{\delta\psi_{\boldsymbol{B}}}'\right)^T \boldsymbol{M}_{\boldsymbol{B}} + \overline{\delta \boldsymbol{q}_{\boldsymbol{B}}}^T\left(-\tilde{\boldsymbol{K}}_{\boldsymbol{B}}\boldsymbol{F}_{\boldsymbol{B}} + \dot{\boldsymbol{P}}_{\boldsymbol{B}} + \tilde{\Omega}_{\boldsymbol{B}}\boldsymbol{P}_{\boldsymbol{B}}\right) + \overline{\delta\psi_{\boldsymbol{B}}}^T\left(-\tilde{\boldsymbol{K}}_{\boldsymbol{B}}\boldsymbol{M}_{\boldsymbol{B}} - (\tilde{\boldsymbol{e}}_1 + \tilde{\boldsymbol{\gamma}})\boldsymbol{F}_{\boldsymbol{B}} + \dot{\boldsymbol{H}}_{\boldsymbol{B}} + \tilde{\Omega}_{\boldsymbol{B}}\boldsymbol{H}_{\boldsymbol{B}} + \tilde{\boldsymbol{V}}_{\boldsymbol{B}}\boldsymbol{P}_{\boldsymbol{B}}\right) \\
&+\overline{\delta \boldsymbol{F}}^T\left(\boldsymbol{e}_1 + \tilde{\boldsymbol{k}}_{\boldsymbol{b}}\boldsymbol{u}_{\boldsymbol{b}} - \boldsymbol{C}^{\boldsymbol{bB}}(\boldsymbol{e}_1 + \boldsymbol{\gamma})\right) - \left(\overline{\delta \boldsymbol{F}}'\right)^T \boldsymbol{u}_{\boldsymbol{b}} + \overline{\delta \boldsymbol{M}}^T\left(\left(\Delta + \frac{1}{2}\tilde{\boldsymbol{\theta}} + \frac{1}{4}\boldsymbol{\theta}\boldsymbol{\theta}^{\boldsymbol{T}}\right)\left(\boldsymbol{C}^{\boldsymbol{Bb}}\boldsymbol{k}_{\boldsymbol{b}} - \boldsymbol{\kappa} - \boldsymbol{k}_{\boldsymbol{b}}\right)\right) - \left(\overline{\delta \boldsymbol{M}}'\right)^T \boldsymbol{\theta} - \overline{\delta \boldsymbol{P}}^T\left(\boldsymbol{v}_{\boldsymbol{b}} + \tilde{\omega}_{\boldsymbol{b}}\boldsymbol{u}_{\boldsymbol{b}} - \boldsymbol{C}^{\boldsymbol{bB}}\boldsymbol{V}_{\boldsymbol{B}}\right. \\
&\left.+\dot{\boldsymbol{u}}_{\boldsymbol{b}}\right) - \overline{\delta \boldsymbol{H}}^T\left(\left(\Delta + \frac{1}{2}\tilde{\boldsymbol{\theta}} + \frac{1}{4}\boldsymbol{\theta}\boldsymbol{\theta}^T\right)\left(\boldsymbol{C}^{\boldsymbol{Bb}}\boldsymbol{\omega}_{\boldsymbol{b}} - \boldsymbol{\Omega}_{\boldsymbol{B}}\right) + \dot{\boldsymbol{\theta}}\right) - \overline{\delta \boldsymbol{q}_{\boldsymbol{B}}}^T \boldsymbol{f}_{\boldsymbol{B}} - \overline{\delta\psi_{\boldsymbol{B}}}^T \boldsymbol{m}_{\boldsymbol{B}}\Big\}\mathrm{d}x_1\mathrm{d}t = \int_{t_1}^{t_2}\left(\overline{\delta \boldsymbol{q}_{\boldsymbol{B}}}^T \widehat{\boldsymbol{F}}_{\boldsymbol{B}} + \overline{\delta\psi_{\boldsymbol{B}}}^T \widehat{\boldsymbol{M}}_{\boldsymbol{B}} - \overline{\delta \boldsymbol{F}}^T \hat{\boldsymbol{u}}_{\boldsymbol{b}} - \overline{\delta \boldsymbol{M}}^T \hat{\boldsymbol{\theta}}\right)\Big|_0^L \mathrm{d}t
\end{aligned} \tag{49}$$

where

$$\overline{\delta \boldsymbol{F}} = \boldsymbol{C}^{\boldsymbol{bB}}\delta \boldsymbol{F}_{\boldsymbol{B}} \tag{50}$$

$$\overline{\delta \boldsymbol{M}} = \left(\frac{\Delta + \frac{1}{2}\tilde{\boldsymbol{\theta}}}{1 + \frac{1}{4}\boldsymbol{\theta}^T\boldsymbol{\theta}}\right)\delta \boldsymbol{M}_{\boldsymbol{B}} \tag{51}$$

$$\overline{\delta \boldsymbol{P}} = \boldsymbol{C}^{\boldsymbol{bB}}\delta \boldsymbol{P}_{\boldsymbol{B}} \tag{52}$$

$$\overline{\delta \boldsymbol{H}} = \left(\frac{\Delta + \frac{1}{2}\tilde{\boldsymbol{\theta}}}{1 + \frac{1}{4}\boldsymbol{\theta}^T\boldsymbol{\theta}}\right)\delta \boldsymbol{H}_{\boldsymbol{B}} \tag{53}$$

Eq. (49) is the mixed-form formulation of GEBT expressed in the frame B. The displacement and rotation components can be expressed in global frame G, which are independent of blade geometry and deflection, with the help of transformation matrices. The details will be discussed below.

$\tilde{\boldsymbol{K}}_{\boldsymbol{B}}$ and $\tilde{\Omega}_{\boldsymbol{B}}$ in Eq. (49) can be expressed in terms of $\boldsymbol{C}^{\boldsymbol{BG}}$ and $\boldsymbol{C}^{\boldsymbol{GB}}$ using [32]:

$$\tilde{\boldsymbol{K}}_{\boldsymbol{B}} = \boldsymbol{C}^{\boldsymbol{BG}}\left(\boldsymbol{C}^{\boldsymbol{GB}}\right)' \tag{54}$$

Please cite this article in press as: Wang L, et al., Nonlinear aeroelastic modelling for wind turbine blades based on blade element momentum theory and geometrically exact beam theory, Energy (2014), http://dx.doi.org/10.1016/j.energy.2014.08.046

$$\tilde{\Omega}_B = -\dot{C}^{BG}C^{GB} + C^{BG}\tilde{\omega}_G C^{GB} \tag{55}$$

where ω_G is the column matrix that contains the angular velocity of un-deformed beam reference line measured in frame G.

The virtual displacement $\overline{\delta q_B}$, virtual rotation $\overline{\delta\psi_B}$, linear momentum P_B, and angular momentum H_B measured in frame B are related to the virtual displacement δu_G, virtual rotation $\overline{\delta\psi_G}$, linear momentum P_G and angular momentum H_G measured in frame G by a transformation matrix C^{BG}, respectively:

$$\overline{\delta q_B} = C^{BG}\delta u_G \tag{56}$$

$$\overline{\delta\psi_B} = C^{BG}\overline{\delta\psi_G} \tag{57}$$

$$H_B = C^{BG}H_G \tag{58}$$

$$P_B = C^{BG}P_G \tag{59}$$

With the help of Eqs. (54)–(59), the following relations can be easily established:

$$\left(\overline{\delta q_B}'\right)^T F_B - \left(\overline{\delta q_B}\right)^T \tilde{K}_B F_B = \left(\delta u_G'\right)^T C^{GB}F_B \tag{60}$$

$$\left(\overline{\delta\psi_B}'\right)^T M_B - \left(\overline{\delta\psi_B}\right)^T \tilde{K}_B M_B = \left(\overline{\delta\psi_G}'\right)^T C^{GB}M_B \tag{61}$$

$$C^{GB}\left(\dot{H}_B + \tilde{\Omega}_B H_B\right) = \dot{H}_G + \tilde{\omega}_G C^{GB}H_B \tag{62}$$

$$C^{GB}\left(\dot{P}_B + \tilde{\Omega}_B P_B\right) = \dot{P}_G + \tilde{\omega}_G C^{GB}P_B \tag{63}$$

$\tilde{k}_b$ and $\tilde{\omega}_b$ in Eq. (49) can be expressed in terms of C^{bG} and C^{Gb} using [32]:

$$\tilde{k}_b = C^{bG}\left(C^{Gb}\right)' \tag{64}$$

$$\tilde{\omega}_b = C^{bG}\tilde{\omega}_G C^{Gb} \tag{65}$$

Defining $\overline{\delta F_G} = C^{Gb}\overline{\delta F}$, $\overline{\delta M_G} = C^{Gb}\overline{\delta M}$, $\overline{\delta P_G} = C^{Gb}\overline{\delta P}$, $\overline{\delta H_G} = (\Delta - \tilde{\theta}/2 + \theta\theta^T/4)\overline{\delta H}$, and with the help of Eqs. (56)–(65), Eq. (49) can be rewritten in the following form:

Eq. (66) is the mixed-form formulation of GEBT expressed in the global frame G. In Eq. (66), u_G, θ_G, F_B, M_B, P_B, and H_B are considered to be the fundamental unknown variables. γ and κ can be expressed in terms of F_B and M_B using Eq. (45). V_B and Ω_B are related to P_B and H_B through Eq. (47). Eq. (66) contains all the information needed for the finite-element implementation of the geometrically exact beam theory. In addition to time-dependent analysis and modal analysis, Eq. (66) can also be used for static analysis when all time-dependent variables in Eq. (66) are eliminated.

7. Implementation of the nonlinear aeroelastic model in COMSOL Multiphysics

COMSOL Multiphysics [28] is used to implement the nonlinear aeroelastic model. The choice is mainly based on the fact that COMSOL Multiphysics 1) allows equation-based modelling, e.g. the chance to define a PDE (partial differential equation) by its weak form; 2) enables MATLAB functions in model settings definition, such as boundary conditions and material properties; and 3) provides interfaces between its GUI (graphical user interface) and MATLAB, which enables direct use of MATLAB scripts in building COMSOL model.

Based on the methods discussed in Sections 3, 4 and 5, a MATLAB program is developed to calculate the applied loads F_{AL}^B (see Eq. (26)), including the aerodynamic loads (calculated based on BEM), gravity loads and centrifugal loads. The mixed-form formulation of GEBT (see Eq. (66)) is implemented using COMSOL 1D Weak Form PDE module. All parameters in Eq. (66) are defined as global and local variables. The combination of BEM and GEBT is achieved by replacing f_B in Eq. (66) with F_{AL}^B calculated using MATLAB program. The computational scheme of the nonlinear aeroelastic model can be divided into the following major steps:

1) Read input file. The main input parameters of the model are the blade structural properties, such as mass per unit length and cross-sectional stiffness, and blade aerodynamic shape, such as chord and twist. These parameters are stored in a .txt file which can be read by MATLAB function.
2) Construct blade geometry using a series of 1D elements. The blade is represented as a series of 1D elements and each element is allowed to have different cross-sectional properties, such as flapwise stiffness and edgewise stiffness [17]. The physics-controlled mesh tool with finer element size, which automati-

$$\int_{t_1}^{t_2}\int_0^L \Big\{\delta u_G'^T C^{GB}F_B + \left(\overline{\delta\psi_G}'\right)^T C^{GB}M_B + \delta u_G^T\left(\dot{P}_G + \tilde{\omega}_G C^{GB}P_B\right) + \overline{\delta\psi_G}^T\Big(-C^{GB}(\tilde{e}_1+\tilde{\gamma})F_B + \dot{H}_G + \tilde{\omega}_G C^{GB}H_B + C^{GB}\tilde{V}_B P_B\Big) + \overline{\delta F_G}^T\Big(-C^{GB}(\tilde{e}_1+\tilde{\gamma})+C^{Gb}\tilde{e}_1\Big) - \left(\overline{\delta F_G}'\right)^T u_G + \overline{\delta M_G}^T\Big(-\left(\Delta+\frac{1}{2}\tilde{\theta}_G+\frac{1}{4}\theta_G\theta_G^T\right)C^{Gb}\kappa\Big) - \left(\overline{\delta M_G}'\right)^T\theta_G + \overline{\delta P_G}^T\Big(C^{GB}V_B - C^{Gb}\tilde{v}_b - \tilde{\omega}_G u_G - \dot{u}_G\Big) + \overline{\delta H_G}^T\left(\Omega_B - \omega_B - C^{bG}\frac{\Delta - \tilde{\theta}_G/2}{1+\theta_G^T\theta_G/4}\dot{\theta}_G\right) - \delta u_G^T C^{GB}f_B - \overline{\delta\psi_G}^T C^{GB}m_B\Big\}dx_1 dt = \int_{t_1}^{t_2}\left(\overline{\delta u_G}^T\widehat{F}_G + \overline{\delta\psi_G}^T\widehat{M}_G - \overline{\delta F_G}^T\hat{u}_G - \overline{\delta M_G}^T\hat{\theta}_G\right)\Big|_0^L dt \tag{66}$$

Please cite this article in press as: Wang L, et al., Nonlinear aeroelastic modelling for wind turbine blades based on blade element momentum theory and geometrically exact beam theory, Energy (2014), http://dx.doi.org/10.1016/j.energy.2014.08.046

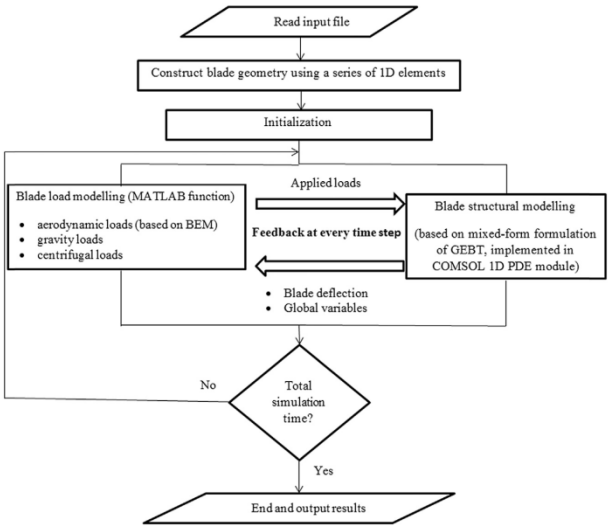

Fig. 4. Flowchart of the nonlinear aeroelastic model.

Table 1
Main parameters of the AWT-27CR2 wind turbine.

Parameters	Values
Rated power (kW)	300
Number of blade	2
Rotor radius (m)	13.757
Rated rotor speed (rpm)	53.333
Cone angle (deg.)	7
Tilt angle (deg.)	0

cally generates meshes that are adapted to the physics in the model, is used in COMSOL Multiphysics to create the mesh.

3) Initialize the independent variables, e.g. blade displacements, and global variables, e.g. time.

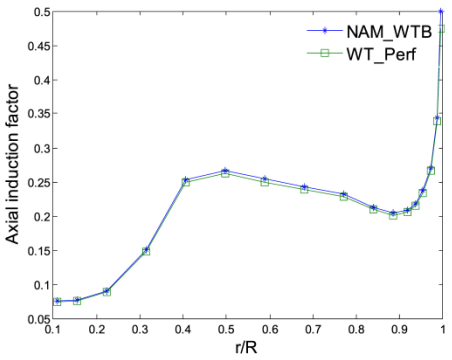

Fig. 5. Calculated axial induction factor distribution.

4) Perform blade load modelling to calculate the applied loads, including aerodynamic loads (based on BEM), gravity loads and centrifugal loads, using MATLAB function.
5) Apply the loads on the blade and perform blade structural modelling based on the fixed-form formulation of GEBT to calculate the deflection of the blade.
6) Go back to step 4 to update the applied loads according to the feedback of blade deflection and global variables.
7) If the current simulation time is less than total simulation time, repeat steps 5–6 using current solution as the initial values for the subsequent steps; otherwise, end the simulation and output results.

The flowchart of the nonlinear aeroelastic model is shown in Fig. 4.

8. Results and discussion

A new nonlinear aeroelastic model, NAM_WTB (Nonlinear Aeroelastic Model for Wind Turbine Blades), is developed based on the above flowchart and validated by a series of benchmark calculation tests. The main components of the NAM_WTB, i.e. the aerodynamic part based on BEM and the structural part based on mixed-form formulation of GEBT, are validated separately. Then a case study is performed to validate the aeroelastic simulation results. After the validation, the nonlinear aeroelastic model is applied to aeroelastic analysis of the parked WindPACT 1.5 MW baseline wind turbine.

8.1. Validation

The validation of the NAM_WTB comprises three parts: 1) validation of its aerodynamic part against an existing widely used aerodynamic code; 2) validation of its structural part against

Please cite this article in press as: Wang L, et al., Nonlinear aeroelastic modelling for wind turbine blades based on blade element momentum theory and geometrically exact beam theory, Energy (2014), http://dx.doi.org/10.1016/j.energy.2014.08.046

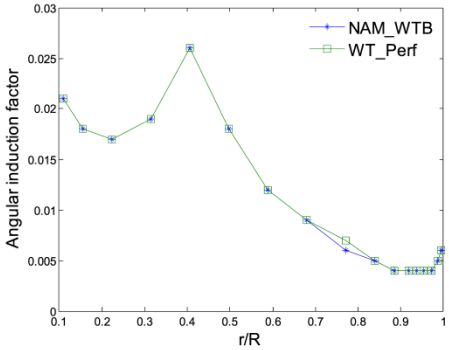

Fig. 6. Calculated angular induction factor distribution.

experimental data; and 3) validation of its aeroelastic simulation results against an existing well-known aeroelastic code.

8.1.1. Validation of the aerodynamic part of NAM_WTB

For the first case study, the aerodynamic part of the NAM_WTB is validated against WT_Perf [33], which is a wind turbine aerodynamic performance predictor developed by Andrew Platt at NREL (National Renewable Energy Laboratory) based on BEM theory. The wind turbine model used in this case study is the AWT-27CR2 wind turbine and the main parameters of the wind turbine are summarized in Table 1. The details of the AWT-27CR2 wind turbine, e.g. its airfoil aerodynamic data, can be found from the test file of WT_Perf [33].

Both NAM_WTB and WT_Perf are used to predict the aerodynamic performance of the AWT-27CR2 wind turbine. In this case, both yaw angle and pitch angle are 0°, and rotor speed is at rated value (53.333 rpm). For the sake of simplicity, the gravity loads and centrifugal loads of the blade are ignored, and the blade is assumed rigid, i.e. no deflections are considered in the calculation of the aerodynamic performance. Figs. 5–7 show the comparisons of the axial induction factor, angular induction factor and normal force distributions along the wind turbine blade at free stream wind speed of 12 m/s, respectively.

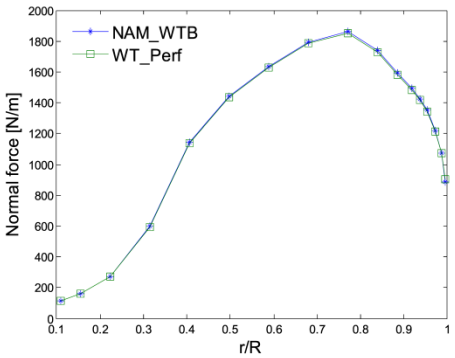

Fig. 7. Calculated normal force distribution.

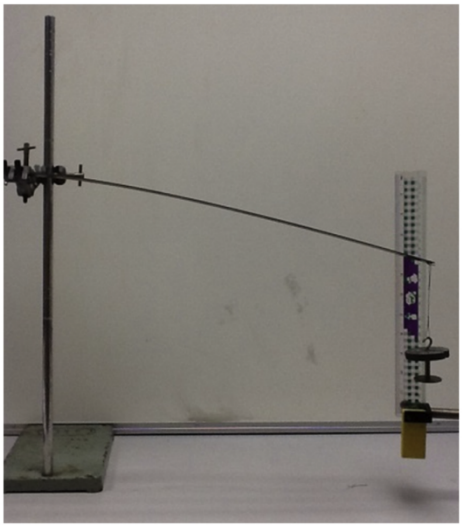

Fig. 8. Experimentally cantilever beam.

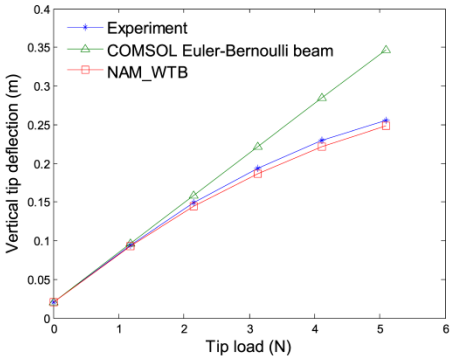

Fig. 9. Tip deflection of the cantilever beam.

Table 2
Tip deflection of the cantilever beam.

Tip load (N)	Vertical tip deflection (m)			%Diff. (COMSOL Euler-Bernoulli beam)	%Diff (NAM_WTB)
	Experiment	COMSOL Euler-Bernoulli beam	NAM_WTB		
0	0.0200	0.0206	0.0205	3.00	2.50
1.176	0.0940	0.0961	0.0926	2.23	1.49
2.156	0.1490	0.1588	0.1444	6.58	3.09
3.136	0.1930	0.2216	0.1870	14.82	3.11
4.116	0.2300	0.2843	0.2213	23.61	3.78
5.096	0.2550	0.3470	0.2486	36.08	2.51

Please cite this article in press as: Wang L, et al., Nonlinear aeroelastic modelling for wind turbine blades based on blade element momentum theory and geometrically exact beam theory, Energy (2014), http://dx.doi.org/10.1016/j.energy.2014.08.046

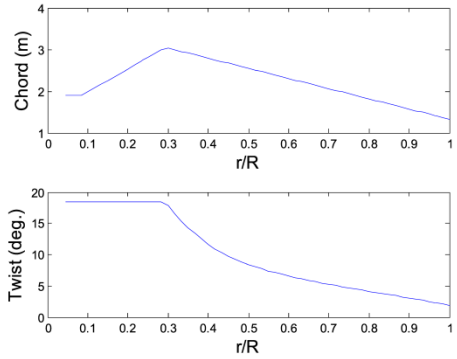

Fig. 10. Chord and twist distribution of the truncated RB70 wind turbine blade.

The results in Figs. 5–7 demonstrate that the calculated axial induction factor, angular induction factor and normal force distributions along the wind turbine blade from NAM_WTB agree with those from WT_Perf very well. This means that the aerodynamic part of NAM_WTB can be utilized well for aerodynamic loads predictions of wind turbine blades.

8.1.2. Validation of the structural part of NAM_WTB

In order to validate the structural part of NAM_WTB, two case studies have been performed. The first case study compares both the structural part of NAM_WTB and the COMSOL Euler-Bernoulli beam model with experimental results obtained in laboratory. The static deflections of an experimentally large-deflection cantilever beam are investigated in this case study. For the second case study, the modal analysis results from structural part of NAM_WTB are validated against experimental data, and a practical wind turbine blade is chosen as an example.

8.1.2.1. Static deflection of large-deflection beam. This case study aims to verify the accuracy of the structural part of NAM_WTB and demonstrate its nonlinear capability by comparing the structural

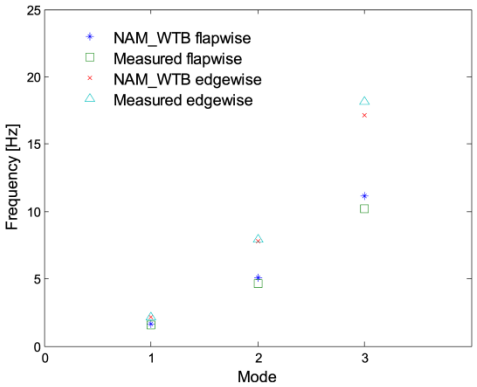

Fig. 11. Flapwise and edgewise mode frequencies of the truncated RB70 blade.

Table 3
Flapwise and edgewise mode frequencies of the truncated RB70 blade.

Mode	Measured values [36]	NAM_WTB	Diff. (%)
1st flapwise (Hz)	1.582	1.637	3.48
2nd flapwise (Hz)	4.630	5.061	9.31
3rd flapwise (Hz)	10.199	11.152	9.34
1st edgewise (Hz)	2.174	2.173	0.05
2nd edgewise (Hz)	7.962	7.772	2.39
3rd edgewise (Hz)	18.138	17.133	5.54

part of NAM_WTB and COMSOL Euler-Bernoulli beam model with experimental results obtained in the laboratory. The example used here is an experimentally large-deflection cantilever beam. Fig. 8 depicts the photograph of the experimental system, which is made up of a steel beam, fixed at one end and loaded at the free end. A vertical ruler is used to measure the vertical deflection of the beam at the free end. The length of the beam is 0.48 m and it has a uniform rectangular cross-section of width 0.02 m and height 0.0012 m.

Both NAM_WTB and COMSOL Euler-Bernoulli beam model are used to numerically calculate the tip deflection of the cantilever beam. The value of Young's modulus used in the numerical calculation is 2.0E11Pa (typical value of Young's modulus for steel). The weight of the beam, 0.87 N, is taken into account in the numerical calculation by applying a uniform distribution load over its entire length with the value of 1.81 N/m. Six values of tip load, i.e. 0, 1.176, 2.156, 3.136, 4.116 and 5.096 N, are used for both experimental test and numerical calculation. The comparison between the predicted vertical tip deflection and measured values are shown in Fig. 9 and Table 2, where relative differences are obtained with respect to the measured values.

From Fig. 9 and Table 2 we can see that 1) the tip deflections calculated using COMSOL Euler-Bernoulli beam model increase linearly and do not coincide with experimental data for the cases that tip loads over 3.136 N, with maximum percentage difference of 36.08% occurring when the tip load is 5.096 N; 2) the tip deflections predicted using NAM_WTB increases nonlinearly and show good agreement with experimental data for all cases, with the maximum percentage difference 3.78% occurring when the tip load is 4.116 N; 3) COMSOL Euler-Bernoulli beam model overestimates tip deflections when large deflections occur because it fails to capture geometric nonlinearities.

This case study clearly demonstrates that 1) NAW_WTB is capable of handling geometric nonlinearities arising from large deflections; 2) when the deflection is small, the error introduced by linear assumptions, e.g. the assumption adopted in COMSOL Euler-Bernoulli beam model, can be ignored; however, when large deflection occurs, the error introduced by linear assumptions should be quantified.

8.1.2.2. Modal analysis of truncated RB70 blade. This case study aims to validate the modal analysis results from the structural part of NAM_WTB against experimental data. The example used here is

Table 4
Main parameters of the NREL Phase VI wind turbine.

Parameters	Values
Rated power (kW)	20
Number of blade	2
Rotor radius (m)	5.029
Rated rotor speed (rpm)	71.9
Cone angle (deg.)	0
Tilt angle (deg.)	0

Please cite this article in press as: Wang L, et al., Nonlinear aeroelastic modelling for wind turbine blades based on blade element momentum theory and geometrically exact beam theory, Energy (2014), http://dx.doi.org/10.1016/j.energy.2014.08.046

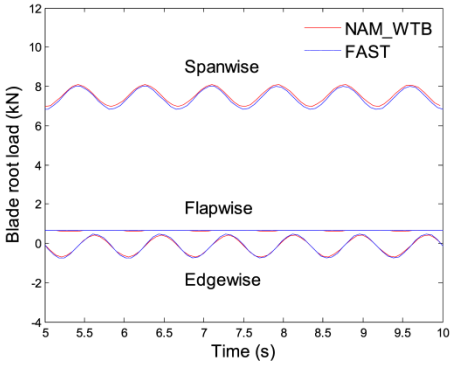

Fig. 12. Calculated blade root load.

the truncated RB70 wind turbine blade [34], which has been subjected to the eigenmode validation within the STABTOOL-3 research project [35]. The chord and twist distributions of the truncated RB70 wind turbine blade are depicted in Fig. 10, and its details can be obtained from Ref. [34].

NAM_WTB is used to perform modal analysis of the truncated RB70 blade. In this case study, the blade is non-rotating and free-vibration (no loads on the blade). The predicted values are compared with measured values reported in Ref. [36], as shown in Fig. 11 and Table 3, where the relative differences are obtained with respect to the measured values.

As can be seen from Fig. 11 and Table 3, the flapwise and edgewise blade mode frequencies calculated from NAM_WTB match well with experimental data, with the maximum percentage difference (9.34%) occurring for the 3rd flapwise mode.

This case study not only further validates the structural part of NAM_WTB, but also demonstrates that representing wind turbine blades as a series of 1D beam elements provides reasonable accuracy if the beam model is constructed properly.

8.1.3. Validation of aeroelastic simulation results of NAM_WTB

This case study aims to validate the NAM_WTB against FAST [19], which is a linear aeroelastic code developed by NREL based on combined BEM and modal approach. The wind turbine model used in this case study is NREL Phase VI wind turbine [37], which is a 10 m-diameter rotor research wind turbine. The main parameters of the turbine are listed in Table 4 and its details can be obtained from Ref. [37].

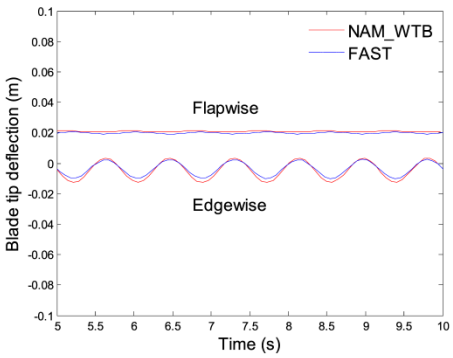

Fig. 13. Calculated blade tip deflection.

Both NAM_WTB and FAST are used to perform aeroelastic modelling of the NREL Phase VI rotor. In this case, yaw angle, pitch angle and rotor speed are 0°, 4.815° and 71.9 rpm, respectively. The gravity loads and centrifugal loads are taken into account, and the blade is considered flexible. The resulting blade root load and blade tip deflection at free stream wind speed of 7 m/s are shown in Figs. 12 and 13 respectively.

Figs. 12 and 13 demonstrate that the results from NAM_WTB show good agreement with those from FAST for this case study. Fig. 13 also indicates that the tip deflection of the blade used in this case study is very small, which is caused by the quite stiff blade design of the NREL Phase VI wind turbine. This case study demonstrates that both NAM_WTB and FAST work well for small deflections.

8.2. Aeroelastic simulation of parked WindPACT 1.5 MW baseline wind turbine

This case study aims to investigate the effects of large blade deflections on the aeroelastic modelling of wind turbine blades. The wind turbine model used in this case study is the WindPACT 1.5 MW baseline wind turbine [29], a reference turbine created by NREL. Its main parameters are summarized in Table 5. In order to investigate the large blade deflection effects, the flapwise stiffness of the WindPACT 1.5 MW wind turbine blade is adjusted by a factor of 0.2 to make the blade more flexible.

Both NAM_WTB and FAST are used to perform aeroelastic modelling of the parked WindPACT 1.5 MW wind turbine blade. In this case, yaw angle, pitch angle and rotor speed are 0°, 2° and 0 rpm, respectively. The resulting flapwise tip deflections at free-stream wind speeds between 15 m/s and 50 m/s are depicted in Fig. 14. For comparison purpose, Fig. 14 also presents the results from a linear aeroelastic model, BEM_COMSOL-Euler-Bernoulli-beam, which is based on combining BEM and COMSOL Euler-Bernoulli beam model and is implemented by replacing the structural part of NAM_WTB with COMSOL Euler-Bernoulli beam model.

Fig. 14 clearly shows that 1) the results from BEM_COMSOL-Euler-Bernoulli-beam show good agreement with the results from FAST for all cases; 2) for this case study, when wind speed is lower than 30 m/s, the results from NAM_WTB show good agreement with the results from FAST; 3) as wind speed further increases, the difference between NAM_WTB and FAST gets big, with maximum percentage difference 23%, which occurs for the case study when the wind speed achieves 50 m/s, and the blade tip deflection predicted by NAM_WTB is less than that predicted by FAST.

It should be noted that the only difference between BEM_COMSOL-Euler-Bernoulli-beam and NAM_WTB is that the

Table 5
Main parameters of the WindPACT 1.5 MW baseline wind turbine.

Parameters	Values
Rated power (MW)	1.5
Number of blade	3
Rotor radius (m)	35
Rated rotor speed (rpm)	20
Cone angle (deg.)	0
Tilt angle (deg.)	5

Please cite this article in press as: Wang L, et al., Nonlinear aeroelastic modelling for wind turbine blades based on blade element momentum theory and geometrically exact beam theory, Energy (2014), http://dx.doi.org/10.1016/j.energy.2014.08.046

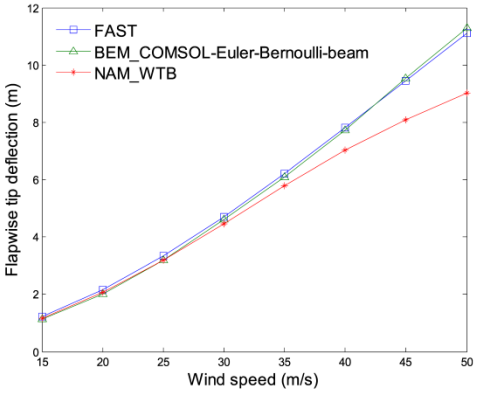

Fig. 14. Calculated flapwise tip deflection.

former one uses the COMSOL Euler-Bernoulli beam model for the structural part while the latter one uses GEBT. As demonstrated in the previous case study of the experimentally large-deflection cantilever beam, COMSOL Euler-Bernoulli beam model overestimates tip deflections when large deflections occur because it fails to capture geometric nonlinearities. Since NAM_WTB uses GEBT for the structural part, the effects of geometric nonlinearities are taken into account. Therefore, NAM_WTB can provide more reliable aeroelastic modelling than linear aeroelastic models, such as FAST and BEM_COMSOL-Euler-Bernoulli-beam, for the cases when large deflections occur.

This case study clearly demonstrates that when the blade deflection is small, the errors introduced by small deflection assumptions, e.g. the assumption adopted in FAST, can be ignored. However, as the blade deflection increases, the errors introduced by these assumptions should be quantified.

9. Conclusion

In this work, a novel nonlinear aeroelastic model for large wind turbine blades has been developed by combining BEM (blade element momentum) theory with a mixed-form formulation of GEBT (geometrically exact beam theory). The nonlinear aeroelastic model takes account of large blade deflections, and is presented here in a code called NAM_WTB (Nonlinear Aeroelastic Model for Wind Turbine Blades) based on COMSOL Multiphysics. NAM_WTB discretises the wind turbine blade into a series of 1D elements using 1D finite-element approach, which is computationally more efficient than 3D finite-element approaches. Validated by a series of benchmark computational tests, the nonlinear aeroelastic model was applied to the aeroelastic analysis of the parked WindPACT 1.5 MW baseline wind turbine. The following conclusions can be drawn from the present study:

1) The aerodynamic part of the NAM_WTB is sufficient accurate for aerodynamic load predictions of wind turbine blades.
2) Good agreement (with maximum percentage difference of 3.78%) is achieved in comparison with the data from experiment of a large-deflection cantilever beam, which indicates the NAM_WTB is capable of handling geometric nonlinearities resulted from large deflections.
3) Good agreement (with maximum percentage difference of 9.34%) is achieved in comparison with the data from modal experiment of a practical wind turbine blade, which further validates the structural part of NAM_WTB. It also demonstrates that representing the blades as a series of 1D beam elements provides reasonable accuracy if the beam model is constructed properly.
4) In case of small deflections, the results of the NAM_WTB are consistent with the results of the linear aeroelastic code FAST, which indicates geometric nonlinearities can be ignored for small blade deflections.
5) Taking account of geometric nonlinearities resulted from large blade deflections, significantly reduced tip deflection based on the presented NAM_WTB code is observed comparing with the linear aeroelastic code FAST. This difference in deflection could be vital for blade designers.

Based on the evidences presented in this paper, it is believed that the NAW_WTB code is a reliable and efficient nonlinear aeroelastic analysis tool for large wind turbine composite blades. Future works include aeroelastic optimisation based on NAW_WTB and aeroelastic experiments to provide more available experimental data for the benchmark test of the nonlinear aeroelastic model.

References

[1] http://vestas.com/en/products_and_services/turbines/v164-8_0-mw#!power-curve-and-aep; accessed 09.03.14.
[2] Peeringa J, Brood R, Ceyhan O, Engels W, Winkel Gd. Upwind 20 MW wind turbine pre-design. ECN; 2011. Paper No ECN-E–11–017.
[3] Hau E, Von Renouard H. Wind turbines: fundamentals, technologies, application, economics. Springer; 2013.
[4] Hansen MOL, Sørensen JN, Voutsinas S, Sørensen N, Madsen HA. State of the art in wind turbine aerodynamics and aeroelasticity. Prog Aerosp Sci 2006;42:285–330.
[5] Glauert H. Airplane propellers. Aerodyn Theory 1935;4:169–360.
[6] Vries O. Fluid dynamic aspects of wind energy conversion. DTIC Document; 1979.
[7] Buhl ML. A new empirical relationship between thrust coefficient and induction factor for the turbulent windmill state. National Renewable Energy Laboratory; 2005.
[8] Milne-Thomson LM. Theoretical aerodynamics. Courier Dover Publications; 1966.
[9] Mikkelsen R. Actuator disc methods applied to wind turbines. Technical University of Denmark; 2003.
[10] Sørensen JN, Shen WZ. Numerical modeling of wind turbine wakes. J Fluids Eng 2002;124:393–9.
[11] Rasmussen F, Hansen MH, Thomsen K, Larsen TJ, Bertagnolio F, Johansen J, et al. Present status of aeroelasticity of wind turbines. Wind Energy 2003;6:213–28.
[12] Zhang L, Liang Y, Liu X, Jiao Q, Guo J. Aerodynamic performance prediction of straight-bladed vertical axis wind turbine based on CFD. Adv Mech Eng 2013;2013.
[13] Zhang P, Huang S. Review of aeroelasticity for wind turbine: current status, research focus and future perspectives. Front Energy 2011;5:419–34.
[14] Malcolm DJ, Laird DL. Modeling of blades as equivalent beams for aeroelastic analysis. In: ASME wind energy symposium AIAA/ASME2003; 2003. p. 293–303.
[15] Cesnik CES, Hodges DH. VABS: a new concept for composite rotor blade cross-sectional modeling. J Am Helicopter Soc 1997;42:27–38.
[16] Bir GS. User's guide to PreComp (pre-processor for computing composite blade properties). National Renewable Energy Laboratory; 2006.
[17] Wang L, Liu X, Guo L, Renevier N, Stables M. A mathematical model for calculating cross-sectional properties of modern wind turbine composite blades. Renew Energy 2014;64:52–60.
[18] Lindenburg C, Schepers J. Phatas-iv aeroelastic modelling: program for horizontal axis wind turbine analysis and simulation. version iv. Technical Report (Draft). Petten, The Netherlands: Energy Research Centre of the Netherlands; 2001.
[19] Jonkman JM, Buhl Jr ML. FAST user's guide. Golden, CO: National Renewable Energy Laboratory; 2005.
[20] Bossanyi E. GH bladed user manual. Garrad Hassan and Partners Ltd; 2003.
[21] Larsen T. How 2 HAWC2, the user's manual. RisøReport, Risø; 2009.
[22] Bauchau O, Craig J. Euler-Bernoulli beam theory. Structural analysis. Springer; 2009. p. 173–221.
[23] Hodges DH. Geometrically exact, intrinsic theory for dynamics of curved and twisted anisotropic beams. AIAA J 2003;41:1131–7.

Please cite this article in press as: Wang L, et al., Nonlinear aeroelastic modelling for wind turbine blades based on blade element momentum theory and geometrically exact beam theory, Energy (2014), http://dx.doi.org/10.1016/j.energy.2014.08.046

[24] Palacios R, Cesnik CE. Structural models for flight dynamic analysis of very flexible aircraft. Boston: Daedalus; 2009. p. 1–17.
[25] Hodges DH. Nonlinear composite beam theory. American Institute of Aeronautics and Astronautics; 2006.
[26] Sotoudeh Z, Hodges DH, Chang C-S. Validation studies for aeroelastic trim and stability of highly flexible aircraft. J Aircr 2010;47:1240–7.
[27] Bossanyi E. GH bladed theory manual. GH & Partners Ltd; 2003.
[28] Multiphysics C. 4.3 user's guide. COMSOL; 2012.
[29] Malcolm D, Hansen A, Concepts GE. WindPACT turbine rotor design study: June 2000–June 2002. National Renewable Energy Laboratory; 2006.
[30] Manwell J, McGowan J, Rogers A. Wind energy explained: theory, design and application. 2nd ed. Wiley; 2009.
[31] Liu X, Wang L, Tang X. Optimized linearization of chord and twist angle profiles for fixed-pitch fixed-speed wind turbine blades. Renew Energy 2013;57:111–9.
[32] Yu W, Blair M. GEBT: a general-purpose nonlinear analysis tool for composite beams. Compos Struct 2012;94:2677–89.
[33] Buhl ML. WT_perf user's guide. National Renewable Energy Laboratory; 2004.
[34] Lindenburg C, Hansen M, Politis E. Structural pitch for a pitch-to-vane controlled wind turbine rotor; 2004.
[35] van Holten T, Chin RTH, Bot E, Hagg F, Holierhoek JG, Joosse PA, et al. Aeroelastic tools to assess the stability of large wind turbines. Final Report STABTOOL Phase III. FM&P-02-004,TU-Delft; June 2002.
[36] Lindenburg C. Bladmode; program for rotor blade mode analysis. Wind Energy 2012;2011:2010.
[37] Hand MM, Simms D, Fingersh L, Jager D, Cotrell J. Unsteady aerodynamics experiment phase VI: test configuration and available data campaigns. National Renewable Energy Laboratory; 2001.

Please cite this article in press as: Wang L, et al., Nonlinear aeroelastic modelling for wind turbine blades based on blade element momentum theory and geometrically exact beam theory, Energy (2014), http://dx.doi.org/10.1016/j.energy.2014.08.046

G3. Paper 3

Xiongwei Liu, Lin Wang, and Xinzi Tang, "Optimized linearization of chord and twist angle profiles for fixed-pitch fixed-speed wind turbine blades," *Renewable Energy* 57 (2013): 111-119.

Renewable Energy 57 (2013) 111–119

Contents lists available at SciVerse ScienceDirect

Renewable Energy

journal homepage: www.elsevier.com/locate/renene

Optimized linearization of chord and twist angle profiles for fixed-pitch fixed-speed wind turbine blades

Xiongwei Liu [a,*], Lin Wang [b], Xinzi Tang [b]

[a] Sustainable Engineering, University of Cumbria, Energus Campus, Workington CA14 4JW, UK
[b] Wind Energy Engineering Research Group, School of Computing, Engineering and Physical Sciences, University of Central Lancashire, Preston PR1 2HE, UK

ARTICLE INFO

Article history:
Received 28 July 2012
Accepted 27 January 2013
Available online

Keywords:
Blade design
Chord
Optimization
Linearization
Wind turbine
FPFS

ABSTRACT

The chord and twist angle radial profiles of a fixed-pitch fixed-speed (FPFS) horizontal-axis wind turbine blade are based on a particular design wind speed and design tip speed ratio. Because the tip speed ratio varies with wind speed, the originally optimized chord and twist angle radial profiles for a preliminary blade design through optimum rotor theory do not necessarily provide the highest annual energy production (AEP) for the wind turbine on a specific site with known wind resources. This paper aims to demonstrate a novel optimal blade design method for an FPFS wind turbine through adopting linear radial profiles of the blade chord and twist angle and optimizing the slope of these two lines. The radial profiles of the blade chord and twist angle are linearized on a heuristic basis with fixed values at the blade tip and floating values at the blade root based on the preliminary blade design, and the best solution is determined using the highest AEP for a particular wind speed Weibull distribution as the optimization criteria with constraints of the top limit power output of the wind turbine. The outcomes demonstrate clearly that the proposed blade design optimization method offers a good opportunity for FPFS wind turbine blade design to achieve a better power performance and low manufacturing cost. This approach can be used for any practice of FPFS wind turbine blade design and refurbishment.

1. Introduction

Small and medium size fixed-pitch fixed-speed (FPFS) horizontal-axis wind turbines have found broad applications due to their unique advantage of direct grid connection using induction generators. Comparing to the fixed-pitch variable-speed (FPVS) wind turbines with permanent magnet synchronous generators which use complex power electronics for grid connection, FPFS wind turbines have the advantage of being simple, robust and reliable, well-proven and low cost.

FPVS wind turbine blade design provides the foundation for small wind turbine blade design. For an FPVS wind turbine, the blade design is based on a particular design tip speed ratio (TSR), i.e. the optimum TSR λ_0, due to the assumption that the wind turbine maintains the maximum power coefficient C_{PRmax} at the design TSR λ_0 for wind speed up to rated wind speed. Therefore the design TSR λ_0 is a very important design parameter for FPVS wind turbines. Other design parameters, such as rated wind speed, airfoil shape and design angle of attack, should also be considered carefully. To make sure the power coefficient C_{PR} is maximum at the design TSR λ_0, the design angle of attack is often selected at the angle where the lift to drag ratio is maximum. Once these fundamental design parameters are selected, the aerodynamic shape, such as the chord and twist radial profiles, is often obtained based on blade element momentum (BEM) theory [1], which is widely used for wind turbine blade design and analysis.

The blade design for an FPFS wind turbine differs from that for an FPVS wind turbine. For an FPFS wind turbine, the rotor speed is fixed and the TSR varies when the wind speed changes. The blade design is based on a particular design wind speed with a particular design TSR, which means only at the design wind speed the power coefficient C_{PR} reaches its maximum value C_{PRmax}. At both sides of the design wind speed, the power coefficient C_{PR} will be lower than the maximum value C_{PRmax}.

Wind turbine blade design optimization has been one of the ongoing research and industrial practices during the last two decades [2]. For FPVS wind turbines, typically, the fundamental design objective is to maximize the power coefficient C_{PR} for low wind speed (up to its rated value). Glauert [3] demonstrated that a constant induction factor contributes to maximum efficiency for an ideal rotor. Wilson et al. [4] extended Glauert's method and carried out a local optimization analysis through maximizing the power

* Corresponding author. Tel.: +44 0 1900 605665x1069.
E-mail addresses: Xiongwei.Liu@Cumbria.ac.uk, xiongweiliu@263.net (X. Liu).

0960-1481/$ – see front matter
http://dx.doi.org/10.1016/j.renene.2013.01.036

contribution at each radial section. The axial induction factors were changed until the power output became stationary. Pandey et al. [5] provided a more analytical approach to take the effects of drag and finite number of blades into account in calculating the axial and angular induction factors. The results showed good agreement with those from Wilson's method. For FPFS wind turbines, efforts have been put on the determination of the optimal rotor speed and design wind speed, which determine the design TSR at the design wind speed. Given the fact that the TSR and angle of attack vary with wind speed, using the optimal angle of attack, where the lift to drag ratio reaches the maximum value for the chosen airfoil, for the blade design may not provide the best solution. The authors investigated the impact of design angle of attack along with design TSR and design wind speed for an FPFS wind turbine, and the outcome proves that the best solution does not necessarily use the so-called optimal angle of attack as the design angle of attack [6].

Linearization of both the chord and twist angle radial profiles has been general practice in wind turbine industry to minimize the manufacturing cost of wind turbine blades. There are different ways for the chord and twist angle linearization. Maalawi and Badr [7] suggested that the linearized chord radial profile should be the tangent line to the theoretical profile at 75% radial station while the twist angle radial profile should be an exponential profile. Burton et al. [8] drew a straight line through the 70% and 90% span points of theoretical chord profile to linearize the chord. Manwell et al. [1] provided two general linear expressions including three coefficients for linearized chord and twist angle radial profiles. Obviously, these studies just demonstrate different ways to linearize the chord and twist angle radial profiles, however do not provide convincing evidence and scientific insight for the criteria of the optimization.

The original chord and twist angle radial profiles are based on a particular design wind speed and design TSR. Because the TSR varies with wind speed for an FPFS wind speed, the originally optimized chord and twist angle radial profiles may not necessarily provide the best power performance for the wind turbine for a particular site, i.e. for a particular wind speed Weibull distribution. Therefore, adjusting the chord and twist angle radial profiles may offer an opportunity to optimize the wind turbine blade design so as to achieve a further optimized power performance, apart from low manufacturing cost.

In terms of mathematical algorithms for wind turbine blade design optimization, Selig and Coverstone-Carroll [9] combined a genetic algorithm (GA) with an inverse design method to optimize blades of stall-regulated wind turbines. The optimum blade chord and twist angle radial profiles were determined for maximizing annual energy production. Yurdusev et al. [10] used artificial neural network (ANN) to estimate the optimal TSR for wind turbines. The ANN method was found to be more successful than the traditional method in estimating the TSR due to its capabilities of parallel data processing and generation. Liu et al. [11] adapted the extended compact genetic algorithm (ECGA) to develop a generalized optimization program for blades of horizontal-axis wind turbines. The program was used to optimize blades of a 1.3 MW stall-regulated wind turbine showing 7.5% increase in annual energy production. Ceyhan [12] developed an aerodynamic design and optimization tool for horizontal-axis wind turbines using both the BEM theory and GA. Blades were optimized for the maximum power output for a given wind speed. Chord, twist angle and a fixed number of sectional airfoil profiles were considered as optimization variables. However, these methods do not include the consideration of chord and twist angle radial profile linearization, which has been practiced in industrial scale wind turbine blade design.

The purpose of this paper is to demonstrate a novel approach for the blade design optimization through adopting linear radial profiles of the blade chord and twist angle and optimizing the slope of these two lines. The baseline wind turbine used for this study is a 25 kW FPFS wind turbine with a well-established airfoil for the blade design.

In this paper, optimum rotor theory [1] is used for a preliminary blade design of the wind turbine, the BEM theory with both Prandtl tip loss correction and wake consideration is employed to calculate the power performance of the blade. The linearization of the chord and twist angle radial profiles is through fixing the values at the blade tip and floating the values at the blade root based on the preliminary blade design, and the best solution is determined using the highest AEP for a particular wind speed Weibull distribution as the optimization criteria with constraints of the top limit power output of the wind turbine.

The paper is structured as follows. For a comprehensive understanding of the methodology, we briefly summarize the BEM theory and the AEP calculation in Sections 2 and 3 respectively. The baseline wind turbine is introduced in Section 4, and the blade design parameters are discussed in Section 5. Section 6 summarizes the wind turbine blade design theory and provides a preliminary blade design. Section 7 analyses the performance of the preliminary blade based on the BEM theory using MATLAB. Section 8 details the optimizing design process, and Section 9 concludes the findings with recommendations.

2. Blade element momentum (BEM) theory

Glauert developed the original BEM theory which combines blade element theory, which is based on the airfoil aerodynamic characteristics, and the momentum theory, which considers the blade as a number of independent stream tubes and ignores the spanwise flow [1]. In the BEM theory, the air flow through the rotor is assumed to be axisymmetric. Eqs. (1) and (2) describe the momentum theory for each stream tube based on the conservation of momentum in both axial and rotational directions:

$$\mathrm{d}T = \rho V^2 4a(1-a)\pi r\mathrm{d}r \tag{1}$$

$$\mathrm{d}Q = 4a'(1-a)\rho V\pi r^3\Omega\mathrm{d}r \tag{2}$$

where $\mathrm{d}T$ and $\mathrm{d}Q$ are the differential thrust force and torque, r is the radius of the stream tube (or blade element), and Ω is the angular velocity of the wind turbine rotor.

Eqs. (3) and (4) describe the aerodynamic normal force, which is the same as the thrust force in Eq. (1), and the torque of the blade element, which is the same as the torque in Eq. (2), based on the known airfoil lift and drag coefficients C_l and C_d with assumed induced relative wind velocity U_{rel} to the airfoil:

$$\mathrm{d}F_N = B\frac{1}{2}\rho U_{\mathrm{rel}}^2(C_l\cos\varphi + C_d\sin\varphi)c\mathrm{d}r \tag{3}$$

$$\mathrm{d}Q = B\frac{1}{2}\rho U_{\mathrm{rel}}^2(C_l\sin\varphi - C_d\cos\varphi)cr\mathrm{d}r \tag{4}$$

where B is the blade number, ρ is the air density, φ is the angle of relevant wind.

Combining the blade element theory and momentum theory leads to both axial and angular induction factors a and a', which are then used for the calculation of the induced relative wind velocity U_{rel} to the airfoil. The induced wind velocity is then used again for the blade element aerodynamic forces calculation, and the above procedure is repeated until the newly calculated induction factors a and a', are within an acceptable tolerance of the previous ones.

In the BEM theory, the accuracy of the airfoil aerodynamic model, i.e. the lift and drag coefficients, is vital for the blade design, load analysis and power performance prediction of a wind turbine. A well-established airfoil aerodynamic model will enhance the wind turbine blade design.

However, the BEM theory is based on a few assumptions and does not accurately describe the real physics of a wind turbine. The first and most important assumption that the air flow through the rotor is axisymmetric is only an approximation with a finite number of blades, typically 3. The effects of the finite number of blades result in the performance losses concentrated near the tip of the blade, which is known as the tip losses and can be handled with the well-accepted tip loss correction factor presented by Prandtl [1,13]:

$$F = \frac{2}{\pi}\cos^{-1}\left(\exp\left(-\left(\frac{B(1-r/R)}{2(r/R)\sin\varphi}\right)\right)\right) \quad (5)$$

The tip loss correction factor, which is always between 0 and 1, characterizes the reduction in the forces at a radius r along the blade that is due to the tip loss at the end of the blade.

The results obtained from the BEM theory with tip loss correction are generally in good agreement with field measurements for attached flows on the surface of blades, i.e. under stall free condition when the blade TSR is maintained at design TSR or higher. This makes the BEM theory as a standard tool for wind turbine blade design.

3. Annual energy production (AEP) calculation

The AEP is calculated using the following formula [14]

$$E = 8760 \times \frac{1}{2}\eta\rho A \int_{\text{cut in}}^{\text{cut out}} v^3 C_{\text{PR}}(v) \times f_{\text{Rayleigh}}(v)\mathrm{d}v \quad (6)$$

where η is the transmission efficiency (in percentage) of both mechanical and electronic systems of the wind turbine; ρ is the air density; A is the swept area of the wind turbine rotor; $C_{\text{PR}}(v)$ is the rotor power coefficient of the wind turbine, which is derived from the power performance analysis based on the BEM theory and is a complex function of the wind speed v or TSR for an FPFS wind turbine; $f_{\text{Rayleigh}}(v)$ is the wind speed Rayleigh distribution.

4. Baseline wind turbine

Let's start from the baseline 25 kW FPFS wind turbine with a 4-pole induction generator. This wind turbine is designed for a specific site with a low annual mean wind speed (AMWS) of 5 m/s. The fundamental parameters of the wind turbine are listed in Table 1.

5. Blade design parameters

5.1. Design wind speed and rated wind speed

Different to variable-speed machines, there are two sets of wind speed we should consider for an FPFS machine, i.e. design wind speed V_{design} and rated wind speed V_{rated}. At the design wind speed V_{design}, the wind turbine rotor power coefficient C_{PR} achieves its maximum value C_{PRmax}. At the rated wind speed V_{rated}, the wind turbine rotor reaches its rated power P_{rotor}, which corresponds to the generator rated power output P_r. Considering the overall transmission efficiency η.

According to IEC61400-2 [15], the design wind speed V_{design} for an FPFS wind turbine should be 1.4 times of the annual mean wind speed V_{AMWS}. In this design case, V_{AMWS} is 5 m/s, therefore, V_{design} is 7 m/s.

The rated wind speed of an FPFS wind turbine is generally not defined at this stage and will be determined from further calculation and analysis.

Table 1
Fundamental design parameters of the baseline 25 kW wind turbine.

Parameters	Unit	Value
Generator rated power output, P_r	W	25,000
Overall transmission efficiency, η	%	0.85
Wind turbine rated rotor power, P_{rotor}	W	29,412
Number of blades, B		3
Rotor diameter	m	15.0

5.2. Rotor speed and design tip speed ratio

For most small wind turbines with 3 blades, the tip speed ratio (TSR) at the design wind speed is in the range of 6–8 [16]. In this case study, we choose the design TSR $\lambda_0 = 6$[1] at the design wind speed 7 m/s, which corresponds to a blade tip speed of 42 m/s and rotor speed of 53.5 rpm. Considering the operation wind speed from 3 m/s to 18 m/s, the TSR λ varies from 2.333 to 14.

5.3. Airfoil and design angle of attack

The airfoil used for the baseline wind turbine blade is DU93W210 [17,18], which is a well-established and tested airfoil for wind turbine blades. The airfoil's performance is affected by Reynolds number (Re), which is defined as [1]:

$$Re = \rho U_{\text{rel}} c/\mu = (\text{Inertial force})/(\text{Viscous force}) \quad (7)$$

where, in terms of the airfoil, μ is the air viscosity, U_{rel} is the relative wind velocity to the airfoil and c is the chord length of the airfoil.

If we estimate that the chord of the middle section of the 7.5 m blade is 0.55 m, the range of Reynolds number can be obtained from the relative wind velocity U_{rel}, which is calculated from the velocity triangle at the middle section of the blade. The estimated Reynolds numbers are shown in Table 2.

As shown in Table 2, because the rotor speed is fixed, the Reynolds number of this wind turbine does not vary significantly, which is in the range of 800,000–1,100,000 when wind speed varies from 3 m/s to 18 m/s. To simplify the design process, we choose Reynolds number 1,000,000 as the design Reynolds number. It should be noted that this simplification may not be suitable for the situation where Reynolds number varies significantly, such as for the case of variable-speed large wind turbines. Fig. 1 depicts the lift and drag coefficients and lift/drag ratio of the airfoil against the interested angles of attack from 0 to 12° at Re = 1,000,000 [17,18].

The lift coefficient is 1.336 and the maximum lift/drag ratio is 118.021 at angle of attack 7.71°. This angle will be selected as the design angle of attack.[2] For FPFS wind turbines, when the wind speed is higher than design wind speed, the blades operate at larger angle of attack than 7.71°, up to 60° for example. Therefore, a wide range of angles of attack is required for further calculation and analysis. As shown in Fig. 2, the available (wind tunnel tested) lift and drag coefficients from the limited range of angle of attack in Fig. 1 can be expanded to the full 360° angle of attack using the Viterna method [19], which has been widely used to predict the post-stall performance of airfoils [20–22].

[1] For the TSR optimization, please refer to Ref. [10].
[2] For optimal design attack angle calculation, please refer to Ref. [6].

Table 2
Estimated Reynolds numbers at different operation wind speed.

v (m/s)	$V_{\tan}$ (m/s)	U_{rel} (m/s)	Re
3	21	21.2	802,944
6	21	21.8	826,681
9	21	22.8	864,797
12	21	24.2	915,497
15	21	25.8	976,823
18	21	27.7	1,046,910

(Note: $V_{\tan} = \Omega r_{\text{mid-section}} = (\text{blade tip speed})/2 = 21$ m/s, $U_{\text{rel}} = \sqrt{V_{\tan}^2 + v^2}$).

6. Preliminary blade design

The preliminary blade design of the wind turbine is to determine the chord and twist angle radial profiles of the blade based on the above design parameters, including the rotor radius $R = 7.5$ m/s, design tip speed ratio $\lambda_0 = 6$, number of blade $B = 3$, design angle of attack $\alpha_{\text{design}} = 7.71$, and the design lift coefficient $C_{l,\text{design}} = 1.336$. The blade is divided into 10 sections or elements. For each element, the chord c_i and twist angle $\theta_{p,i}$ are calculated based on optimum rotor theory [1], which is summarized here:

$$\lambda_{r,i} = \lambda_0(r_i/R) \tag{8}$$

$$\varphi_i = \left(\frac{2}{3}\right)\tan^{-1}\left(\frac{1}{\lambda_{r,i}}\right) \tag{9}$$

$$c_i = \frac{8\pi r_i}{BC_{l,\text{design},i}}(1 - \cos\varphi_i) \tag{10}$$

$$\theta_{p,i} = \varphi_i - \alpha_{\text{design},i} \tag{11}$$

where i indicates the ith blade section, $\lambda_{r,i}$ is the speed ratio of the ith blade section, r_i is the distance from the ith blade section to the rotor center, φ_i is the angle of relative wind at the ith blade section. $C_{l,\text{design},i}$ and $\alpha_{\text{design},i}$ are the design lift coefficient and design angle of attack at the ith blade section respectively. For the preliminary blade design, at design wind speed 7 m/s, the design lift coefficient and design angle of attack are considered constant along the blade. Therefore, in the following sections, we use $C_{l,\text{design}}$ and α_{design} to represent $C_{l,\text{design},i}$ and $\alpha_{\text{design},i}$ respectively.

Figs. 3 and 4 show the calculated initial chord and twist angle radial profiles based on Eqs. (8)–(11). The chord at the blade root section ($0.1R$) is over 1 m, and the twist angle distributes from 32.5° at the blade root to −1° at the blade.

7. Wind turbine rotor performance analysis

The wind turbine rotor power is contributed from each individual blade element of the three blades, and therefore the calculation is based on each blade element's performance analysis.

The performance parameters of each blade element is calculated through an iterative procedure [1,23], which is summarized below:

(1) Estimate an initial (the first iterative) value for the axial induction factor a and angular induction factor a':

$$\varphi_{i,1} = \left(\frac{2}{3}\right)\tan^{-1}\left(\frac{1}{\lambda_{r,i}}\right) \tag{12}$$

$$a_{i,1} = \frac{1}{\left[1 + \dfrac{4\sin^2(\varphi_{i,1})}{\sigma_i' C_{l,\text{design}}\cos\varphi_{i,1}}\right]} \tag{13}$$

$$a'_{i,1} = \frac{1 - 3a_{i,1}}{(4a_{i,1}) - 1} \tag{14}$$

where i indicates the ith blade element. σ_i' is the local solidity, defined by:

$$\sigma_i' = Bc_i/2\pi r_i \tag{15}$$

(2) Start the iterative procedure for the jth iteration. For the first iteration, follow step 1), $j = 1$. Calculate the relative wind angle and Prandtl tip loss factor:

$$\tan\varphi_{i,j} = \frac{1 - a_{i,j}}{\left(1 + a'_{i,j}\right)\lambda_{r,i}} \tag{16}$$

$$F_{i,j} = \left(\frac{2}{\pi}\right)\cos^{-1}\left[\exp\left(-\left(\frac{(B/2)[1 - (r_i/R)]}{(r_i/R)\sin\varphi_{i,j}}\right)\right)\right] \tag{17}$$

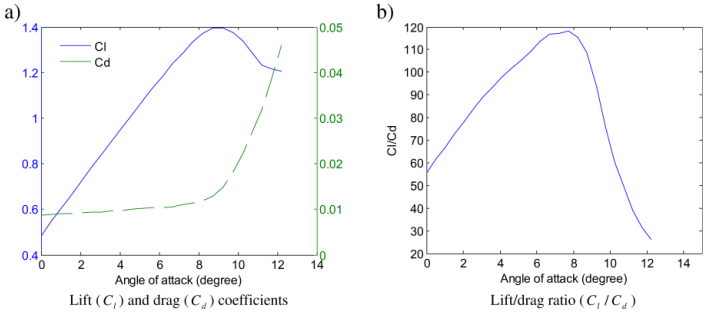

Lift (C_l) and drag (C_d) coefficients — Lift/drag ratio (C_l / C_d)

Fig. 1. Aerodynamic characteristics of DU93W210 airfoil at $Re = 1{,}000{,}000$.

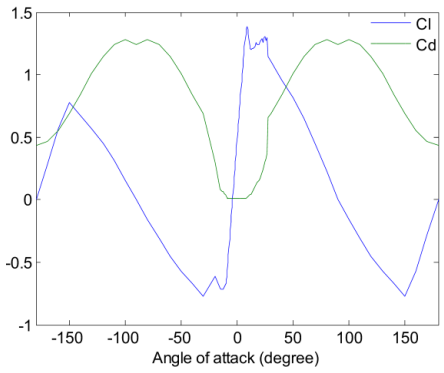

Fig. 2. Lift and drag coefficients of DU93W210 at full 360° range of angle of attack based on Viterna method.

(3) Then calculate the local angle of attack of the ith blade element:

$$\alpha_{i,j} = \varphi_{i,j} - \theta_{p,i} \tag{18}$$

followed by $C_{l,i,j}$ and $C_{d,i,j}$, which are obtained from the airfoil lift and drag coefficient curve against the angle of attack, as illustrated in Figs. 1 and 2.

(4) Then update the axial induction factor a and angular induction factor a' for next iteration, considering the drag effects:

$$a_{i,j+1} = \frac{1}{\left[1 + \frac{4F_{i,j}\sin^2(\varphi_{i,j})}{\sigma'_i\left(C_{l,i,j}\cos\varphi_{i,j} + C_{d,i,j}\sin\varphi_{i,j}\right)}\frac{1}{H}\right]} \tag{19}$$

$$a'_{i,j+1} = \frac{1}{\frac{4F_{i,j}\sin\varphi_{i,j}\cos\varphi_{i,j}}{\sigma'_i\left(C_{l,i,j}\sin\varphi_{i,j} - C_{d,i,j}\cos\varphi_{i,j}\right)} - 1} \tag{20}$$

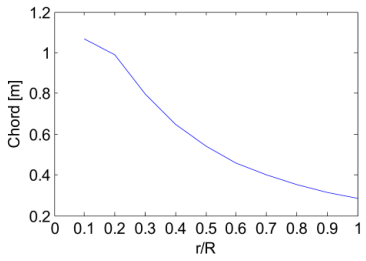

Fig. 3. Chord profile.

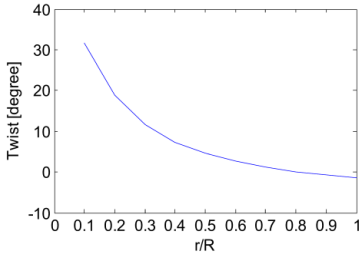

Fig. 4. Twist angle profile.

The parameter H is introduced for the situation when large induction factors occur. When the axial induction factor a is greater than 0.5, the expression for thrust coefficient [1]:

$$C_T = 4a(1-a) \tag{21}$$

must be replaced by the empirical expression [23]:

$$C_T = 0.6 + 0.61a + 0.79a^2 \tag{22}$$

In order to obtain a smoother transition, GH-bladed adopted a transition to the empirical model for axial induction factor greater than 0.3539 rather than 0.5.

The parameter H is defined as follows [23]:

$$\text{for } a_{i,j+1} \le 0.3539, H = 1.0 \tag{23}$$

$$\text{for } a_{i,j+1} > 0.3539, H = \frac{4a(1-a)}{\left(0.6 + 0.61a + 0.79a^2\right)} \tag{24}$$

If the deviation between the $j+1$th and the jth induction factors is within an acceptable tolerance, then confirm the local relative wind angle φ_i, tip loss factor F_i and angle of attack α_i, which determines the local lift and drag coefficients $C_{l,i}$ and $C_{d,i}$ for the ith blade element; (if not, then go back to step 2).

Having obtained the above performance parameters for each blade element, according to Eq. (4), the torque generated by the blade element is equal to [1]:

$$dQ_i = F_i B \frac{1}{2}\rho U^2_{\text{rel},i}(C_{l,i}\sin\varphi_i - C_{d,i}\cos\varphi_i)c_i r_i dr \tag{25}$$

The total rotor torque and power are calculated from Ref. [1]:

$$Q = \sum_{i=1}^{n} dQ_i \tag{26}$$

$$P = Q\Omega \tag{27}$$

The wind turbine rotor power coefficient is then determined by Manwell [1]:

$$C_{PR} = \frac{P}{\frac{1}{2}\rho\pi R^2 V^3} \tag{28}$$

Based on the above procedure, a Matlab program is developed to calculate the C_{PR}–λ curve. For verification purpose, GH-bladed software is also employed for the calculation of the C_{PR}–λ curve. As shown in Fig. 5, the result from Matlab program agrees with GH-bladed software very well.

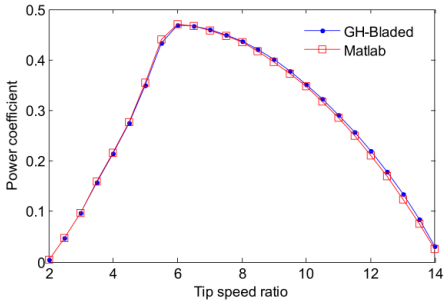

Fig. 5. Calculated C_{PR}–λ curve.

The calculated wind turbine rotor power curve is shown in Fig. 6, which indicates at wind speed of 13 m/s, the wind turbine rotor power reaches its top value 30.47 kW, which is slightly higher than the rated value 29.412 kW, as listed in Table 1. This is acceptable, because the generator can tolerate up to 20% overloading. It should be noted that when the wind speed is above the design wind speed, the angle of attack is above the design (optimal) value, stall will take place, particularly when the wind speed is well above the design wind speed. A more accurate calculation is needed to consider stall-delay [24], dynamic stall [25] and other 3D effects, for industrial design practice.

Given the annual mean wind speed (AMWS), using Eq. (6), the annual energy production (AEP) is calculated, as listed in Table 3.

8. Blade design optimization

8.1. Method

The chord and twist angle of the preliminary blade design are non-linear profiles, as shown in Figs. 3 and 4. For easy manufacture purpose, the chord and twist angle radial profiles are generally linearized in industrial practice. Apart from that, optimum rotor theory only guarantees that the blade works at the optimal condition when the wind turbine operates at the design wind speed 7 m/s. Therefore, the aerodynamic performance of the preliminary

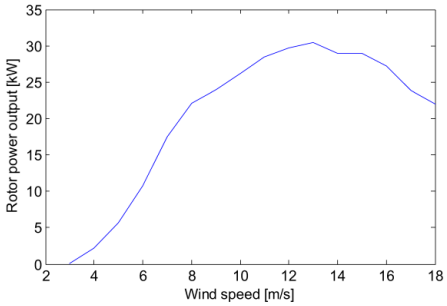

Fig. 6. Calculated power curve of the wind turbine rotor.

Table 3
Annual energy production (AEP).

AMWS (m/s)	AEP (kWh)
4.0	36,186
4.5	48,828
5.0	61,605
5.5	74,011
6.0	85,694
6.5	96,408
7.0	105,984

blade is not necessarily better than a linearized one. In other words, a better performance may be achieved through linearization of the chord and twist angle radial profiles. As shown in Figs. 3 and 4, the value of the chord and twist angle decreases gradually from the blade root to the blade tip. In order to linearize the chord and twist angle radial profiles, one way[3] is to fix the chord and twist angle at the blade tip, and change the value at the blade root to linearize the chord and twist angle radial profiles using the following equations:

$$c_{i,n} = c_{t,0} + (0.7c_{r,0} - c_{t,0})\ \frac{(n-1)\,r_i}{N\quad R} \quad n = 1,2,...,N+1 \tag{29}$$

$$\theta_{i,n} = \theta_{t,0} + (\theta_{r,0} - \theta_{t,0})\ \frac{(n-1)\,r_i}{N\quad R} \quad n = 1,2,...,N+1 \tag{30}$$

where n indicates the nth linearized chord line, $c_{i,n}$ is the chord at the ith blade element of the nth linearized chord line, $\theta_{i,n}$ is the twist angle at the ith blade element of the nth linearized twist line. $c_{t,0}$ and $c_{r,0}$ are the chords at the blade tip and root of the preliminary blade respectively, $\theta_{t,0}$ and $\theta_{r,0}$ are the twist angles at the blade tip and root of the preliminary blade respectively, N is the number of division.

8.2. Result

Assuming the number of division $N = 18$ for Eq. (29) and $N = 30$ for Eq. (30),[4] which results in 589 combinations with 19 choices of chord profile lines and 31 choices of twist angle profile lines, as shown in Figs. 7 and 8. Following the same procedures outlined in Section 7, the annual energy production (AEP) of the 589 combinations of the wind turbine blade design for an annual mean wind speed (AMWS) of 5 m/s are calculated, and the outcomes are illustrated in Fig. 9.

Fig. 9 reveals:

(1) For any linearized twist angle profile, the AEP increases with the blade root chord.
(2) When the blade root chord is larger than 0.598 m, the AEP of the linearized blade is higher than that of the preliminary blade (61,605 kWh) for a certain range of blade root twist angle.
(3) For any linearized chord, the relationship between the AEP and the blade root twist angle appears similar to a parabolic curve, and when the blade root twist angle is about 17.5°, the AEP achieves its maximum value.

[3] There are other ways to do so, this paper aims to demonstrate the optimization strategy, and is not intended to try all the other different ways.
[4] We tried different N before we start to write the paper. Finally, we choose $N = 18$ and $N = 30$ for the linearized equation of the chord and twist respectively. The changing steps of the twist and chord at the blade root are about 1° and 0.026 m respectively, which are small enough for this case study.

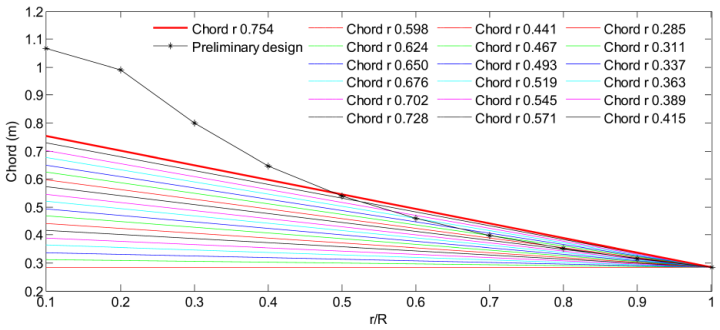

Fig. 7. 19 Choices of chord linearized profile lines.

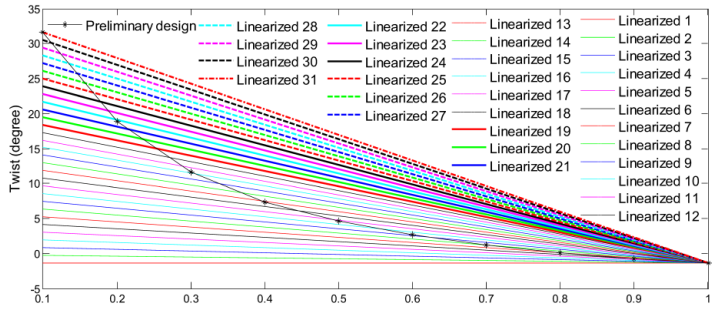

Fig. 8. 31 Choices of twist angle linearized profile lines.

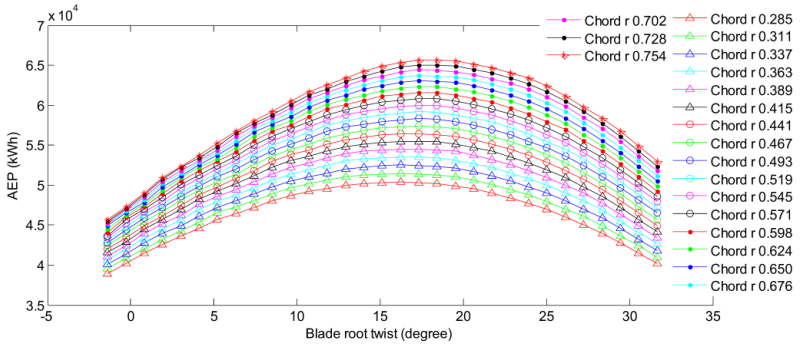

Fig. 9. AEP of the 589 design solutions for AMWS 5 m/s.

(4) If we only consider the highest AEP as the optimization criteria, the best linearized blade is the one which has a blade root chord of 0.754 m and a blade root twist angle of 17.5° as shown in Fig. 9. However, the baseline wind turbine is a 25 kW wind turbine, the maximum overloading to the generator is assumed to be 120%. Therefore the maximum rotor power should be limited to 29,412 W*120% = 35,294 W, which should be added as a constraint for the blade design optimization. Considering the maximum rotor power constraint, the optimal blade is the one which has a blade root chord of 0.728 m and a blade root twist angle of 14.02°.

The radial profiles of the chord and twist angle of the optimal blade are depicted in Figs. 10 and 11 along with the profiles of those of the preliminary blade.

Figs. 10 and 11 reveal that the optimal blade simplifies the geometry of the blade, and at the same time removes materials close to the blade root, which should reduce the manufacturing cost of the blade.

Fig. 12 compares the calculated power coefficients of both the preliminary blade and the optimal blade, which reveals that the power coefficient of the optimal blade has a wide "flat top" curve, which is desirable for the wind turbine; and the power coefficient of the optimal blade has higher value than that of the preliminary blade with only exceptions for the tip speed ratio between 5.4 and 7.3, which is near the design tip speed ratio of 6.

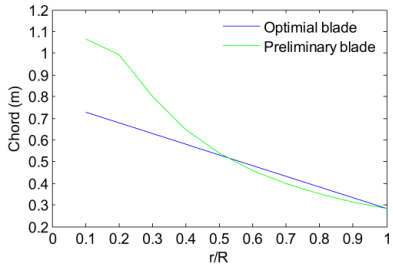

Fig. 10. Chord profiles of the optimal blade and the preliminary blade.

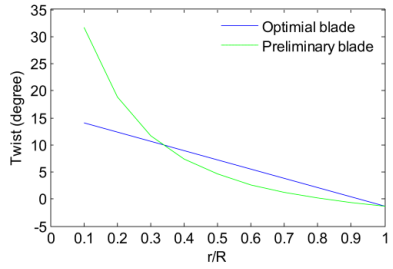

Fig. 11. Twist angle profiles of the optimal blade and the preliminary blade.

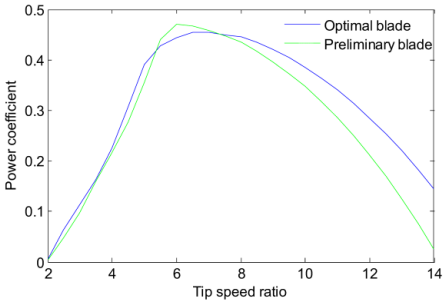

Fig. 12. Power coefficient of the optimal blade and the preliminary blade.

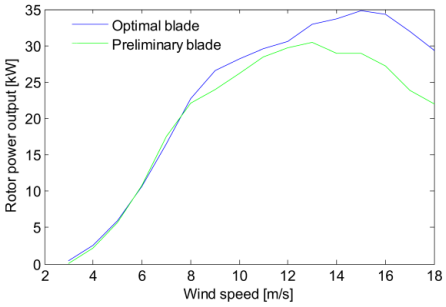

Fig. 13. Rotor power output of the optimal blade and the preliminary blade.

The calculated wind turbine rotor power curves of the preliminary blade and the optimal blade are shown in Fig. 13. The outcome demonstrates that the output from the optimal blade design is higher than that from the preliminary blade design with only exceptions for the wind speed between 6 m/s and 7.6 m/s, which is near the design wind speed 7 m/s. It also shows that the top rotor power is 34.85 kW, which happens at wind speed 15 m/s and is within the 120% overloading limit.

The calculated AEP of the wind turbine with the optimal blade and preliminary blade is shown in Table 4. The outcome demonstrates that there is a significant increase of the AEP of the optimal blade design for the whole range of annual mean wind speed from 4.0 m/s to 7.0 m/s.

Table 4
AEP of the optimal blade and the preliminary blade.

AMWS (m/s)	AEP (kWh)_preliminary blade	AEP (kWh)_optimal blade	Increase rate
4.0	36,186	37,246	2.93%
4.5	48,828	50,285	2.98%
5.0	61,605	63,656	3.33%
5.5	74,011	76,847	3.83%
6.0	85,694	89,498	4.44%
6.5	96,408	101,348	5.12%
7.0	105,984	112,198	5.86%

9. Conclusions and recommendations

This paper presents a heuristic approach for the blade design optimization through linearization of both the chord and twist angle radial profiles for fixed-pitch fixed-speed small wind turbines through the case study of a 25 kW baseline wind turbine with DU93W210 airfoil. The conclusions and recommendations are:

(1) Linearization of the chord and twist angle radial profiles with fixed values at the blade tip from a preliminary blade design offers a promising optimization strategy for FPFS wind turbine blade design to improve power performance and reduce both materials and manufacturing cost.
(2) With consideration of the constraints for top limit of the maximum rotor power, an optimal blade design is achieved through linearization of the chord and twist angle radial profiles with fixed values at the blade tip, and the optimal design achieves an improvement of 3.33% higher annual energy production than its preliminary design version at the design annual mean wind speed 5 m/s for the case study baseline wind turbine, with a reduced materials and manufacturing cost for the blade, which is difficult to estimate the value at the design stage.
(3) This method can be used for any practice of fixed-pitch fixed-speed wind turbine blade design.
(4) This method can be used for wind turbine blade refurbishment based on an existing baseline wind turbine, which uses the existing gearbox and generator with fixed rotor speed.

References

[1] Manwell JF, McGowan JG, Rogers AL. Wind energy explained. Wiley Online Library; 2002.
[2] Jureczko M, Pawlak M, Mężyk A. Optimisation of wind turbine blades. Journal of Materials Processing Technology 2005;167:463–71.
[3] Glauert H. Airplane propellers. Aerodynamic Theory 1935;4:169–360.
[4] Wilson RE, Lissaman PBS, Walker SN. Aerodynamic performance of wind turbines. Corvallis (USA): Oregon State Univ.; 1976.
[5] Pandey M, Pandey K, Ojha T. An analytical approach to optimum design and peak performance prediction for horizontal axis wind turbines. Journal of Wind Engineering and Industrial Aerodynamics 1989;32:247–62.
[6] Wang L, Tang X, Liu X. Blade design optimisation for fixed-pitch fixed-speed wind turbines. ISRN Renewable Energy, www.isrn.com/journals/re/aip/682859.pdf; 2012.
[7] Maalawi K, Badr M. A practical approach for selecting optimum wind rotors. Renewable Energy 2003;28:803–22.
[8] Burton T, Sharpe D, Jenkins N, Bossanyi E. Wind energy: handbook. Wiley Online Library; 2001.
[9] Selig MS, Coverstone-Carroll VL. Application of a genetic algorithm to wind turbine design. Journal of Energy Resources Technology 1996;118:22.
[10] Yurdusev M, Ata R, Çetin N. Assessment of optimum tip speed ratio in wind turbines using artificial neural networks. Energy 2006;31:2153–61.
[11] Liu X, Chen Y, Ye Z. Optimization model for rotor blades of horizontal axis wind turbines. Frontiers of Mechanical Engineering in China 2007;2:483–8.
[12] Ceyhan O. Aerodynamic design and optimization of horizontal axis wind turbines by using BEM theory and genetic algorithm. Master Thesis. Aerospace Engineering Department, METU: Ankara; 2008.
[13] Vries O, editor. Fluid dynamic aspects of wind energy conversion. Advisory Group for Aerospace Research and Development, North Atlantic Treaty Organization; 1979. AGARD-AG-243.
[14] Hau E. Wind turbines: fundamentals, technologies, application, economics. Springer Verlag; 2006.
[15] I. E. Commission. IEC 61400–2: wind turbines–part 2: design requirements for small wind turbines. IEC; 2006.
[16] Tabesh A, Iravani R. Small-signal dynamic model and analysis of a fixed-speed wind farm-a frequency response approach. Power Delivery, IEEE Transactions on 2006;21:778–87.
[17] Bertagnolio F, Sorensen N, Johansen J, Fuglsang P. Wind turbine airfoil catalogue. Risø-R-1280 (EN). Roskilde, Denmark: Risø National Laboratory; 2001.
[18] Timmer W, van Rooij R. Summary of the Delft University wind turbine dedicated airfoils. Journal of Solar Energy Engineering 2003;125:488–96.
[19] Viterna LA, Corrigan RD. Fixed pitch rotor performance of large horizontal axis wind turbines. Large Horizontal-Axis Wind Turbines 1982;1:69–85.
[20] Butterfield CP, Scott GN, Musial W. Comparison of wind tunnel airfoil performance data with wind turbine blade data. Golden, CO (USA): Solar Energy Research Inst.; 1990.
[21] Resor B, Wilson D, Berg D, Berg J, Barlas T, van Wingerden JW, et al. Impact of higher fidelity models on simulation of active aerodynamic load control for fatigue damage reduction. In: Proceedings of the 48th AIAA/ASME; 2010.
[22] Jonkman JM. Modeling of the UAE wind turbine for refinement of FAST_AD. National Renewable Energy Laboratory; 2003.
[23] Bossanyi E. GH bladed theory manual. GH & Partners Ltd.; 2003.
[24] Breton SP, Coton FN, Moe G. A study on rotational effects and different stall delay models using a prescribed wake vortex scheme and NREL phase VI experiment data. Wind Energy 2008;11:459–82.
[25] Leishman J, Beddoes T. A semi-empirical model for dynamic stall. Journal of the American Helicopter Society 1989;34:3–17.

G4. Paper 4

Lin Wang, Xinzi Tang, and Xiongwei Liu. "Optimized chord and twist angle distributions of wind turbine blade considering Reynolds number effects," Oral presentation at WEMEP (Wind Energy: Materials, Engineering and Policies), India, 22-23 November, 2012.

International Conference on Wind Energy: Materials, Engineering and Policies (WEMEP-2012)

Optimized chord and twist angle distributions of wind turbine blade considering Reynolds number effects

L. Wang[a], X. Tang[a], X. Liu[b]
[a]Wind Energy Engineering Research Group, School of Computing, Engineering and Physical Sciences, University of Central Lancashire, Preston, PR1 2HE, UK
[b]Sustainable Engineering, University of Cumbria, Energus Campus, Workington, CA14 4JW, UK
Lwang@uclan.ac.uk, XTang4@uclan.ac.uk, Xiongwei.liu@cumbria.ac.uk

ABSTRACT

The aerodynamic performance of a wind turbine depends very much on its blade geometric design, typically based on the blade element momentum (BEM) theory, which divides the blade into several blade elements. In current blade design practices based on Schmitz rotor design theory, the blade geometric parameters including chord and twist angle distributions are determined based on airfoil aerodynamic data at a specific Reynolds number. However, rotating wind turbine blade elements operate at different Reynolds numbers due to variable wind speed and different blade span locations. Therefore, the blade design through Schmitz rotor theory at a specific Reynolds number does not necessarily provide the best power performance under operational conditions. This paper aims to provide an optimal blade design strategy for horizontal-axis wind turbines operating at different Reynolds numbers. A fixed-pitch variable-speed (FPVS) wind turbine with S809 airfoil is chosen as a case study and a Matlab program which considers Reynolds number effects is developed to determine the optimized chord and twist angle distributions of the blade. The performance of the optimized blade is compared with that of the preliminary blade which is designed based on Schmitz rotor design theory at a specific Reynolds number. The results demonstrate that the proposed blade design optimization strategy can improve the power performance of the wind turbine. This approach can be further developed for any practice of horizontal axis wind turbine blade design.

Keywords: Blade design, optimization, chord, twist angle, Reynolds number, wind turbine

1. INTRODUCTION

Blade design optimization is one of the major research and design areas for wind turbine technologies. Basically, there are three rotor design models: Glauert model, Wilson model and Schmitz model. As an extension of Glauert model, Wilson model includes the influence of the drag and tip loss[1]. Schmitz explained the aerodynamic design principle in a new way and the design results of Schmitz model are coincident with those of Wilson model[2]. All the models calculate the chord and twist angle distributions on the basis of airfoil aerodynamic data at a specific Reynolds number. However, rotating wind turbine blade elements operate at variable Reynolds numbers due to variable wind speed and blade span locations. This means blade design based on a specific Reynolds number may not provide the best power performance.

The purpose of this paper is to demonstrate a heuristic approach for the blade design optimization for a fixed-pitch variable-speed (FPVS) wind turbine operating at different Reynolds numbers. The baseline wind turbine for the study is a 25kW FPVS wind turbine with airfoil S809 for the blade design.

In this paper, the Schmitz rotor design theory[3] is used to design the preliminary blade and a Matlab program is developed to calculate the performance of the blade. Then the best chord and twist angle for each blade element are optimized and determined considering the Reynolds number effects. The criterion used for the optimization is the highest annual energy production (AEP) based on a particular wind speed Rayleigh distribution $f_{\text{Rayleigh}}(v)$, which is a special case of Weibull distribution. The AEP can be calculated using the following formula[4]:

$$E = 8760 \times (\frac{1}{2}\eta\rho A \int_{\text{cut-in}}^{\text{rated}} v^3 C_{\text{PR}}(v) \times f_{\text{Rayleigh}}(v)dv + P_{rated} \int_{\text{rated}}^{\text{cut-out}} f_{\text{Rayleigh}}(v)dv) \quad (1)$$

Where η is the transmission efficiency (in %) of both mechanical and electronic systems of the wind turbine, ρ is the air density, A is the swept area of the wind turbine rotor, $C_{\text{PR}}(v)$ is the rotor power coefficient of the wind turbine.

2. BASELINE WIND TURBINE INTRODUCTION

Let's start from the baseline 25kW FPVS wind turbine. The wind turbine is designed for a specific site with annual mean wind speed of 6m/s. The fundamental parameters of the wind turbine are listed in Table 1.

Table 1: Fundamental design parameters of the baseline 25kW wind turbine

Parameter name	Unit	Value
Generator rated power output P_r	W	25000
Overall transmission efficiency η	%	0.86
Wind turbine rated rotor power P_{rotor}	W	29070
Number of blades B		3
Rotor radius R	m	7.5
Cut-in wind speed	m/s	3
Cut-out wind speed	m/s	16

3. BLADE DESIGN PARAMETERS

3.1 Design wind speed

According to IEC61400-2[5], the design wind speed V_{design} for a wind turbine can be estimated as 1.4 times of the annual mean wind speed V_{AMWS}. In this case, $V_{AMWS} = 6$m/s, therefore, $V_{design} = 8.4$ m/s. For a FPVS wind turbine, the rated wind speed is generally equal to the design wind speed.

3.2 Rotor speed and design tip speed ratio

For most wind turbines with 3 blades, the tip speed ratio λ_0 at the design wind speed is in the range of 6~8[6]. In this case, $\lambda_0 = 8$. Therefore, the rotor speed is 85.6rpm and the blade tip speed is 67.2m/s at the design or rated wind speed.

3.3 Airfoil and design attack angle

The airfoil used for the baseline wind turbine is S809, and its performance is affected by Reynolds number (Re), which is defined by[3]:

$$Re = \rho V_{ref} c / \mu \qquad (2)$$

Where μ is the air viscosity, V_{ref} is the relative wind velocity and c is the chord length of the airfoil.

Assuming the chord of the middle section of the blade is 0.46m, the Reynolds number can be calculated based on the relative wind velocity V_{ref}, which is calculated from the velocity triangle at the middle section of the blade. This paper focuses on optimizing the performance of the blade operating between the cut-in wind speed and rated wind speed due to we assume that the power output of the generator will remain at the rated power between the rated wind speed and cut-out wind speed. The estimated Reynolds numbers of this wind turbine is in the range of 390,000~1,100,000 for wind speed between cut-in and rated wind speed. Figure 1 depicts the Cl/Cd of S809 airfoil against the interested attack angles from 0 to 20° with Reynolds number in the range of 300,000~1,200,000[7].

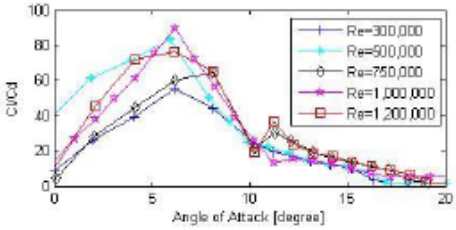

Fig. 1. Cl/Cd of S809 with Reynolds number in the range of 300,000~1,200,000

A moderate Reynolds number is generally chosen as the design Reynolds number for wind turbine blade design.

Therefore, in the preliminary design, Reynolds number 750,000[1] is chosen as the design Reynolds number, the lift coefficient is 0.9 and maximum lift/drag ratio is 64.7482 at attack angle 8.1°, which is selected as the design attack angle.

4. PRELIMINARY BLADE DESIGN

The blade geometry is divided into 10 elements. Figure 2 and Figure 3 show the initial chord and twist angle distributions, which are obtained with Schmitz rotor theory[3].

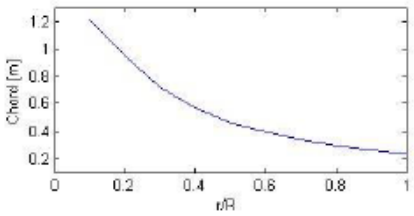

Fig.2. Chord distribution

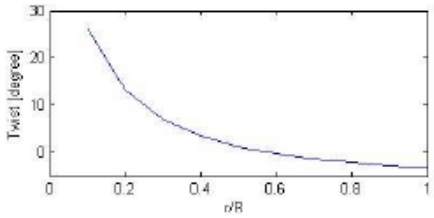

Fig.3. Twist angle distribution

5. ROTOR PERFORMANCE ANALYSIS

5.1 Rotor performance analysis ignoring Reynolds number effects

If the Reynolds number effects are ignored, the performance parameters of each blade element can be calculated through the following iterative method [3, 8]:

Step 1: Guess an initial value for the axial induction factor a and angular induction factor a'.

Step 2: Begin the iterative solution procedure for the jth iteration of the ith blade element. For the first iteration, $j=1$. Calculate the angle of the relative wind $\varphi_{i,j}$ and tip loss factor $F_{i,j}$.

Step 3: $C_{l,i,j}$ and $C_{d,i,j}$ can be obtained from the airfoil aerodynamic model using:

$$\alpha_{i,j} = \varphi_{i,j} - \theta_{p,i} \qquad (3)$$

where $\alpha_{i,j}$ and $\theta_{p,i}$ are the attack angle and twist angle at the ith blade element respectively.

Step 4: Update a and a' considering the drag effect for the next iteration.

Step 5: If the deviation between the current and previous induction factors is within an acceptable tolerance, then calculate other performance parameters, such as φ_i and λ_i; otherwise start the procedure again from step 2.

Having obtained the performance parameters of each blade element, the torque generated by the blade element is equal to:

$$dQ_i = B\frac{1}{2}\rho V_{ref,i}^2 (C_{l,i}\sin\varphi_i - C_{d,i}\cos\varphi_i) c_i r_i dr \qquad (4)$$

where B is the blade number, c_i is the chord length at the ith blade element, r_i is the distance from the ith blade element to the rotor center.

The total torque and rotor power output can be calculated from:

$$P = \Omega Q = \Omega \sum_{i=1}^{n} dQ_i \qquad (5)$$

where Ω is the angular velocity of the wind turbine rotor.
The power coefficient can be determined by:

[1] The Reynolds number effects may be different if a different Reynolds number is selected in the preliminary design.

$$C_P = P/(0.5 * \rho \pi R^2 V^3) \quad (6)$$

Based on the above method, a Matlab program has been developed to calculate the $C_P - \lambda$ curve. As shown in Figure 4, the result from the Matlab program agrees with that from GH-Bladed software very well.

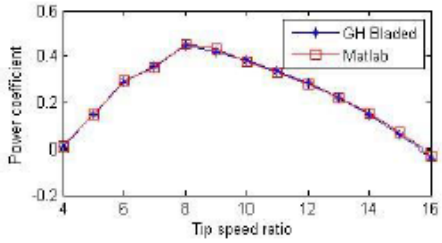

Fig.4. $C_p - \lambda$ curve

5.2 Rotor performance analysis considering Reynolds number effects

Figure 4 shows that the power coefficient is related only to the tip speed ratio, which ignores the Reynolds number effects. This means that if the tip speed ratio remains the same, the power coefficient will remain the same when the wind speed varies. However, in practice this is invalid due to the fact that variable wind speed will affect the Reynolds number, which in turn has influence on the aerodynamic performance of the airfoil and the power coefficient of the blade. Therefore Reynolds number effects should be considered to improve the accuracy of the blade aerodynamic analysis.

In order to account for Reynolds number effects, another step in the iterative procedure, defined as Step 2b here, should be added between Steps 2 and 3.

Step 2b: Calculate the relative wind speed and Reynolds number:

$$V_{reff,i,j} = V(1-a_{i,j})/\sin\varphi_{i,j} \quad (7)$$

$$Re = \rho V_{reff,i,j} c_i / \mu \quad (8)$$

Apart from that, Step 3 should be changed to:

Step 3a: Use Equation (3) to calculate the attack angle.

Step 3b: Determine $C_{l,i,j}$ and $C_{d,i,j}$ through interpolation based on the aerodynamic models of the airfoil under different Reynolds numbers (please refer to Figure 1).

Based on the above method, the power coefficient of the blade at the design tip speed ratio 8 is recalculated, as shown in Figure 5, which indicates an apparent effect of the Reynolds number on the power coefficient at different wind speed.

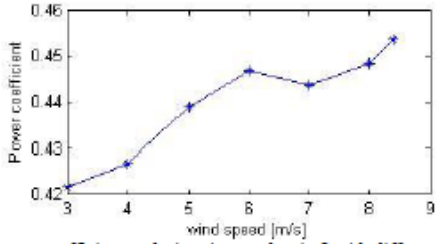

Fig.5. Power coefficient at design tip speed ratio 8 with different wind speeds

Based on Eq.(1), the calculated AEP which includes Reynolds number effects is 92,103kWh for annual mean wind speed (AMWS) 6m/s.

6. BLADE DESIGN OPTIMIZATION

6.1 Optimization method

The chord and twist angle distributions of the preliminary blade design are determined based on the airfoil aerodynamic data at the specific Reynolds number 750,000. However, the operating wind turbine blade elements experience different Reynolds numbers due to variable wind speed and different blade span locations. Therefore, the preliminary blade design does not necessarily provide the best power performance under practical operation conditions with different Reynolds numbers along the blade span.

In order to find out whether a modified chord and twist angle distribution can make a difference on the power performance considering the Reynolds number effects, a strip is defined along the chord distribution and twist angle distribution, as shown in Figure 6. There are two main reasons for choosing the boundaries of the strips of the chord and twist angle distributions:

1) The preliminary blade design is already an optimal design based on Schmitz rotor design theory ignoring Reynolds number effects at different blade elements. Therefore, it is believed that the best chord and twist angle of each blade element considering Reynolds number effects should be close to the preliminary design value.

2) Apart from considering the lowest AEP, the cost of the blade manufacture should be also considered. Therefore, the preliminary chord distribution is chosen as the upper boundary of the chord distribution.

In order to narrow the range of the chord and twist angles for each blade element and thereby reducing the calculation time, the boundaries of the strips are determined by means of offsetting the preliminary chord and twist distributions, as shown in figure 6, which are based on the following equations:

$$c_{i,n} = (c_{i,0} - 0.3) + 0.3\frac{(n-1)}{N} \qquad n = 1,2,...,N+1 \qquad (9)$$

$$\theta_{i,n} = (\theta_{i,0} - 6) + 12\frac{(n-1)}{N} \qquad n = 1,2,...,N+1 \qquad (10)$$

where n indicates the n th case, $c_{i,n}$ and $\theta_{i,n}$ are the chord and twist angle at the i th blade element of the n th case respectively. $c_{i,0}$ and $\theta_{i,0}$ are the chord and twist angle at the i th blade element of preliminary blade respectively, N is the number of divisions.

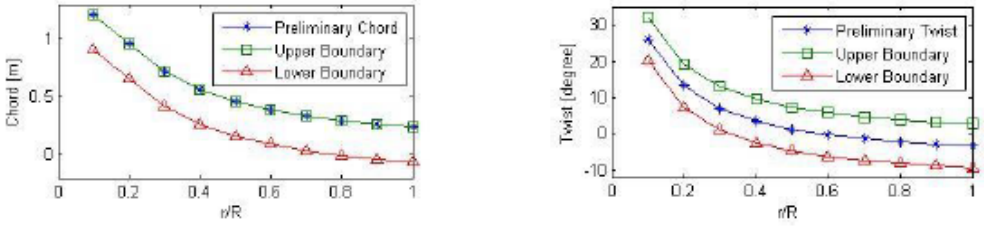

a) Chord Boundary b) Twist Boundary

Fig. 6. Chord and twist angle boundary

Once the strip boundaries of the chord and twist angle distributions are defined, a Matlab program is developed to account for Reynolds number effects on each blade element based on the method described in section 5.2, which is then used to calculate the performance of each combination of the chord and twist angles from the specified range. Through searching and comparing all the combinations, the optimal chord and twist angle of each blade element can be determined. The criterion used for the optimization is the highest annual energy production (AEP).

6.2 Result

Assuming the number of divisions N is 30 for Eq. (9) and N is 120 for Eq. (10) results in 3751 combinations with 31 choices of chord and 121 choices of twist angle for each blade element. Through comparing the AEP of all the combinations for each blade element, the optimal blade is determined. The distributions of the chord and twist angle and power coefficient of the optimal blade are depicted in Figures 8 and 9 along with the distributions of those of the

preliminary blade.

Figure 7 shows that the chord distribution of the optimal design is almost identical to the preliminary design, and the twist angle distribution is slightly improved with a reduced twist angle difference between the blade root and blade tip. Figure 8 demonstrates an apparent improvement of the power coefficient of the optimal blade comparing to the preliminary blade.

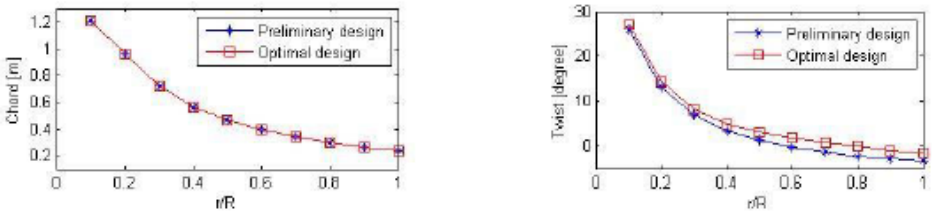

a) Chord distributions b) Twist distributions

Fig. 7. Chord and twist angle distributions of the optimal blade and the preliminary blade

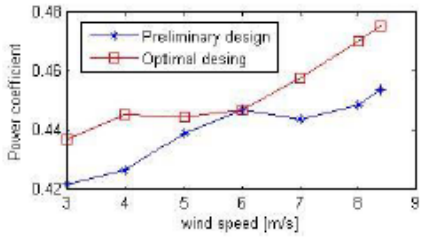

Fig. 8. Power coefficient of the optimal blade and the preliminary blade

The calculated AEP of the wind turbine with the optimal blade for AMWS 6m/s is 93,423kWh, which is 1.4% higher than that of the preliminary blade.

7. CONCLUSIONS

This paper presents a heuristic approach for the blade design optimization for a fixed-pitch variable-speed (FPVS) wind turbine operating at different Reynolds numbers through the case study of a 25kW baseline wind turbine with S809 airfoil. The case study demonstrates that considering the Reynolds number effects on the aerodynamic model of the airfoil, an optimal blade design is achieved through searching the optimal chord and twist angle for each blade element within a specific range of options. Comparing with the preliminary blade design, the optimal design offers 1.4% improvement of annual energy production at the design annual mean wind speed 6m/s for the baseline wind turbine.

References

[1] T. Guo, D. Wu, J. Xu, and S. Li, "The method of large-scale wind turbine blades design based on Matlab programming," 2009, pp. 1-5.

[2] L. Dong, M. Liao, Y. Li, X. Song, and K. Xu, "Study on Aerodynamic Design of Horizontal Axis Wind Turbine Generator System," 2009, pp. 841-844.

[3] J. F. Manwell, J. G. McGowan, and A. L. Rogers, *Wind energy explained*: Wiley Online Library, 2002.

[4] E. Hau, *Wind turbines: fundamentals, technologies, application, economics*: Springer Verlag, 2006.

[5] I. E. Commission, "IEC 61400-2: Wind Turbines–Part 2: Design requirements for small wind turbines," IEC, 2006.

[6] A. Tabesh and R. Iravani, "Small-signal dynamic model and analysis of a fixed-speed wind farm-a frequency response approach," *Power Delivery, IEEE Transactions on*, vol. 21, pp. 778-787, 2006.

[7] M. Hand, D. Simms, L. Fingersh, D. Jager, J. Cotrell, S. Schreck, and S. Larwood, "Unsteady aerodynamics experiment phase VI: Wind tunnel test configurations and available data campaigns. Rapport technique," NREL/TP-500-29955, National Renewable Energy Lab., Golden, CO.(US)2001.

[8] E. Bossanyi, "GH bladed theory manual," *GH & Partners Ltd,* 2003.

G5. Paper 5

Lin Wang, Xinzi Tang, and Xiongwei Liu, "Blade Design Optimisation for Fixed-Pitch Fixed-Speed Wind Turbines," *ISRN Renewable Energy*, vol. 2012, Article ID 682859, 8 pages, 2012. doi:10.5402/2012/682859

International Scholarly Research Network
ISRN Renewable Energy
Volume 2012, Article ID 682859, 8 pages
doi:10.5402/2012/682859

Research Article

Blade Design Optimisation for Fixed-Pitch Fixed-Speed Wind Turbines

Lin Wang, Xinzi Tang, and Xiongwei Liu

Wind Energy Engineering Research Group, School of Computing, Engineering and Physical Sciences, University of Central Lancashire, Preston PR1 2HE, UK

Correspondence should be addressed to Xiongwei Liu, xliu9@uclan.ac.uk

Received 7 April 2012; Accepted 4 July 2012

Academic Editors: A. Bosio, B. S. Hyun, and Z. A. Zainal

Fixed-pitch fixed-speed (FPFS) wind turbines have some distinct advantages over other topologies for small wind turbines, particularly for low wind speed sites. The blade design of FPFS wind turbines is fundamentally different to fixed-pitch variable-speed wind turbine blade design. Theoretically, it is difficult to obtain a global mathematical solution for the blade design optimisation. Through case studies of a given baseline wind turbine and its blade airfoil, this paper aims to demonstrate a practical method for optimum blade design of FPFS small wind turbines. The optimum blade design is based on the aerodynamic characteristics of the airfoil, that is, the lift and drag coefficients, and the annual mean wind speed. The design parameters for the blade optimisation include design wind speed, design tip speed ratio, and design attack angle. A series of design case studies using various design parameters are investigated for the wind turbine blade design. The design outcomes are analyzed and compared to each other against power performance of the rotor and annual energy production. The design outcomes from the limited design cases demonstrate clearly which blade design provides the best performance. This approach can be used for any practice of FPFS wind turbine blade design and refurbishment.

1. Introduction

Wind energy has been receiving more and more attention as one of the most viable renewable energy sources. Wind turbine technologies have been developed to achieve better performance for harvesting the energy in the wind in the last two decades. One of the major R&D areas for wind turbine technology development is blade design optimisation [1].

For small- and medium-size wind turbines, fixed-pitch or stall-regulated horizontal-axis wind turbine is one of the two common topologies in both research and industrial sectors, and the other one is pitch-controlled wind turbine [2].

For fixed-pitch wind turbines, there are two different rotor speed control strategies, that is, fixed speed and variable speed [2, 3].

Due to the nature of fixed-speed control, a fixed-pitch fixed-speed (FPFS) wind turbine uses asynchronous or induction generator with gearbox connected to the rotor, and the generator can be directly tied to the grid [2].

Because of the unique advantage of direct grid connection using asynchronous generators, even though with relative lower rotor power coefficient C_{PR} than its variable-speed version at wind speed away from design wind speed, there are still much interest in both research and industrial sectors in developing efficient wind turbines of the type [4–6].

It is obvious that the rotor design of fixed-speed wind turbines differs from variable-speed wind turbines. There are a few questions to ask so as to determine an optimal rotor or blade design. What is the optimal design wind speed given the rated power of the wind turbine and wind resources, that is, annual mean wind speed? What is the optimal rotor speed for the wind turbine? What is the best attack angle for the blade design given the blade airfoil and its aerodynamic characteristics?

Compared to variable-speed wind turbines which use complicated converters for grid connection, fixed-speed wind turbines have the advantageous of being simple, robust, and reliable, well proven and of low cost [5]. Venkatesh

and Kulkarni's research work demonstrated that with high values of Weibulls shape parameter, FPFS wind turbines are fairly competitive in terms of annual energy production (AEP), which is about 88% of its variable-speed version [6]. Therefore, they are used widely in small and medium wind energy market [7].

Blade aerodynamic design and analysis is the first step to achieve the expected power performance. The blade design parameters include airfoil shape, design attack angle, design tip speed ratio, and rated wind speed, which are to be considered in the wind turbine blade aerodynamic design stage. The selection of these blade parameters is often based on blade element momentum (BEM) theory [8].

Further blade design optimisation is essential to achieve a better power performance. Previous research indicates that wind turbine blade design optimisation has been carried out based on BEM theory, generally in an iterative way [9]. Bak's research work on the sensitivity of key parameters in wind turbine blade design on power performance demonstrated that the design tip speed ratio should be between 5.5 and 8.5 depending on the airfoil performance [10].

Researchers have been trying to use advanced computational fluid dynamics (CFD) methods for wind turbine blade design optimisation. For example, CFD was used by Thumthae and Chitsomboon to calculate the optimal attack angles so as to achieve maximum power outputs for an untwisted horizontal axis wind turbine blade [11]. This is partly due to the flows passing through and around the rotating blades tending to interact, which can only be modelled in 3D flow domain. The other reason is that 2D aerodynamic data from wind tunnel testing are generally not available at high attack angles. At a high attack angle, the flow around the airfoil starts to separate, which leads to stall. 3D CFD aerodynamic models have been therefore developed with the aim to obtain a detailed 3D flow but have not yet become a well-accepted engineering tool due to uncertainties [12]. It remains a challenge to predict the stall accurately, which is typical for FPFS wind turbines under high winds or high attack angles. The aerodynamic behaviours of rotating wind turbine blades at high attack angles have not been fully understood.

Modern artificial intelligence (AI) control algorithms are also used in wind turbine blade design optimisation. For example, artificial neural networks were also presented to estimate the optimal tip speed ratio for wind turbines [13, 14]. However, the AI optimization methods are dealing with individual design parameters, which are intertwined and should be considered simultaneously. There is a need to address the selection principles of these parameters before executing blade design codes and evaluate the impacts of these parameters on the annual energy production (AEP).

This paper aims to demonstrate a practical method for the blade design optimisation for FPFS wind turbines through a 10 kW wind turbine blade design case study using airfoil DU93W210 based on maximum AEP for low wind speed sites and, in particular, to highlight the importance of selection of the design wind speed, design tip speed ratio, and design airfoil attack angle for the optimum blade design.

In this paper, we put together different design cases of the wind turbine blade and we use the Schmitz rotor theory [8] to estimate the shape of blades. Then, we use GH-Bladed [15] to calculate the performance of these blades. The modelling of rotor aerodynamics provided by GH-Bladed is based on the blade element momentum (BEM) theory [8]. The criterion for the optimisation used in this paper is the highest AEP based on a particular wind speed Weibulls distribution.

This paper is structured in the following way. For a comprehensive understanding of the methodology, we briefly summarize the AEP calculation in Section 2. The baseline wind turbine is then introduced in Section 3. The design parameters are discussed in Section 4. Section 5 details the case studies with findings. Section 6 concludes the paper with recommendations.

2. Annual Energy Production Calculation [16]

2.1. Wind Turbine Generator Power. The power output of a wind turbine generator can be expressed as

$$P = \frac{1}{2}\eta C_{\mathrm{PR}} \rho A v^3, \tag{1}$$

where η is the transmission efficiency of the wind turbine, including both mechanical and electrical efficiency, C_{PR} is the rotor power coefficient of the wind turbine, $C_P = \eta C_{\mathrm{PR}}$ is the power coefficient of the wind turbine, ρ is the air density, $A = \pi R^2$ is the rotor swept area, and v is the wind velocity.

2.2. Wind Speed Weibulls Distribution. The wind power density is given by

$$p_w = \frac{1}{2}\rho v^3. \tag{2}$$

The annual mean wind power density can be expressed as

$$\overline{P}_w = \frac{1}{2}\rho \times \frac{1}{8760} \times \int_{\mathrm{year}} v^3 dt. \tag{3}$$

Considering the natural wind speed frequency distribution throughout the year, that is, Weibulls distribution:

$$f_{\mathrm{Weibulls}}(v) = \frac{k}{a}\left(\frac{v}{a}\right)^{k-1} \exp\left(-\left(\frac{v}{a}\right)^k\right), \tag{4}$$

where k is the shape parameter and a is the scale parameter, which depends on the wind resource of the site. The characteristics of wind resources differ from site to site.

Then, we have the annual mean wind power density:

$$\overline{P}_w = \frac{1}{2}\rho v^3 f_{\mathrm{Weibulls}}(v). \tag{5}$$

If the shape parameter is unknown, the calculation of the AEP for a wind turbine should be based on Rayleigh distribution, which assumes a shape parameter of $k = 2$ in Weibulls distribution:

$$f_{\mathrm{Rayleigh}}(v) = \frac{\pi}{2}\frac{v}{\overline{v}^2} \exp\left(-\frac{\pi}{4}\frac{v^2}{\overline{v}^2}\right). \tag{6}$$

Table 1: Basic design parameters of the base-line 10 kW at 9 m/s wind turbine.

Generator rated power output P_r	10000 W
Transmission efficiency η	0.85%
Wind turbine rated rotor power P_{rotor}	11765 W
Number of blades B	3
Rotor diameter	9.0 m

Here, $\overline{v}$ is the annual mean wind speed (AMWS):

$$\overline{v} = \frac{1}{8760}\int_0^{\infty} f_{\text{Weibulls}}(v)dv. \quad (7)$$

2.3. Annual Energy Production. The AEP for a wind turbine for a specific site can be expressed as

$$E = 8760 \times \frac{1}{2}\eta\rho A \int_{\text{cut in}}^{\text{cut out}} v^3 C_{\text{PR}}(v) \times f_{\text{Rayleigh}}(v)dv, \quad (8)$$

where $C_{\text{PR}}(v)$ is the rotor power coefficient of the wind turbine, which is a complex function of the wind speed (or tip speed ratio) for a fixed-pitch fixed-speed wind turbine.

3. Baseline Wind Turbine

Let us start from the baseline 10 kW at 9 m/s fixed-pitch fixed-speed wind turbine with a 4-pole asynchronous generator. The basic parameters of the wind turbine are listed in Table 1.

4. Design Parameters

4.1. Rotor Speed. Due to noise issue for small- and medium-size wind turbines, which are generally installed close to properties, the wind turbine blade tip speed should not exceed 70 m/s.

For variable-speed machines, a high blade tip speed, such as between 65 m/s and 70 m/s, is normally considered, so as to achieve high rotor power coefficient C_{PR} and wind turbine power performance [10]. However, for fixed-speed machines, we should address the blade tip speed carefully.

Consider the operation wind speed from 3 m/s to 20 m/s and define the blade tip speed 68 m/s, then the tip speed ratio λ in the operation wind speed range varies from 22.667 to 3.4. This basically means at low wind speed, such as at 5 m/s, $\lambda = 13.6$, the rotor power coefficient C_{PR} will be very low [8]. If we define blade tip speed 40 m/s, then the tip speed ratio λ in the operation wind speed range varies from 13.333 to 2. Then at wind speed 5 m/s, $\lambda = 8$, which is likely to exhibit much better performance for sites with low annual mean wind speed.

Therefore, let us first consider three blade tip speeds 40 m/s, 50 m/s, and 60 m/s, which correspond to rotor speeds 84.883 rpm, 106.103 rpm, and 127.324 rpm, respectively.

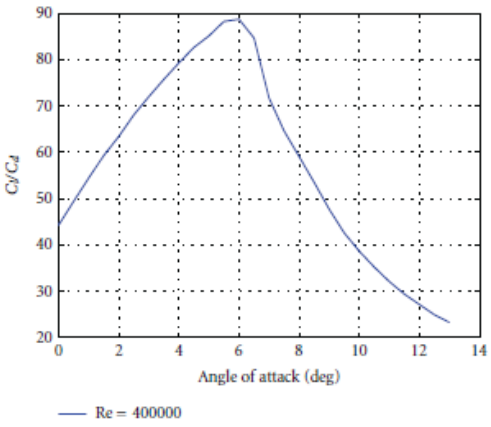

Figure 1: Lift/drag ratio of airfoil DU93W210 at Re = 400,000.

4.2. Airfoil and Design Attack Angle. The airfoil used for the baseline wind turbine is DU93W210. The airfoil performance is affected by Reynolds number, which is defined by [8]:

$$\text{Re} = \frac{\rho U L}{\mu}, \quad (9)$$

where, in terms of wind turbine airfoil, ρ is the air density, μ is the air viscosity, U is the relative wind velocity, and L is the chord length of the airfoil.

Generally, the Reynolds number of each blade section is not exactly the same. By means of estimation using the method provided by Singh et al. [17], the Reynolds number of each blade section is between $3\times10^5 - 5\times10^5$ for this wind type turbine. To simplify the design process, we choose the Reynolds number 4×10^5 as the design Reynolds number. The aerodynamic performance of DU93W210 airfoil at different Reynolds numbers can be calculated using XFoil software, which is widely used to design and analyze airfoils [18]. Figure 1 depicts the lift/drag ratio of the airfoil against the interested attack angles from 0 to 13°.

The maximum lift/drag ratio is $C_l/C_d = 88.72$ at attack angle $\alpha_0 = 6.0°$.

For the design cases, we offset one design attack angle on both side of the attack angle $\alpha_0 = 6.0°$ with maximum lift/drag ratio, with a step of 0.5° in between, and the three design attack angles are $\alpha_0 = 5.5°$, $\alpha_0 = 6.0°$, and $\alpha_0 = 6.5°$. Table 2 lists their C_l, C_d, and C_l/C_d.

4.3. Design Wind Speed and Rated Wind Speed. Different to variable-speed machines, there are two sets of wind speed we should consider for fixed-speed machine, that is, maximum power coefficient wind speed and rated wind speed V_{rated}. We call the former the design wind speed V_{design}, which means at this wind speed, the rotor power coefficient C_{PR} achieves

Table 2: Design attack angles and aerodynamics characteristics of DU93W210 airfoil.

α_0 (°)	C_l	C_d	C_l/C_d
5.5	1.129	0.0128	88.20
6.0	1.180	0.0133	88.72
6.5	1.219	0.0144	84.65

Table 3: Design tip speed ratio λ_0 for the chosen blade tip speeds and design wind speeds.

	40 m/s	50 m/s	60 m/s
5.5 m/s	7.273	9.091	10.909
6.5 m/s	6.154	7.692	9.231
7.5 m/s	5.333	6.667	8
8.0 m/s	5	6.25	7.5
8.5 m/s	4.706	5.882	7.059
9.0 m/s	4.444	5.556	6.667

Table 4: Design blade tip speed.

	$\lambda_0 - 5$	$\lambda_0 - 6$	$\lambda_0 - 7$	$\lambda_0 - 8$	$\lambda_0 - 9$	$\lambda_0 - 10$
5.5 m/s			38.5	44	49.5	55
6.5 m/s		39	45.5	52	58.5	65
7.5 m/s	37.5	45	52.5	60	67.5	
8.0 m/s	40	48	56	64		
8.5 m/s	42.5	51	59.5	68		
9.0 m/s	45	54	63			

its maximum value. At the rated wind speed V_{rated}, the rotor power achieves its nominal power output.

In terms of the Rayleigh distribution of wind speed, wind turbine blade design should try to focus on the best power performance at prevailing wind speed range. For sites with low wind speed, the prevailing wind speed varies between 4 m/s and 8 m/s.

Therefore, let us consider the design wind speeds V_{design} at 5.5 m/s, 6.5 m/s, 7.5 m/s, 8.0 m/s, 8.5 m/s, and 9.0 m/s.

Then, we have the design tip speed ratio λ_0 in terms of the blade tip speeds in Section 4.2, which are listed in Table 3.

Now we have 18 different blade tip speed ratios listed in Table 3. Obviously there is no point to consider all of them. Let us choose 5, 6, 7, 8, 9, and 10 as the design tip speed ratio λ_0 for the design cases, then we have 18 combinations of design cases with three attack angles (as listed in Table 2).

For the operation, let us consider the combinations of tip speeds listed in Table 4.

Take the example of $\lambda_0 = 5$, at design wind speed 7.5 m/s, the tip speed is 37.5 m/s, there are three design cases with $\alpha_0 = 5.5°$, $\alpha_0 = 6.0°$, and $\alpha_0 = 6.5°$, respectively.

During the design exercise, we should make sure that the maximum rotor power output does not exceed 11,765 W*120% = 14,118 W. We are designing a 10 kW wind turbine, the maximum overloading to the generator is 120%, and we should rule out any case with maximum rotor power output over 14,118 W. Otherwise, we are not talking about 10 kW wind turbine. Additionally, with this approach, the rated wind speeds will result from further calculation and analysis.

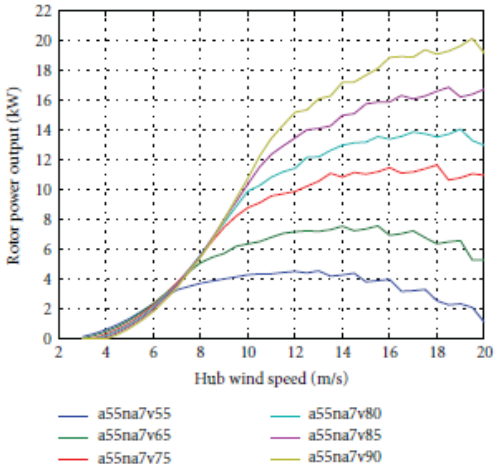

Figure 2: Rotor power output based on $\alpha_0 - 5.5°$ and $\lambda_0 - 7$.

5. Design Case Studies

5.1. With Different Design Wind Speeds. Let us first consider design attack angle $\alpha_0 = 5.5°$ and design tip speed ratio $\lambda_0 = 7$. Using GH-Bladed we can calculate the rotor power for design wind speed $V_{\text{design}} = 5.5$ m/s, 6.5 m/s, 7.5 m/s, 8 m/s, and 9 m/s, respectively, as depicted in Figure 2.

In Figure 2, for the expression "a***na*v**", "a" represents attack angle, a55 means $\alpha_0 = 5.5°$; "na" represents design tip speed ratio, na7 means $\lambda_0 = 7$; "v" represents design wind speed, v55 means $V_{\text{design}} = 5.5$ m/s.

Figure 2 reveals that design wind speed $V_{\text{design}} = 5.5$ m/s and $V_{\text{design}} = 6.5$ m/s are too low for the wind turbine because the wind turbine rotor cannot achieve expected rotor power output 11,765 W for the whole operation wind speed range. Also, when the design wind speed is above 8.5 m/s, the rotor power output exceeds the rated power too much and therefore is not a valid design as well. We should only consider design wind speed between 7.5–8 m/s.

Figure 2 also reveals that with higher design wind speed, the rotor exhibits higher power output when the wind speed is higher than about 8 m/s; however, the rotor exhibits lower power output when the wind speed is lower than about 8 m/s. Figure 3 enlarges the figure section for the wind speed between 3–8 m/s. This figure also indicates that higher design wind speed means higher cut-in wind speed.

Figure 4 shows the annual energy production (AEP) for annual mean wind speed (AMWS) from 3.5 m/s to 8 m/s, and Figure 5 enlarges the figure section for AMWS between 3.5–4.5 m/s.

Figures 4 and 5 reveal that with higher than 4.5 m/s AMWS, higher design wind speed exhibits higher AEP.

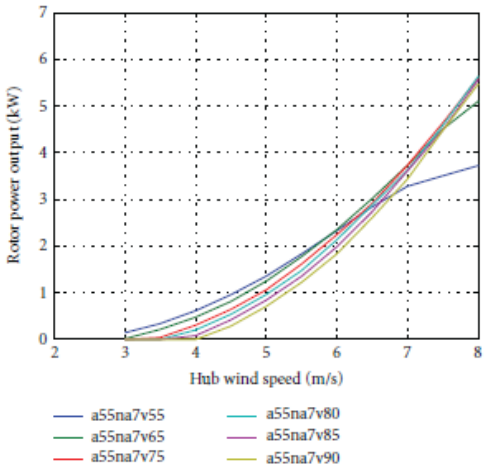

FIGURE 3: Rotor power output based on $\alpha_0 = 5.5^\circ$ and $\lambda_0 = 7$ for wind speed between 3–8 m/s.

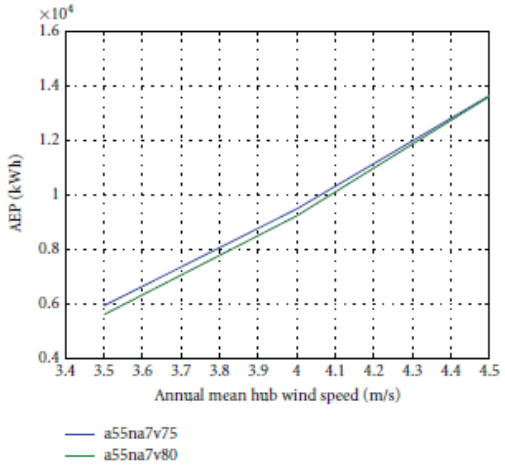

FIGURE 5: AEP based on $\alpha_0 = 5.5^\circ$ and $\lambda_0 = 7$ for AMWS between 3.5–4.5 m/s.

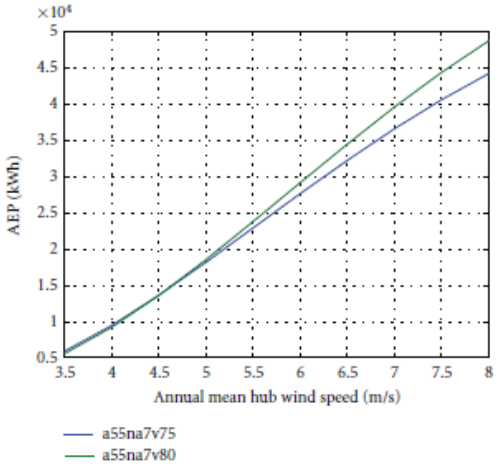

FIGURE 4: AEP based on $\alpha_0 = 5.5^\circ$ and $\lambda_0 = 7$ for AMWS between 3.5–8 m/s.

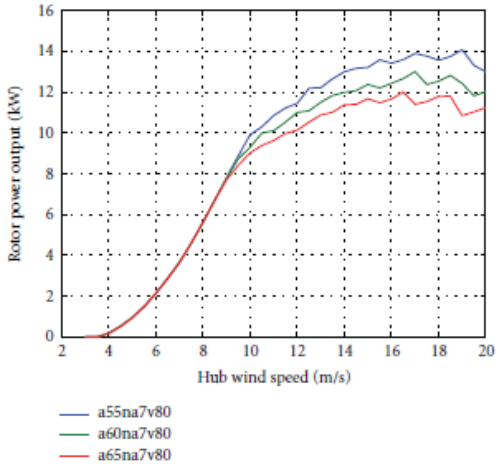

FIGURE 6: Rotor power output based on $V_{design} = 8$ m/s and $\lambda_0 = 7$.

However when the AWMS is less than 4.5 m/s, things are different. Generally when the AMWS is less than 4.5 m/s, wind energy project should not be considered. Therefore, we can conclude here that design wind speed 8 m/s exhibits better power performance than design wind speed 7.5 m/s.

5.2. With Different Design Attack Angles. Now let us consider different design attack angles by keeping design wind speed $V_{design} = 8$ m/s and design tip speed ratio $\lambda_0 = 7$. Figure 6 depicts the rotor power performances of this set of design cases.

Similar to Figure 2, in Figure 6, for the expression "a***na*v**", "a" represents attack angle, a55 means $\alpha_0 = 5.5^\circ$; "na" represents design tip speed ratio, na7 means $\lambda_0 = 7$; "v" represents design wind speed, v80 means $V_{design} = 8.0$ m/s.

Figure 7 shows the annual energy production (AEP) for annual mean wind speed (AMWS) from 3.5 m/s to 8 m/s.

Figures 6 and 7 demonstrate that $\alpha_0 = 5.5^\circ$ exhibits better power performance than $\alpha_0 = 6.0^\circ$ and $\alpha_0 = 6.5^\circ$, even though the maximum lift/drag ratio appears at attack angle $\alpha_0 = 6.0^\circ$.

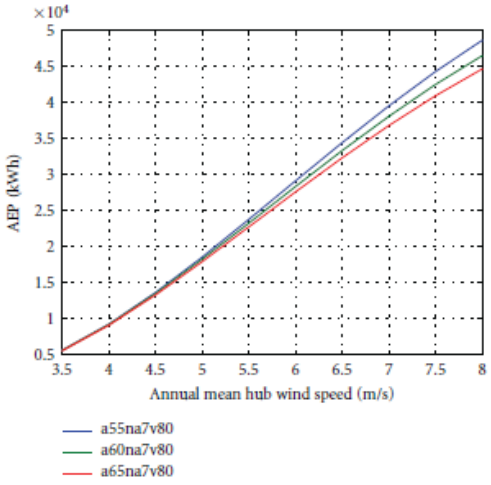

FIGURE 7: AEP based on V_{design} = 8 m/s and λ_0 = 7 for AMWS between 3.5–8 m/s.

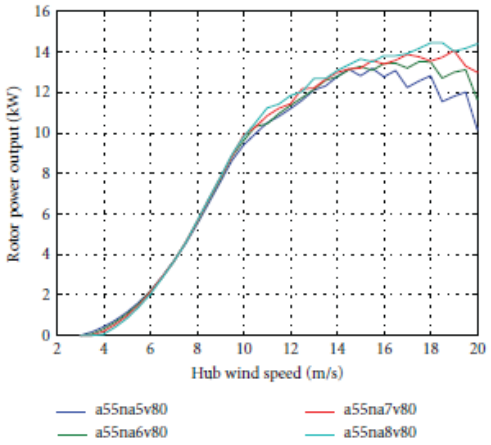

FIGURE 8: Rotor power output based on V_{design} = 8 m/s and α_0 = 5.5°.

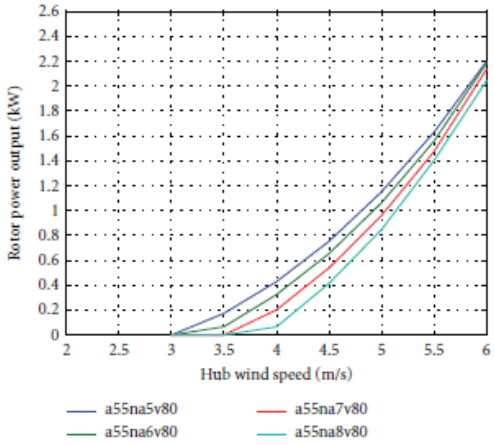

FIGURE 9: Rotor power output based on V_{design} = 8 m/s and α_0 = 5.5° for wind speed between 3–6 m/s.

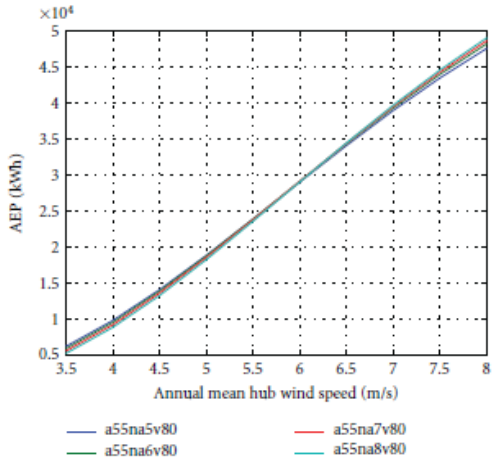

FIGURE 10: AEP based on V_{design} = 8 m/s and α_0 = 5.5° for AMWS between 3.5–8 m/s.

5.3. With Different Design Tip Speed Ratio. Now let us consider different design tip speed ratio by keeping design wind speed V_{design} = 8 m/s and design attack angle α_0 = 5.5°. Figure 8 depicts the rotor power performances of this set of design cases.

Similar to Figure 2, in Figure 8, for the expression "a***na*v**", "a" represents attack angle, a55 means α_0 = 5.5°; "na" represents design tip speed ratio, na7 means λ_0 = 7; "v" represents design wind speed, v80 means V_{design} = 8.0 m/s.

Figure 8 demonstrates that with higher design tip speed ratio, the rotor exhibits higher power output when the wind speed is higher than about 7 m/s; however, the rotor exhibits lower power output when the wind speed is lower than about 7 m/s. Figure 9 enlarges the figure section for the wind speed between 3–6 m/s. This figure also shows that higher design tip speed ratio means higher cut-in wind speed.

Figure 10 shows the annual energy production (AEP) for annual mean wind speed (AMWS) from 3.5 m/s to 8 m/s, and Figure 11 enlarges the figure section for AMWS between 3.5–7.0 m/s.

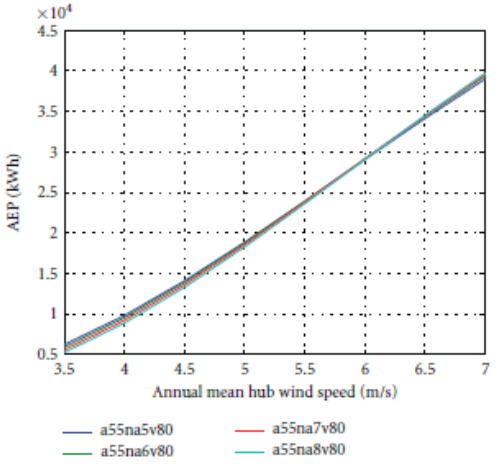

FIGURE 11: AEP based on $V_{design} = 8$ m/s and $\alpha_0 = 5.5^\circ$ for AMWS between 3.5–7.0 m/s.

Figures 10 and 11 reveal that with higher than roughly 6.35 m/s AMWS, higher tip speed ratio exhibits higher AEP. However when the AWMS is less than approximately 6.35 m/s, higher tip speed ratio exhibits lower AEP. At sites in rural areas in the UK, the AMWS is unlikely to be above 6.35 m/s at the hub height for a 10 kW wind turbine. Therefore, a low tip speed ratio should be considered, such as $\lambda_0 = 5$-6 if the AMWS is between 5 m/s and 6 m/s.

6. Conclusions and Recommendations

Through case studies, this paper demonstrates a practical selection method for determining the optimum blade design parameters, that is, design wind speed, tip speed ratio, and attack angle, for a fixed-pitch fixed-speed small wind turbine with a given baseline wind turbine and its blade airfoil. The conclusions and recommendations are as follows:

(1) the best design attack angle for fixed-pitch fixed-speed wind turbine is not necessarily the angle with the maximum C_l/C_d. For the design case, the best attack angle is $\alpha_0 = 5.5^\circ$ even though the maximum C_l/C_d appears at the attack angle $\alpha_0 = 6.0^\circ$;

(2) the design wind speed should be considered carefully for a baseline wind turbine with fixed-pitch fixed-speed control strategy. If the design wind speed is too low, the wind turbine rotor cannot achieve expected rotor power output for the whole operating wind speed range. If the design wind speed is too high, the wind turbine rotor exceeds the rated power too much. For the design case, design wind speed $V_{design} = 8$ m/s exhibits best performance for any site with annual mean speed above 4.5 m/s;

(3) in terms of design tip speed ratio for a fixed-pitch fixed-speed wind turbine, low tip speed ratio is recommended when the annual mean wind speed is low. However, high tip speed ratio yields more energy when the annual mean wind speed is high. For the design case, $\lambda_0 = 5$-6 should be considered if the annual mean wind speed is between 5 m/s and 6 m/s;

(4) this method can be used for any practice of fixed-pitch fixed-speed wind turbine blade design;

(5) this method can be used for wind turbine blade refurbishment. Due to use of the existing gearbox and generator, the rotor speed is fixed, and there is very limited space to change the rotor diameter and blade tip speed. Therefore, when selecting the design attack angle, design wind speed and design tip speed ratio according to the findings of this paper, the above constraint should be considered.

References

[1] M. Jureczko, M. Pawlak, and A. Mężyk, "Optimisation of wind turbine blades," *Journal of Materials Processing Technology*, vol. 167, no. 2-3, pp. 463–471, 2005.

[2] F. D. Bianchi, H. D. Battista, and R. J. Mantz, *Wind Turbine Control Systems: Principles, Modelling and Gain Scheduling Design*, Springer, London, UK, 2007.

[3] P. G. Pierce and K. G. Migliore, "Maximizing energy capture of fixed-pitch variable-speed wind turbines," Tech. Rep. NREL/CP-500-27551, 2000.

[4] S. Li and T. A. Haskew, "Simulation study of fixed speed wind energy conversion system and compensation using PSpice," in *Proceedings of the International Conference on Power and Energy Systems (PES '07)*, vol. 539, January 2007.

[5] D. Saheb-Koussa, M. Haddadi, M. Belhamel, S. Hadji, and S. Nouredine, "Modeling and simulation of the fixed-speed WECS (wind energy conversion system): application to the Algerian Sahara area," *Energy*, vol. 35, no. 10, pp. 4116–4125, 2010.

[6] G. C. Venkatesh and S. V. Kulkarni, "Energy yield of passive stall regulated fixed speed wind turbine with optimal rotor speed," *Electric Power Systems Research*, vol. 76, no. 12, pp. 1019–1026, 2006.

[7] J. Zhang, A. Dyśko, J. O'Reilly, and W. E. Leithead, "Modelling and performance of fixed-speed induction generators in power system oscillation stability studies," *Electric Power Systems Research*, vol. 78, no. 8, pp. 1416–1424, 2008.

[8] J. F. Manwell, J. G. McGowan, and A. L. Rogers, *Wind Energy Explained: Theory, Design and Application*, Wiley, New York, NY, USA, 2nd edition, 2009.

[9] A. Vardar and B. Eker, "Principle of rotor design for horizontal axis wind turbines," *Journal of Applied Sciences*, vol. 6, no. 7, pp. 1527–1533, 2006.

[10] C. Bak, "Sensitivity of key parameters in aerodynamic wind turbine rotor design on power and energy performance," *Journal of Physics*, vol. 75, no. 1, Article ID 012008, 2007.

[11] C. Thumthae and T. Chitsomboon, "Optimal angle of attack for untwisted blade wind turbine," *Renewable Energy*, vol. 34, no. 5, pp. 1279–1284, 2009.

[12] M. O. L. Hansena, J. N. Sorensena, S. Voutsinasb, and H. A. Madsenc, "State of the art in wind turbine aerodynamics and

aeroelasticity," *Progress in Aerospace Sciences*, vol. 42, pp. 285–330, 2006.

[13] N. S. Çetin, M. A. Yurdusev, R. Ata, and A. Özdemir, "Assessment of optimum tip speed ratio of wind turbines," *Mathematical and Computational Applications*, vol. 10, no. 1, pp. 147–154, 2005.

[14] M. A. Yurdusev, R. Ata, and N. S. Çetin, "Assessment of optimum tip speed ratio in wind turbines using artificial neural networks," *Energy*, vol. 31, no. 12, pp. 2153–2161, 2006.

[15] E. A. Bossanyi, "GH bladed theory manual," Tech. Rep. 282/BR/009, 2008.

[16] E. Hau, *Wind Turbines: Fundamentals, Technologies, Application, Economics*, Springer, London, UK, 2nd edition, 2006.

[17] R. K. Singh, M. R. Ahmed, M. A. Zullah, and Y. H. Lee, "Design of a Low Reynolds number airfoil for small horizontal axis wind turbines," *Renewable Energy*, vol. 42, pp. 66–76, 2011.

[18] M. Drela, "XFOIL: an analysis and design system for Low Reynolds number airfoils," in *Proceedings of the Conference on Low Reynolds Number Airfoil Aerodynamics*, University of Notre Dame, June 1989.